FAKULTÄT
FÜR !NFORMATIK

Faculty of Informatics

Spatio Temporal Modelling of Dynamic Developmental Patterns

DISSERTATION

zur Erlangung des akademischen Grades

Doktorin der Technischen Wissenschaften

eingereicht von

Dipl.-Ing. Roxane Licandro, BSc

Matrikelnummer 0442108

an der Fakultät für Informatik

der Technischen Universität Wien

Betreuung: Privatdoz. Dr. techn. Dipl.-Ing. Martin Kampel
Zweitbetreuung: Assoc. Prof. Dr. techn. Dipl.-Ing. Georg Langs

Diese Dissertation haben begutachtet:

Henning Müller	Jorge Cardoso

Wien, 4. Februar 2021

Roxane Licandro

Spatio Temporal Modelling of Dynamic Developmental Patterns

DISSERTATION

submitted in partial fulfillment of the requirements for the degree of

Doktorin der Technischen Wissenschaften

by

Dipl.-Ing. Roxane Licandro, BSc
Registration Number 0442108

to the Faculty of Informatics

at the TU Wien

Advisor: Privatdoz. Dr. techn. Dipl.-Ing. Martin Kampel
Second advisor: Assoc. Prof. Dr. techn. Dipl.-Ing. Georg Langs

The dissertation has been reviewed by:

Henning Müller	Jorge Cardoso

Vienna, 4th February, 2021

Roxane Licandro

Technische Universität Wien
A-1040 Wien ▪ Karlsplatz 13 ▪ Tel. +43-1-58801-0 ▪ www.tuwien.ac.at

Erklärung zur Verfassung der Arbeit

Dipl.-Ing. Roxane Licandro, BSc
Klitschgasse 7, 1130 Wien

Hiermit erkläre ich, dass ich diese Arbeit selbständig verfasst habe, dass ich die verwendeten Quellen und Hilfsmittel vollständig angegeben habe und dass ich die Stellen der Arbeit – einschließlich Tabellen, Karten und Abbildungen –, die anderen Werken oder dem Internet im Wortlaut oder dem Sinn nach entnommen sind, auf jeden Fall unter Angabe der Quelle als Entlehnung kenntlich gemacht habe.

Wien, 4. Februar 2021

_____

Roxane Licandro

Acknowledgements

Kurzfassung

Die spatio temporale Modellierung spielt eine wichtige Rolle in der personalisierten Medizin, in virtuellen klinischen Studien oder in der Identifikation von Wirkungsspektren von Medikamenten. Diese Modellierungsform ermöglicht es Trajektorien von komplexen Erkrankungen, metabolischen Prozessen oder Entwicklungsprozessen zu kodieren, individuelle Therapien zu planen und kann für die Bestimmung und den Vergleich von Stadien herangezogen werden. Dynamische Entwicklungsmuster stellen hier die Hauptherausforderung dar, bestehend aus unvollständigen und irregulären Beobachtungen, Variabilität zwischen Patienten und einflussreichen Faktoren wie Komorbidität, Alter oder der individuellen Therapieantwort. Der Fokus dieser Arbeit liegt in der Bereitstellung und Erforschung neuer Strategien für die spatio temporale Modellierung von dynamischen Entwicklungsmustern, um Baseline-Trajektorien entkoppelt von Entwicklungs- und Krankheitsdynamiken verstehen und analysieren zu können, welche während eines Krankheitsverlaufes oder der Entwicklung auftreten. Daher ist es zum einen essentiell, geeignete Baseline-Stadien zu identifizieren und zum anderen neue Techniken zu entwickeln, die es ermöglichen Unterschiede und Beziehungen zwischen Baseline und Dynamiken zu analysieren. In dieser Arbeit wird gezeigt, dass das entwickelte Konzept im Stande ist, dynamische Entwicklungsmuster flexibel (unabhängig von der Bildmodalität für verschiedene Populationen/Altersgruppen) zu modellieren und zur Beantwortung von Forschungsfragen im Feld der Computer Vision, Krebsforschung, Hirnentwicklung und funktionalen Konnektivitätsnetzwerkanalyse herangezogen werden kann. Dies führt zur Entwicklung neuer Datenrepräsentationsformen, Segmentierungsstrategien, neuer Klassifizierungsprozeduren und zeitabhängige Vorhersagemethoden, welche state-of-the-art Ansätze übertreffen.

Abstract

Spatio Temporal Modelling plays an important role in personalized medicine, virtual clinical trials or drug target identification. It enables the encoding of trajectories of complex diseases, metabolic or developmental pathways, to optimise an individual's disease treatment or determine a developmental status. Dynamic Developmental Patterns (DDP) form the main challenge in modelling trajectories, constituted of the incompleteness and irregularity of observations, inter-patient variability and impairing factors like co-morbidity, age or individual treatment response. The focus of this thesis lies in providing new strategies for the spatio-temporal modelling of dynamic developmental patterns, to encode and understand baseline trajectories disentangled from time-dependent or systemic dynamics. Thus, on the one hand the identification of suitable baseline states is essential and on the other hand the development of techniques to analyse the dynamics' deviations and relations to the baseline. Here, it is demonstrated that the proposed modelling concept is capable to flexibly model DDPs independent of the imaging modalities, of different populations/age ranges and applications to answer research questions in the field of computer vision, cancer research, brain development and functional connectivity network analysis. It leads to the development of novel data representation forms for DDPs, segmentation strategies, classification procedures and time-dependent prediction approaches, outperforming state of the art methods.

Contents

CHAPTER 1

Introduction

"It's easier to resist at the beginning than at the end, [Leonardo da Vinci (1452 - 1519)]

Predictive modelling plays an important role in personalized medicine, virtual clinical trials, or drug target identification, since it enables the investigation of trajectories of complex diseases or developmental processes, signalling, metabolic or gene regulatory pathways. It allows to optimise an individual's disease treatment or to analyse the developmental stadium [202] [142]. DDP form the main challenge in modelling trajectories. In medicine on the one hand challenges arise according to systemic dynamics, which encompass incompleteness and irregularity of observations, interpatient variability [231] and impairing factors such as co-morbidity, age or individual treatment response. On the other hand time-dependent dynamics are present, e.g. disease evolution patterns, developmental patterns or regeneration patterns which progress in parallel. DDP in medicine are observed in the *feature domain* as a collection of selected measured features/random variables (e.g. medical record data like blood pressure, cell antigen expression, cognitive test score, age, body temperature, radiomic features, extracted biomarker etc.) or by analysing medical imaging data in 2D (e.g. X-ray), 3D (e.g. Computer Tomography (CT), Magnetic Resonance Imaging (MRI)) or 4D (e.g. functional Magnetic Resonance Imaging (fMRI)) in the *image domain*. In this thesis the modelling of DDP is studied, with the focus on the following four:

- DDP in Fetal Brain Development: The fetal brain developmental process involves a variety of dynamics. On the one hand the dynamics at specific gestation time points caused by inter subject variability, inaccuracy in determination of the gestational age or pathologies [153][197] or on the other hand changes occurring over gestation, e.g. in size according to rapid brain growth, changes in morphology, due to the progress of cortical folding, disappearing of the germinal matrix and deceleration of the proliferation of ventricular cells [204].

1

- DDP in Developing Functional Connectivity: The challenge of longitudinal studies among children to model functional connectivity trajectories is induced by the age and developmental related dynamics of the brain triggered by learning and experience (natural plasticity)[6], but also by pathology related modifications and functional and structural reorganisation (adaptive plasticity) of brain tissue [105]. After a damage, plasticity and vulnerability of the brain influence recovery together with the injuries severity, the age and the time since damage [6].

- DDP during Childhood Leukaemia: Leukaemia is a cancer disease affecting the proliferation patterns of blood cells [87][175]. The dynamics of patterns of non-leukaemic cells are intersubject variabilities according to different phenotypes, the influences by the child's developmental stage, treatment and regeneration effects, and co-morbidities [68]. The focus of leukaemia treatment is to remove leukaemic cells leading to disappearing of these cell clusters, but in case of relapse also to a reappearing of these clusters [43]. Additionally, the setup of data acquisition can cause dynamics, e.g. according to different machine calibrations, standard operating procedures for acquisitions, or country dependent regulations [162].

- DDP in MM: This disease affects the proliferation patterns of plasma cells, which further influence the bone absorption and remodelling processes [221][1]. In this disease the time-dependent dynamics of focal bone lesion development (including disappearing and appearing of lesions) as well as the evolution of diffuse bone infiltration patterns are a main challenge to assess the progression trajectories of the disease. Also influencing factors like co-morbidity, the patient's age as well as the response to therapy form a main challenge in modelling dynamics in MM.

Spatio Temporal Modelling is the process of estimating an optimal way on encoding trajectories in space and over time, where in state-of-the-art spatio-temporal modelling concepts it can be differentiated between subject-specific and time-specific approaches [54]. Subject-specific methods aim to average individual trajectories for obtaining a typical growth scenario. In this case the inter-subject variability is assumed to be constant over time (cf. Figure 1.1 (left)) and provides a reference model at each time point [54]. Time-specific modelling makes it possible to describe the inter-subject variability over time by a mean scenario of progression/development (cf. Figure 1.1 (right)) and provides a reference at each time point [54]. It can be differentiated between two strategies: (1) where the focus lies first on modelling time specific states and on defining transitions and dependencies between states and (2) in longitudinally learning the dependencies by observing the data space over all time points at once. These models can be used to optimise the treatment according to the prediction of an individual's disease progress, for performing automatic segmentation, for the assessment of shape and structural changes or for the classification of a disease or developmental stage [108][134][203][157].
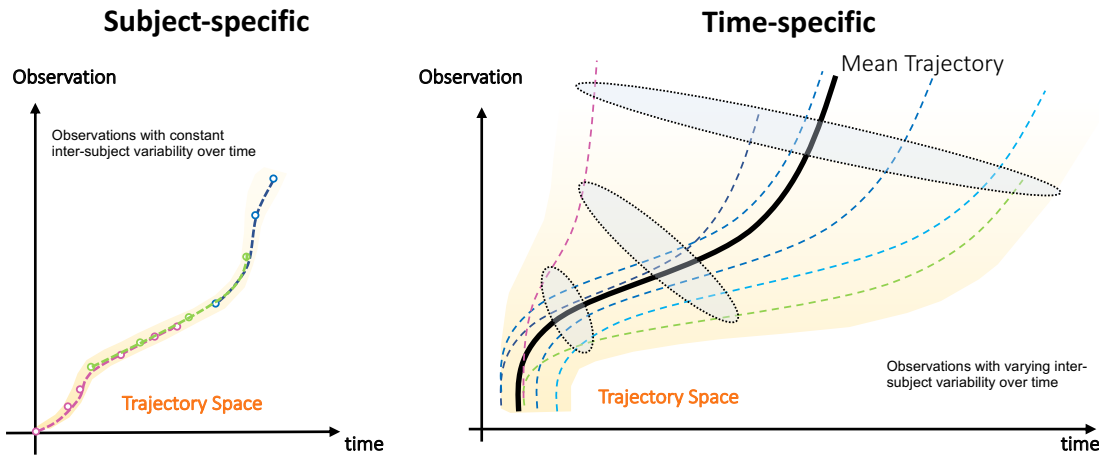
Figure 1.1: Longitudinal modelling concepts: Subject-specific trajectory modelling is visualised with assumed constant inter-subject variability over time (left) and time-specific trajectory modelling, encoding mean trajectory of development, with varying inter-subject variability over time (right). Figure inspired by [54].

1.1 Spatio Temporal Modelling of DDP - The Big Picture

In this thesis a novel Spatio Temporal Model (STM) concept for DDP is proposed involving knowledge and approaches from the fields of computer vision, statistics, medical imaging, machine learning and medicine. Here, the focus is set in the medical domain, but the concept is also applicable in domains, where time dependent dynamics are present, e.g. in the field of video analysis, progression pattern assessment in biology or spatio temporal models for weather forecasts.

1.1.1 Role of the Proposed Concept in Computer Science

Dynamics of developmental patterns especially in the medical field are versatile in space and also over time and require to be addressed in all their aspects without deciding on preserving time point specific dynamics or between time-dependent dynamics. The concept *Spatio Temporal Modelling of Dynamic Developmental Patterns* proposed in this thesis provides a novel strategy to address the gaps in current longitudinal modelling approaches and provides a strategy to handle dynamics in space and also over time. The focus lies in the disentanglement of the trajectory space into areas of (1) baseline trajectories, (2) a space addressing time-dependent dynamics and (3) systemic dynamics as illustrated in Figure 1.2 on the left. It assists to encode and understand baseline longitudinal trajectories (e.g. developmental trajectories or stable regions in videos), which are shared over observation time and within the observed data, and to address dynamics using the baseline model. Thus, on the one hand the identification of suitable baseline states and corresponding representation is essential and on the other hand the development of techniques to analyse the dynamics' deviations and relations to the

baseline.

1.1.2 The Concept

Spatio Temporal Model of Dynamic Developmental Patterns
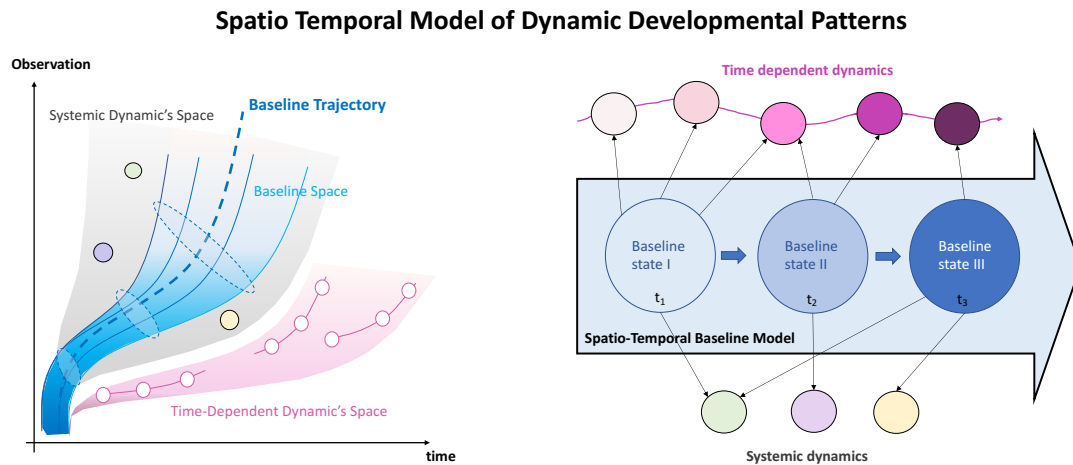
Figure 1.2: Schematic illustration of a spatio temporal model for dynamic developmental patterns with three baseline states and systemic and time-dependent dynamics.

In Figure 1.2 on the right a schematic illustration of the concept's components and their interaction patterns are visualised:

- **Baseline stadia:** These are learned from imaging and medical record data. It can be defined as a stable pattern shared within a population at a specific time point and develops over the observed time. The motivation of using a baseline formulation is to being able to model common properties and behaviour of the DDP observed and to establish time correspondence in the spatio temporal model.

- **Dynamics (time-dependent/systemic)**: Dynamics encode a disease or a sub-population related outlier property of the data. It can be categorized into *systemic dynamics* and into *time-dependent* dynamics. *Systemic dynamics* are present at defined time points or at all timepoints, i.e. one or more baseline states can have the same systemic dynamics. These dynamics show no explicit progression behaviour over time, but interaction patterns with time specific baseline states. *Time-dependent dynamics* can be entangled from the trajectory of the baseline state and encode a separate progression pattern over time. Within this thesis it is investigated if dynamics can be addressed and identified using baseline-states and how data is representable by a combination of base-line and dynamic states.

- **State Transitions:** The third component of the concept summarizes the following three types of transitions: (1) Transitions that connect baseline stadia with each other. These encode the common trajectory over the observed time span. (2)

4

Transitions which connect a baseline state with a systematic dynamic, it encodes the combination strategy between outlier and baseline components and the relation between these, as well it enables to model dynamic appearance or disappearance of outlier states. (3) Transitions between time-dependent dynamics, which do not necessarily follow the time-dependencies of a baseline trajectory.

1.1.3 Application of the Concept

In the (medical) computer vision field the proposed spatio-temporal model can be used for the *classification* of a developmental stadium or a stadium during (disease) progression, a new input is classified by aligning a time-corresponding baseline state and by consequently analysing the baseline specific identified outlier properties. Also for morphometric analysis the STM can be used to encode developing (anatomical) structures as a baseline and consequently be used in an atlas-based *segmentation* procedure. A further application of the concept proposed is the *prediction* of a future state given a pre-state. A future state is predicted by first aligning the current state with its corresponding time-specific basis component. Subsequently, the spatio-temporal model is used to estimate the trajectory to the desired state and predicts the future outcome and aligns an observation with the information of a subsequent time point.

An example of using the concept in computer vision would be e.g. the modelling of DDP of human behaviour to predict these in video based observations. In this case the concept can be used to disentangle the baseline appearance of the environment over time (background), the person specific pose variations (systemic dynamics which interact with the baseline), and the variability of pose sequences (time-dependent dynamics). Prediction could be performed by first determining the baseline-state of the environment, subsequently detecting when a person enters the scene (baseline based anomaly detection), and predicting the behaviour based on the observed baseline and dynamics.

1.2 Research Questions and Contribution of this Thesis

Research questions in this thesis are divided into questions regarding the spatio temporal concept proposed and field specific research questions. In total four different types of DDPs are observed in this thesis. The underlying dynamics and processes modelled in this work as well as the corresponding medical background are summarized in Chapter 2: *"Understanding Dynamic Developmental Patterns in Medicine"*. Within this thesis graph-based, embedded-based, density-based and image-based representation techniques are analysed for FlowCytoMetry (FCM) data, T2 fetal MRI, resting state functional Magnetic Resonance Imaging (rsfMRI) and T1 whole body Magnetic Resonance Imaging (wb-MRI) (cf. Chapter 4:*"Datasets of Dynamic Developmental Patterns"*). This thesis documents how the modelling concept can be used to extract baseline properties for different imaging modalities and representation techniques, how dynamics can be separated from stable patterns and how dynamics can be described using the baselines (cf. Chapter 5: *"Time Specific Analysis of Disentanglement Strategies in Space"*). The proposed spatio temporal

models (cf. Chapter 6:*"Spatio Temporal Modelling of Dynamic Developmental Patterns"*) are specifically designed for four different DDPs, however all modelling strategies follow the concept proposed in this thesis. The contribution of this thesis can be summarized by the following key points:

1. Identifying suitable approaches for the representation of DDP for medical data in the feature and image domain.

2. Development of a novel concept for creating a STM, which provides novel strategies to flexibly encode DDP in space and over time.

3. Testing the proposed concept and its applicability on different data types, patient cohorts and research fields.

The following subsections summarize the field specific motivation, contributions and research questions, which are grouped by the medical research fields covered by this thesis.

1.2.1   STM of Fetal Brain Development

Motivation: The development of the human brain is a complex process guided by an orchestrated interplay of environmental factors and genetic programs, starting in early pregnancy. Its maturation continues through adulthood and lasts until senescence [169]. For the comparison of brains of adult patients an atlas (reference model) is required as a standard space, where the brains are mapped to a standardized coordinate system according to marked anatomical locations. However, the fetal brain is a developing structure, which undergoes structural changes in size and in morphology between the second and the third trimester of pregnancy. In comparison to building an atlas of an adult brain, the fast change of a fetal brain due to rapid growth and the progress of cortical folding has to be taken into account. Also, fetal brains at a certain Gestation Week (GW) show differences in shape and size. Possible reasons are the inaccuracy in determination of the gestational age, inter-patient variability or pathological growth processes [153][197]. The motivation for building a spatio temporal model of fetal brain development is the possibility to achieve comparability between fetal brains for studying brain development, fetal pathology locations, fetal abnormalities or anatomy.

Research Questions: What are the morphological dynamics affecting the brain anatomy during gestation? How can these properties be encoded in a spatio temporal model? How can this model be used for automatic fetal brain tissue segmentation? Is it possible to encode the dynamics in a single baseline time-dependent deformation field?

Dataset: In this work the time-series dataset *FETAL* is used, which is introduced in Section 4.1. It contains 45 fast-spin echo T2 weighted MRI acquisitions of fetuses between GW 18 - 30.

Contribution: In this work the concept proposed is used to create a spatio temporal brain model (atlas) for the automatic segmentation of the developing fetal brain. Therefore, a fetal brain tissue (cortex, ventricle) labeling framework from GW 18 to GW 30 is proposed, by incorporating a baseline longitudinal fetal brain atlas and a labeling procedure. In this work it is demonstrated that geodesic image regression is capable to build a spatio-temporal atlas of the fetal brain and is able to model a mean trajectory encoding the changes occurring during brain development as a baseline in a single diffeomorphic deformation. This learned deformation is parametrizable by gestational age and can be used to transform Magnetic Resonance (MR) acquisitions as well as brain tissue annotations to a specific time point in gestation, i.e. to provide a gestation specific atlas. This proposed STM of fetal brain development for tissue segmentation is presented and discussed in more detail in Section 6.1.

Results: It is demonstrated that the morphological dynamics of the developing fetal brain can be encoded in a spatio temporal atlas using a novel geodesic image regression registration scheme. The proposed STM acts as an estimator for time-dependent baseline (atlas-based) segmentations, while the occurring subject and time dependent dynamics of brain growth, cortical folding as well as ventricular thinning are addressed by a graph-cut based labeling procedure, and age range dependent regularizations. The automatic tissue labeling framework estimates cortical labels with a Dice Coefficient (DC) of up to 0.85 and ventricle segmentations with a DC of up to 0.60.

Peer Reviewed Publications

- **R. Licandro**, G. Langs, G. Kasprian, R. Sablatnig, D. Prayer, E. Schwartz, "A Longitudinal Diffeomorphic Atlas-Based Tissue Labeling Framework for Fetal Brains using Geodesic Regression", *Computer Vision Winter Workshop*, February 2016. [125]

Abstracts and Posters

- **R. Licandro**, G. Langs, G. Kasprian, R. Sablatnig, D. Prayer, E. Schwartz, "Longitudinal Atlas Learning for Fetal Brain Tissue Labeling using Geodesic Regression", *Woman in Computer Vision (WiCV) Workshop at the IEEE Conference on Computer Vision and Pattern Recognition*, July 2016. [124]

1.2.2 STM of Developing Functional Connectivity and Reorganisation Dynamics after Paediatric Stroke

Motivation: The development of the human brain starts during pregnancy and proceeds in building structural as well as functional trajectories through adulthood until senescence [169]. Morphological, functional, and cognitive maturation is shaped by genetic and environmental influence such as learning processes and experience after

birth, and the resulting structure varies substantially across individuals [247]. While the functional and morphological organization of the adult's brain is known to a large extent, we are only starting to understand its emergence and maturation [169]. The development of the brain's connectivity architecture is particularly interesting, since it is suspected that it has a major role connected to our cognitive capabilities. However, state of the art observations primarily focus on the comparison of age snapshots, and do not capture multivariate temporal change patterns of the connectome. There is a particularly critical gap in knowledge concerning normal development confronted with disease or adverse events such as stroke. The challenge of longitudinal studies among children to identify functional connectivity is induced by the age and developmental related changes of the brain triggered by learning and experience (natural plasticity)[6], but also by pathology related modifications, and functional and structural reorganisation (adaptive plasticity) of brain tissue [105]. After a damage, plasticity and vulnerability of the brain influence recovery together with the injuries severity, the age and the time since damage [6]. Resting state fMRI enables the study of these processes driving the functional and structural organisation. Ultimately they can lead to improved functional outcome of children suffering from brain injuries, by developing novel interventional techniques or adapting therapy, dependent on the developmental stage of a disease [105]. A deeper understanding of individual continuous maturation processes, their interaction, and their link to cognition is essential for our understanding of the functional brain architecture, treatment and optimal promotion of children [93].

Research Questions: By formulating a baseline model for the development of functional connectivity networks the analysis of the following research questions is performed: How do functional connectivity networks evolve over age, specifically how does the development of long-range and short-range functional connectivity networks take place during healthy development? Which representation technique is suitable for these measurements? Which longitudinal modelling strategy is effective? Is it possible to use the proposed baseline model to assess the dynamics, which are induced by stroke and the following regeneration processes? How do the adaptive plasticity processes reorganise functional connectivity networks? How do the dynamics of a developmental stage interact with these processes? Are healthy dynamics separable from stroke induced dynamics?

Dataset: For this work the dataset *CHILD-STROKE* is used (cf. Section 4.2) consisting of 32 resting state functional MRI acquisitions of healthy children and children who had an ischaemic stroke. It is a time-series dataset with the age range between 7 and 17 years.

Contribution: In this work the thesis' core concept is used to provide a spatio temporal model to analyse the development and modification of resting state connectivity networks in the pediatric brain between 7 and 17 years. The contribution can be divided in three components: (1) Adaptive plasticity and the relations to the developing connectivity networks in the healthy brain using the Pearson correlation coefficient and graph based

measures [193] of brain signals are analysed. It is hypothesized that adaptive plasticity processes after stroke influence the formation of long-range and short-range connectivity over age, related to re-organisational processes and the development of brain lesions after stroke [6]. Sepulcre et al. [206] computed the local and distant degree and physical distance between correlating regions in adults. They observe a strong local connectivity in the motor area, primary sensory area and strong distant connectivity in regions of high-order cognitive functions (attentional, memory and language processing). The adaptation of these measures for the child's brain provide the possibility to analyse the influence of stroke on the distribution of short and long-range connectivity over age. (2) The second component provides a technique to quantify connectivity pattern deviation in the development of functional connectivity, and (3) a method to *track* regions which exhibit similar connectivity characteristics as *source* regions (such as an area impacted by stroke) after reorganization.

Results: It is demonstrated that graph-based representations of rsfMRI acquisitions of children is a suitable technique to assess the development of long-range and short-range connectivity networks as well as reorganisation patterns after ischaemic stroke. The spatio temporal baseline is formed by acquisitions of control cases and region-based linear regression of graph based representations. It is demonstrated that the proposed baseline is suitable for the assessment of age dependent dynamics using the proposed connectivity deviation score, where stroke subjects show a higher deviation compared to control subjects, especially more on the hemisphere of the stroke location. It is shown that the proposed reorganisation score is able to identify possible indicators for reorganisation in developing resting state networks in ipsi-lateral and symmetric networks in the neighbourhood of the stroke location.

Peer Reviewed Publications

- **R. Licandro**, K.-H. Nenning, E. Schwartz, K. Kollndorfer, L. Bartha-Doering, G. Langs, "Changing Functional Connectivity in the Child's Developing Brain Affected by Ischaemic Stroke", *MICCAI PerInatal, Preterm and Paediatric Image (PIPPI) Analysis Workshop*, October 2016. [127]

- **R. Licandro**, K.-H. Nenning, E. Schwartz, K. Kollndorfer, L. Bartha-Doering, H. Liu, G. Langs, "Assessing Reorganisation of Functional Connectivity in the Infant Brain", *MICCAI Fetal and InFant Image (FIFI) Analysis Workshop*, September 2017. [121]

Abstracts and Posters

- **R. Licandro**, K.-H. Nenning, K. Kollndorfer, L. Bartha-Doering, G. Langs, "Longitudinal influence assessment of paediatric stroke events on resting state networks", *5th Biennial Conference on Resting State Brain Connectivity*, September 2016.

1.2.3   STM of Blood Cell Antigen Progression Patterns During Acute Leukaemia Treatment of Children

Motivation: Childhood acute leukaemia is a disease affecting the blood generation process in children, where an effective treatment and measurement of its response is particularly important to determine the clinical outcome and to be able to stratify the risk for relapse. The observation of genetic features at defined timepoints enables the retrieval of the Minimal Residual Disease (MRD), a prognostic value which is an indicator of treatment response and plays an important role in guiding treatment intensity of an individual patient [194][87]. Therefore, the proportion of leukaemic blasts (cancer cells) among the amount of normal cells has to be estimated and requires strategies to accurately distinguish cancer from non-cancer cells. FCM enables a reliable MRD assessment in comparison to polymerase chain reaction [68] and thus is the data acquisition technique of choice.

Research Questions: In this thesis it is explored if the proposed STM modelling concept is capable of modelling the progression patterns of healthy blood cell populations over treatment timepoints and how pathology related dynamics of two childhood blood cancer types can be addressed: (1) Acute Lymphoblastic Leukaemia (ALL) and (2) Acute Myeloid Leukaemia (AML). Additionally, it is investigated: Which data representation and normalization strategy is suitable to form baseline and dynamic states? Can baseline states of different treatment timepoints be combined to detect cancer cell populations? How do healthy blood cell populations change over treatment and affect the automatic MRD assessment strategies developed? Which machine learning technique performs best for automatic MRD assessment over several treatment time points?

Datasets: For this work three FCM datasets are used: *BLOOD-ALL* (cf. Section 4.3.1) consisting of longitudinal acquisitions of 200 paediatric ALL patients at three treatment time points each, *BLOOD-ALLk0* containing data of 24 paediatric patients in remission without cancer cells (cf. Section 4.3.3) and *BLOOD-AML* (cf. Section 4.3.2) with 32 FCM measurement of paediatric AML patients at treatment day 15.

Contribution: In this work the core concept developed in this thesis is used to learn a spatio temporal model for automatic MRD assessment in childhood leukaemia during treatment. The contribution is four-fold: (1) a novel representation technique for FCM data is proposed using a Wasserstein Generative Adversarial Network (GAN) based approach and demonstrates improved cancer cell identification performance in comparison to state-of-the-art representation and embedding techniques (cf. Section 5.1.3 [130]) even in case of decreased availability of training data. (2) A novel normalization strategy of FCM data represented by a probability density function is introduced for the interpolation between time-specific baseline states encoding healthy blood cell populations (cf. Section 6.3 [126]). (3) The third component of the contribution is a strategy of extracting and combining baseline states of blood cell populations of different treatment timepoints and

of different leukaemia types to increase the amount of training data and longitudinal analysis of cancer cell dynamics over treatment (cf. Section 5.1.1[129] and Section 5.1.2 [128]). (4) A novel anomaly detection strategy for the automatic MRD assessment is introduced based on the STM concept proposed and used to address AML dynamics (cf. Section 5.1.2 [128]).

Results: It is shown that using a Gaussian Mixture Model (GMM) based representation of FCM measurements enables the extraction of baseline states and dynamics of blood cell clusters during leukaemia treatment. Additionally, a Wasserstein Generative Adversarial Network (WGAN) based embedding technique is proposed especially for this task to classify cancer and non-cancer cells, outperforming state-of-the-art embedding techniques and supervised classification approaches. The baseline STM is formed by non-leukaemic blood cells over leukaemia treatment by introducing a novel GMM interpolation scheme. The dynamics of leukaemic cell clusters are addressed by a GMM based anomaly detection strategy using the provided baseline cell clusters.

Peer Reviewed Publications

- **R. Licandro**, P. Rota, M. Reiter, M. Kampel, "Flow Cytometry Based Automatic MRD Assessment in Acute Lymphoblastic Leukaemia: Longitudinal Evaluation of Time-Specific Cell Population Models", *14th International Workshop on Content-based Multimedia Indexing*, June 2016. [129]

- **R. Licandro**, M. Reiter, M. Diem, M. Dworzak, A. Schumich and M. Kampel. "Application of Machine Learning for Automatic MRD Assessment in Paediatric Acute Myeloid Leukaemia". *In Proceedings of the 7th International Conference on Pattern Recognition Applications and Methods - Volume 1: ICPRAM*, pages 401-408. January 2018. [128]

- **R. Licandro** and T. Schlegl, M. Reiter, M. Diem, M. Dworzak, A. Schumich, G. Langs, M. Kampel, "WGAN Latent Space Embeddings for Blast Identification in Childhood Acute Myeloid Leukaemia, *24th International Conference on Pattern Recognition (ICPR) 2018*, August 2018. [130]

- J. Scheithe, **R. Licandro**, P. Rota, M. Reiter, M. Diem, M. Kampel, "Monitoring Acute Lymphoblastic Leukemia Therapy with Stacked Denoising Autoencoders", In: Peter J., Fernandes S., Eduardo Thomaz C., Viriri S. (eds) *Computer Aided Intervention and Diagnostics in Clinical and Medical Images*. Lecture Notes in Computational Vision and Biomechanics, vol 31. Springer, Cham, January 2019. [198]

- **R. Licandro**, K. Miloserdov, M. Reiter, M. Kampel, "GMM Interpolation for Blood Cell Cluster Alignment in Childhood Leukaemia", *Proceedings of the ARW & OAGM workshop 2019*, May 2019. [126]

Abstracts and Posters

- **R. Licandro** and T. Schlegl, M. Reiter, M. Diem, M. Dworzak, A. Schumich, G. Langs, M. Kampel, "Blast Identification in Childhood Acute Myeloid Leukaemia using WGAN Latent Space Embeddings", *Medical Imaging Summer School (MISS 2018)*, July 2018.

- **R. Licandro**, P. Rota, M. Reiter, F. Kleber, M. Diem, M. Kampel, "Automatic Detection of Leukaemic Cells in Flow Cytometric Data for Minimal Residual Disease Assessment", *EuroScience Open forum (ESOF) – Marie Sklodowska-Curie Actions Satellite Event 'Research and Society'*, July 2016.

- **R. Licandro**, P. Rota, M. Reiter, M. Kampel, "AutoFLOW: a novel heuristic method to automatically detect leukaemic cells in flow cytometric data", *3rd Austrian Biomarker Symposium 2016 on early diagnostics*, March 2016. Best poster award (3rd place).

1.2.4   STM of Whole Body Bone Lesion Evolution in Multiple Myeloma

Motivation: MM is the second most common blood cell disorder affecting the plasma cells (myeloma cells) and consequently disregulating the bone remodelling process [109]. The resulting bone infiltration processes span from the precursor state of this disease (Monoclonal Gammopathy of Undetermined Significance (MGUS)) followed by the intermediate stage of smoldering Multiple Myeloma (sMM) to progress to symptomatic MM and lead to the forming of focal and diffuse bone lesions as well as osseous destructions in later stages. The gold standard for observing these patterns is whole body MRI [102] [49] [151] and low-dose CT [112]. Since recent studies [148] report a clear benefit for patients with early therapy of MM, it is particularly important to monitor and predict high-risk sMM cases, which might develop MM. The identification of bone regions with high risk of evolving towards diffuse or focal lesions in the future can serve as basis for effective treatment planning, diagnostic imaging management, focused observation of high risk regions and response assessment during MM precursor states.

Research Questions: In this work it is investigated if bone lesion infiltration patterns can be encoded in a spatio temporal model developed by the proposed concept for predicting high risk regions. Which property in the progression pattern of bone lesions can be used to act as a baseline in the spatio temporal model? Are there different progression and appearance patterns of lesions in dependency of the body region observed? How can we address the disbalance between the size of lesion regions and body regions? Is there a relation between prediction duration and lesion location and size? Is it possible to model lesion emergence based on a pre-stage, where no lesions are present? How do bone anomalies affect the prediction result?

Datasets: For this work the longitudinal dataset *BONE* (cf. Section 4.4) is used, consisting of T1 and T2 weighted whole body MRI acquisitions of 63 patients, with at least 2 acquisitions per patient with a median observation time of 46 months and an age range between 29 and 76 years.

Contribution: In this work the presented concept is used to develop a spatio temporal model of lesion progression for the prediction of high-risk locations in wb-MRI to develop focal lesions in the future. In the course of this thesis a novel architecture for time-conditioned prediction is proposed (*asymmetric cascade conditioned U-Net*) to incorporate the modelling concept. The baseline extraction is mirrored by the first component of the architecture, which focuses on automatically segmenting the bone structure in wb-MRI. The second component of the architecture addresses the time-dependent bone infiltration dynamics, by performing patch-based lesion prediction in the determined bone region. The prediction is parametrizable by the prediction duration and enables the forecast of evolution risk to defined time points in the future. The proposed STM of whole body bone lesion evolution in MM is presented and discussed in detail in Section 6.4.

Results: It is demonstrated that time-conditioned risk prediction of MM progression is performable based on precursor state acquisitions of this disease. The evolution of focal bone lesions and underlying dynamics can be disentangled by dividing the risk prediction task into the process of extracting the bone structure as baseline and into the process of lesion prediction within the region. This strategy assisted to overcome the challenges emerging from the high disbalance between lesion size and image size, and in the increased variability according to possible organ deformation, appearances and tissue contrast. It is shown that the main trigger for false positive predictions is formed by bone anomalies, especially by diffuse bone infiltrations.

Peer Reviewed Publications

- **R. Licandro**, J. Hofmanninger, M. Perkonigg, S. Roehrich, M.-A. Weber, M. Wennmann, L. Kintzele, M. Piraud, B. Menze, G. Langs, "Spatio Temporal Risk Prediction of Future Focal Bone Lesion Emergence in Multiple Myeloma", *IEEE Transactions on Medical Imaging*, submitted September 2020.[119]

- **R. Licandro**, J. Hofmanninger, M.-A. Weber, B. Menze, G. Langs, "Early Predictors of Bone Infiltration in Multiple Myeloma Patients from T2 weighted MRI images", *Proceedings of the 42nd Austrian Association for Pattern Recognition (OAGM/AAPR) workshop, pages 9-12*, May 2018. [122]

- **R. Licandro**, J. Hofmanninger, M.-A. Weber, B. Menze, G. Langs, "Predicting Future Bone Infiltration Patterns in Multiple Myeloma", *4th International Workshop on Patch-based Techniques in Medical Imaging (MICCAI Patch-MI 2018)*, pages 76-84, September 2018. [123]

Abstracts and Posters

- **R. Licandro**, J. Hofmanninger, M. Perkonigg, S. Roehrich, M.-A. Weber, M. W., L. Kintzele, M. Piraud, B. Menze, G. Langs, "Evolution Risk Prediction of Bone Lesions in Multiple Myeloma", *European Congress of Radiology (ECR)*, March 2020.

- **R. Licandro**, J. Hofmanninger, M. Perkonigg, S. Röhrich, M.-A. Weber, M. Wennmann, L. Kintzele, M. Piraud, B. Menze, G. Langs, "Asymmetric Cascade Networks for Focal Bone Lesion Prediction in Multiple Myeloma", *International Conference on Medical Imaging with Deep Learning (MIDL)*, July 2019.

- **R. Licandro**, J. Hofmanninger, M.-A. Weber, B. Menze, G. Langs, "Whole-body MRI based lesion prediction in multiple myeloma", *European Congress of Radiology (ECR) 2019*, February 2019.

- **R. Licandro**, J. Hofmanninger, B. Menze, M.-A. Weber, G. Langs, "Whole body image analysis for diagnosing patients with monoclonal plasma cell disorders", European Project Space on Intelligent Systems and Machine Learning (EPS-IST), *7th International Conference on Pattern Recognition Applications and Methods*, January 2018.

1.3   Thesis Outline

This thesis provides an introduction to dynamic developmental patterns and corresponding medical background in Chapter 2. An overview of state of the art approaches fitting the research fields and developed approaches is given in Chapter 3. In Chapter 4 a summary of the 6 datasets is given including acquisition procedures and preprocessing steps. The contribution regarding the analysis, development and evaluation of representation techniques of DDP is summarized in Chapter 5. The spatio temporal models of DDP proposed as well as their analysis, evaluation and diverse applications are presented in Chapter 6. This thesis concludes with Chapter 7 with a brief summary, a reflection of the work and possible future directions.

CHAPTER 2

Understanding Dynamic Developmental Patterns in Medicine

"Nothing in life is to be feared, it is only to be understood. Now is the time to understand more, so that we may fear less." [Marie Curie (1867 - 1934)]

This chapter summarizes the medical background regarding DDP analysed and modelled within this thesis. This work is not restricted to developing cohorts (fetal or pediatric), also the progression patterns of diseases and the longitudinal assessment of treatment response form dynamic developmental patterns. Thus, in the following sections an introduction to healthy (baseline) development in different medical disciplines (neuroscience, blood cell generation pathways, bone remodel processes) is given and further more the explanations are extended to the pathological dynamics. To be able to model DDPs, beside understanding the medical interactions and dependencies, a further key issue is to understand the acquisition procedure and possible artefacts and limits of the representation of the data. Thus, a brief overview of state of the art acquisition techniques is introduced as well.

2.1   Morphological and Functional Brain Development

The development of the human brain is a complex process guided by an orchestrated interplay of environmental factors and genetic programs, starting in early pregnancy [204]. Its maturation continues through adulthood and lasts until senescence [169]. In this section developmental patterns of brain morphology from cells to adulthood are introduced and furthermore the evolution of brain activity (functional and cognitive) and corresponding dynamic patterns in developing cohorts is discussed. These maturation

15

processes are shaped by internal and environmental influences, e.g. ageing, learning or post birth experiences, which consequently trigger the high variability of brain architectures across individuals [247][179].

2.1.1 From a Cell to a Developing Brain

The forming of the neuronal system starts in the embryonic phase during pregnancy, between GW 1 to 8. In the first week of gestation after the fertilisation, the egg undergoes a series of mitotic divisions (cleavage), until a solid ball of cells (morula) at Gestation Day (GD) 4 emerges, until at GD 6 it forms a hollow cell ball filled with fluid (early blastocyst)[159] (cf. Figure 2.1). Subsequently, in the gastrulation process the blastocyte envolves to a pre-embryo with a embryonic disc with two layers (late blastocyst) at GD 10. The last step of the gastrulation process forms the gastrula around GD 16
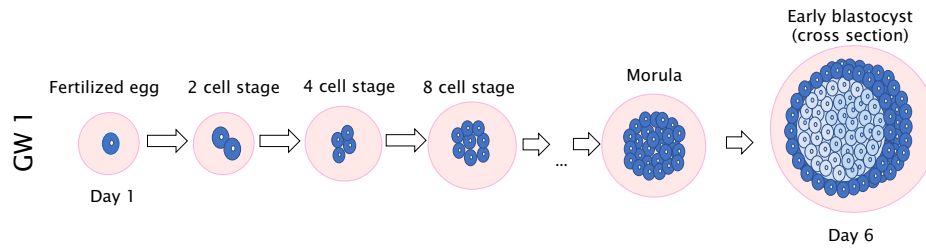
Figure 2.1: Cellular processes during the first week of gestation.

by the differentiation and forming of the elongated embryonic disk, to three tissue layers: ectoderm, mesoderm and endoderm [23] (cf. Figure 2.2 on the left). At the
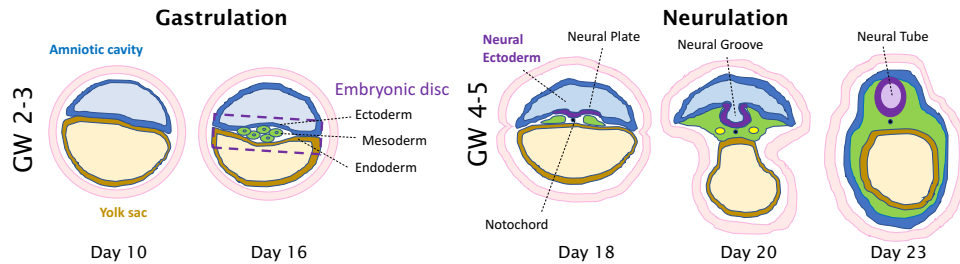
Figure 2.2: Visualisation of the gastrulation processes on the left and the neurulation processes on the right.

beginning of the third GW the dorsal ectoderm becomes thicker and builds the primitive streak (a landmark delineating the midline of the embryo), which is the base for the development of the cephalic and caudal end in the future [24]. In the fourth GW the thickened ectoderm (neural plate) undergoes accelerated growth, which further leads to the emerge of the neural folds and building of a neural groove, and later on closes to the neural tube [24, 159] (cf. Figure 2.2 on the right). Figure 2.3 schematically

visualises the lateral view of an embryo at GD 27 on the left and in the middle the corresponding isolated central nervous system in the lateral view is shown. The rostral part (the part situated towards the oral or nasal region) of the neural tube differentiates into the proencephalon (forebrain), mesencephalon (midbrain) and rhombencephalon (hindbrain) - also called primary brain vesicles. The caudal portion (the inferior part oriented towards the tail of the organism) of the neural tube develops to the spinal chord [159][133]. Between the fifth and sixth GW the primary brain vesicles differentiate into
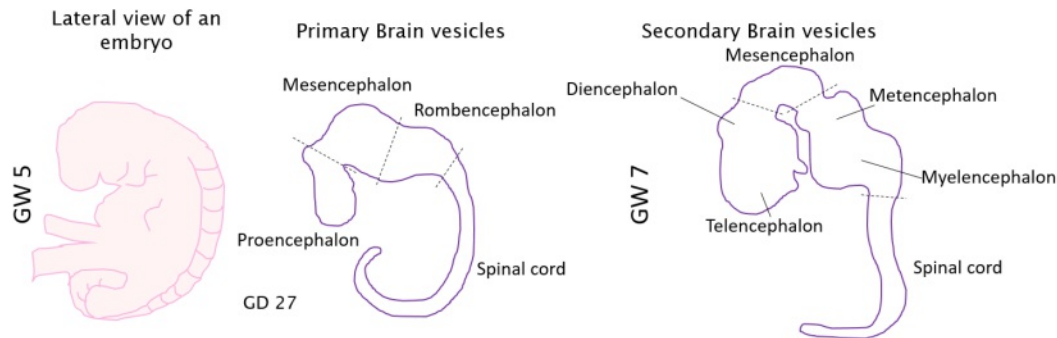
Figure 2.3: Lateral illustration of an embryo at GW 5 (left) with corresponding visualisation of the primary brain vesicles (middle) and secondary brain vesicles at GW 7 (right).

the secondary brain vesicles and the outline of the nervous system becomes apparent [24] (cf. Figure 2.3). In Table 2.1 the brain division processes are summarized: The

Table 2.1: Developing Brain Structures in the Embryo

Primary Brain Vesicles	Secondary Brain Vesicles	Derivatives Wall	Derivatives Lumen
Proencephalon	Telencephalon	Cerebral hemispheres	Lateral ventricles, rostral part of third ventricle
	Diencephalon	Epithalamus, thalamus, hypothalamus, pineal	Third ventricle
Metencephalon	Mesencephalon	Midbrain	Cerebral aqueduct
Rhombencephalon	Metencephalon	Pons, cerebellum	Superior part of fourth ventricle
	Myelencephalon	Medulla	Inferior part of fourth ventricle

forebrain differentiates into the telencephalon and the diencephalon. The telencephalon consists of two hemispheres and contains the hippocampus, the cerebral cortex, the motor centres (basal nuclei) and amygdala as well the lateral ventricles and rostral part of the third ventricle. The diencephalon differentiates into the epithalamus, thalamus,

hypothalamus and pineal and contains most of the third ventricle. The metencephalon develops to the mesencephalon and differentiates to the midbrain and cerebral aqueduct. The rhombencephalon differentiates into the metencephalon and the myelencephalon. The myelencephalon develops further into the medulla while the metencephalon into the pons and the cerebellum. The pons is a connecting structure between the telencephalon, the cerebellum and the medulla oblungata [133]. The gestational months after the second are dominated by rapid brain growth, where the telencephalon starts to cover the diencephalon in the third, the mesencephalon in the sixth and the metencephalon in the eigth gestational month until the brain reaches its rough adult shape [133].

Ventricle Development

The ventricle system lies within the neural tube and remains connected during the brain development. A schematic illustration is given in Figure 2.4[1]. This system is divided
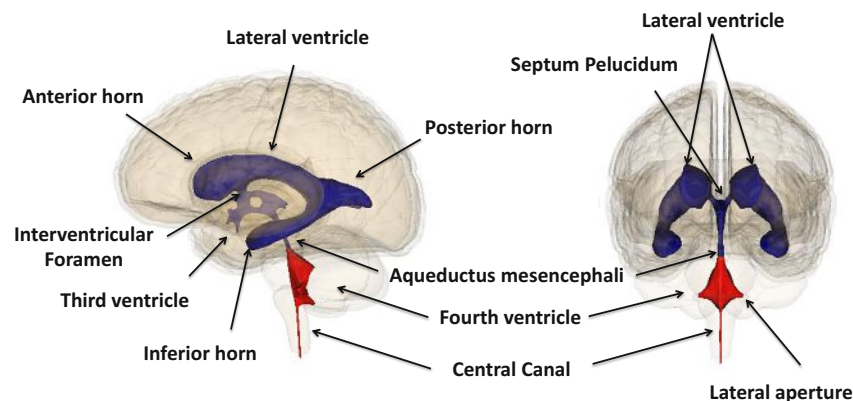
Figure 2.4: Illustration of the ventricle system.

into parts, where the segment in the rhombencephalon develops to the fourth ventricle with a ground shaped like a rhombus. The medulla segment accomodates the canalis centralis, while the midbrain contains a tight canal named acqueductus mesencephali. The third ventricle lies within the diencephalon and the lateral ventricles are hosted by the cerebrum hemispheres. The main function of the ventricular system is the production of Cerebro Spinal Fluid (CSF). It preserves the brain from hitting against the cranial bone, regulates temperature and contains nutrients for the neural tissue. Ventricles are often used as reference points in imaging, since they are easy to distinguish and indicators for developmental deviations or diseases [23] [133].

---

[1]Image modified from https://commons.wikimedia.org/wiki/Category:Fourth_ventricle#/media/File:Fourth_ventricle.png; [accessed 2021-02-04]

Cortical Development

The dynamics behind the cortical development involve cellular mechanisms, cortical folding patterns and expansion patterns. The *early cortical development* starts at GW 4, where neuroepithelial cells divide symmetrically and Marginal Zone (MZ) and Ventricular Zone (VZ) are apparent. *Neurogenesis* is visualised in Figure 2.5. This process is
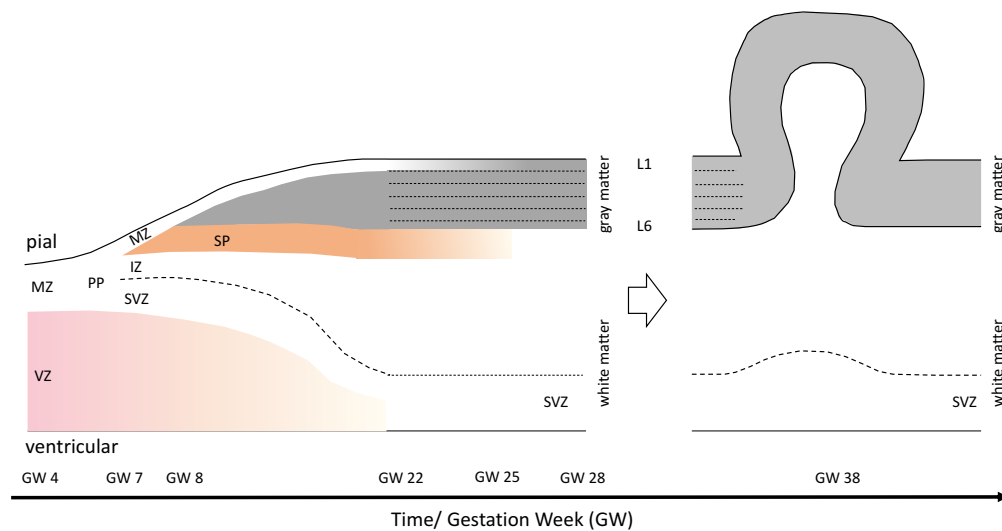
Figure 2.5: Schematic illustration of the cortical development between GW 5 and 38.

mirrored by a complex sequence of cellular migration and division starting at GW 5 with a switch from symmetric to asymmetric cell division at the ventricle's margin. At GW 7 Intermediate Zone (IZ) and SubVentricular Zone (SVZ) differentiate. The intermediate zone will become White Matter (WM) tissue together with the SVZ, which is responsible for coordinating the migration of pyramidal- and inter-neurons. Later, these start to move tangentially between the MZ and IZ. Progenitor cells in the SVZ and VZ start forming to become the basis for the pyramidal neurons and migrate from inside to outside to form the six characteristic cortical layers (L1 - L6) of the grey matter until GW 18. In parallel the VZ gets thinner by the outward migration of its cells [30]. Between GW 25 and 30 the gyral formation and cortical folding takes place [238] and originates from the parieto-occipital and central sulci. Between GW 25 - 27 the VZ gets thinner while the SVZ proliferates and the SubPlate (SP) starts to diminish. The development of the first cortical layer is fulfilled by GW 28. From GW 24 - 34 axonal elongation and maturation of axons in the white matter takes place (myelination) as well the IZ becomes WM tissue. This results in cortical stress since different growth patterns between the inner layers and the cortical plate occur, which is one trigger of the cortical folding process. Radial glial cells are responsible for the tangential expansion of the cortex, while intermediate progenitor cells influence the radial expansion [30]. During *gyrification* (formation of gyri and sulci) these processes are continued and conclude in the second year after birth [118].

Developing Structural Connectivity

During normal brain development, connections between the migrating and dividing cells are established (*structural connectivity*). There is no direct connection between the central nervous system and the cortex before mid-gestation, but indirect connections between the SP, cortical and subcortical tissues. In the second half of pregnancy direct connectivity evolves by the multiplication and forming of the axons' branches, which further elongate towards cortical and subcortical targets to connect with other neurons [30]. The formation of connections proliferates inside-out. After GW 18 horizontal intra cortical connections evolve, where younger neurons in the upper cortical layers form connections later in comparison to older neurons in deeper cortical layers (Layer 6)[30][133]:

- GW 17-18, Layer 6: Branch extension to basal gray matter

- GW 17-18, Layer 5: Connections within internal capsule, brainstem, spinal cord

- GW 22-27, Layer 4: Thalamo-cortical connections

- GW 28-32, Layer 3 and 2:

  - Interhemispheric cortico-cortical association fibers (connection between a brain lobe's nerve cells in a hemisphere)
  - Intrahemispheric commissural fibers (connections between two brain hemispheres, provided by the corpus callosum which differentiates to the commissural plate)
  - Projection fibers (connection of the cortex with deeper areas of the central nervous system - long and short distance axonal connections).

- GW 28, Layer 1: Fully developed at this time point and primarily filled with intrinsic tangential axons, arborizations of apical dendrites and a few neurons

- GW 32-47, Short horizontal connections in the Gray Matter (GM) and WM develop

Also other cell types despite neurons (e.g.astrocytes, oligodendrocytes, microglia cells, and capillaries) are part of the formation of neuronal structural connectivity [30].

2.1.2   Developing Functional Connectivity and Plasticity

The fetal brain undergoes a variety of developing dynamics to obtain the shape and structure observable in adult cohorts. Beside the morphological and structural connectivity evolution, the organization of signaling pathways and the development of the functional brain systems during the fetal period is essential to healthy development [5] and to learn how to perform complex cognitive tasks. In the late 80s of the 20th century it was discovered that there are fundamental differences between the synapse formation in the early developing brain compared to the adult brain [79]. In early development

overproduction of neurons and connections takes place (peak age 1-2 years). During development non required cells and connections are eliminated by *synaptic pruning* and results in measurable cortical thinning (until the age of 20), which has been also correlated to the behavioural development in recent studies [104]. Beside the selective synapse loss, experiences also trigger selective synapse formation, which can be summarized under the term of brain *plasticity*. The *natural plasticity* of the developing brain helps the central nervous system to adapt to external factors, which influence developmental trajectories of the brain and consequently the behaviour as adult [104]. We can differentiate between environmental (experiential) factors (sensoric, drugs, diet, hormones, stress stimuli), genetic factors (experience can trigger gene expression), or age sensitive factors (pre- and postnatal) [104][6]. *Adaptive plasticity* refers to structural and functional reorganisation processes after brain injury [105].

Paediatric Ischaemic Stroke

A type of brain injury that triggers adaptive plasticity processes is paediatric Ischaemic Stroke (IS). It is caused by ischaemia (reduced blood flow in cerebral vessels) and leads in the irreversible case to brain cell death and the evolvement of brain lesions [141]. IS is a rare disease in the paediatric cohort reporting an incidence of 1.2 to 13 cases per 100,000 children per year with age younger 18 years [227]. IS surviving children suffer their whole life from motoric or cognitive deficits, have developmental disturbances or learning difficulties, with varying outcome dependent on the age, location of the stroke or comorbidities [141].

2.2 Generation of Blood Cells and Blood Cancer

The generation pathway of blood cells starts hierarchically from haematopoietic stem cells in the bone marrow (medullary), continues via forming of progenitor cells (specialized for several or single cell lineages) and ends with the differentiation to mature blood cells [160, 90]. Figure 2.6 gives an overview of these baseline processes and cells involved. It can be differentiated between three main lineages:

1. Erythropoiesis: Generation pathway of red blood cells (erythrocytes). The adult human blood contains around 5 million erythrocytes per microliter, which are involved in the oxygen delivery and production of haemoglobin, lifespan 120 days [57].

2. Thrombopoiesis: Generation pathway of platelets (thrombocytes). Platelets play a key role in the thrombosis and haemostasis with a lifespan of few days [218].

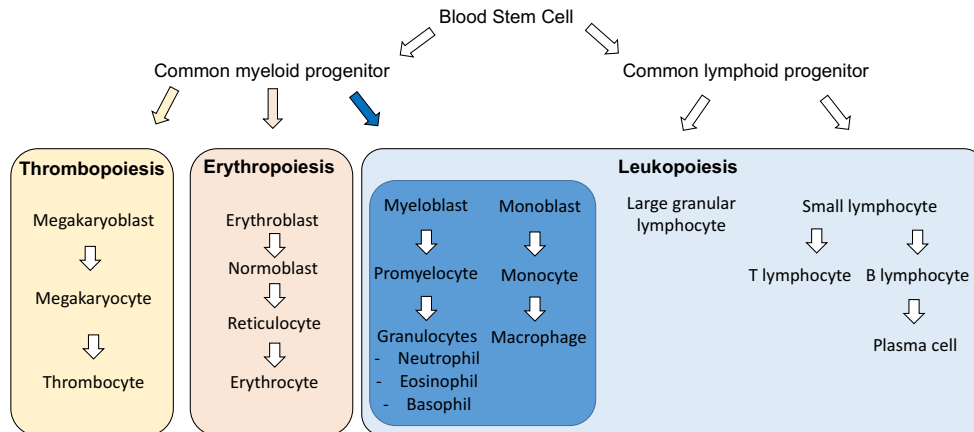3. Leukopoiesis: Generation pathway of white blood cells (leukocytes).

Figure 2.6: Generation pathways of blood cells.

2.2.1   Childhood Acute Leukaemia

Childhood acute leukaemia is a disease, which affects progenitor blood cells by genetic lesions. In this thesis dynamic developmental patterns of two different types of acute leukaemia are observed: ALL and AML. In ALL we can differ between T-ALL, if progenitor of T-cells are affected, and B-ALL if the generation of B-cells are influenced by genetic lesions of progenitor cells. Consequently, these disturbances lead to the proliferation of undifferentiated leukaemic cells (blasts). In contrast to this, AML is present if genetic lesions affect the myeloid progenitor cells during hematopoiesis, resulting in an increased count of malignant progenitor cells and a decrease of mature blood cell counts [175].

Leukaemia Epidemiology   Childhood acute leukaemia is the most common cancer form in the paediatric cohort with an incidence of 10 to 45 per 1 million children per year [78]. ALL is more common in younger cohorts (peak of incidence between 2 to 5 years for B-ALL, 10 years for T-ALL [78]) compared to AML, which is the most common leukaemia type in adults [174][87]. The incidence of AML increases with the subject's age [94] and accounts for 20 percent of leukaemia cases in paediatric cohorts [43]. The incidence of AML in the United States is 18.4 per million at age 0 to 1 year, 4.3 per million for ages 5 to 9 years, and 7.7 per million at age 10 to 14 [175]. If children are diagnosed with AML younger than 15 years, the five year survival rate lies approximately (subtype dependency) at 70 percent [43].

Therapy Response Assessment in Leukaemia   For the assessment of therapy response and clinical outcome in acute leukaemia clinicians observe genetic features of blood cells [194] to derive patterns of leukaemic cells and consequently to retrieve a prognostic value called MRD. It encodes the ratio between leukaemic blasts among the number of non-leukaemic cells during therapy. Thus, it is important to achieve reliable
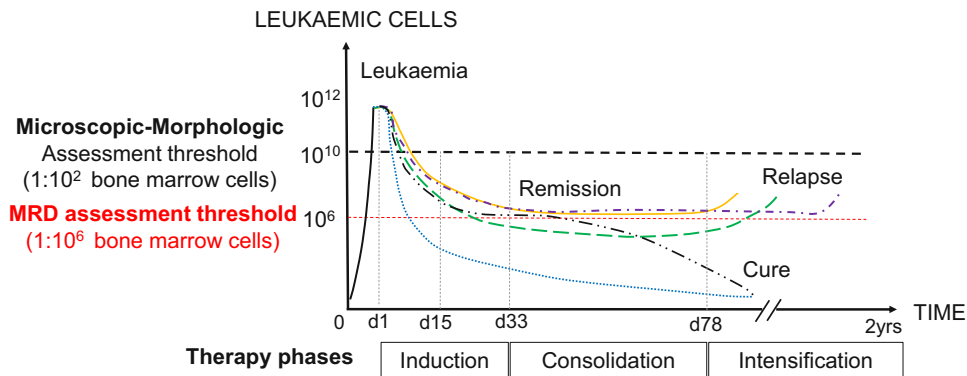
Figure 2.7: MRD assessment in different therapeutic stadia of leukaemia.

estimates of remaining leukaemic cells at defined therapeutic phases [29]. MRD is used as an indicator of the clinical outcome and to stratify the risk of relapse during therapy, and furthermore acts as guiding diagnostic tool for planning patient specific treatment intensity. In Figure 2.7 the relations between the prognostic MRD value and different therapy time points are visualised.

Leukaemia Treatment

Treatment in leukaemia is guided by treatment protocols and to guarantee quality and safety their effect is evaluated on bases of international clinical trials over several years [42]. As observable in Figure 2.7, acute leukaemia treatment strategies can be divided in three phases (Induction, Consolidation, Intensification) [138], [194], [42], although the medication substances and sub-treatment sequences vary dependently on the leukaemia type and patients' therapy response:

- Day 1 - Day 33 Induction Phase: The first phase also called *remission induction* targets a Complete Remission (CR). The CR state is achieved if blasts are completely removed from the circulation system - i.e. no presence of extramedullary leukaemia, less than 5% of blasts are in the cellular marrow and a regeneration of platelets and granulocytes is observable by increased counts of these.

- Day 33 - Day 78 Consolidation Phase: The consolidation phase aims at the removal of MRD after the patients have recovered from the previous phase in a rest period [138].

- After Day 78 Intensification Phase: The third phase spans the treatment strategies after remission and can span up to 2 years. In the intensification phase a prolongated

chemotherapy (1-2 years) is performed or a Stem Cell Transplantation (SCT) [138], especially allogeneic Hematopoetic SCT (HSCT) is strongly recommended for most children with AML after relapse [194].

Beside the effects of the disease of acute leukaemia itself, infections, haemorrhage or side effects by the highly haematotoxic and immunosuppresive treatments are as well a cause of morbidity and mortality [43]. In parallel to the leukaemia treatments, prophylactic therapies are performed as supportive therapy or to decrease the incidence of fungal or bacterial infections [193].

2.3   Bone Remodelling and Infiltration Patterns in Multiple Myeloma

The remodelling of bone structure in the human is a dynamic process to adapt the architecture of the bone according to the mechanic stress or to perform bone tissue repair after injury. It is a complex interplay of biological events between different cells and follows a five stage sequence [103]:

1. Activation: this phase is started after a chemical or mechanical stimulus and activates bone resorbing cells (*osteoclasts*). Osteoclasts are derived from hemopoietic precursors in the bone marrow and can penetrate the blood vessels. They attach on the bone surface and initiate the bone resorption.

2. Resorption: In this phase the attached osteoclasts resorb the bone mineral and organic components of the bone matrix (osteoid) by secreting hydrogen ions, acid phosphatases and various enzymes. After the forming of resorption pits, the osteoclast migration and their apoptosis (cell death) initiates.

3. Reversal: After the resorption phase, mononuclear cells differentiate into macrophages and initiate the reversal phase, by cleaning up the remaining debris, so bone formation can start.

4. Formation: this phase can last between 4-6 months, where bone forming cells (*osteoblasts*) are activated. These cells are derived from the mesenchymal stem cells in the bone marrow and mineralise the osteoid to form new bone structure in a layered way. After this phase osteoblasts either undergo cell death or are incorporated into the new bone layer as osteocytes.

5. Termination: The last phase of the bone remodelling process is terminated when the same amount between resorbed and formed bone is achieved. This is a strictly guided coupling process to keep the balance between removed and restored bone.

In Figure 2.8 in the first row the bone remodelling process is visualised following the five step sequence introduced. In the second row the processes how MM affects and disturbs the bone remodelling process are shown, which is introduced in detail in Section 2.3.1.
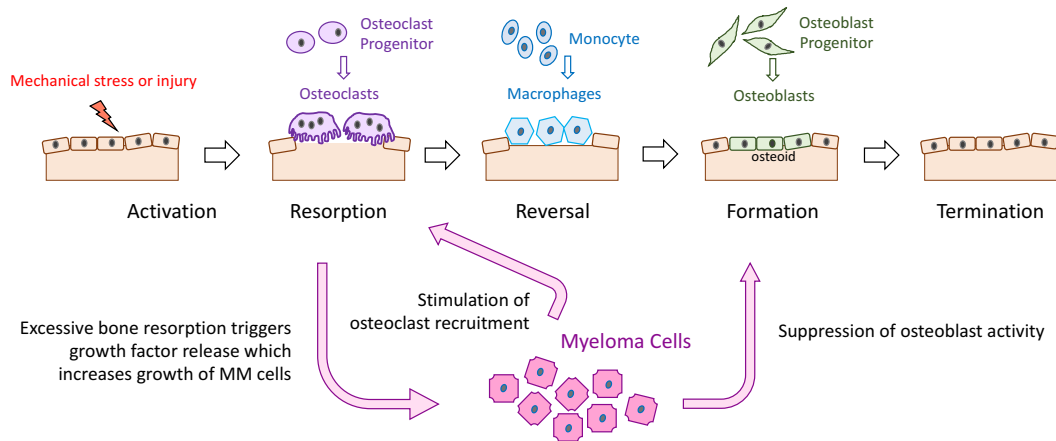
Figure 2.8: Bone remodelling process stages and influence of myeloma cells on these.

2.3.1   Multiple Myeloma

MM is the second most common blood cell disorder affecting the proliferation of plasma cells and B-lymphocytes [180] and accounts for 10% of all bone marrow malignancies [109]. The global age-standardized incidence rate reported by a study from 2016 is 2.1 per 100000 persons [41] and increases with age, with a median age about 73 years starting with 40 years. Despite the improvement of therapy in the past decade MM is still not curable [181].

Symptoms and Diagnosis

The increased amount of plasma cells in MM triggers the production of non-functional monoclonal antibodies, affecting the functionality of the kidney, leading to deficiency enhancement in immune response and further to the alteration of bone remodelling mechanisms [226]. A precursor state of MM is *MGUS* [102], where the CRAB features (hypercalcaemia, renal failure, anaemia and bone lesions) are still absent, which refer to the underlying plasma cell disorder. In 0.5-1% of the cases, MGUS predictably progresses to symptomatic MM via the intermediate stage of *sMM* [102]. In sMM CRAB features are also absent, with increased monoclonal protein level and increased bone-marrow plasma cell counts. MM and corresponding symptoms were defined by the International Myeloma Working Group (IMWG). These criteria entail the overreaching of the clonal bone marrow plasma cell level of 10%, if MM cells are found in the bone or extramedullar after biopsy, or if one ore more CRAB features are present. The bone lesion CRAB feature is met when osteoporoses or osteolytic bone destruction (lesions ≥ 5 mm in size) are present [180].

Myeloma Bone Disease

The myeloma bone disease is caused by a dysregulated bone remodelling process. The increased amount of plasma cells (*myeloma cells*) surpresses the osteoblast activity and stimulates the recruitment and differentiation of osteoclasts, resulting in excessive bone resorption. As a consequence of resorption an increased amount of growth factors is released, which furthermore triggers the myeloma tumor growth in a destructive cycle [221] (cf. Figure 2.8).

2.4   Data Acquisition Techniques

This Section focuses on a brief overview of acquisition techniques to assess dynamic developmental patterns in the medical domain.

2.4.1   Fetal Brain Magnetic Resonance Imaging

Since 1983 the fetal MRI technique was proposed as alternative to sonography [212], where a confirmation or a differential diagnose is required, in most cases of neurological abnormality. Recent studies report an improvement of 22% of diagnosing brain anomalies with fetal MRI compared to ultrasound [39] and this technique enables the visualisation of different tissue types and structures in the fetal lung, liver, kidney and bowel [195]. Fetal MRI is non-invasive, since it does not involve ionizing radiation and is recommended to be performed after 17th week of gestation [195] [34]. In utero MRI has no effect on the fetal growth or movement, fetal heart rate nor reported evidence on mutagenic influence [77]. Due to the constantly changing position and motion patterns of the fetal movement the imaging is challenging and causes unsharpness and imaging artefacts [37]. Especially, the limitations lie in the diagnostic information in early gestational age, due to the fetus' small size and increased possibility to move [195]. Thus, specific imaging protocols with reduced scanning time were developed to counteract these effects. The standard sequence is the Single-Shot Fast Spin Echo (SSFSE) protocol for T2 weighted acquisitions using a 1.5 Tesla superconducting magnet. This sequence offers a high signal-to-noise ratio and contrast and is more robust to imaging artefacts caused by motion. For obtaining a high resolution image a key preprocessing step after MRI acquisition is super-resolution reconstruction. The SSFSE sequence combines the usage of an increased slice thickness (3 mm - 8 mm) with a 1-2 mm gap, a field of view of 320 mm - 400 mm and reduced examination time under 20 seconds per volume [63] [27]. In this case the slices of a volume are acquired separately in the axial, sagital and coronal plane to the body of the fetus, so motion affects only specific slices. In Figure 2.9 the three different slice-based acquisitions are visualised on the left. Interleaved MRI acquisitions help to reduce signal intensity loss caused by cross-talk between sections, were the gap size has to be chosen equal to the thickness of the section [195] (cf. Figure 2.9 on the upper right for a schematic illustration). For obtaining a 3D high resolution volume of isotropic size, Super Resolution Reconstruction (SRR) is performed (cf. Figure 2.9 on the lower right).
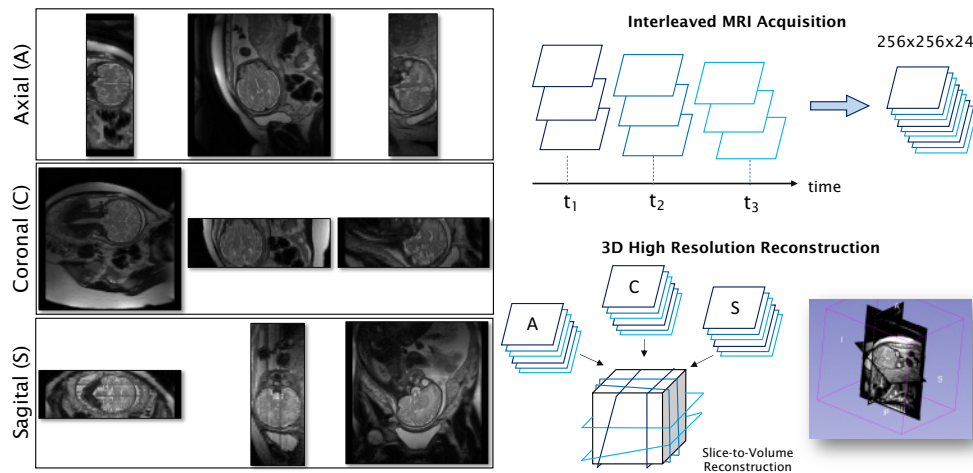
Figure 2.9: Illustration of the Single-Shot-Fast-Spin-Echo sequence acquired in 3 orthogonal planes (left) and schematic illustration of the interleaved acquisition modus (upper right) and SRR routine. Image courtesy of Medical University of Vienna (MUW).

2.4.2 Fetal and Paediatric Functional Magnetic Resonance Imaging

While we know the underlying reorganisational processes in the adult brain [111], we still do not understand completely how evolving dynamics interact with reorganisation processes in the developing cohort. The fMRI technique makes the assessment of functional brain reorganisation and development possible [32]. We can differentiate between task-based fMRI where neural activation is imaged dependent on a stimulus (sound, visual, pain, stress), while rsfMRI enables the analysis of brain signals due to their temporal correlation during rest independent of a stimulus [4] and recently gained more importance in investigating the spatial temporal distribution of neural networks in fetuses [201][5][91], children [32][107] and adolescents [223][4].

Fetal Resting State Functional Magnetic Resonance Imaging

The fetal fMRI in comparison to imaging the adult is particularly challenging because of the fetus' constantly changing position and movement, as well artefacts caused by maternal breathing. This may lead to an artificial increase of correlations between activity time lines observed on the brain's surface and consequently leading to distorted study results [170]. Therefore, specific functional imaging protocols and preprocessing techniques are used in fetal functional neuro-imaging studies. In comparison to structural imaging of the fetal brain (cf. Section 2.4.1), the SSFSE sequence is used to image neural activity in one plane (axial, coronal or sagital) over several time-points.

27

Paediatric Resting State Functional Magnetic Resonance Imaging

The pediatric fMRI technique enables the observation and study of developing neural connectivity networks of the whole-brain in children in a non-invasive way [223] [4], but with high sensitivity to motion. Especially in the paediatric cohort, a key issue is to reduce motion artefacts, by a specific preparation of the child and motivation before scans: Pillows can be used as fixation of the child's head, headphones to reduce noise level and also introductory videos explicitly designed for children showed to be helpful in the preparation phase [237][222]. In comparison to fetal rsfMRI single-shot, gradient-recalled, echo-planar imaging protocols are used, where no high resolution reconstruction is required.

2.4.3   Blood Cell Antigen Pattern Assessment with Flowcytometry

FCM plays a central role in the diagnostic pathway of haematologic malignancies and is used in combination with morphologic, molecular, cyogenetic methodologies to identify the optimal treatment [115]. In leukaemia it is used to reliably assess the MRD, by detecting immunophenotypes of blood or bone marrow cells related specifically to leukaemia [15, 56]. It is more cost- and time-effective compared to polymerase chain reaction [68]. The blood consists of a variety of cell types with distinct antigen expression on the surface. In leukaemia research, this property is used to identify cancer and different types of non-cancer cells within a measured *sample* (all cells of a patient's FCM measurement). Therefore, cells are *stained* with a combination of specific fluorescence labelled antibodies which attach to the corresponding antigens on the cell's surface. The FCM technique uses lasers of different wavelengths for cell measurement. The stained cells are first lined up in a fluid stream, subsequently hit with the lasers to measure the cell specific emitted fluorescence patterns and physical properties (granularity, size) [190]. In Figure 2.10 a schematic illustration of the FCM measurement pipeline and required sample preparation steps are visualized. On the right side a flowcytometry 2D dot plot is shown, where every point represents a measured blood cell and the axis the observed antibody types. The dot's position is determined by the level of fluorescence measured by the FCM, which makes a derivation of the attached antibody and corresponding antigen expression pattern on the cell's surface possible. The scale of each plot's axis is of logarithmic scale and one dimension corresponds to an FCM measured feature.

Identifying Cancer Cells in Flowcytometry

For the determination of cell types of interest manual annotation is performed in the clinical routine following a defined gating hierarchy. Especially for the treatment response assessment in leukaemia, it is important to accurately identify and quantify the number of remaining cancer cells to derive the MRD during therapy. In the clinical routine FCM based MRD assessment is performed manually by operators. Thus, the multidimensional FCM measurements are assessed by looking at multiple 2D dimensional dot plots of specific combinations of antibodies or antibodies vs.physical measures. Polygons (gates)
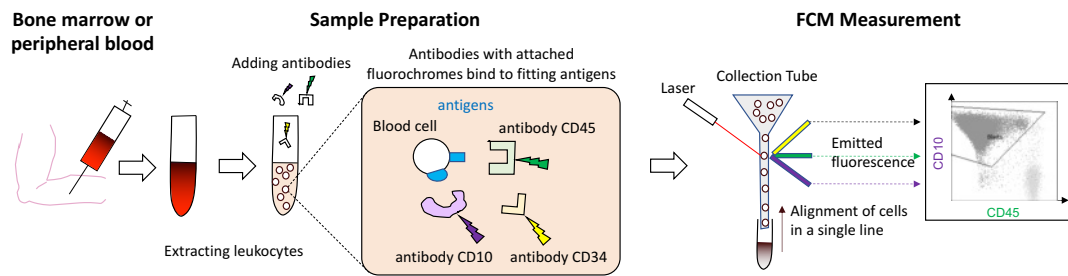
Figure 2.10: Schematic illustration of the sample preparation and flowcytometry measurement pipeline.

are drawn around cell clusters of interest in defined plots following a specific gating hierarchy. The identified cells of interest of a gating step serve as input of the subsequent gate in the hierarchy. In Figure 2.11 a gating hierarchy specific for identifying blasts in a patient with AML is visualised as an example. In the first plot in Figure 2.11 the *singlets* gate is drawn to exclude cells that were attached to other cells during measurement. Within the singlets gate (second image) the *viable* gate is drawn by observing the physical measurement for size (Front Scatter (FS INT)) and granularity (Side Scatter (SS INT)). This step is performed to identify nucleated cells and exclude dirt and non-cell particles. In the next step (third image) a pregate is drawn looking at the combination of antibody CD45 (leukocyte common antigen - protein tyrosine phosphatase) and SS INT to extract relevant leukocytes (green). The last step contains the drawing of the *blast gate* to extract cancer cells (blasts), by observing cells that have a positive antibody expression of CD34 (hematopoietic stem cell marker) and CD33 (myeloid lineage cell marker). Additionally, also CD 117 (hematopoietic stem cell marker) positive cells are observed to annotated blasts, which are visualised in red in all images. The gating hierarchies vary depending on
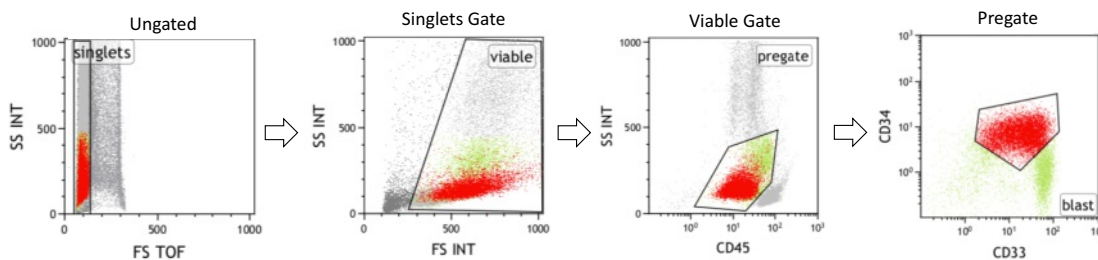
Figure 2.11: Illustration of a sample obtained by a flowcytometer and the followed gating hierarchy to determine blast populations (red) in a patient with AML. Image courtesy St. Anna Children's Hospital.

the leukaemia type, and the antibody panel used. This procedure is strongly dependent on the operator's expertise and skills, time-consuming and highly subjective. Thus, recent computational approaches where proposed to automatically identify MRD in

the multidimensional space directly (cf. Section 2.2 for an overview of state-of-the-art approaches for automatic MRD assessment). One of the main challenge in flowcytometry is the limited number of available cells in the measured probe and the acquisition of small cell populations composing about 0.1 % of all cell types observed (e.g. low MRD in late therapy phases of induction and consolidation), which is important to adapt therapy if a risk of relapse is determined. Additionally, measurement variances occur age- or treatment related, as well as depending on the regeneration status of the bone marrow precursors [68].

2.4.4   Imaging Bone Infiltration in Multiple Myeloma

Imaging in MM is used additionally to laboratory derived parameters to stage the tumor process, provides prognostic information and enables the evaluation of treatment response. Cross-sectional imaging has replaced conventional X-ray skeletal acquisitions in recent years [106]. The bone infiltration processes in multiple myeloma start first with the formation of focal or diffuse bone marrow infiltration. The gold standard for observing these initial infiltration patterns is wb-MRI (T1, T2) [49][151][102]. Subsequently, the progression of the disease leads to the building of osseous destructions (osteolytic lesions), which are observable using low-dose whole-body Computer Tomography (CT) [112]. Figure 2.12 illustrates the infiltration pattern of a focal lesion evolving in the sacrum of one patient over multiple examination time points of a single patient.
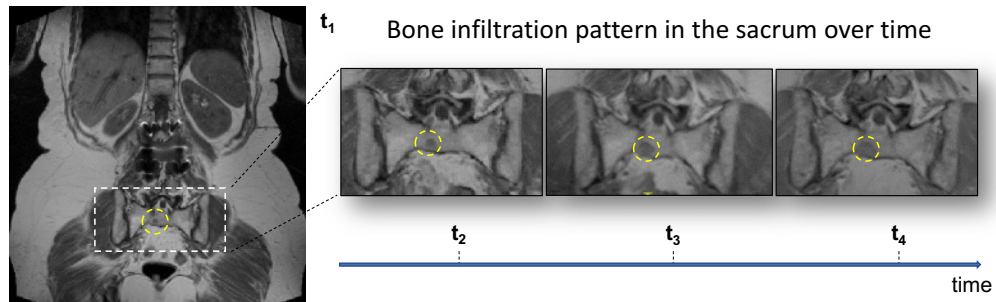

Figure 2.12: Visualisation of an infiltration pattern of a focal lesion (yellow circle) in the sacrum using T1 weighted wb-MRI scans over multiple examination time points t of one patient. Image courtesy Medical University of Vienna.

CHAPTER 3

State of the art

"If we knew what it was we were doing, it would not be called research, would it?" [Albert Einstein (1879 - 1955)]

The following chapter summarizes the state of the art methodologies underlying the thesis' topic. It illustrates medical data representation techniques (cf. Section 3.1), alignment and normalizations strategies of feature distributions or imaging data (cf. Section 3.2), anomaly detection and prediction approaches (cf. Section 3.4) and longitudinal modelling concepts (cf. Section 3.5) for dynamic developmental patterns.

3.1 Representation of Medical Data in Space

A key issue on making medical data comparable is on the one hand the definition of representable reference spaces and on the other hand the data alignment. This section summarizes first data representation approaches for feature based measurements and imaging data of developmental patterns observed within this thesis. Subsequently, application specific state of the art approaches with focus on blood, brain and bone developmental patterns are presented.

3.1.1 Density and Feature Based Representation

Feature based representation is an appearance of data in the medical domain, that can be defined as a collection of selected measured features (random variables e.g. blood pressure, antigen expression, cognitive test score, age, body temperature, radiomic features, extracted biomarker, etc.) used to perform multivariate statistical analysis, predictions or classifications [88]. Instead of observing and analysing a single variable, multivariate analysis involves information about the relationship between features observed and shows improved results in contrast to univariate analysis. Following two categories to search for

patterns and structure in the high-dimensional data can be defined [88]:

Unsupervised Learning (descriptive data mining) - focuses on discovering clusters of patterns, outliers or relationships without a-priori knowledge of experts involved. In contrast to this, *supervised learning* (predictive data mining) focuses on building models and trajectories based on a-priori knowledge about the cluster location and applying it to unseen data to evaluate predictive accuracy and performance [88].

In multivariate data analysis we can differentiate between parametric and non-parametric model techniques to obtain a density based representation: In case of *non-parametric* models no assumption regarding the distribution of the data are made to estimate the underlying probability density function. In contrast to this, *parametric* density estimations focus on estimating the parameters of the assumed underlying model instead of estimating an unknown function [52].

Density Representation of Flowcytometry Data   Features in the FCM domain (cell antigen expression measurements) have no spatial relations, compared to neighbouring pixels in imaging data. The aim for FCM data description is to find a parameter combination to detect spatial varying populations in the multi-dimensional feature space. In [155], [183], [128] Gaussian Mixture Models are used to model the probability density function of blood cell populations in an unsupervised way, by finding a parameter combination consisting of the mean, covariance and weights of every Gaussian component in the mixture model, to estimate spatial varying cell populations in the multi-dimensional feature space. In [176] a multivariate finite mixture model based on Expectation Maximization (EM) and skew-t distributions is used to analyse and represent flowcytometric data. Lo et al. [135] replaced the Gaussian distributions in a GMM with t-distributions (parametrisable using normal-gamma compound distributions) to obtain an outlier robust FCM data representation. Finak et al. [64] extended this work, by incorporating the number of cell populations to be identified as additional parameter.

Density Representation of Neuroscience Data   In [114] the distribution of functional connectivity measures in an embedding space of adult subjects is represented with a GMM to create an atlas of a cognitive process decoupled from anatomy. Kim et al. [100] use GMM to represent the probability density function of ensemble average propagator fields (EAPs) acquired via diffusion weighted MRI, to simulate EAP profiles for denoising and upsampling Diffusion weighted MRI data.

3.1.2   Graph Based Representation

The aim of graph-based representations is to encode discrete features in the observation space, which are represented as nodes in a graph. Nodes can represent voxels or regions of interest (anatomical or functional brain regions) in the image domain, single measurement or clusters of interest in the data domain. Edges in a graph encode the relation between nodes in a weighted, directed or non-directed way [52]. Graph based representations enable the study and analysis of complex networks by deriving topologies of network

representations, to quantify networks by computable measures settled in graph theory and can serve for defining reference representation to establish comparability and to reveal abnormalities [193].

Graph Based Representations in Neuroscience In functional brain imaging, graph based representations are popular since they are simply computable, well interpretable and widely estalished [62],[219],[193][216]. This type of representation enables the determination of a cognitive state's origin, the analysis of neural architecture and gives insights into the global and integrative properties of function in the brain [217]. Fair et al. [62] and Supekar et al. [219] use graph based analysis (e.g. path-length, hierarchy, clustering-coefficient and regional connectivity) of rs-fMRI data of the child's healthy brain and demonstrate an increase of long-range connectivity and a lower scattering of local connectivity during the development of the central nervous system. Supekar et al. [219] observe that children have a similar global (small-world) organisation of the brain, but show differences in interregional connectivities and the hierarchy of organisation. Gordon et al. [73] apply Independent Component Analysis (ICA) on Diffusion Tensor Imaging (DTI) and rsfMRI data of children between 7 and 13 to identify resting state networks.

Graph based representations in Cancer Research In [243] graph based representations are used for FCM measured blood cells to express the similarity between cells and act as basis for spectral clustering techniques.

3.1.3 Embedding Based Representation

In medicine and life science where thousands of data per patient are acquired (e.g. 300,000 measured blood cells per patient in leukaemia research using flowcytometry), the visualization of samples becomes challenging as well their exploration [184]. Data embeddings represent high-dimensional information in a reduced dimensionality, and therefore enable the assessment of multiple observations. **Principal Component Analysis (PCA)** identifies principal components (normalized eigenvectors of the data's covariance matrix), which show the maximum variation. Samples can be reconstructed from the low k-dimensional linear space by using few principal components instead of thousand of values [184]. **Independent Component Analysis (ICA)** is related to PCA. This technique identifies statistically independent components instead of uncorrelated components to represent samples [184]. The **NonLinear Component Analysis (NLCA)** approach has been proposed [52] using a multi-layer neural network architecture (***Autoencoder***) consisting of learning an encoding from input to a low dimensional representation (encoder) and a mapping from this space back to the input space (decoder). In an unsupervised way the network is trained to learn a low dimensional and non linear representation of non linear components of the input data, by minimizing the reconstruction error [17]. Recently, ***Generative Adversarial Networks*** for feature based data (e.g. words or measured values in a medical report) [71] or image based

data [178] were proposed. These type of networks consist of a generator (a multilayer perceptron to learn the distribution of the data in a low dimensional latent space) and a discriminator (a second multilayer perceptron), which maximizes the probability of the label assignment to generated data samples out of the learned distribution by the generator. These network components are trained simultaneously, where the generator is trained to generate realistic looking data to fool the discriminator, until the discriminator fails in differentiating between the generated and real sample. **Latent Dirichlet Allocation (LDA)** is a generative probabilistic hierarchical baysian model used to embed discrete (feature based) data. By computing finite mixture models for defined topics, an explicit representation of the data can be provided, where the data itself is represented as a finite mixture [22]. **Spectral Embedding Techniques** explore how to embed relational graphs represented as graph adjacency matrices in a pattern space by computing spectral properties of this matrices' eigenmode [140].

Embedding Based Representations in Neuroscience   In [147] principal gradient embedded representation of connectivity data of humans and macaque monkeys is proposed for situating the default-mode network. In [203] a dataset consisting of connectivity matrices of a developing cohort is embedded in the manifold of symmetric positive definite matrices, reporting improved analysis results compared to Euclidean space based embeddings. In [114] functional connectivity structure is embedded in a low-dimensional embedding space. For deriving the data structure, correlations of fMRI time courses are represented as graphs and diffusion processes are computed based on these. In this field the embedding based representation enables the decoupling of the functional from the anatomical location in the brain and building an atlas of functional connectivity patterns.

Embedding Based Representations in Cancer Research   For the analysis of FCM data recent approaches focus on the observation of the multidimensional feature space at once instead of multiple observations of 2D feature representations. However, the interpretation and visualisation of multidimensional FCM data remains challenging. In [48] embedding techniques are used to represent multidimensional FCM data in reduced dimensionality. They use subsampled data of 10 control subjects to create t-SNE maps (cf. [228] for more details) for the subsequent visual MRD assessment in ALL by projecting a patient's data into the embedding space using the transformation learned. The limit lies in the restricted amount of cells that are observable per subject ($2 * 10^4$ out of 10^6) according to increasing computational burden with increasing cell counts. Van Unen et al. [229] address this issue by providing a hierarchical stochastic neighbourhood embedding of gastrointestinal disorders mass cytometry data.

3.1.4   Atlas Based Image Representation

An atlas is formed by a reference model on the one hand and a labelling procedure on the other hand [33]. Labels for non annotated images are estimated automatically by mapping

an atlas based image representation to unlabelled data via a registration procedure. For creating an atlas based image representation all-to-one, pairwise or groupwise approaches are proposed.

- All-to-one Atlas: An image out of the whole dataset is chosen as reference and all other images are registered on to it. This can cause bias towards the chosen reference, if it does not represent the average geometry of the dataset.

- Pairwise Atlas: All images in the dataset are pairwise registered to a selected reference image. Subsequently, the resulting (inverse of the) affine or non-rigid transformations are averaged, to build an average reference image.

- Groupwise Atlas: This approach avoids the need for an initial reference space and constructs an unbiased average atlas. For estimating the unknown average template space all images in the dataset are used. During the registration the unknown template is updated to obtain an optimized unbiased reference model.

- Spatio Temporal Atlas: To obtain a continuous spatio-temporal model, the retrieved anatomical templates have to be set into relation dependent on a parameter that characterizes the time. We can differentiate between pairwise concatenation strategies of time dependent atlases and image regression approaches. Cf. Section 3.5 for a summary of spatio temporal atlases and trajectory modelling approaches.

Anatomical MRI Brain Atlases

The aim of *brain mapping experiments* is to create maps (templates), based on investigations, to understand structural brain organization. These maps are also called brain atlases and are an important research instrument e.g. for the identification of structural changes in the brain to identify neurological diseases or psychiatric disorders [158] or are used for surgical planning [47]. Talairach and Tournoux [220] proposed one of the first clinical relevant reference coordinate systems for the adult brain. Although it was one of the most influential atlases, it was derived from a single subject post-mortem [47], with incomplete clinical record. Related atlases are e.g. the Montreal Neurological Institute (MNI) 152 [26]. Since then, image registration methods improved as well as feature extraction approaches, resulting in improved **morphological MRI adult brain atlases** [158] (multi-class brain atlas [136], probabilistic brain atlas using Bayesian inference [116], a 4D probabilistc atlas from age 18 until 90 years [149], multi-channel atlas based on groupwise registration [186]). Additionally, the focus in adult brain atlas learning moved to incorporating knowledge from larger populations, different age ranges, ethnicity, sex, cognitive testing, to cover the high variability and to achieve an increased generalizability in large cohort studies (Allen Brain Map[1], Hammer Adult Atlases[2]). In contrast to atlases of the adult

---

[1]https://portal.brain-map.org/ [accessed 2021-02-04]
[2]https://brain-development.org/brain-atlases/adult-brain-atlases/ [accessed 2021-02-04]

brain, building an atlas of the developing brain has additional challenges, according to changing shape, size, cortical folding processes as well as signal intensity profile differences and decreased tissue contrast. Thus, it is recommended to use age specific templates in developing brain studies [47][158]. There exist probabilistic **fetal brain atlases** for in-vivo fetal brains based on pair-wise affine registration combined with kernel-regression [108], pairwise non-rigid registration combined with adaptive kernel-regression [207], time-varying atlas with application on segmentation [82], longitudinal atlas based on Kärcher Means and Large Deformation Diffeomorphic Metric Mapping [185], a normative spatio temporal atlas computed by symmetric diffeomorphic registration for automatic segmentation and analysis of early brain growth [70] and e.g. post mortem fetal brain atlases using groupwise diffeomorphic registration [245]. Also specific **atlases for the neonatal brain**[3] [208] [3], [75] have been proposed e.g. for the evaluation of term- and preterm born children, as well as probabilistic 4D neonatal atlases for cortical and subcortical image segmentation [146] or for high resolution T1 MRI brain acquisitions [97]. Besides fetal and neonatal atlases also **infant brain atlases**[4] are proposed [76], [210], [225].

Functional MRI Brain Atlas - Parcellations

The aim of functional brain mapping is to create maps (models), to understand functional brain organization and how cortical areas interact with each other [72]. Especially, for resting state functional networks in the **healthy adult brain functional atlases** have been proposed [51]: In [213] adult functional connectivity resting state networks of 30,000 subjects were analysed. Yeo et al. [241] provide a organizational map of the human cerebral cortex by analysing intrinsic functional connectivity data from 1,000 subjects between 18 to 35 years. Shirer et al. [211] define ninety functional regions of interest across 14 large-scale resting-state brain networks for the classification of cognitive states (quiet rest, remembering events of the day, number subtraction, silently sang lyrics). Doucet et al. [50] identify 23 resting-state networks based on rsfMRI acquisitions of 180 healthy subjects using ICA. The identified networks are hierarchically clustered and analysed level wise. Langs et al. [114] propose a functional connectivity atlas for mapping language regions in tumor patients by decoupling function and anatomy. Also a **functional brain atlas for the adolescent population** has been proposed. Gordon et al. [72] propose a cognitive atlas for the adolescent cortical surface for representing putative cortical areas[5]. They apply a boundary mapping technique, that has been used to identify transition zones in limited sections of the cortex. Resting state fMRI data from 120 subjects between the age 19 - 32 was acquired for this study. In the paediatric population Shi et al. [209] propose a **functional parcellation of the infant brain** using a graph-based clustering approach (NCUT). RsfMRI data from 230 neonates,

---

[3]https://brain-development.org/brain-atlases/neonatal-brain-atlases/ [accessed 2021-02-04]

[4]BrainSpan http://www.brainspan.org/static/atlas [accessed 2021-02-04]

[5]http://www.nil.wustl.edu/labs/petersen/resources/ [accessed 2021-02-04]

143 1-year olds and 107 2-year olds was acquired and analysed regarding associated developmental trends.

3.2 Alignment and Normalization of Medical Data

Normalization techniques are required to establish correspondence of different data in space, but also over time or to align a precomputed model (e.g. an atlas or reference image) with a new observation for image classification or segmentation. In this section, state of the art alignment techniques and normalization strategies for medical measurements and imaging data are presented.

3.2.1 Feature Cloud Alignment Strategies

Multi-dimensional patient specific or population data can be represented by estimating their underlying probability density function and corresponding parameters. Alignment strategies are necessary to find correspondences among shifted distributions of measured features in the multi-dimensional space and over time. The cause of distributional shifts and variances of medical data lies in instrument dependent drifts and calibrations, different acquisition protocols and standard operating procedures, patient specific variances or treatment response [162].

For the alignment of density based represented data two components have to be defined: (1) A suitable statistical distance measure for describing the shift between the source and the target datasets observed and (2) a suitable regularizer for defining the way of interpolation. The alignment is performed using a procedure which minimizes the chosen distance on the one hand and produces on the other hand a step-wise transformation of a source towards the target, which preferentially should lie on the same manifold as the input, e.g. an interpolation scheme for k-GMMs should provide an output that lies on the k-GMM manifold and minimizes the underlying distance between the source and target k-GMM [100].

The required feature cloud alignment strategy can be formulated as an optimal transport problem, which focuses to transport a given source distribution on a specified representation manifold in a way that it overlaps with the target distribution without loss of mass [35]. For this task the definition of an optimization function is required to find the optimal interpolation path on the manifold by minimizing a defined distance between the source and target distribution. There are a variety of distance metrics, which have to be carefully selected in dependence of the data observed. In the following sections a few examples of well known distance measures are summarized and corresponding applications for FCM data and as GMM represented data are introduced. In [163] the *Kolmogorov-Smirnov distance* is used to find close clusters of image intensity distributions in a non-parametric way for image segmentation. In [19] the *Bhattacharyya Bound (BB)* is proposed for measuring the distance between two probability distributions. If it is assumed that these distributions have the same standard deviations, the distance is refered to as *Mahalanobis distance* [144] (a special case of the BB). It goes towards zero

in case of similar distribution means, while the BB increases with growing standard deviation differences of two distributions. Other examples for distance measures between distributions are also *f-divergences*, with the special cases of *Kullback-Leibler divergence, Jensen-Shannon divergence, Hellinger distance* and *total variation distance* [131].

FCM Data Alignment Strategies

In [162] a comparison strategy of FCM based measurements of expression levels of biomarker in cell populations is proposed using the *Wasserstein distance*, also called (Earth Mover's Distance) as a metric. This distance measure has the advantage that it enables the estimation if small shifts are caused by biological significant differences or instrumental drifts. Additionally, the Wasserstein distance between two samples involves the magnitude of change and the proportion of cells whose antigen expression has changed. In [161] a matching strategy for FCM and mass cytometry data is proposed based on quadratic formcluster (QF Match). This scheme entails a multivariate extension of the quadratic form metric.

Gaussian Mixture Alignment Strategies

In this section various state of the art approaches for the registration and interpolation of GMM based representations is summarized. One focus lies on GMM since it is a widely used representation technique of FCM data. In [20] a robust alignment scheme of GMM representations of point sets is proposed using L^2 (also called L^2 norm or Euclidean distance) as metric. In [183] the L^2 *distance* is minimized between two distributions represented as GMM for feature space transformation for FCM data. The advantage of using L^2 distance is, that it provides a closed-form solution for GMM without a requirement of tuning parameter specification. The drawback lies in the interpolation between two GMMs, since in the intermediate evolution step it is not guaranteed that the result lies on the manifold of K-component GMM. Additionally, the minimization of this metric causes instability according to many local optima. To overcome this instability Kim et al. [100] introduced *cross-entropy* as metric including a closed form solution for GMM registration.

3.2.2   Image Normalization Strategies

According to anatomical differences between patients or due to disease, growing or surgery induced changes of a patient, as well as movement during acquisition, methods are required, which establish spatial correspondence between images [215]. It enables the performance of longitudinal studies, atlas-based labeling, image alignment or the comparison of different modalities. In an optimization procedure the optimal spatial transformation is determined between a source (template) image and a target image, where feature-based [145][196] and intensity-based approaches can be differentiated [215]. The normalization strategy can be parametric or non parametric, where in the first case the geometric transformation is estimated by finding the optimal parameters of

the deformation [248][13]. Linear registration uses rigid, affine or perspective-projective transformations for the alignment [145][248]. In contrast to this, deformable (non-rigid) registration allows local deformation based on physical models (elastic, fluid, diffeomorphic, demons diffusion curvature), interpolation models (radial basis function, basis-function, free-form deformation B-splines, locally affine) or knowledge-based geometry (statistical deformation, biomechanical finite element) [215][233]. The deformable registration process can be seen as an optimisation problem, where an optimal transformation function ϕ from a source I_0 to a target image I_1 minimises a defined cost-term E.

$$E = \operatorname*{argmin}_{\phi} \left[E_S(I_1, I_0 \circ \phi,) + \lambda E_R(\phi) \right] \tag{3.1}$$

In Equation 3.1 the general formulation of such an energy term is noted, consisting of a similarity measure E_S between target I_1 and transformed source image $I_T = I_0 \circ \phi$ and a regularisation term E_R. For the assessment of the quality of alignment of two images (global) or image sections (local) **similarity metrics** are used to measure the difference between transformed source and target image after every iteration [74][44]. This metric is chosen dependent on the imaging modality, should be smooth and have an extremum in case of image alignment and be differentiable as well as easy computable [215][44]. Common similarity metrics for mono-modal registration are sum of absolute difference (SAD), sum of squared differences (SSD) or correlation ratio (CR), while for multi-modal registration Mutual Information (MI) or Normalized Cross Correlation (NCC) are widely used [44][28]. In deformable registration infinite solutions for transforming an image non-rigidly exist. **Regularisation** is required to constrain the optimized deformation to be volume-, rigidity- or topology preserving as well as to remove solutions that are unstable or ill-conditioned [192] and enables the introduction of prior knowledge regarding tissue properties [215].

3.3 Clustering and Classification of Medical Data

Classification of medical data can be defined as an assignment of a label to a pixel or voxel (image segmentation), image (image classification) or a set of medical measurements (data classification) that represents the underlying anatomical structure, disease type or property (e.g. cancer, non-cancer). In the medical field this is required to make diagnosis, to assess treatment response, to perform medical simulations or for different types of treatment planning (preoperative, postoperative, radiation treatment)[89] [143]. Clustering or Classification approaches differentiate between manual, annotation-based (supervised) or automatic methods (unsupervised) [16]. This section gives an overview of state of the art clustering and labeling approaches for the data and medical research fields observed in this thesis.

3.3.1 Blood Cell Classification for Automatic MRD Assessment in Leukaemia

Automatic gating procedures (cf. Section 2.4.3 for details regarding manual gating of FCM data) to identify blood cell populations gained more interest in recent years, since it strongly relies on the operator's skills and expertise, is highly subjective and time-consuming. The main goal lies in the observation of the multidimensional space at once to replace the multiple observation of 2D feature representations. However, visualisation and interpreting multi-dimensional data remains challenging. Thus, state-of-the-art approaches [155, 244, 224, 14, 2] have as main goal the automatic assignment of a biologically meaningful population to every observed cell. Existing approaches are divided into unsupervised and supervised clustering methods.

Unsupervised Approaches: An **unsupervised approach** is proposed by Pyne et al. [176]. They use a multivariate finite mixture model based on Expectation Maximization (EM) and skew-t distribution, since they discover skew and heavily-tailed characteristics of the data clusters of interest observed. Finak et al. [64] extend the work of Lo et al. [135] by including the possibility to define the amount of cell populations that have to be identified. Naim et al. [155] propose an unsupervised clustering algorithm, adapted for using a revised Expectation Maximization (EM) for Gaussian Mixture Model (GMM) with an integrated splitting and merging procedure and focus on outlining small biologically meaningful populations.

Supervised Approaches: Toedling et al. [224] propose a **supervised approach** using clinical data for training a Support Vector Machine (SVM) classifier. It is tuned to automatically detect leukaemic cell populations and not only for discriminating different cell clusters. In contrast to this, Costa et al. [40] use Principal Component Analysis (PCA) to project an annotated training set to a 2D-principal subspace. Subsequently, new cells are categorised using nearest neighbour classification.

3.3.2 Automatic Fetal Brain Tissue Labeling

Fetal brain segmentation approaches are divided into supervised classification and automatic segmentation based methods [31]. Weisenfeld et al. [235] use probabilistic atlases for training a classifier for fetal MR tissue segmentation in an supervised way. In contrast to this, Prastawa et al. [172] use probabilistic atlases as features for classification. Xue et al. [240] perform non-supervised statistical tissue masking. They use label propagation as a prior in a Baysian framework. Habas et al. [83] propose an Expectation-Maximization (EM) Framework for building a probabilistic atlas for automatic fetal brain segmentation. Claude et al. [36] focus on automatic atlas-based labeling of the posterior fossa. Cuadra et al. [12] present a tissue labeling approach using an Expectation Maximization Markov Random Field (EM - MRF) procedure. Keraudren et al. [98] propose an approach for automatic segmentation of 2D MR slices for motion correction using Scale-Invariant Feature Transform (SIFT) and a combination of Maximally Stable Extremal Regions (MSER) and a Conditional Random Field (CRF). Wright et al. [238] adapt the automatic brain extraction algorithm of Eskildsen et al. [59] for fetal brains. This

approach is based on nonlocal segmentation techniques and the resulting segmentations are used to investigate the cortical folding patterns of fetuses' brains. Gholipour et al. [69] propose an automatic segmentation procedure for studying ventriculomegaly using a multi-atlas multi-shape approach. In recent years also deep learning strategies evolved for the extraction of the fetal brain and also for tissue labeling. Ebner et al. propose [58] an automatic pipeline for the localization, segmentation and reconstruction for fetal brain MRI using a Convolutional Neural Network (CNN). Khalili et al. [99] proposed a cascade of CNN architecture for first extracting the intracranial fetal brain volume with the first CNN and second for automatically labelling seven tissue classes.

3.3.3 Automatic Bone Segmentation and Lesion Tracking

In this section a brief summary of automated bone segmentation techniques for whole body acquisitions is given as well as an overview to bone lesion tracking techniques.

Bone Segmentation In [101] an automatic bone segmentation technique for whole-body CT images of MM patients is proposed. They use a U-Net inspired architecture, which is trained using 18 whole body CT scans and report a mean DC of 0.92. In [214] a 3D U-Net architecture is proposed for segmenting bones in dual-energy CT data of 21 patients, achieving a mean DC of 0.96. In [7] a shape-based averaging technique in combination with statistical atlas fusion is proposed to perform bone segmentation in whole body MRI for PET-MRI attenuation correction. The algorithm is evaluated on a dataset of 21 patients achieving a DC of 0.75.

Lesion Tracking Machine learning approaches have contributed to our ability to *detect* lesions. U-Nets have been used for the segmentation of 2D medical images, such as microscopy images [187], or for the detection of brain lesions [95], or bone lesions. Franzle et al. [67] quantified overall bone tumor volume in MM in lumbar vertebrae using T1 and T2 weighted MR image features of 4 patients with a random forest classifier. Perkonigg et al. [166] used transfer learning to detect bone lesions in CT scans of MM patients. In [239] a W-Net architecture (two cascaded 3D V-Nets) segments bone lesions in whole body CT/PET data of 12 patients.

3.4 Anomaly Detection and Prediction

The *detection of anomalies* (dependent on the application also called novelties or outliers) in data, can be defined as the task of assessing the difference of test data or deviating properties in respect to a given data distribution trained on normal data. In the past, novelty detection got attention for the application in detecting failures in industry systems or structural damage, robotics, video surveillance or text mining (cf. [167] for a review). Recently anomaly detection approaches are also used in the medical domain. Approaches can be differentiated in feature based approaches and image based approaches. In the feature domain outlier detection is used e.g. to monitor the condition of premature

infants in intensive care [177]. In [38] a one class Support Vector Machine (SVM) is used for novelty detection to assess the outcome of patient in hospitals and for detecting if a patient's physiological condition deteriorates. In the image space [110] the distribution of imaging features of normal mammogramm images are modelled and the anomaly is identified by thresholding the BB distance between the learned distribution and the test image. Schlegl et al. [200] propose a deep convolutional Generative Adversarial Network (GAN) for anomaly detection, by learning the distribution of normal retina images acquired by optical coherence tomography. They detect retinal fluid or hyper reflective foci as anomalies in pathologic retina data. In [164] Bayesian neural network ensembles are used to learn the true posterior of the training data in a first step. After training, the uncertainty score of a prediction provided by the trained ensemble is used to estimate their distributional parameters (mean, standard deviation). The detection of an outlier is performed using a defined threshold for these parameters.

Progression Prediction In [205] future multiple sclerosis disease activity is predicted in MR images using a modified 3D U-Net architecture for lesion labeling and a CNN for lesion prediction. As input of the network multi-modal MR sequences are required to predict a lesion label. They report a significant improvement of the prediction accuracy by including lesion labels at baseline, which leads to drawing the attention of the network to the location of lesions. In [132] the transition from at a mild cognitive impairment stage to Alzheimer's Disease (AD) is predicted. CNNs are trained with MRI patches of the ADNI[6] dataset to extract imaging features. An extreme learning machine classifier is used to predict the transition to AD. In [117] AD future scores are predicted based on longitudinal MRI data. They train a regression framework consisting of a joint learning procedure for feature selection and a deep polynomial network for feature encoding. Finally, support vector regression is used to predict the clinical scores.

3.5   Spatio Temporal Modelling of Medical Data and Dynamics over Time

In this section spatio temporal modelling concepts for medical data is briefly summarized. The approaches are divided into methods designed for (1) medical record/measurements over time and (2) medical image time-series or longitudinal acquisitions.

3.5.1   Spatio Temporal Modelling in the Medical Feature Domain

Disease progression models are used to model dynamic patterns of disease development by encoding trajectories of complex diseases based on medical records, biomarkers or symptoms. Thus, these models are also used to optimise the treatment according to the prediction of an individual's disease progress [202]. The basic idea of state-of-the-art concepts lies in defining disease states based on the data analysed and by defining

---

[6]http://adni.loni.usc.edu/[accessed 2021-02-04]

transitions and dependencies between states. **Boolean networks** use boolean variables to represent active or inactive stadia of a biological process. It is possible to design gene regulatory networks, to identify attractors (steady stadia), to analyse the robustness of networks and to model signalling pathways [142]. **Bayesian networks** are probabilistic graphs consisting of nodes, which represent random variables for encoding a stadium, and edges, which express a probabilistic transition function between two stadia, which is dependent on the values of connected input nodes. It is used to model gene regulatory pathways and signaling networks. Wang et al. [231] learn a model of disease progression in an unsupervised way, using a Bayesian network and Markov jump process. They evaluate the proposed approach on Chronic Obstructive Pulmonary Disease (COPD) patients. In Table 3.1 a spatio temporal modelling approaches in the medical feature domain are summarized. In a dynamic formulation Bayesian networks are also able to model feedback

Table 3.1: Spatio temporal modelling of features extracted from the data domain

Approach	Methodology	Trajectory modelled
Dagum 1993 [45]	Dynamic Bayesian NW	Sleep Apnea Prediction
Exarchos 2013 [60]	Dynamic Bayesian NW	Coronary atherosclerosis progression
Wang 2014 [231]	Bayes. NW, Markov Jump Process	COPD progression
Liu 2015 [134]	Hidden Markov Model	Glaucoma progression, Alzheimer's disease

loops [142]. Dagum et al. [45] use a dynamic network model to forecast sleep apnea, incorporating contemporaneous and non-contemporaneous dependencies. Exarchos et al. [60] use dynamic Bayesian networks for the modelling of coronary artheroslerosis progression. **Petri nets** are based on a bipartite graph formulation, differentiating between two types of nodes (places, transition) connected with directed edges. They are used to model metabolic pathways, gene regulatory networks and signalling networks or to integrate different types of networks [142]. **Constraint-based models** have been used to model metabolic pathways for flux analysis. This technique enables it to be defined in a multi solution way by defining a space of possible different phenotypes corresponding to defined constraints [142]. **Differential equations** are used to model dynamic biological pathways, representable by a change of continuous variables. Subtypes are ordinary differential equations, partial- and stochasic, piecewise linear differential equations. **Hidden Variable Models** compute disease states by the abstraction of latent variables. The definition of dynamical priors and constraints enable the modelling of noisy and irregular measurements. Liu et al. [134] use continuous time Hidden Markov Models (HMM) to encode the occurrence of the transition between hidden states and the arrival of observation at different time-points. They use the introduced approach to predict glaucoma progression and to model temporal interaction of Alzheimer's disease markers.

3.5.2 Spatio Temporal Modelling in the Medical Image Domain

Time-dependent developmental processes in the image domain are modelled using continuous time-varying templates, to assess shape changes and structural changes. Previously published approaches encode differences appearing over time as local spatial transformation using non-linear techniques [185][11][157][125]. Another possibility to model changes are statistical techniques. **Parametric approaches** (e.g. Hierarchical Linear model, General Linear model) are limited to the spatial resolution of the data as well and to the arbitrary definition of model complexity [137]. In Table 3.2 a summary of examples for spatio temporal modelling concepts in the image domain is given. **Non**

Table 3.2: Spatio temporal modelling approaches in the image domain

Approach	Methodology	Trajectory modelled
Durrleman 2009 [54]	Spatio temporal regression model for shape evolution	Evolution of the hominid's skull's shape
Wang 2010 [234]	Hidden Markov Models	Brain changes in elderly people
Niethammer 2011 [157]	Geodesic regression for image time-series	Morphology changes of the ageing brain
Ashburner 2012 [11]	Non linear diffeomorphic technique	Morphology of Alzheimer's disease progression
Zhan 2013 [245]	Non linear diffeomorphic technique	Morphology changes of the developing fetal brain
Lorenzi 2015 [137]	Gaussian process	Alzheimer's disease progression
Hwang 2016 [86]	Coupled harmonic bases, graph based representation embedding space	Brain network of structural connectivity

parametric approaches have been proposed for analysis of brain signals, but for high-resolution images a decrease of performance according to computational complexity is observable. **Gaussian process models** are non-parametric and based on Bayesian statistics. They can be used to model aging, time-series and to predict and model in the manifold domain [182]. Lorenzi et al. [137] propose a spatio temporal disease progression model based on a Gaussian process formulation to analyse time-series MR images of Alzheimer's patients. Wang et al. [234] use **HMM** to encode brain changes in elderly people by defining subsequent probabilistic transitions between discrete states. They are capable to detect abnormal changes by enabling the comparison to healthy trajectories. Hwang et al. [86] use coupled harmonic bases for creating a longitudinal model of brain networks. They perform longitudinal coupling of states in the embedding space of a graph based representation of the data.

CHAPTER 4

Datasets of Dynamic Developmental Patterns

"Life isn't about finding yourself. Life is about creating yourself." [George Bernard Shaw, (1856 - 1950)]

This chapter summarizes the datasets used to evaluate the concepts of spatio temporal models of dynamic developmental patterns proposed. In total 6 different datasets are used in this thesis, consisting of 3 FCM datasets (Section 4.3), 1 fetal MRI time-series dataset (Section 4.1), 1 rsfMRI time-series dataset (Section 4.2) and 1 longitudinal whole-body MRI dataset (Section 4.4).

4.1 Dataset FETAL

The non-public dataset *FETAL* is a time-series MRI dataset of 45 healthy fetal brains with an age range between 18 and 30 GW acquired and provided by the Medical University of Vienna [125]. All participants' guardians (parents) were informed about the aim of the study and gave their written, informed consent prior to inclusion. The protocol of this study was approved by the Ethics Committee of the Medical University of Vienna and performed in accordance with the Declaration of Helsinki (1964), including current revisions and the EC-GCP guidelines. As introduced in Section 2.4.1 for obtaining short acquistion times an interleaved protocol is used for acquiring planes of coronal, sagital and axial orientation. The MR image acquisition is performed using an 1.5 Tesla Philips Gyroscan superconducting unit scanner performing a single-shot, fast spin-echo T2-weighted MR sequence. In Table 4.1 the imaging parameters are summarized. Figure 4.1 visualises examples of the dataset *FETAL*. 2D slices of fetal MRIs at different GWs are shown (the abbreviation D stands for gestational day). It is observable, that over gestational age the fetal brain's position and orientation varies, as well its size and shape.

45

Table 4.1: MR acquisiton protocol for dataset *FETAL*

In-plane resolution	$0.78 - 0.9$ pixels per mm
Slice thickness	$3 - 4.4$ mm
Acquisition matrix	210×210
FOV (Field Of View)	$200 - 230$ mm
SAR (Specific Absorption Rate)	$< 100\%$ /4.0W/kg
TE (Echo Time)	$100 - 140$ ms
TR (Repetition Time)	$9,000 - 19,000$ ms
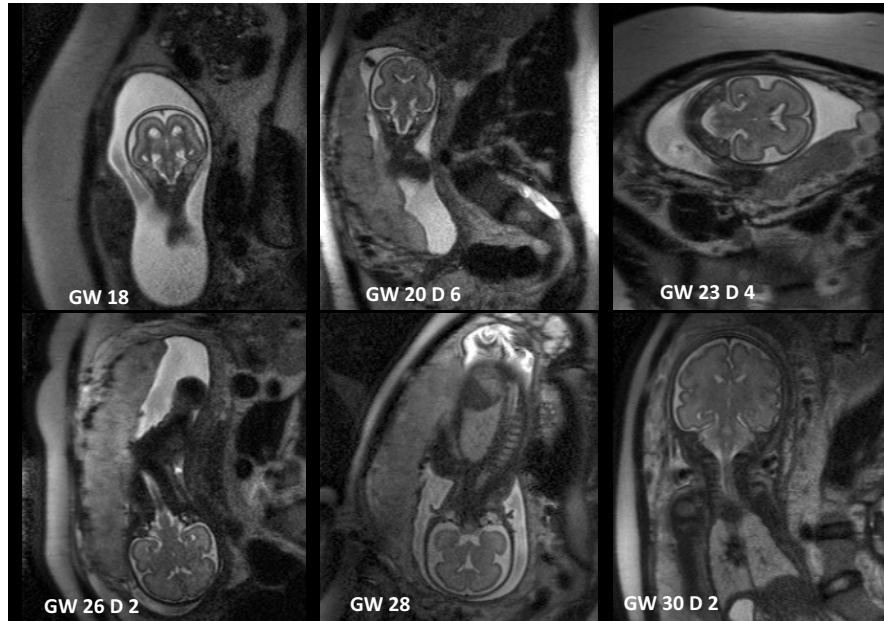
Figure 4.1: MRI slices of healthy fetuses between GW 18 and GW 30 GD 2 of the dataset for 2D analysis. MR images courtesy of Medical University of Vienna.

Also beside the fetal brain, the surrounding mother tissue is captured. For learning a longitudinal atlas of the fetal brain development (introduced in Section 6.1) a data preprocessing pipeline is setup based on preliminary experiments: For obtaining an isotropic super resolution 3D volume of a fetus' brain, a subject's MR images in axial, coronal and sagital orientation are motion corrected and registered using the toolkit proposed by Rousseau et al. [191]. This step is performed, since it increases the voxel grid density and removes the effect of motion during acquisition. Annotations of brain tissue (white matter, grey matter, germinal matrix), ventricles, left and right eye are provided by medical experts as well as the marking of the occipital foramen magnum. Based on preliminary experiments, it was decided to rigidly align the brains, since the core of the atlas learning procedure is to encode brain developmental changes, and not appearance changes according to the fetuses' orientation in the womb. Rigid alignment

is performed automatically by a self-developed routine. This routine first estimates the triangle spanned between the left eye, right eye and the occipital foramen magnum and computes its barycenter. Second, the orientation of the triangle surface is estimated, by computing the surface's normal vector in the barycenter. Third, a reference orientation of the triangle is setup and the rotation and translation parameters are estimated. After rigid alignment of the fetal brains the preprocessing concludes with a brain masking step, since preliminary registration experiments for non-rigid brain alignment show increased performance, by excluding the surrounding mother tissue.

4.1.1 Notation

In the time-series dataset *FETAL* following notations are defined:

- $p = \{1, \ldots, P\}$, where P denotes the number of fetuses in the dataset

- t denotes the gestation age of a fetus

- I denotes an MR acquisition of a fetus, where $I \in \mathbb{R}^{N \times M \times d}$

- $m = \{1, \ldots, M\}$ and $n = 1, \ldots, N$, where M and N denote the dimension of one slice in an acquired volume

- $d = \{1, \ldots, D\}$, where D denotes the number of slices in an acquired volume

- S_{tissue} denotes a segmentation of the brain tissue, where $tissues = \{cortex, ventricle\}$, $S \in \mathbb{R}^{N \times M \times d}$

- x_i : denotes the position of the i_{th} voxel in an image I

4.2 Dataset CHILD STROKE

The non-public dataset *CHILD STROKE* consists of rsfMRI acquisition of 32 children between 7 and 17 years, which was provided by the Medical University of Vienna [127][121]. In total 16 control cases and 16 ischaemic stroke cases are acquired. The ischaemic stroke events occurred at different spatial locations on the Right Hemisphere (RH) and Left Hemisphere (LH). The children's handedness was right-, left- or mixed handed. The time frame between the scan time point and stroke event, as well as the range of the age at stroke of the children ranges from 0 to 15 years. A summary of these facts is summarized in the participant's demographics in Table 4.2. In Figure 4.3 the age distribution at examination of control and stroke cases are visualised and additionally for every subject in the stroke cohort the age at stroke and time between stroke and image acquisition is plotted. All participants' guardians (parents) were informed about the aim of the study and gave their written, informed consent prior to inclusion. The protocol of this study was approved by the national ethics committee of the Medical University of Vienna and performed in accordance with the Declaration of Helsinki (1964), including
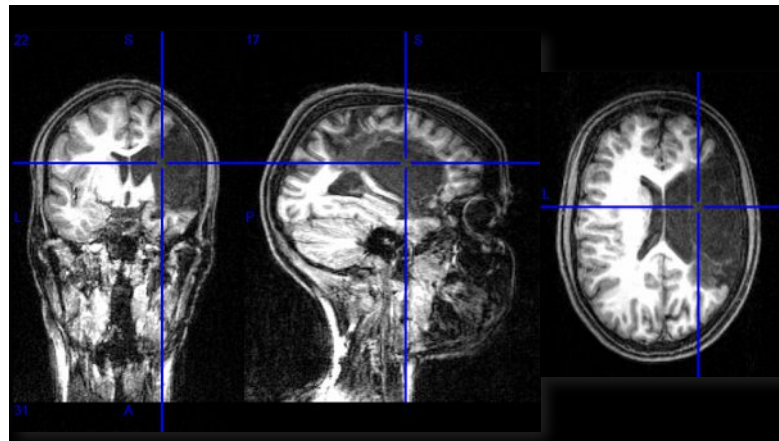
Figure 4.2: Visualisation of an MRI acquisition of a severe medial infarct in the RH of the dataset *CHILD STROKE* at age 17, stroke event at age 10. Image courtesy Medical University of Vienna.

Table 4.2: Participants' demographics.

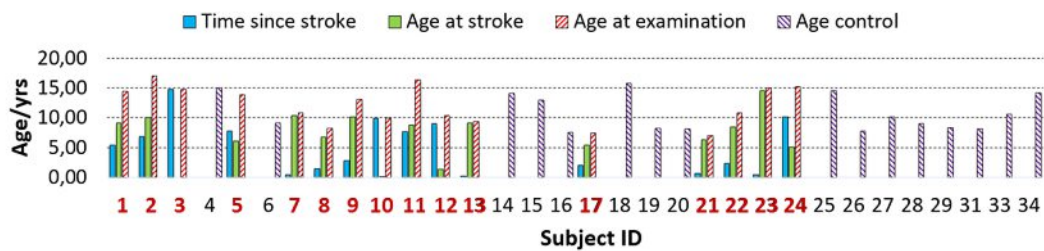|	Control	Pediatric stroke
Sample size	16 (7 female)	16 (5 female)
Excluded	4	5
Mean age, yr (Standard Deviation)	11.2 (3.19)	11.63 (3.14)
Stroke location (number of subjects)	-	RH (7), LH (7), RH+LH (2)

Figure 4.3: Distribution of data: For every control subject we show age, for stroke patients, age at stroke, age at examination, and time since stroke [127].

current revisions and the EC-GCP guidelines. The scanning was performed on a 3T TIM Trio System (Siemens Medical Solution, Erlangen, Germany) Scanner and rsfMRI measurements are performed using single-shot, gradient-recalled, echo-planar imaging with the setup summarized in Table 4.3: All subjects are scanned in an awake state with open eyes for 5 minutes. To restrict head motion, pillows are used as fixation on both sides of the child's head. The probands wore headphones to attenuate the noise level during scan. All study participants watched a video, explicitly designed for children,

Table 4.3: rsfMRI acquisition protocol for dataset *CHILD STROKE*

Slice thickness	4 mm
Gap between slices	1 mm
Acquisition matrix, slices, frames	210×210, 20 (slices), 150 (volumes)
TE (Echo Time)	42 ms
TR (Repetition Time)	2000 ms

which showed and explained an MRI acquisition procedure.

Anatomical and Functional Preprocessing: Subject No.15 (control), No.17 (stroke), and No.21 (stroke) were excluded, due to technical issues during acquisition. During the preprocessing phase three stroke Subjects (No.3, 10 and 22) and control Subjects (No.26, 33 and 34) were excluded because of high motion artefacts and severe stroke (more than the half of the size of a hemisphere was affected). Anatomical and functional preprocessing is performed using Freesurfer[1][65] and FSL[2][92], two well established toolboxes in the field, which entail standard functional MRI preprocessing routines. Based on preliminary experiments a preprocessing pipeline is setup, following the guidelines presented in [168]. The *anatomical image preprocessing* pipeline includes motion correction, intensity correction, normalisation to MNI305 standard space, skull stripping, automatic subcortical segmentation, WM segmentation, surface tesselation and smoothing (standardized meshspace). The *functional preprocessing* includes a registration to the anatomical data, slice-timing correction, head motion regression and bandpass temporal filtering (0.01 - 0.1 Hz) to remove constant offsets and linear trends. Cerebral signals of the stroke and control cases are resampled to common FreeSurfer *fsaverage5* space [66]. After this alignment every subject's cortical surface is represented as a standardized mesh consisting of 20,484 nodes. After resampling the data are spatially smoothed using a 4 mm FWHM Gaussian filter.

4.2.1 Notation

For the time-series dataset *STROKE* following notations are defined:

- $p = \{1, \ldots, P\}$, where P denotes the number of children in the dataset

- I denotes an rsfMRI acquisition of a child, where $I \in \mathbb{R}^{K \times L \times S \times T}$

- $k = \{1, \ldots, K\}$ and $l = \{1, \ldots, L\}$, where K and L denote the dimension of one slice in an acquired volume

- $s = \{1, \ldots, S\}$, where S denotes the number of slices in an acquired volume

---

[1]http://surfer.nmr.mgh.harvard.edu, [accessed 2021-02-04]
[2]http://fsl.fmrib.ox.ac.uk/fsl/fslwiki/FSL[accessed 2021-02-04]

- $t = \{1, \ldots, T\}$, where T denotes the acquisition time point of the rsfMRI

- C denotes a control case and S denotes a stroke case

- $x_i(t)$: denotes the BOLD signal at acquisition time point t in region i

4.3 Dataset Flowcytometry

The non-public FCM datasets used in this thesis were generated in collaboration with experienced clinicians from the Children's Cancer Research Institute in Vienna[3] in the course of the European project AutoFLOW[4] [129] and the national project FlowCLUSTER[5] [128]. All participants' guardians (parents) and patients were informed about the aim of the study and gave their written, informed consent prior to inclusion. For every patient in average 300,000 cells are measured using FCM (cf. Section 2.4.3). Partial overlapping of fluorescence spectra of different fluorochromes is removed by *spillover compensation*. The preprocessing concludes with a normalization of the measured parameter values between 0 and 1.

4.3.1 Dataset ALL

The dataset *ALL* consists of longitudinal FCM measurements of 116 patients with B-ALL (type of ALL, which involves B-cells) acquired at treatment day 15, 33 and 78. The patient's therapy was guided by the AIEOP-BFM 2009 protocol[6]. At the Children's Cancer Research Institute all samples have been prepared and annotated according to the international standard operating procedure for 6 color FCM. For every cell ten FCM based features are measured - 3 optical features, providing information regarding cell size (Front SCatter - Area (FSC-A), Front SCatter - Width (FSC-W)) and granularity (Side SCatter - Area (SSC-A)) and 7 fluorescence based features (antibodies): CD20, CD10, CD45, CD34, SYTO41, CD19, CD38. The antibodies only attach to the corresponding antigens like a key/lock system and thus can be used as a marker/stain. Antigens form expression patterns on the cell surface, which are specific for every blood or cancer cell type. In Table 4.4 the marker specific properties[7] are summarized. Figure 4.4 visualises a sample of a patient of the dataset *ALL* as a collection of 2D plots, created by the combination of two measured features. Blasts are marked in red. The gating hierarchy with corresponding amount of cells per gate are visualised on the bottom right. Please continue following Section 2.4.3 for a description regarding the gating procedure.

---

[3]https://science.ccri.at/ [accessed 2021-02-04]

[4]https://cvl.tuwien.ac.at/project/autoflow/ [accessed 2021-02-04]

[5]https://cvl.tuwien.ac.at/project/flowcluster/ [accessed 2021-02-04]

[6]AIEOP-BFM 2009 is a conducted randomized clinical trial for ALL between age 1-18 years in 10 countries in- and outside Europe, with approximately 1000 patients observed per year [55]) https://bfminternational.wordpress.com/ [accessed 2021-02-04]

[7]http://www.pathologyoutlines.com/cdmarkers.html [accessed 2021-02-04]
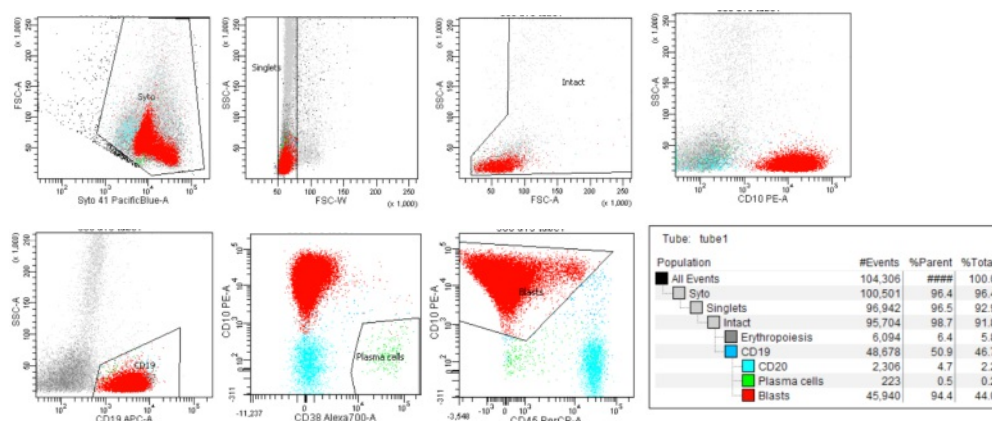
Figure 4.4: Visualisation of a data sample of one patient of the FCM dataset *ALL*. Image courtesy Children's Cancer Research Institute Vienna.

Table 4.4: Cluster of Differentiation (CD) Marker Properties for Antibody Panel used in dataset *ALL*.

Antibody	Explanation
CD20	B-cell marker
CD10	Marker for leukaemic ALL cells which derive from pre-B lymphocytes
CD45	Marker of hematopoietic cells (leukocytes), not mature red blood cells, platelets or megakaryocytes
CD34	Marker for hematopoietic progenitor cells
SYTO41	Binds to nucleic acids, i.e. enables the differentiation between debri or leaving cells
CD19	B-cell marker
CD38	Marker of plasma cells and plasmablastic differentiation, used for the diagnosis of multiple myeloma and chronic lymphoblastic leukaemia

4.3.2 Dataset AML Diagnose

The dataset *AML Diagnose* consists of FCM measurements of 13 AML patients (please cf. Section 2.2 for more details regarding the disease) whose therapy was guided according to the AML BFM 2004 treatment protocol [43][8]. As introduced in Section 4.3.1 specific antibodypanels are used to stain the cell specific antigen patterns on the cells' surfaces.

[8]AML BFM 2004 (https://www.kinderkrebsinfo.de/health_professionals/clinical_trials/closed_trials/aml_bfm_2004/index_eng.html) is a conducted randomized clinical trial for children and adolescents with AML between age 0-18 years with 722 patients [accessed 2021-02-04]

For every cell twelve FCM based features are measured - 2 optical features, providing information regarding cell size (Front Scatter INT (FSINT)) and granularity (Side Scatter INT (SSINT)) and 10 fluorescence based features per *DURACLONE*[9] tube:

- LAIP tube: CD15, CD7CD19, CD34, CD117, CD33, CD13, CD11b, CD14, HLA-DR, CD45.

- CFU tube: CD38, CD99, CD34, CD117, CD33, CD371, CD123, CD45RA, HLA-DR, CD45.

In Table 4.5 the staining properties of the antibodies used in the *DURACLONE* panels are summarized. Every subject's sample is preprocessed and annotated at the Children's Cancer Research Center in Vienna for paediatric AML, following the international standard operating procedure for MRD detection using FCM. The AML dataset is acquired using FCM measurements of in total 15 AML diagnosed subjects containing blasts and non-blasts.
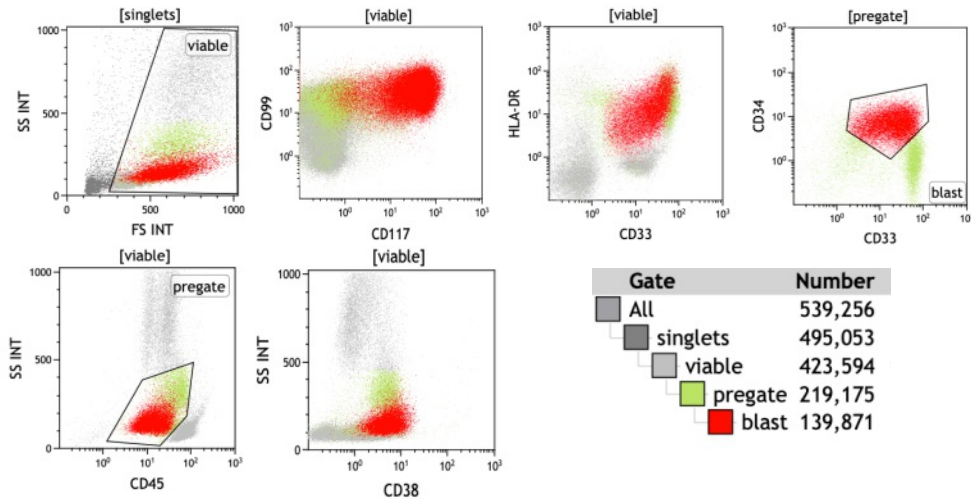
Figure 4.5: Visualisation of a data sample of one patient of the FCM dataset *AML Diagnose*. Blasts are marked in red. The gating hierarchy with corresponding amount of cells per gate are visualised on the bottom right. Image courtesy Children's Cancer Research Institute Vienna.

4.3.3 Dataset ALL-k0

The *ALL-k0* dataset consists of FCM measurements of 30 patients that have been diagnosed with ALL in the remission phase, i.e. where no blasts are present and thus

---

[9]https://www.beckman.com/reagents/coulter-flow-cytometry/antibodies-and-kits/duraclone-panels [accessed 2021-02-04]

Table 4.5: Antibody Panel used in datasets *AML Diagnose* and *ALL-k0*.

Antibody	Explanation
CD11b	Common myeloid and natural killer cell antigen marker, pos. preB ALL and acute promyelocytic leukaemia
CD13	Marker for myeloid cells and monocytes, for B cell ALL diagnosis
CD14	Marker for macrophages and monocytes, B cells, pos. myelomonocytic leukaemia
CD15	Marker for lymphoid and mature granulocytes, promyelocytes and monocytes, used as poor prognostic marker in acute promyelocytic leukaemia [150]
CD7CD19	T-cell (CD7) B-cell (CD19) interaction marker in early lymphoid development
CD34	Marker for hematopoietic progenitor cells
CD38	Marker of plasma cells and plasmablastic differentiation, used for the diagnosis of multiple myeloma and chronic lymphoblastic leukaemia
CD117	Marker of proto-oncogene activated in GIST tumors
CD33	Marker of progenitor and other myeloid cells (decreasing expression) with maturation
HLA-DR	Human Leukocyte Antigen marker, macrophages, B-cells
CD45RA	Marker of leukocytes with subepitope RA and T lymphocytes
CD45	Marker of hematopoietic cells (leukocytes), not mature red blood cells, platelets or megakaryocytes
CD99	Marker for thymocytes and used for Ewing's sarcoma tumors, Hodgkin lymphoma classification
CD123	Marker of myeloid precursors, basophils, mast cells, macrophages, dendritic cells, megakaryocytes, subset of lymphocytes
CD371	Marker for monocytes, granulocytes, NK cells and basophils

no annotations on cell-level are available. The same antibody panel as for the *AML Diagnose* dataset is used (cf. Section 4.3.2). The therapy was guided according to the AIEOP-BFM 2009 trial. The sample preparation and manual MRD assessment are performed at the national diagnostic reference center for paediatric AML according to the current international standard operating procedure for 10 color FCM-MRD detection. For each cell, thirteen parameters are obtained by the FCM measurement, consisting of three optical (FSC-A, FSC-W, SSC-A) and ten fluorescence based parameters (CD15, CD7CD19, CD34, CD117, CD33, CD13, CD11b, CD14, HLA-DR, CD45) which are tuned according to the leukaemia type. One feature represents a dimension in the multidimensional data space.

4.3.4 Notation

For the longitudinal dataset *BLOOD* following notations are defined:

$n = \{1, \ldots, N\}$, where N denotes the number of cases in the dataset
$m = \{1, \ldots, M\}$, where M denotes the number of cells measured
$d = \{1, \ldots, D\}$, where D denotes the number of antigens/features measured per cell
t denotes the treatment day, where $t = \{15, 33, 78\}$
X denotes the dataspace of FCM acquisitions, where $X \in \mathbb{R}^{N \times M \times D}$
x denotes a cell specific (event-based) measurement, where $x \in \mathbb{R}^D$

4.4 Dataset BONE

The non-public datasets *BONE* consists of 220 longitudinal wb-MRIs of 63 patients acquired between 2004 and 2011 at the University Hospital Heidelberg [236] following the guidelines proposed in [53]. At the point of the first examination patient's were diagnosed a pre-cursor form of MM (i.e.smoldering multiple myeloma) and were scanned over several time points while the symptomatic form of MM evolved. At least one wb-MRI was performed per patient. For every dataset medical experts annotated focal lesions manually, starting at a lesion size from 5 mm on (as described in [236]), following the IMWG consensus statement considering this as the threshold for symptomatic myeloma with therapy requirement [49]. Table 4.6 shows the demographics of the study participants. The protocol of this study was approved by the institutional ethics

Table 4.6: Participants' demographics

Patients	63 (24 female)
Therapy	Radiation or resection
Median age at initial MRI (yrs)	55
Age range (yrs)	29 - 76
Median interval between MRIs	13 months
Median observation time	46 months

committee for retrospective analysis of imaging data from patients with monoclonal plasma cell disorders with waiver of informed consent [236]. The scanning was performed on a 1.5 Tesla Magnetom Avanto (Siemens Healthineers, Erlangen, Germany) scanner. According to [236] the following setup for the scanning sequence was used:*"T1-weighted turbo-spin echo sequences (repetition time (TR), 627 milliseconds [ms]; echo time (TE), 11 ms; section thickness (ST), 5 mm; acquisition time (TA), 2:45 min) and T2-weighted short-tau inversion recovery sequences (TR, 5300 ms; TE, 74 ms; ST, 5 mm; TA, 3:00) of the head, thorax, abdomen, pelvis, and legs in coronal orientation; T1-weighted turbo-spin echo sequences (TR, 621 ms; TE, 11 ms; ST, 3 mm; TA, 1:38) and T2*-weighted turbo-spin echo sequences (TR, 4000 ms; TE, 93 ms; ST, 4 mm; TA, 2:30) of the spine in sagittal orientation"*. No contrast medium was administered. The duration of a scan was approximately 40 minutes. The median interval between two MRIs was 13 months.
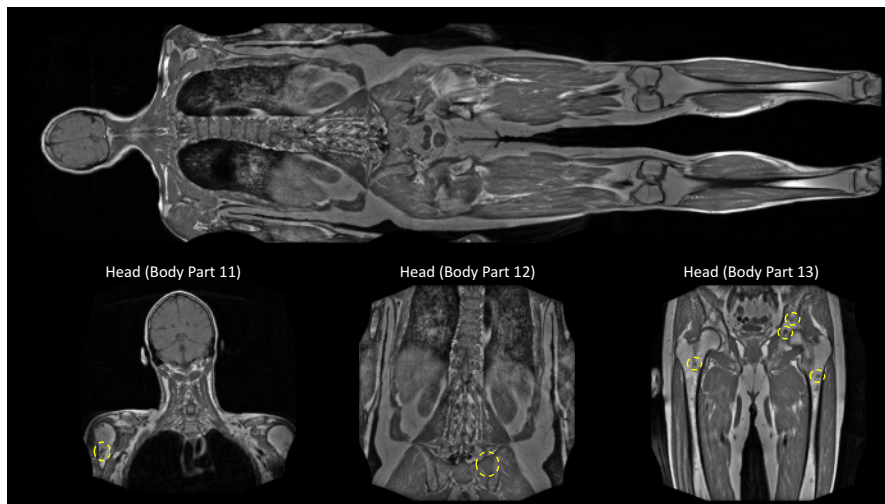
Figure 4.6: Whole body T1 weighted MRI acquisition of one patient with multiple bone lesions distributed over the whole body. Image courtesy Medical University of Vienna.

Whole-body MRIs were acquired in four steps consisting of the head/shoulder BodyPart (BP), the thorax/abdomen BP, the pelvis/superior legs' and knees BP and the inferior legs' and feet BP.

For obtaining a standardized representation of one patient's longitudinal acquisitions, it was decided to first perform bias field correction using FAST[10] [92]. Second, to achieve longitudinal correspondence all patients' scans were registered to the baseline scan (first acquisition time point). The aim of this study was to assess and predict the progression patterns of focal bone lesions in MM and consequently to track changes and deformations of lesions. Based on preliminary experiments using an affine global registration procedure showed the best correspondence results and mirrored the expected deformation patterns of the bones monitored. For the initial affine registration a block matching method for global registration (NiftyReg toolbox function *reg_aladin*[11] [152]) was used. Registration quality was assessed by visual inspection of overlay visualisations of aligned image pairs and evaluated regarding the correspondence of the bones' and lesions' position between two time points. All registrations were considered satisfactory.

4.4.1 Notation

For the longitudinal dataset *BONE* following notations are defined:

- $p = \{1, \ldots, P\}$, where P denotes the number of patients in the dataset

- $t = \{1, \ldots, T\}$, where T denotes the time point of acquisition

---

[10]https://fsl.fmrib.ox.ac.uk/fsl/fslwiki/FAST [accessed 2021-02-04]
[11]https://github.com/KCL-BMEIS/niftyreg/wiki [accessed 2021-02-04]

- $I_p(t)$ denotes an wb-MRI acquisition of a patient p at timepoint t, where $I \in \mathbb{R}^{N \times M \times D}$

- $m = \{1, \dots, M\}$ and $n = \{1, \dots, N\}$, where M and N denote the dimension of one slice in an acquired volume

- $d = \{1, \dots, D\}$, where D denotes the number of slices in an acquired volume

- BP denotes the body part of acquisition, where $BP = \{head, thorax, legs\}$

- x_j denotes the position of the j_{th} voxel in an image I

CHAPTER 5

Time Specific Analysis of Disentanglement Strategies

"Everything should be made as simple as possible, but not simpler." [Albert Einstein (1879 - 1955)]

This chapter summarizes the first part of the contribution of this thesis: *Creating a suitable representation concept for dynamic developmental medical data.* During medicine studies, students first learn how scans, medical examination and reports look like in healthy cohorts, to be able to detect deviations caused by disease, treatment response or other environmental factors. In computational modelling of imaging or medical record scores we can use these strategies as well. The main idea is to focus on modelling baseline stable patterns (not necessarily corresponding to healthy cohorts) in a first place and use these afterwards to detect and classify dynamics. Instead of learning all possible dynamics and variations in the data, which requires a huge and versatile dataset, baselines can be used to address new dynamics, to establish correspondence over time and to separate disease dependent from development dependent variations.

In this thesis the focus specifically lies on answering the following research questions:

- Can we extract *baseline* properties, which encoding stable patterns, for different representation techniques?

- Can dynamics be disentangled from stable patterns? What influence has the representation technique on the disentanglement?

- Can we describe dynamics using these stable patterns?

57

The developed methodologies and corresponding results were published in [129],[128] and [130] for FCM data, and in [127] for MRI data. Since in this thesis different medical applications and data formats are covered, additionally every section addresses field specific research questions, with the representation concept and disentangle strategy proposed.

5.1   Representation of Dynamics in Childhood Leukaemia

This section summarizes the contribution and results proposed for addressing the dynamics captured by FCM in childhood leukaemia. The analysis of dynamic developmental patterns in ALL is summarized in Section 5.1.1 [129], and for AML in Section 5.1.2 and 5.1.3 [128, 130]. The following research questions are addressed regarding representation of FCM data for MRD assessment:

1. Can healthy blood cell populations be used as baseline state at a defined treatment time point? Which data representation strategy is suitable?

2. Can a baseline state of an earlier treatment time point also be used to determine baseline states in a subsequent treatment time point? Do healthy blood cell populations change over treatment and affect the automatic MRD assessment?

3. Which machine learning technique performs best for automatic MRD assessment over several treatment time points?
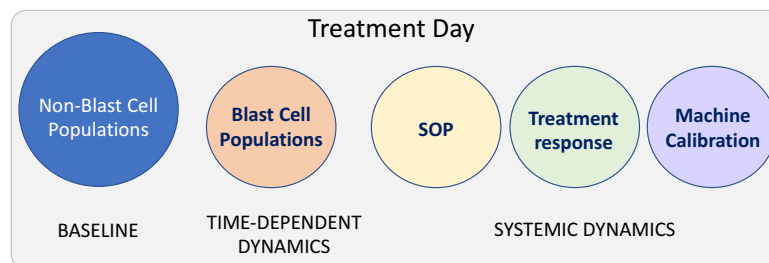
Figure 5.1: Disentanglement of baseline properties and dynamics in leukaemia research at a specific treatment time point. The baseline is formed by non-blast populations, which is further used to address the time-dependent dynamics of blast cell populations and systemic dynamics induced by machine calibration, Standard Operating Procedure (SOP) or treatment response.

In Figure 5.1 the components for the representation concept for FCM data at a specific treatment time-point are illustrated. The baseline is formed by non-blast populations, time-dependent dynamics are formed by blast-cell populations and systemic dynamics by Standard Operating Procedures (SOP), treatment response or machine calibration. In the following section different representation and disentangle strategies are analysed for

FCM data.

Following input and outputs for the analysis pipeline can be defined:

- The input of the analysis are blood cell FCM measurements X_p of P patients.

- Different representation and disentangle techniques are analysed and compared against state-of-the-art approaches regarding their ability to classify cancer and non-cancer cells.

  - Analysis of GMM based and Stacked AutoEncoder (SAE) embedding based representations for FCM at different treatment time points (Section 5.1.1).
  - Analysis of GMM based representation and anomaly detection as disentanglement strategy (Section 5.1.2).
  - Analysis of WGAN embedding based representations for blast identification (Section 5.1.3).

- As output a MRD value is provided for every patient and a label l for every cell observed, where $l = \{$Blast (1), Non-Blast (0)$\}$.

5.1.1 Longitudinal Analysis of Time-Specific Cell Population Models in Acute Lymphoblastic Leukaemia

As introduced in Section 2.2 leukaemia treatment response is assessable by estimating the MRD at defined timepoints during therapy using FCM based measurements. For the analysis of suitable representation techniques for blood cells over treatment time, a longitudinal dataset *Blood ALL* is used, where for every B-ALL patient 3 FCM measurements at treatment day 15, 33 and 78 are available (cf. Section 4.3.1 for more details regarding the dataset).

Previous work by Rota et al. [188] analysed FCM measurements at treatment day 15 and demonstrated that a generative model (GMM and Bayes decision) determines MRD with higher accuracy compared to SVM and a Deep Neural Network (DNN). Thus, the focus of the proposed analysis scheme is set on evaluating the performance of GMM, SVM and DNN as well and by observing the leukaemic cell classification performance at additional treatment time points in dependence of the therapy's duration. Additionally, it is analysed if blood cell population models of earlier timepoints can be used to determine leukaemic and non leukaemic cells in subsequent states, since in [96] it was reported that risk stratification of precursor B-ALL is improved by the combination of MRD assessments of two therapy timepoints.

Methodology

For the longitudinal analysis of time-specific cell population models an automatic classification framework is proposed for blood cell type determination (blast (cancer) and non blast (non cancer) cells) consisting of an SAE, GMM and SVM. This experiment is

an extension of the case study presented in [189], which was performed on ALL FCM data on treatment day 15 only. For this experiment data from additional treatment time points (day 33 and day 78) is used as well as time-specific representations are evaluated regarding their ability to the disentanglement of clusters of interest and consequently their performance in assessing the treatment response via the MRD value.

Stacked Denoising Autoencoder
As the first methodology for the automatic classification of blood cells and corresponding populations a deep neural network architecture is introduced. It is a data-driven learning approach and fully-discriminative, which enables the computation of highly non-linear decision functions, with huge parameter sets, efficiently in time. For this work a particular architecture is used named SAE [18, 230] to classify FCM data. SAEs are easily adaptable to different data types, compared to a CNN layout, are designed to compute a multi-dimensional hyperplane, dividing the data into two classes $\{C_{blasts}, C_{non-blasts}\}$. During the SAE training, important structures among the input data's features [18] are learned. In this approach proposed, two training phases ((1) unsupervised and (2) supervised) are used and are illustrated in Figure 5.2. The architecture of the network is defined by finding a compromise between classification accuracy and speed performance of the network.
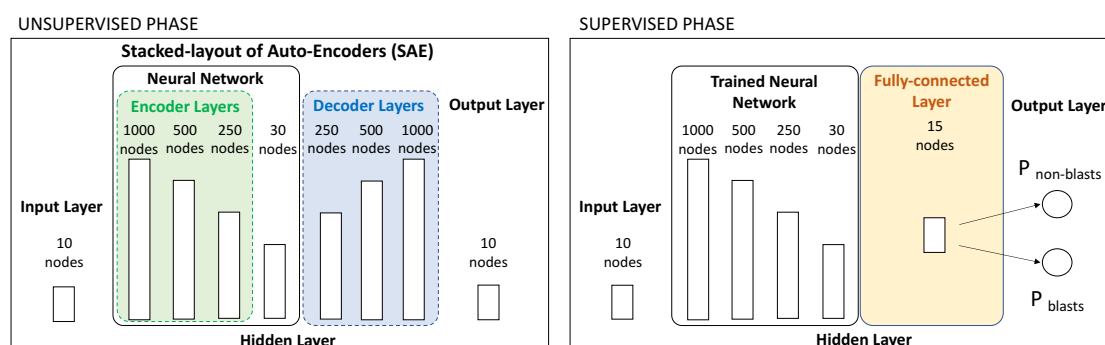
Figure 5.2: Schematic illustration of the stacked auto-encoding procedure proposed for blood cell classification of FCM measurements. Modified from [190].

In the unsupervised training phase (cf. Figure 5.2 on the left) the structure of the data is learned using an SAE architecture, consisting of a cascade of modules called encoder and decoder, with an equal number of layers. The first layer (input layer) consists of 10 nodes representing the number of measured features per cell. To train the neural network (green) the output of the decoder is the input of the encoder and the optimisation is performed by minimising the encoding/decoding error. The hidden layer is enclosed between the input and output layer (last layer) and consequent layers are fully connected, while no connections are present within the nodes of each layer. A node (neuron) in a hidden layer is active (is firing), if it reaches an activation h close to 1. The corresponding activation function f of this neuron, in this case a tanh function is used, incorporates

the weights W_i of incoming connections to nodes x_i (i = 1,...,n) of connected layers and a bias term b (cf. Equation 5.1).

$$h_{W,b} = f(\sum_{i=1}^{n} W_i x_i + b) \tag{5.1}$$

In the supervised training phase (cf. Fig. 5.2 on the right) label based information of the measured cells are incorporated into the procedure to validate the training performance regarding the classification of cancer and non-cancer cells. Each event is separately used as input of a fully-connected layer to adapt the weights of the previously trained neural network of the unsupervised phase to produce the final classification weights. Position related information of the populations of an event in the feature space is not considered.

Gaussian Mixture Model
As second methodology for automatic cell classification a GMM[1] based formulation is used to cluster and detect cell populations. It is widely spread and flexible in FCM data analysis and is less computational demanding compared to kernel model estimation based approaches [155], [21]. This generative approach is able to fit point cloud distributions, while keeping the model based description and using a restricted amount of parameters. For being able to analyse very small blast populations of ALL data, two different models, one for blasts and one for non-blasts are learned by using an adapted EM algorithm with an excluded split and merge phase [155]. The distributions of blast and non-blast populations are modelled using 15 and 3 Gaussian distributions, considering the typical shapes and size of the corresponding distributions in the training sample. The final model is obtained by weighting of the distribution's components in a merging procedure. Besides the discrimination of different populations we aim to identify blasts. For this task we use the posteriors obtained from the GMM components as input of a Bayes decision based classifier, which priors are set according to the average relative frequencies of leukaemic events in the training sample.

Support Vector Machine
The SVM approach is used as a baseline to provide a comparison between its classification and those performed by SAE and GMM. In the experiment proposed we use a RBF kernel based formulation of SVM, using cross-validation for parameter estimation. Sample classification is performed based on cells, without including information about the neighboured cells or the different populations observed.

Evaluation Setup

The evaluation is performed in two phases using dataset *Blood ALL* (cf. Section 4.3.1). The methodologies introduced in Section 5.1.1 are used to separately train time-specific population models for day 15, 33 and 78 of treatment. Therefore, the time specific

---

[1]cf. Bishop et al. [21] for the theoretical description of GMM.

samples of the patients' dataset are extracted and randomly divided into two groups, consisting of a training set of 184 and a test set of 16 samples. One sample of a patient consists of approximately 10^6 measured cells. k-fold cross validation is performed (k is set to 5) to enlarge the test to a final size of 80 samples. Equation 5.2 expresses the computation of MRD, represented by the ratio between the number of blast (B) cells N_B and number of all living cells (ALL) in a sample N_{ALL}.

$$MRD = \frac{N_B}{N_{ALL}} \tag{5.2}$$

To assess the quality of the MRD assessment three different measures for every experiment are computed (precision, recall and f-score).

Results

In the treatment-time-specific evaluation phase, a time-specific model is used to classify cell populations' appearance at the corresponding therapy time point. The time-specific evaluation results regarding the quality of MRD assessment are summarised in Table 5.1. The graphical results of the time-specific evaluation are illustrated in Figure 5.3a (SAE),

Table 5.1: Numerical results of the evaluation of time-specific models computed using GMM, SVM and SAE. Training is performed for treatment day 15, 33 and 78 separately and evaluated on a time-corresponding dataset (15-15, 33-33, 78-78).

Method	Precision			Recall			f-score		
	15-15	33-33	78-78	15-15	33-33	78-78	15-15	33-33	78-78
SAE	**0.962**	0.647	0.200	0.935	0.647	**0.999**	**0.948**	0.785	0.333
GMM	0.944	**0.997**	**0.560**	0.922	0.907	0.917	0.932	0.950	**0.696**
SVM	0.924	0.996	0.100	**0.963**	**0.963**	0.998	0.943	**0.979**	0.182

(a) DNN Time-Specific   (b) GMM Time-Specific   (c) SVM Time-Specific
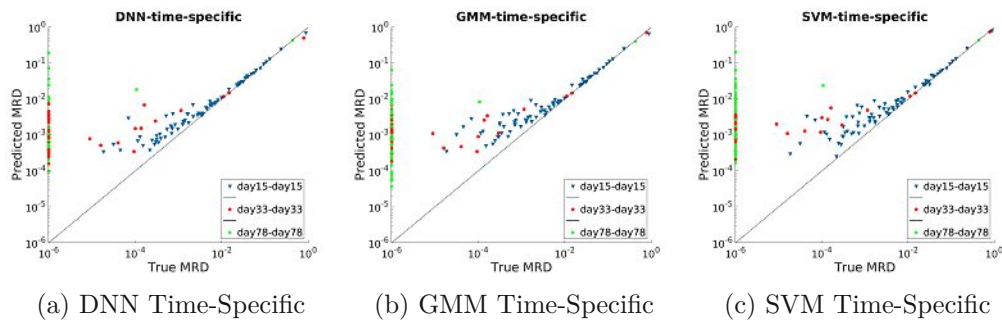
Figure 5.3: Results of time-specific blast identification using SAE (DNN) (Figure 5.3a), GMM (Figure 5.3b) and SVM (Figure 5.3c) [129].

5.3b (GMM) and 5.3c (SVM). Each point represents a test sample (one patient), where the 2D coordinates are obtained by the value of true MRD in relation to the quantity

predicted, i.e. an optimal solution is represented as a plot with samples along the line (true MRD = predicted MRD).

In contrast to the time specific analysis, the longitudinal evaluation phase focuses on estimating the cell classification performance using a treatment-time-specific model of day 15 to estimate cell populations at treatment day 15, 33 and 78. The longitudinal evaluation results regarding the quality of the MRD assessment are summarised in Table 5.2.

Table 5.2: Numerical results of longitudinal evaluation of GMM, SVM and SAE (DNN) trained on data at day 15 and evaluated on dataset at day 15, 33 and 78 (15-15, 15-33, 15-78).

Method	Precision			Recall			f-score		
	15-15	15-33	15-78	15-15	15-33	15-78	15-15	15-33	15-78
SAE	**0.962**	**0.998**	**0.091**	0.935	0.933	**0.998**	**0.948**	0.964	**0.166**
GMM	0.944	**0.998**	0.077	0.922	0.643	0.963	0.932	0.782	0.141
SVM	0.924	0.997	0.076	**0.963**	**0.949**	**0.998**	0.943	**0.973**	0.142

(a) DNN Longitudinal   (b) GMM Longitudinal   (c) SVM Longitudinal
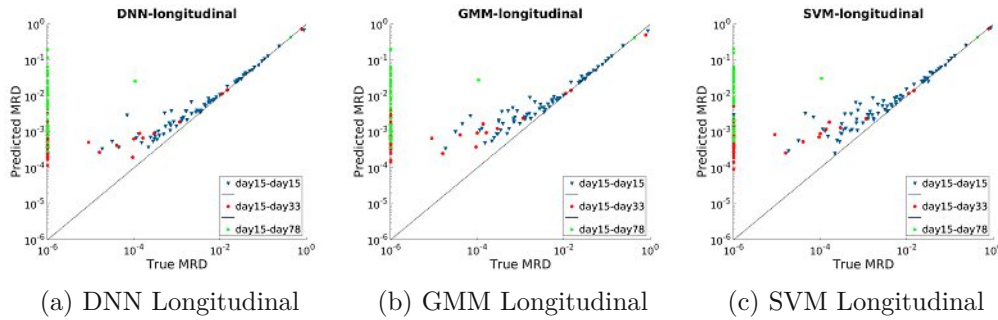
Figure 5.4: Results of longitudinal evaluation of time-specific population models for blast identification (cf. Figure 5.4a, 5.4b and 5.4c) using SAE, GMM and SVM respectively [129].

The graphical results of the longitudinal evaluations are visualised in Figure 5.4a, 5.4b and 5.4c.

Discussion

The *time-specific evaluation results* are best, independent of the approach used, for predicting blasts at day 15 using a time-specific model trained on data acquired at treatment day 15. The best precision for day 33 and 78 is achieved by GMMs. This is motivated by the fact that GMM is considering the whole sample in comparison to SAE and SVM, which observe cells (events) in an uncorrelated way. The worst precision of MRD assessment with a value between 0.1 and 0.56 is achieved at day 78. A possible

reason is the low number of predictable blasts at this stage of therapy, which leads to an overestimation of this cell type, by accidentally misclassifying regenerating cells as leukaemic cells, which show a similar antibody pattern. The same parameter sets for SVM, DNN and GMM are used to train time-specific population models. Thus, a possibility for improvement lies in defining time dependent parameter sets to fit the training dependent on the current status of the cell populations and to evaluate if an improvement of MRD assessment at day 33 and 78 is achievable.

The results of the *longitudinal evaluation phase* report that a time-specific model learned at day 15 is not capable to precisely assess MRD at day 33 and 78. It is concluded that the treatment induced dynamic changes of cell population are not representable and predictable using one single time-specific model of blast and non-blast cells. Thus, for being able to model time-dependent changes of cell populations, time-specific baseline models are required.

5.1.2 Analysis regarding the Disentanglement of Blast an Non Blast Populations using GMM

For the analysis of the separability of blast and non-blast populations, the extraction of suitable baseline states to address dynamics in AML are investigated. As introduced in Section 2.2 AML is a rare type of blood cancer in the paediatric cohort with a maximum of 10 cases per year in Austria. Thus, a further focus here lies in investigating strategies to increase the training set. Therefore, it is analysed if the combination and merging of baseline representations of different leukaemia types is suitable to increase the number of samples.

Recent automated machine learning approaches focused on classifying leukaemic and non leukaemic cells of FCM measurements in childhood ALL [2], [14], [183]. It is firstly demonstrated, that state of the art machine learning algorithms are applicable on FCM childhood AML data, secondly a novel baseline formulation for a GMM based representation is proposed to assess MRD distributions in AML of small size. Finally, the combination of baseline populations (non-cancer cells) of ALL and AML samples are analysed and evaluated, regarding the ability to identify outlier distributions which furthermore can determine the dynamic appearance of leukaemic cells more efficiently compared to simple backgrounds.

Methodology

For this experiment a baseline representation with Gaussian Mixture Models for leukaemic cell detection is analysed. For the experimental setup two additional machine learning approaches (Random Forest and Support Vector Machine) are evaluated regarding the automatic cell classification performance. For every approach the MRD is computed following Equation 5.2 introduced in Section 5.1.1, after automatically assessing the cell counts of blast and non-blast cells for every measured sample. The motivation of analysing a GMM based representation is to observe, if these are as well suitable to separate cancer dynamics from baseline healthy cells in AML in the multidimensional

64

feature space in contrast to manual labeling procedures. The 13 features measured (cf. Section 4.3.2 and 4.3.3 for more details regarding the datasets used: dataset *AML Diagnose*, dataset *ALLko*) in this case correspond to the expression of ten different types of antibodies on the cell surface and three physical FCM measures. Dependent on the condition of the patient, approximately $10^5 - 10^6$ cells are measured per subject. Additionally, manual annotations of blast and non blast cells are provided by medical experts.

Gaussian Mixture Models for the Representation of Baseline Populations
As the first approach a GMM based formulation is used to cluster and automatically classify cells into leukaemic and normal cells. The distribution of non-blast populations are modelled as a baseline, since more baseline data without blasts are available. Therefore an adapted EM algorithm is used to learn a GMM of non-blast cell populations with 2 Gaussian distributions. Subsequently, outlier cell populations lying outside the learned probability density function are extracted. A cell is classified as non-blast, if the log probability is greater than 0, and as outlier, if it is smaller. In a next step the outliers are modelled using an additional GMM with one component. A cell in the outlier population is classified as blast if the log probability is greater than 3 and as non-blast if it is smaller. The number of Gaussian distributions and the log probability were estimated based on the results of preliminary experiments, where different parametrisations were tested. In
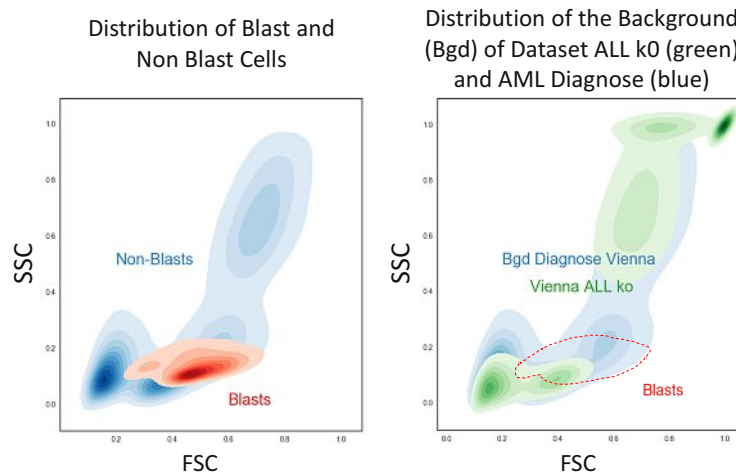
Figure 5.5: Visualisation of the distribution of non blast and blast blood cell populations of the dataset *AML Diagnose* (left). On the right the difference between the background of the dataset *AML Diagnose* (blue) and *ALLk0* (green) are visualised and their relations to the blast population (red line) in the dataset *AML Diagnose* [128].

.

Figure 5.5 on the left side the distribution of background cells (blue) of 13 samples of diagnosed AML cases are visualised (*dataset blood AML*), where blasts are visualised in red. On the right the same background (blue) is shown in relation to the background

(green) extracted from 30 subjects diagnosed with ALL (*dataset blood ALLk0*) in the remission state where no blasts are present. Firstly, it is observable that the different background distributions have an overlying appearance in the feature space and secondly, blast populations lie in regions of less density of the background's distribution.

Random Forest Classifier
As the second approach the ensemble classifier Random Forest (RF) [25] is evaluated. Its formulation is based on decision trees, where a random training subset of the FCM data is defined for each tree. For finding a maximum separation between blast and non blast cells, every node in the decision tree performs thresholding on the measured antibody features. By searching over a random subset of these features a new node in the decision tree is constructed [113] taking into account the decisions of the higher tree levels. In comparison to the GMM approach the RF is trained in a supervised way using the manual annotation labels of every cell. In the test phase one label for every cell of a new input sample (1 blast, 0 non-blast) is computed based on the RF trained.

Support Vector Machine
The SVM approach is used as a baseline to provide a comparison between its classification and those performed by RF and GMM. In the experiment proposed, an RBF kernel based formulation of SVM is used. Sample classification is performed based on cells, without including information about the different cell populations observed. Also the SVM is trained in a supervised way. In the test phase one label for every cell of a new input sample (1 blast, 0 non-blast) is computed based on the SVM trained.

Evaluation Setup

For evaluating the cell classification performance of the three approaches evaluated, Leave One Out Cross Validation was performed, since only a small amount of annotated AML data was available. The proposed GMM approach is trained using the non-blast annotated cells only, while RF and SVM are trained on blast and non blast populations. The pipeline is implemented using the scikit-learn package for Python [165]. For the SVM the following parametrisation was used: C=1.0, cachesize=200, degree=3, gamma='auto', kernel='rbf', tol=0.001. For the Random Forest classifier 1000 estimators and the following additional parameters were set: criterion='gini', minimal samples split=2, min samples leaf=1, min weight fraction leaf=0.0, min impurity split=1e-07, bootstrap=True. For the GMM approach 2 Gaussian distributions for modelling non blasts and one Gaussian distribution to model outliers was defined, covariance type='full', n iter=10000 and n init=1. The parametrisation of every approach was set based on the best performance achieved in preliminary experiments. Additionally, precision, recall and f-score are computed as quantitative score to compare approaches and labeling results of different samples [171].

Results Automatic MRD Assessment with Baseline Representations

In a first step the performance of three algorithms is evaluated regarding their classification accuracy of blast populations in childhood *AML Diagnose* data. Baseline models are trained based on the background (non-blast cells) of cases in this dataset. Table 5.3 summarizes the evaluation results of the RF, SVM and GMM) approach, where SVM shows the best f-score while RF has a higher precision compared to the other approaches.

Table 5.3: MRD assessment performance of childhood AML with baseline representations.

Method	Precision	Recall	f-score
RF	**0.76219**	0.46249	0.57567
SVM	0.61986	**0.58044**	**0.59951**
GMM	0.44836	0.26391	0.33226
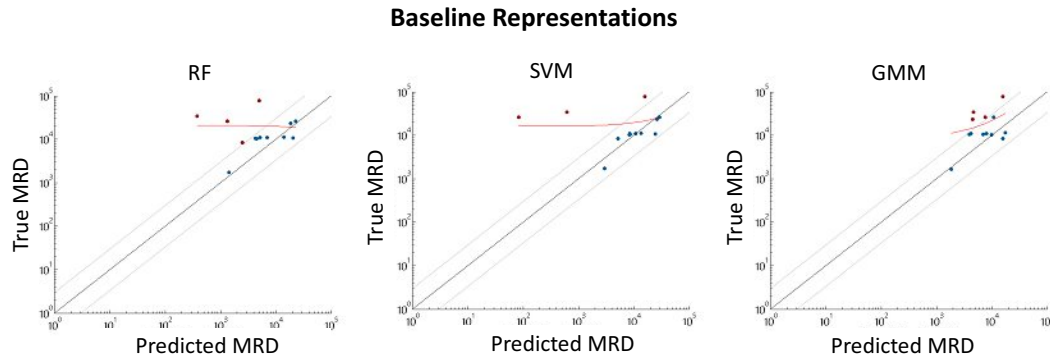
Figure 5.6: Visualisation of MRD assessment in AML using RF, SVM and Background GMM with simple baseline training [128].

Results MRD Assessment with Combined Baseline Representations

In a second step the performance of RF, SVM and GMM regarding their classification accuracy of blast populations in childhood AML Diagnose data, but with a combined background is analysed. Therefore non blast cells from the *dataset ALLk0* and *dataset AML Diagnose* are merged and used for training. In Table 5.4 the evaluation results are summarized. In comparison to the simple background evaluation a decrease of performance of RF and GMM is observable and an increase of the SVM precision, when a combination of backgrounds is used. Figure 5.6 visualises the MRD assessment accuracy of the evaluated algorithms for simple and combined background. A point corresponds to a sample of a patient for which the true and predicted MRD is plotted. Samples lying outside the accuracy threshold are drawn red, samples inside are visualised blue. The

Table 5.4: MRD assessment performance of childhood AML with combined baseline representations.

Method	Precision	Recall	f-score
RFBgd	**0.74169**	0.39596	0.51629
SVMBgd	0.68014	**0.53149**	**0.59669**
GMMBgd	0.43861	0.26099	0.32725

accuracy threshold was defined by clinicians. In case of GMM the failed predictions of MRD lie closer to the true MRD compared to RF and SVM failed cases, which underestimated the MRD in a wider range. In Figure 5.8 the classification results of the simple background (1st and 3rd row) and combined baseline (2nd and 4th row) analysis are qualitatively visualised for RF (1st column), SVM (2nd column) and GMM (3rd column) for two subjects. The corresponding manual annotations are shown in column 4. Additionally, the computed MRD values for every experiment are provided.
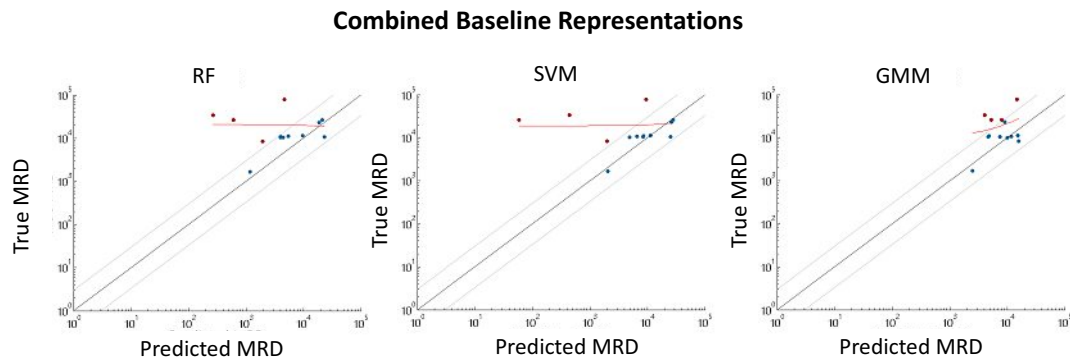
Figure 5.7: Visualisation of MRD assessment in AML using RF, SVM and Baseline GMM with combined baseline training [128].

Discussion

In this experiment the applicability of machine learning approaches is analysed regarding the automatic MRD assessment perfomance in childhood AML, which includes the determination of separability of dynamics and baseline cell clusters. Three different methodologies are evaluated for AML routine data, where best results are achieved using RF and SVM. However, these approaches show a higher variance in MRD estimations compared to GMM, which underestimates MRD in a lower range. A baseline representation strategy using GMM is presented and shows that learned distributions of non cancer blood cells can be used to identify blast populations in AML data. Additionally, it is demonstrated that combinations of baseline representations of different leukaemia types lead to similar performance of the supervised and unsupervised approaches evaluated
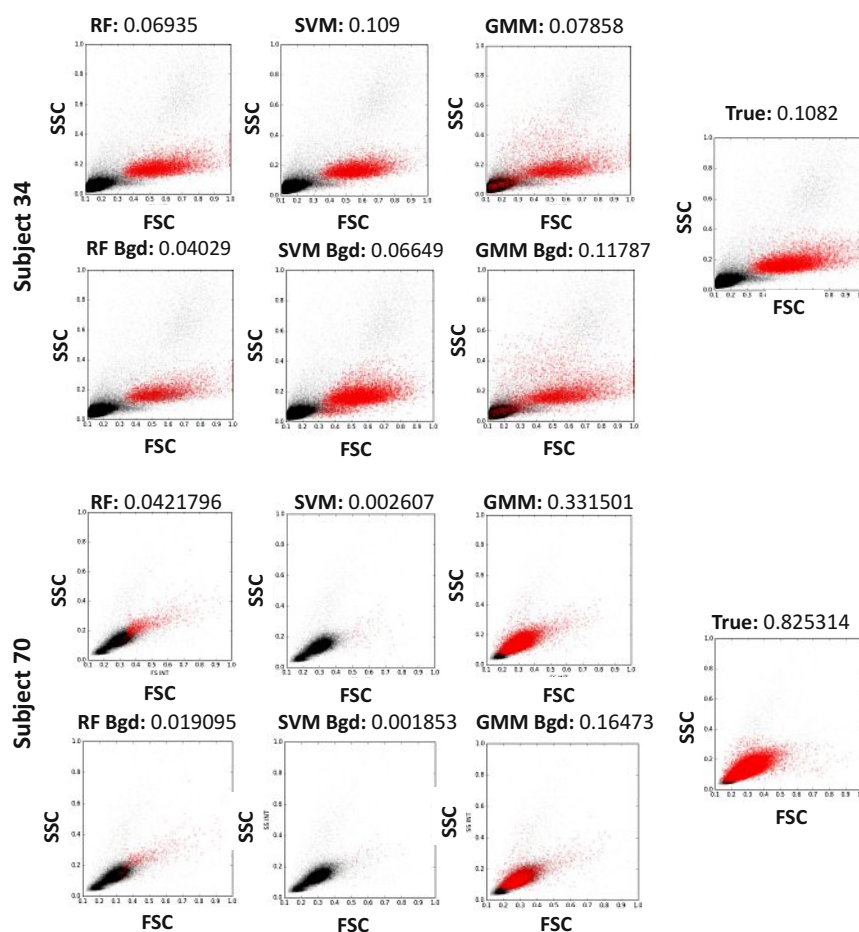
Figure 5.8: Visualisation of qualitative results and quantitative MRD estimation of two subjects by Random Forest (RF), Support Vector Machine (SVM) and Gaussian Mixture Model (GMM) using a simple baseline trainingset. The annotation results (True) are shown in column 4. Blasts are visualised in red and non-blasts in black [128].

in detecting blasts in AML data. It is shown that MRD can be estimated on basis of non-blast observations only, which is a huge benefit in the case of rare diseases, where only a limited number of data is available.

5.1.3 WGAN Latent Space Embedding Based Representation for Blast Identification in Flowcytometry

Depending on the condition of a leukaemia patient, 10^5 - 10^6 blood cells with up to 12 features per cell are measured per subject. The aim of this experiment is to develop a new representation technique to overcome the high-dimensionality of FCM data, to reduce the computational costs in population analysis and to improve blast identification

performance. Compared to existing embedding approaches [48][228], the whole amount of cells in a blood sample of a patient is considered without the need of subsampling. The proposed embedding based representation technique is evaluated on FCM data against two baseline approaches and regarding their ability to estimate MRD in AML patients.

Methodology

In this experiment a semi-supervised WGAN architecture for MRD assessment is proposed as alternative low-dimensional representation technique of FCM data for SAEs. The datasets *AML Diagnose* and *ALLk0* are used (cf. Section 4.3.3 and 4.3.2 regarding more details). As suggested in [128] the technique of combined baseline representations is used. Nine features are measured per cell which consist of two physical FCM measures and seven distinct antibody types. The data are annotated by medical experts.

WGAN Embedding Based Representation
The proposed embedding technique is based on a WGAN architecture, which is inspired by the work of [199], where a Deep Convolutional Generative Adversarial Network (DCGAN) [178] is used for anomaly detection. Schlegl et al. [199] report that the proposed generative model and mapping procedure enables the differentiation between control anatomy and subtle anomaly regions in image space. In this experiment it is evaluated if an embedding based representation of FCM data with WGAN can be used to identify antigen patterns of blasts as anomaly from antigen patterns of normal blood cells. Here, the WGAN is utilized to learn a low-dimensional *baseline embedding of healthy blood cell* FCM measurements in an unsupervised way. In Figure 5.9 the proposed framework is visualised, which consists of three components: (1) unsupervised *Baseline Training* using WGAN, (2) mapping procedure from data space to embedding space, (3) supervised *Dynamics Training* using a Fully Connected Neural Network Classifier (FNN).

Unsupervised WGAN Baseline Training: A general GAN consists of a generator G and a discriminator D component. The *generator* is implemented as fully connected decoder network and maps a non-blast sample's representation z from a low-dimensional latent space $\mathcal{Z}$ (3 dimensions) to the original high-dimensional data space (9 dimensions) X. G is trained to generate realistic "looking" data samples $\hat{x}$ from random inputs $z \in \mathcal{Z}$ that are sampled from the normal distribution ($z \sim \mathcal{N}(\mu, \sigma^2)$). The *discriminator* maps from original data space (9 dimensions) to a single neuron (1 dimension), which output encodes the probability, if the discriminator's input has been a real image x from the training data or a generated image $\hat{x}$ from the generator ($\hat{x} = G(z)$). The optimization procedure for generator and discriminator is performed simultaneously, while the discriminator focuses on maximizing the probability of assigning the correct label to generated and real samples, while the generator's focus lies in fooling the discriminator by learning a model distribution $\mathcal{P}_m$ from the data's distribution $\mathcal{P}_{data}$ and consequently improving the generation of realistic looking data. This game can be formulated as a minimax objective
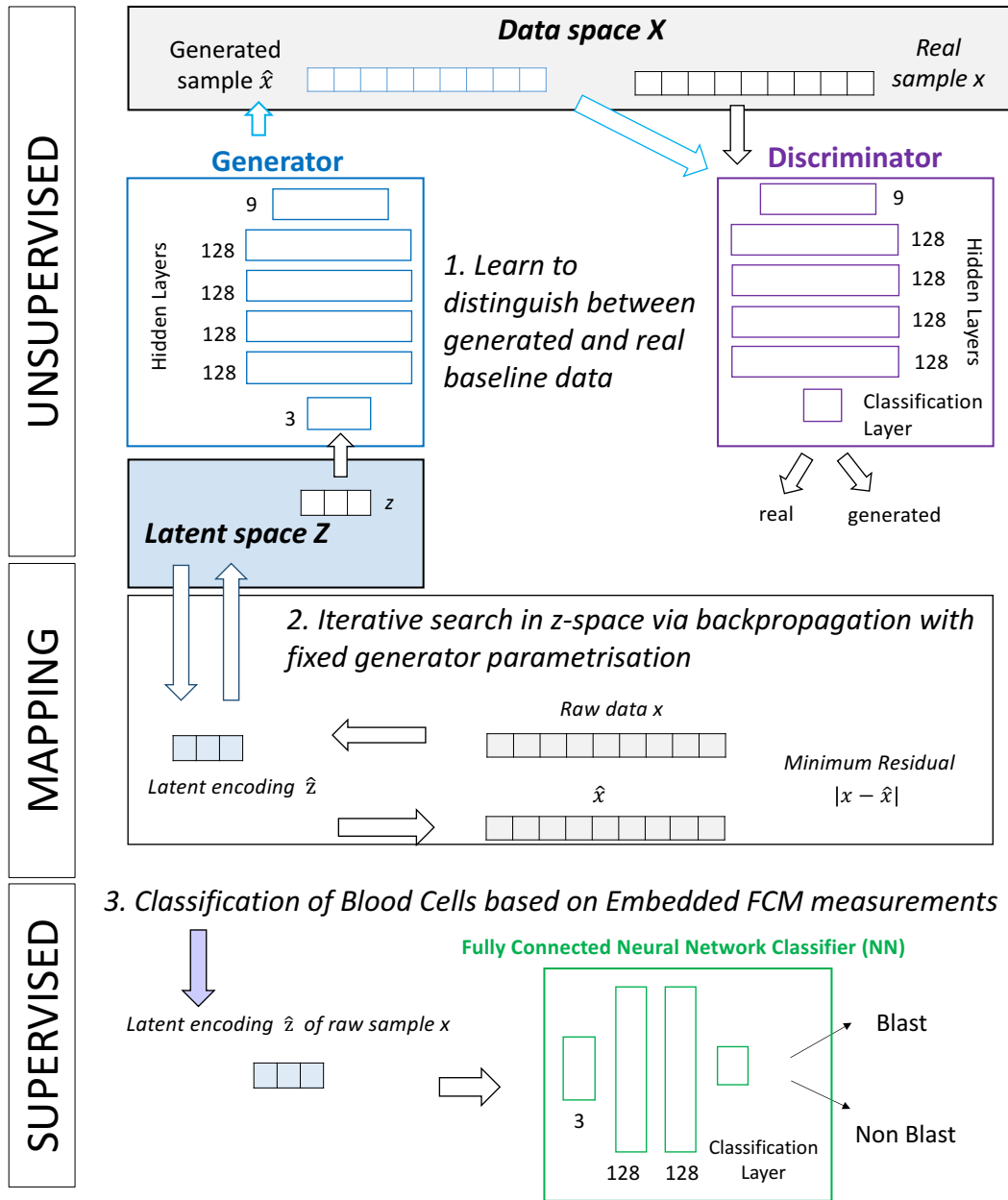
Figure 5.9: Proposed WGAN architecture including latent space learning strategy for blast identification in acute myeloid leukaemia.

function $\mathcal{O}(G, D)$ [81] expressed in Equation 5.3

$$\mathcal{O}(G, D) = \min_G \max_D \mathbb{E}_{x \sim \mathcal{P}_{data}} [log D(x)] + \mathbb{E}_{\hat{x} \sim \mathcal{P}_m} [log(1 - D(\hat{x}))] \tag{5.3}$$

The proposed WGAN [8] is trained, following the improved WGAN training procedure [81]. In the original GAN training procedure [71], the Jensen-Shannon divergence is minimized between $\mathcal{P}_{data}$ and $\mathcal{P}_m$, while in the proposed training scheme the smoother metric (*Wasserstein* Distance (WD)) is used. This metric intends to stabilize and improve the training procedure. The minimizing of the objective function under an optimal discriminator minimizes $WD(\mathcal{P}_{data}, \mathcal{P}_m)$ with respect to the generator's parameters [81]. For generator and discriminator a fully connected network architecture is used. The generator's decoder and the discriminator's encoder network consist both of 4 hidden layers with 128 neurons and an output layer with 3 (G) and 1 (D) neuron. As generator's activation functions a Rectified Linear Unit (ReLU) [156] is used. On top of the linear output layer a *tanh*-function is configured. The discriminator utilizes leaky ReLU activation functions and a linear output layer.

Embedding of FCM Data: After the WGAN training the parametrization of the *generator* is fixed. As introduced in [199] for a given data sample x the optimal $z \in \mathcal{Z}$ is found by an iterative process, which uses n back-propagation steps. In this procedure only z coordinates are adapted to optimize the mapping from the latent space to the generated sample $\hat{x}$ by finding the minimum residual M (cf. Equation 5.4).

$$M = |x - \hat{x}| \tag{5.4}$$

Supervised Dynamics Training using a Neural Network Classifier: For training all the input data training samples $x \in \mathcal{X}$ are mapped via this procedure to latent space $\mathcal{Z}$, which represents our low dimensional embedding space. For assessing the dynamics to distinguish between blast and non-blast cells a neural network classifier Neural Network Classifier (NN) is trained on top of the WGAN embeddings. The embedded data is fed into a *fully connected NN* comprising two hidden layers with 128 neurons each and a classification layer. Rectified linear units are used as activation function. The NN is trained using a cross entropy loss.

Principal Component Analysis (PCA)
As baseline approach Principal Component Analysis is utilized to compute low-dimensional FCM data representations in a feature space of reduced dimensionality (3 dimensions). This technique is used in an unsupervised way to learn a new *baseline representation* of decorrelated components (principal components) in terms of a linear combination of the original variables. It has been used for the analysis for FCM data since 1984 [139], but for MRD assessment of AML in developing cohorts, to our knowledge, no application has been reported yet. PCA is used as a baseline for an embedding technique in the evaluation scheme proposed.

Fully Connected Network Classifier (FNN)

In contrast to the simple neural network classifier that is trained on top of the low-dimensional embeddings, a deep fully connected feed forward neural network is used as evaluated reference approach. Based on this model, the performance of a state-of-the-art classifier are analysed, which is trained on a large annotated dataset. This network comprises 4 hidden layers with 128 neurons followed by 2 hidden layers with 32 neurons and a classification layer. The activations of the hidden units are computed applying ReLU activation functions. This network is solely trained on original data without any prior embedding or preprocessing, and thus the optimal discriminative feature representation has to be learned during classifier training.

Evaluation Setup

To keep comparability of the embedding approaches evaluated, the same training set consisting of *dataset ALLk0* and *dataset AML Diagnose* samples are used to learn an embedding without subsampling of the data in an unsupervised way. Only non-blast cells are used. As PCA implementation the Incremental Principal Component Analysis (IPCA) toolbox is used, which is integrated in scikit learn Python framework[2] with the number of components set to 3. The WGAN is trained in an unsupervised way with a latent space of three dimensions. The blast identification performance is evaluated using two different scenarios of annotated training data sizes: In *Scenario small dataset* 32 cells per case (i.e. patient) were used and in *Scenario large dataset* 50,000 cells per case, which reflect scenarios of low and high annotation burden, respectively. For both strategies, 3-fold cross-validation was performed with 5 cases per split and every patient occurs only in one split. In every iteration, 2 splits were used for training and 1 split was used for validation. In the testing phase no subsampling was performed. For the assessment of the blast identification performance the following metrics are computed for evaluation: precision, recall, f-score, specificity and Area Under the Curve (AUC) [171].

Results Automatic MRD Assessment and Blast Identification

In Table 5.5 the evaluation parameters for the *small dataset* scenario and in Table 5.6 for the *large dataset* scenario for every approach are illustrated. The numbers are computed via averaging the values of the patient specific clinical performance measures. In scenario *large dataset*, WGAN-NN and FNN outperform the PCA-NN approach. This suggests, whenever large amounts of annotated data for supervised classifier training are available, there is no additional performance gain, when classification training is performed on an embedding learned in a preceding unsupervised training step, since the FNN is already capable to learn the data representation. In contrast to this, in scenario *small dataset* (i.e. a case of a small number of available annotated data) WGAN outperforms the FNN classifier. In Figure 5.10 an example for qualitative results for a test sample of a subject

---

[2]`http://scikit-learn.org/stable/modules/generated/sklearn.decomposition.`
`IncrementalPCA.html` [accessed 2021-02-04][165]

Table 5.5: Blast Identification Performance of the proposed WGAN-NN classifier and two alternative approaches, PCA-NN and FNN, trained on a small annotated dataset.

Methodology	Scenario *small* dataset				
	Precision	Recall	f-score	Specificity	AUC
PCA-NN	0.5471	0.7690	0.5829	0.8151	0.7952
FNN	**0.6037**	0.7543	0.6164	**0.8594**	0.8336
WGAN-NN	0.5502	**0.9049**	**0.6483**	0.7452	**0.8592**

Table 5.6: Blast Identification Performance of our proposed WGAN-NN classifier and two alternative approaches, PCA-NN and FNN, trained on a large annotated datasets.

Methodology	Scenario *large* dataset				
	Precision	Recall	fscore	Specificity	AUC
PCA-NN	0.5986	0.9213	0.6893	0.7916	0.9008
FNN	**0.6526**	**0.9250**	**0.7305**	0.7933	0.8892
WGAN-NN	0.6320	0.8942	0.7147	**0.8364**	**0.9139**
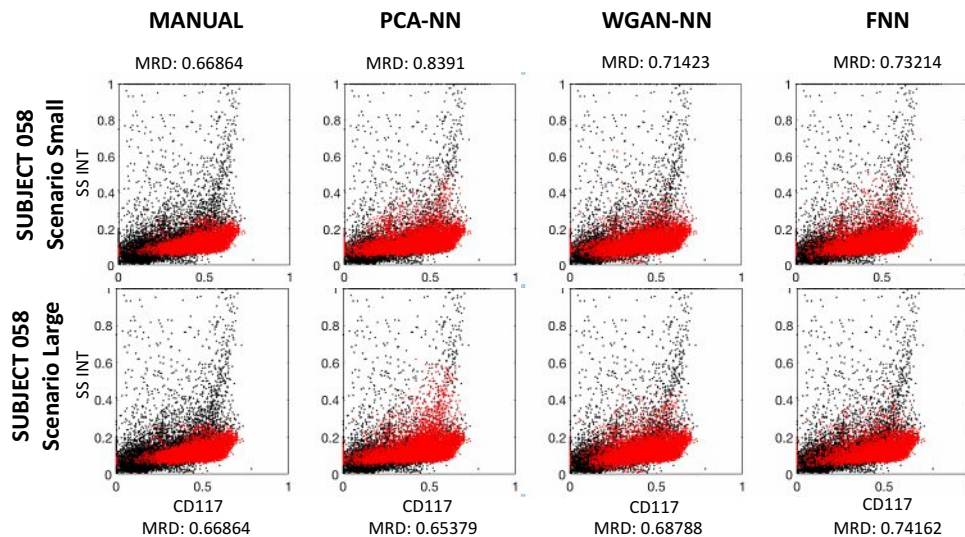
Figure 5.10: Qualitative results for *scenario small* (first row) and *scenario large* second row) of identified blasts by PCA-NN, WGAN-NN and FNN of a subject's testsample compared to manual blast annotations in AML data for the features SS INT and CD117 [130].

on *scenario small* (top) and *scenario large* (bottom) are visualised with corresponding MRD values. Blasts are shown in red and non-blasts in black. The manual annotations are presented in the first column, while the identified labels are shown in the second column for PCA-NN, third column for WGAN-NN and for FNN in the fourth column.
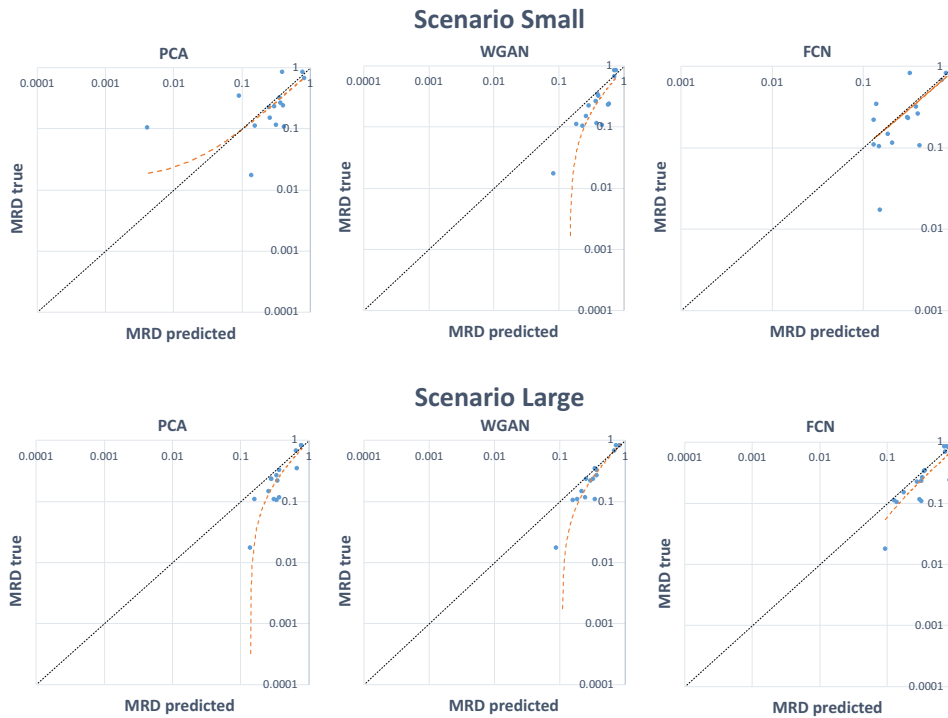
Figure 5.11: Visualisation of MRD assessment in AML with *scenario small* (first row) and *scenario large* (second row). Image modified from [130].
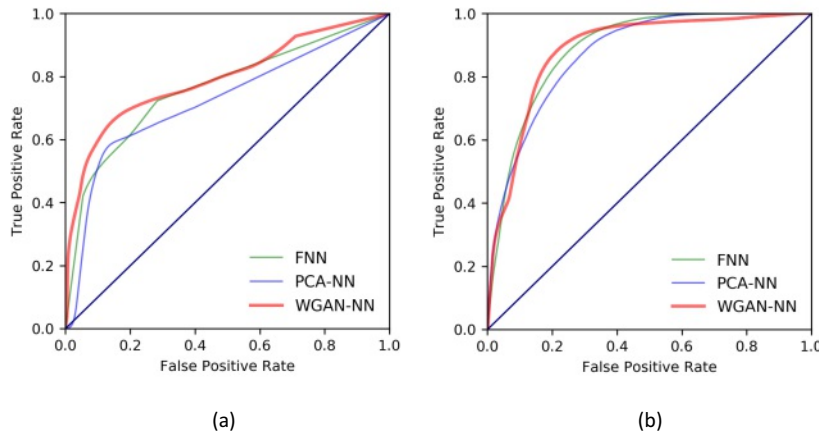
Figure 5.12: Receiver Operating Characteristic (ROC) curves. Binary classification performance of a simple neural network classifier trained on a WGAN embedding (WGAN-NN) or trained on a PCA embedding (PCA-NN), and a deep fully connected neural network classifier (FNN) soley trained on original input data. (a) Scenario *small* annotated dataset. (b) Scenario *large* annotated dataset [130].

In Fig. 5.11 the predicted MRD values are plotted versus the true MRD values. Every point represents a subject and should lie on the diagonal in the optimal case. It is observable that the samples of PCA-NN and FNN deviate more from the optimal line compared to the WGAN-NN approach, especially in the small scenario. Figure 5.12 illustrates the Receiver Operating Characteristic (ROC) curve for the blast identification performance for all patients' cells observed of a simple neural network classifier that has been trained on WGAN embedding (red), on a PCA embedding (blue) and a fully connected network classifier (green), that has been trained on original input data. The results of the *small* annotated dataset scenario are visualised on the top and on the bottom the *large* annotated dataset scenario is shown.

Discussion

In this section a novel semi-supervised learning approach is presented. It is based on a latent space space embedding and a simple fully connected neural network. Two evaluation schemes are provided: In the first scenario large annotated datasets are used and results show, that WGAN-NN and FNN outperform the PCA-NN approach. According to the rareness of the disease, only a limited number of annotated data is available. Thus, a second evaluation scenario is created comprising a small dataset simulating this fact, where the results show that WGAN-NN outperforms both, the PCA-NN and FNN approach.

5.2   Representation of Dynamics of Developing Functional Connectivity

This section summarizes the contribution and results proposed for addressing the dynamics of functional brain connectivity captured by rsfMRI acquisitions of children. The following research questions are formulated regarding the representation of rsfMRI data for functional connectivity analysis:

1. Which representation technique is suitable to model and analyse functional connectivity development?

2. What is the baseline development of healthy controls? Which features can be used to assess it?

3. What are the functional connectivity dynamics of reorganizing patterns after ischaemic stroke? How can we use baseline states to assess these and how do dynamics deviate from these baselines?

In Figure 5.13 the components for the representation concept of rsfMRI data at specific age time points are illustrated. The baseline representation is formed by acquisitions of control subject, the underlying reorganisation processes in stroke subjects are represented by the time-dependent dynamics' components. Systemic dynamics which challenge
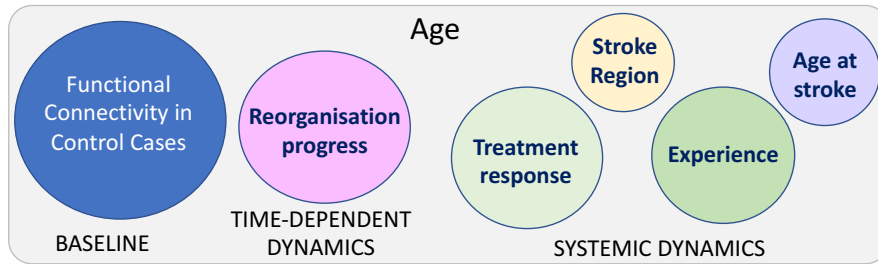
Figure 5.13:   Disentanglement of baseline properties and dynamics of functional connectivity at a specific time point. The baseline is formed by functional connectivity networks of controls, which is further used to address the time-dependent dynamics of reorganisational processes and systemic dynamics induced by experience, stroke region, age at stroke or treatment response.

functional connectivity analysis are e.g. the stroke region, the age of the subject, when the stroke occurred, response to treatment or different experiences. In the following section different representation and disentangle strategies are analysed for rsfMRI data. Following input and outputs for the analysis pipeline can be defined:

- The input of the analysis are rsfMRI acquisitions $I = \{I_1, \ldots, I_P\}$ of P children, where $I_p \in \mathbb{R}^{L \times K \times S \times t}$, L and K denote the dimension of one slice, S denotes the number of slices in an acquired volume, and t denotes the acquisition time point of the rsfMRI.

- Graph-based representations are analysed for specific age time-points and corresponding disentangle strategies for functional connectivity networks. Every node x_i ($i = \{1, \ldots, N\}$) in the graph corresponds to a position on the cortical surface, where the acquired BOLD signal $x_i(t)$ is observed and analysed regarding the correlation to other node's signal and to determine functionally connected networks.

- As output of the analysis procedure graph based features are obtained to assess and compare the networks' dynamics in stroke and control cases.

  - Short/Long range connectivity ratio R_i
  - Node degree D_i

5.2.1   Evaluation of Baseline and Dynamic Connectivity Changes Initiated by Stroke

The aim of the analysis is to extract baseline developing patterns of function connectivity and study the dynamics and modification of resting state connectivity networks in the pediatric brain after stroke between 7 and 17 years. For this research the dataset *Child Stroke* (cf. Section 4.2 for more details) is used.
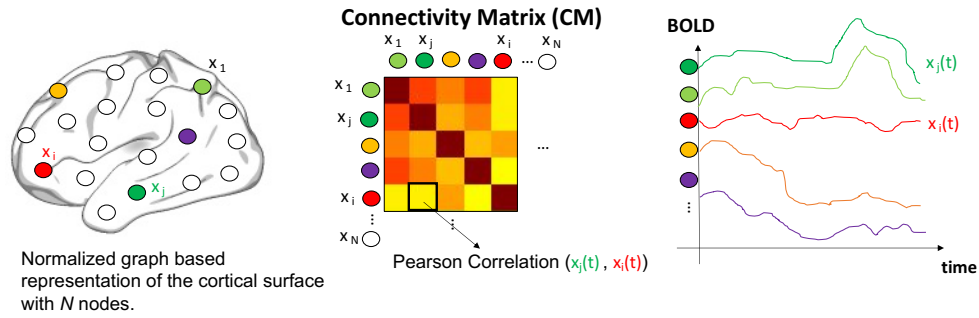
Figure 5.14: Schematic illustration of establishing a graph based representation for functional brain connectivity analysis.

Methodology

As basis for the analysis a graph based representation of functional connectivity networks in children is chosen, since it is widely used in state of the art approaches [62, 219, 216, 206] and demonstrates the ability to determine a cognitive state's origin, the analysis of neural architecture and the possibility to give insights into the global and integrative properties of the function in the brain [217]. Nodes in the graph can represent voxels or brain regions and edges the weighted relation between these. Here, the relation of focus is the functional Bold Oxygination Level Dependent (BOLD) signal correlation of brain regions. Figure 5.14 schematically illustrates the identification of functional correlating brain regions, by computing the Pearson correlation coefficient (cf. Eq. 5.5) between the time courses of all possible node pairs $x_i(t)$ and $x_j(t)$. This results in a correlation coefficient Matrix $CM_{i,j} \in \mathbb{R}^{N \times N}$ for every subject, expressed in Equation 5.5, where N is the number of nodes observed, i the ith row and j the jth column of the matrix, $t = \{1, \ldots, T\}$ the time frame and $\bar{x}_i$, $\bar{x}_j$ the average activity intensity across all of the time points at position i and j [206].

$$CM_{ij} = \frac{\sum\limits_{t=1}^{T} [(x_i(t) - \bar{x}_i)(x_j(t) - \bar{x}_j)]}{\sqrt{\sum\limits_{t=1}^{T} [(x_i(t) - \bar{x}_i)^2 \sum\limits_{t=1}^{T} (x_j(t) - \bar{x}_j)^2]}}$$ (5.5)

Here, adaptive plasticity and the relation to the developing functional connectivity networks in the child's healthy brain is analysed. Therefore, the introduced graph based representation technique in combination with Pearson correlation coefficient analysis and graph based measures [193] of brain signals are used.

Baseline feature extraction for developing functional connectivity
For the definition of a baseline for the representation of functional connectivity changes over age two features are extracted: (1) Connectivity Ratio and (2) the graph based

degree measure:

Connectivity Ratio: The extraction of Long Range (LR) and Short Range (SR) connectivity patterns over time as baseline feature was inspired by the work of Sepulcre et al. [206], who computed the local and distant degree and physical distance between functional correlating regions in the adult brain. They observe a strong local connectivity in the motor area, primary sensory area and strong distant connectivity in regions of high-order cognitive functions (attentional, memory and language processing). For the analysis these measures are adapted for the child's brain for assessing the influence of stroke on the baseline distribution of short and long-range connectivity over age. It is hypothesized that adaptive plasticity processes after stroke influence the formation of LR and SR connectivity over age, related to re-organisational processes and development of brain lesions after stroke [6] and consequently can be used to address the functional dynamic developmental patterns. The distance between two connected nodes is used to define long- and short-range connections, similar to [62, 219, 206] and compare their characteristics in the stroke- and control cohort. To establish age independent definition of long- and short-range, the Euclidean distance E_{ij} is computed between the coordinates of connected nodes on the cortical surface atlas *fsaverage5*. For the analysis a neighbourhood Q of ≤ 15 mm is defined for SR and > 15 mm for LR connectivity. Since these limits match for the adult brain a normalized representation of the data on a *fsaverage5* brain is required. Finally, following Sepulcre et al. [206], the ratio R between the number of short-range and the number of all connections to correlating nodes is evaluated, to be able to express relationships between the appearance and disappearance of these connectivity types over time (cf. Equation 5.6).

$$R_i = \frac{\sum\limits_{j=1}^{N} (E_{ij} \leq Q_{SR})}{\sum\limits_{j=1}^{N} E_{ij}}, \text{ where } i = \{1, \ldots, N\}, i \neq j. \tag{5.6}$$

Node Degree: As additional baseline feature the degree value D_i is used. It is a network measure which enumerates the number of edges connected to a node i. For its computation all brain surface voxels are represented as nodes in a graph, with edges connecting pairs of nodes with a positive signal correlation above a threshold. Firstly, the CM is used to extract node pairs with a correlation above a threshold of 0.4, and the degree is computed using the Brain Connectivity Toolbox [193] (Equation 5.7):

$$D_i = \sum\limits_{j=1}^{N} d_{ij}, \text{ where } i = \{1, \ldots, N\}, i \neq j. \tag{5.7}$$

Results

Two developmental patterns are analysed: (1) The baseline pattern of the maturation of functional connectivity in controls and (2) the dynamics and deviations of these patterns in the stroke cohort. Therefore, the dataset *CHILD Stroke* (cf. Section 4.2 for more details regarding the data and preprocessing) is used. The previous introduced features are computed for every subject and it is analysed whether there are regions in which this ratio is different for individuals affected by stroke compared to the baseline. Subsequently, the overall degree characteristics of cortical points in the two cohorts are compared, and it is investigated whether these two measures can be used to distinguish between developmental and stroke induced dynamics.

Long- and short-range characteristics of the functional connectivity in the child's healthy brain showed an evolving towards the characteristic of the adult brain but contrary traits in the case of the developing brain affected by stroke: In Figure 5.15 for single subjects at age 8, 9 and 14 the mean LR (row 1 and 2) and the mean SR (row 3 and 4) connectivity of each node on the fsaverage5 inflated brain surface are visualised. In both cohorts high SR connectivity is present in the superior part of the postcentral gyrus (primary somatosensory cortex), the precentral gyrus (primary motor cortex) and superior parietal part. In the control case these regions tend to increase in size from age 8 to 14 years, which locations overlap with observation in the adult brain [206]. For stroke cases no longitudinal trend is observable. For the control group the posterior cingulum shows an increase and higher SR connectivity values (> 150) in comparison to stroke cases. In contrast to this, LR connectivities show a higher grade of variability compared to SR connectivity. This might reflect the link between their emergence and experience and learning processes over time, which vary among subjects. It could be a possible explanation of the higher grade of variability in LR compared to SR connectivity. The change of the ratio between SR and all connectivities is evaluated in 6 brain regions separately: Broca's Area (BA 44, BA 45), Primary visual area (V1), Secondary visual area (V2) and Primary motor areas (BA 4a, BA 4p) anterior and posterior. In Fig.5.16 the corresponding results are illustrated. Each subplot shows for one region the ratio of control and stroke cases for the RH and LH separately. In all regions, but with highest manifestation in the primary motor area a decrease of R over time is observable in the control cohort (except LH of BA 45 Broca Area). This can be interpreted as a decrease of SR connectivity on the one hand and an increase of LR connectivity on the other hand during ageing. These results correlate with the observation of Supekar et al. [219]. They report high local connectivity (neighbourhood of ≤ 14 mm) preferentially in regions with primary sensory and motor areas and distant cortical-cortical interaction in heteromodal association areas (neighbourhood > 14 mm), in addition to a weakening of SR functional connectivity and strengthening of LR functional connectivity during childhood. For stroke cases a contrary characteristic is observable. In the Broca' Areas (BA 45) (areas associated with speech) asymmetry between LH and RH in the control cohort is visible. Figure 5.17 visualises the slope difference between the control and stroke cohort of SR connectivity (a) LR connectivity (b) and ratio changes (c). Values are normalized
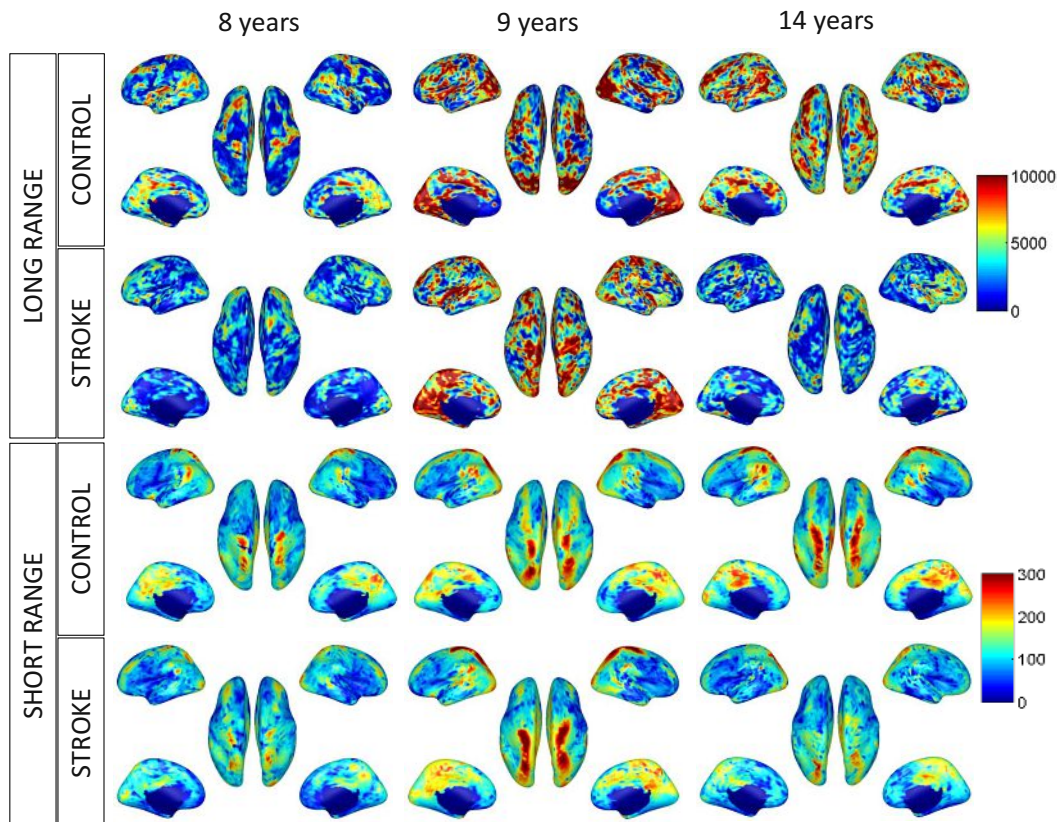
Figure 5.15: Visualisation of LR and SR connectivity networks of single subjects in the control (c) and stroke (s) cohort at age 8, 9 and 14 years [127].

according to the values of the control cohort. A higher change of the connectivity ratio for controls (positive slope difference of ratio connectivity between control and strokes) is observable in the corpus callosum, (the part of the brain which connects RH and LH) and superior motor area in both hemispheres. Asymmetric appearances of these differences are observable in the temporal pole and the Broca's area pars triangularis, Broca's area pars opercularis and orbital frontal area of RH. In contrast to this for the stroke cohort the regions of higher changes of connectivity ratio (negative slope difference of ratio connectivity between control and strokes) appear asymmetrically: In the LH the posterior cingular cortex in the limbic lobe is observable, which is involved in processing, learning and memory tasks as well as in the formation of emotion. It also forms a central node in the default mode network [61]. The supra marginal area shows higher changes of the connectivity ratio in stroke cases, which plays an important role in the perception of language. In the RH higher slope changes for stroke lie in the inferior parts of post (primary somatosensory area) and precentral areas (primary motor area).
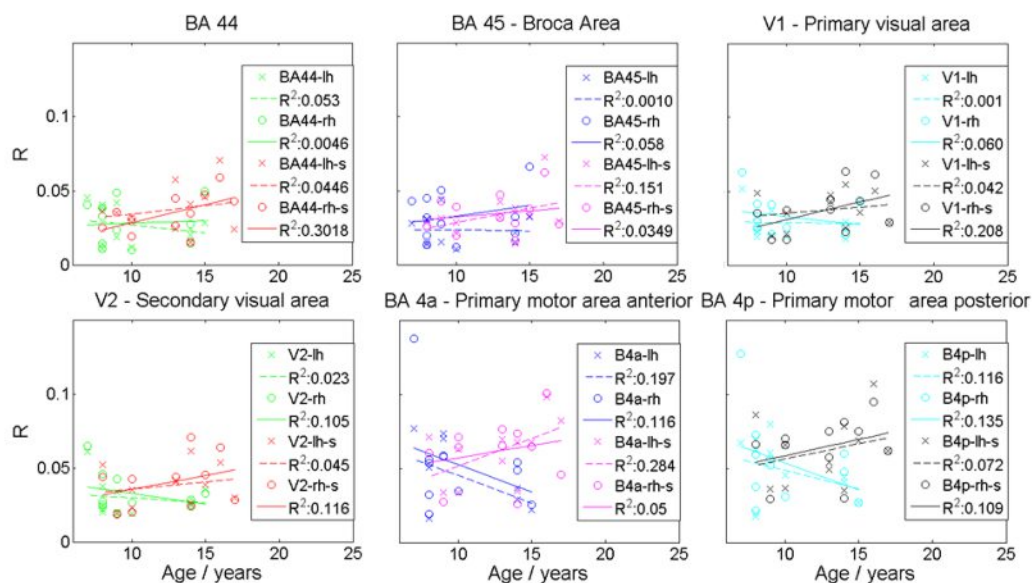
Figure 5.16: Ratio development within the BA44 Broca's Area pars opercularis, BA45 Broca's Area pars triangularis, V1 primary visual area and V2 secondary visual area, BA 4 primary motor area anterior (a) and posterior (p). For every plot the ratio values for LH and RH for control and stroke (s) are visualised as well as the regression lines for these values with corresponding R^2 estimates [127].

(a) LR connectivity   (b) SR connectivity   (c) Connectivity ratio
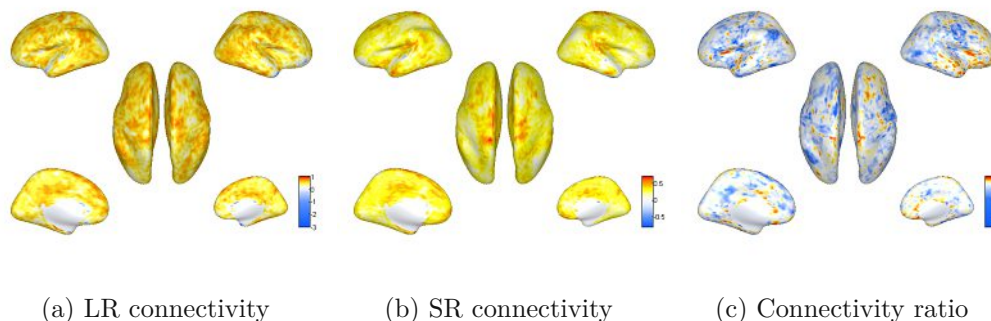
Figure 5.17: Comparing control subjects and stroke patients: the difference of the slope for linear models of LR connectivity changes,SR connectivity changes, and ratio changes during ageing. Red areas indicate higher values for stroke patients, blue areas indicate higher values for control subjects [127].

With increasing age in the healthy brain an increase of degree and the emergence of specialised network nodes is observable, whereas the brain affected by stroke shows a decrease in degree: For the same brain region age dependent changes of the average degree distribution are measured. The graph based representation of the fsaverage5 surface
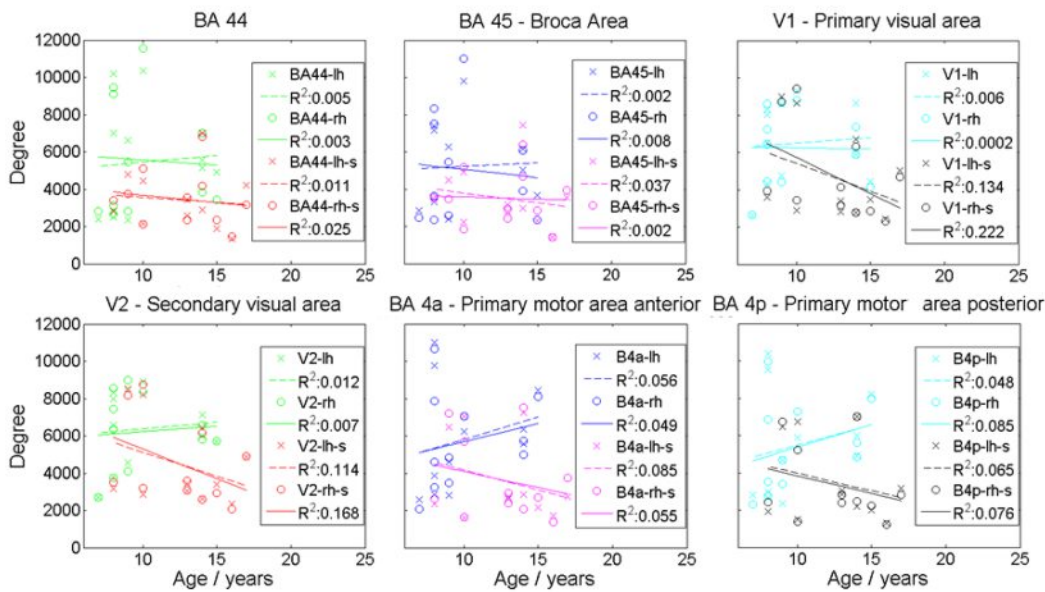
Figure 5.18: Degree development within the BA44 Broca's Area pars opercularis, BA45 Broca's Area pars triangularis, V1 primary visual area and V2 secondary visual area, BA 4 primary motor area anterior (a) and posterior (p). For every plot the degree values for LH and RH for control and stroke (s) are visualised as well as the regression lines for these values with corresponding R^2 estimates [127].

consists of 20,484 nodes, 10,242 for every hemisphere. The degree is only estimated between correlating nodes (> 0.4). In Figure 5.18 the corresponding results are illustrated. Each sub plot shows for one region the degree of control and stroke cases for the RH and LH separately over the age. The control cases exhibit higher degree compared to stroke cases on average. In the healthy cohort at age between 7 and 8 the nodes of degree 5,000 are located in the distant poles of the brain (frontal and occipital pole), where in contrast to this primary motoric centers show nodes of degree < 2500. With increasing age more specialised spots of nodes with degree $>10,000$ are observable, which correlates with an increase of degree over age in Figure 5.18. In the stroke case a contrary behaviour is observable.

Discussion

Here, it is demonstrated that graph-based representations of changing functional connectivity in the children affected by ischaemic stroke are suitable to assess baseline and dynamic trends of SR and LR connectivity maturation patterns towards characteristics of the adult brain observed by [206]. The initial results report, that stroke patients exhibit a development in the ratio of SR and LR connectivity and degree substantially different from control subjects. It is observable that a stronger change of SR /LR connectivity ratio

after stroke in regions involved in the evolving default mode network occurs compared to healthy brains, where the Default Mode Network (DMN) develops over time, starting from subtle connections in childhood [62]. The initial results indicate asymmetric differences between control subjects and stroke patients of the development of the connectivity ratio in regions involved in speech perception. The one-sided-lateralization for language is evident in infancy and increases with age [231][80], and might be linked to these findings. The current results present initial findings and valid statements require additional analysis and experiments. The location of stroke appearance and size varies across patients in this experiment. Also the age at stroke and the time since stroke vary among the study population. Thus, the focus of this experiment lied on deriving baseline trends of functional connectivity over age and not subject specific characteristics or stroke specific influences. The findings demonstrate the feasibility of graph based representations and corresponding computations and value of functional network analysis in the developing brain.

5.3   Discussion

In this chapter representation techniques and disentanglement strategies for dynamics in childhood leukaemia and of developing functional connectivity are analysed and corresponding results are presented.
Coming back to the research questions, in this first part of the thesis the following findings can be summarized:

Can we extract baseline properties encoding stable patterns for different representation techniques? Can dynamics be disentangled from stable patterns? What influence has the representation technique on the disentanglement?

It was demonstrated that density based and embedding based representations of FCM as well as graph-based representations of rsfMRI data, are suitable to extract baseline states and address corresponding dynamics.
In case of FCM it was shown that healthy blood cell clusters have stable properties in comparison to blast clusters in ALL or AML. It was demonstrated that these extracted baselines of AML and ALL can even be merged to obtain a richer training set, if the same antibody panel is used for measurement. This leads to a novel strategy to increase baseline training samples in case of rare disease types (like AML in the paediatric cohort) where less data is available [128]. In contrast to this it was discovered that baselines of extracted healthy blood cell populations over treatment time change according to the applied therapies and cell regeneration processes. This leads to the conclusion that treatment time specific baseline states in ALL are required and cannot be covered by a single baseline state. Additionally, it was observable that in late treatment time points the baseline states based on healthy cells are less suitable, since the more recent upcoming regenerating patterns have a similar appearance of blast clusters in the feature space, which leads to an over estimation of blasts [129].

In case of rsfMRI acquisitions of children it was demonstrated that time-specific functional connectivity networks in the healthy brain can be used as a baseline for analysing reorganisation dynamics initialised by ischaemic stroke [127]. It was shown that also in developing cohorts graph-based representations as well as from this representation derived measures are suitable to distinguish between the dynamics and baseline of a cohort.

Can we describe dynamics using these stable pattern?

In [128] and [130] it was demonstrated that baseline states of different leukaemia types (AML and ALL) are combinable, and can be used to increase the number of training data. Especially in cases of rare disease this fact enables the increase of available data, by incorporating baselines from more common diseases. The extraction of the same baseline properties of different leukaemia types and their combination were investigated and lead to a novel data augmentation strategy. It was demonstrated that the density based representation of baseline blood cell populations can be used to detect the deviation dynamics caused by leukaemia cell populations [128].

In [127] and in [121] it was shown that functional connectivity patterns of controls can be used as baselines, however age specific states are required according to the observed changes of functional connectivity. It was shown that baseline of connectivity patterns can be used as reference for finding possible target regions of reorganisation.

It was observed that the representation technique used as well as the type of baseline extracted is dependent on the medical domain, dimensionality of the data as well as the modality. As possible baseline candidates healthy functional connectivity patterns, healthy blood cell clusters as well as stable structures like bones can be used. The dynamics are assessable via anomaly detection [128], [127], functional connectivity pattern reorganization drift [121] and patch extraction [126].

CHAPTER 6

Spatio Temporal Modelling of Dynamic Developmental Patterns

"The only reason for time is so that everything does not happen at once." [Albert Einstein (1879 - 1955)]

This chapter summarizes the second part of this thesis' contribution: *Modelling Spatio Temporal Dynamic Developmental Patterns* using baseline states to establish correspondence over time and identify anomalies and dynamics using this longitudinal baseline model. In the following sections the developed spatio temporal modelling concept together with novel techniques are presented and evaluated for:

- Different medical disciplines (cancer research, brain development and functional connectivity analysis)

- Modalities (flowcytometry, whole-body MR, fetal MR, functional paediatric MR)

- Populations (fetuses, children, adults)

- Applications (segmentation, reorganization assessment, data normalization, prediction)

6.1 Spatio Temporal Modelling of DDP in the Fetal Brain for Tissue Segmentation

The spatio temporal model presented in this section focuses on the modelling of DDP of the fetal brain for the automatic segmentation of cortical and ventricle brain tissue. In Figure 6.1 the application of the proposed concept for fetal brain tissues segmentation is visualised. In this application the baseline model is formed by a longitudinal fetal brain

87

atlas trained on healthy cases. The subject dynamics' assessment is performed by pairwise registering age specific (GW 18 to GW 30) atlas-based templates and corresponding segmentations on the one hand, and on the other hand by incorporating a labelling procedure with a graph-cut based refinement step. For this study the time-series dataset
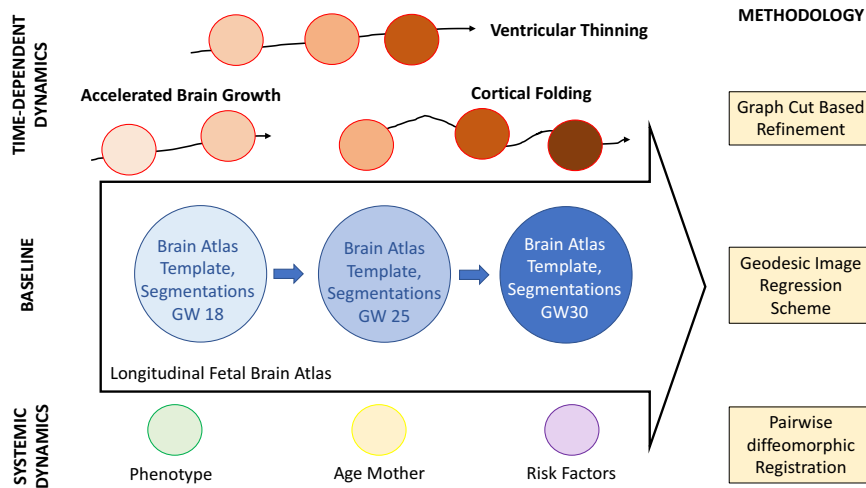
Figure 6.1: Application of the STM concept on DDP of the fetal brain.

FETAL is used (acquisition details and preprocessing steps are summarized in Section 4.1). In [157, 54, 84], image regression for time-series data have been evaluated only using adult- and child-brain datasets, which record also changes of brain structure over time but not in that amount and variety as it occurs in the fetal brain. Here, it is demonstrated that geodesic image regression is capable to build a spatio-temporal atlas of the fetal brain and is able to model a mean trajectory encoding the changes occurring during brain development as a baseline in a single diffeomorphic deformation. This learned deformation is parametrizable by gestational age t and can be used to transform MR acquisitions or brain tissue annotations to a specific time point in gestation, i.e. to provide a gestation specific atlas. As visualised in Figure 6.2, new data I_{new} at time
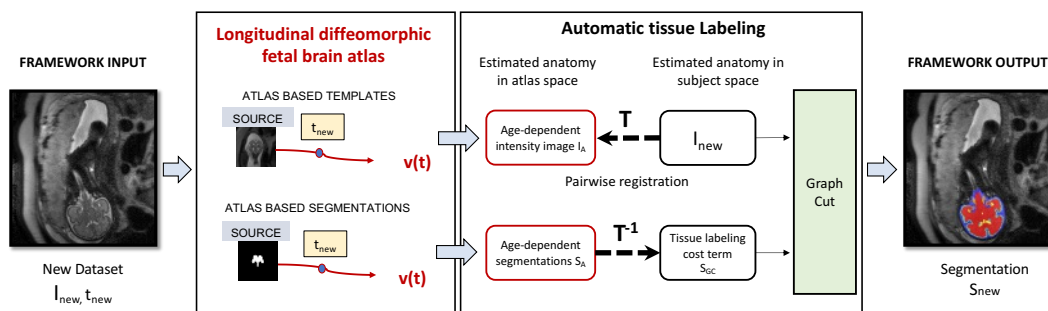
Figure 6.2: Fetal brain tissue labelling framework. MR images courtesy of MUW.

point t_{new} is labelled automatically by aligning the corresponding time specific template I_A and annotation S_A to the data and refining it via a graph cut based approach. The modelling process of DDP in the fetal brain can be summarized as follows:

- **Input:** MRI acquisitions of P fetuses at age t

- **Representation:** image-based representation as matrices $X = \{I_1, \ldots, I_P\}$, where $I_p \in \mathbb{R}^{N \times M \times D}$, M and N denote the dimension of one slice, D denotes the number of slices in an acquired volume, $S = \{S_{tissue}^1, \ldots, S_{tissue}^P\}$ denote corresponding manual annotations of two tissue types, where $tissue = \{brain, ventricle\}$.

- **Baseline Modelling:** Geodesic Image Regression to obtain a spatio temporal baseline of fetal brain development encoded in a time-dependent velocity vector field $v(t)$

- **Output:** Atlas-based age dependent intensity images I_A and segmentations S_A, Graph-Cut refined segmentations S_{GC}

- **Evaluation Strategy:**

  - Evaluation of 21 regularization kernels regarding the ability to encode time-dependent dynamics of brain volume growth, cortical surface area expansion or ventricle volume change over gestational age

  - Evaluation of graph cut segmentation performance comparing 3 penalty terms

  - Evaluation of cortical and ventricle segmentation performance over gestational age

6.1.1 Methodology

Spatio Temporal Atlas Learning
Brain development is considered to be modelled continuously over gestation time by geodesic image regression. For this purpose the "Diffeomorphic Anatomical RegistraTion using Exponential Lie algebra" (DARTEL) algorithm has been adapted and evaluated for longitudinal fetal brain registration [10, 9][1]. For encoding the brain development in a single diffeomorphic deformation the energy term E (cf. Equation 6.1[10]) is optimized:

$$E = \frac{1}{2} \|Av_0\|^2 + \frac{1}{2} \sum_{n=1}^{N} \left(\int_{x \in \Omega} \|I_{t_0} - I_{t_n}(\varphi_{t_n})\|^2 \, dx \right) \tag{6.1}$$

It consists of a regularization term and a data term. The data term measures the similarity between source image I_{t_0} at timepoint t_0 and the transformed target I_{t_n} at time point t_n using the forward deformation φ_{t_n} from source to target, where $n = 1, \ldots, N$.

---

[1]DARTEL is integrated in the Statistical ParaMetric (SPM) tool box `http://www.fil.ion.ucl.ac.uk/spm/`; [accessed 2021-02-04]

The regularisation measures the smoothness of the velocity field and constraints the deformation to be diffeomorphic. $A = L^{\dagger}L$ represents a model of the "inertia" of the system, i.e. a linear operator which operates on a time-dependent velocity that mediates the deformation over unit time [10]. It is introduced to derive an initial momentum m_0 through an initial velocity v_0:

$$u_0 = A * v_0 \tag{6.2}$$

The ordinary differential equation associated to the flow of the time-dependent velocity vector field $\dot{\phi}_t = v_t(\phi_t), t \in [0, 1]$ is formulated in Equation 6.3 and shows that the velocity is given at any time by the initial velocity or momentum.

$$\dot{\phi}_t = K \left(\left| D\phi_t^{-1} \right| (D\phi_t^{-1})^T (u_0 \circ \phi_t^{-1}) \right) \tag{6.3}$$

D denotes the Jacobian tensor, ϕ_t^{-1} the inverse of the diffeomorphic mapping and the operator K the (pseudo-) inverse (Green's function) of $L^{\dagger}L$. It is applied to smooth the result. The **conservation of momentum** is the formulation of each iteration of the registration as an initial value problem. Geodesic shooting requires the following steps: The deformation at time point zero ϕ_0 is set to the identity transform (Id). Afterwards the initial momentum from the initial velocity is computed ($u_0 = L^{\dagger}L * v_0$) and the dynamical system $\dot{\phi}_t$ is integrated over unit time. The velocity field $v(x)$ at position x is represented using B-splines. (cf. Equation 6.4)

$$v(x) = \sum_i c_i \rho_i(x) \tag{6.4}$$

These are parametrisable using a linear combination of i basis functions, which consist of a vector of coefficients c_i and a ith first degree B-spline basis function $\rho_i(x)$ [9]. For deriving an optimized parametrisation of c, the energy cost term E in Equation 6.1 is reformulated in terms of finding the coefficients of c for a given dataset D with maximum probability (cf. Equation 6.5). By maximizing the probability its negative logarithm is minimized, which enables the interpretation of the registration of data D as a minimization procedure of the objective function $(-\log p(c, D))$ expressed in Equation 6.5. This function consists of a prior term (prior probability $-\log p(c)$) and a likelihood term $(-\log p(D|c))$ [9].

$$-\log p(c, D) = -\log p(c) - \log p(D|c) \tag{6.5}$$

The likelihood term encodes the probability of c given the data D [9] and corresponds to the mean-squared difference between a warped template deformed by the calculated transformation and the target image. A concentration matrix K (inverse of a covariance matrix) is used to encode spatial variability, constraints the behaviour of the deformation (bending energy, stretching, shearing) as well as the divergence and amount of volumetric expansion or contraction [9]. For the computation of $K [\lambda_0, \lambda_1, \lambda_2, \lambda, \mu]$ five parameters have to be defined:

- λ_0 encodes the penalisation of absolute displacements.

- λ_1 penalises the difference between two neighboured vectors by observing the first derivatives (linear term) of the displacements.

- λ_2 penalises the difference between the first derivatives of two neighboured vectors by observing the second derivatives of the displacements.

- λ denotes the variability of the spatial locations (divergence of each point in the flow field) with a constant value. Increasing λ leads to increasing smoothing of the flow vector field and preserves volumes during the transformation.

- μ encodes the variance according to symmetric components, rotations and the penalisation of scaling and shearing.

The update of the computed vector field is expressed in Equation 6.6 where H^{iter} denotes the Hessian, g^{iter} the gradient and K the concentration matrix. Details regarding the computation of v_0^{iter+1} are explained in [9, 10].

$$v_0^{iter+1} = v_0^{iter} - \epsilon(K + H^{iter)^{-1}}(Kv_0^{iter} + g^{iter}) \tag{6.6}$$

A full multi grid approach with a Gauß-Newton optimisation is used to update the vector field after every iteration. The full multi grid approach takes images of different scales as input, where in every resolution level the vector field is estimated recursively. This routine starts at the coarsest scale and computes the residual to solve the update equations on the current grid. Subsequently, the solution is prolongated to the next finer grid [9].

Graph Cut Refinement for Automatic Tissue Segmentation
The automatic labelling procedure is based on a continuous max flow formulation of a multi label graph cut [242]. For this approach the definition of three parameters is required: (1) data term (gray value volume I_{new} at age t_{new}), (2) cost term, and (3) penalty term. The *cost* term is defined by smoothed atlas based segmentations for cortex and ventricle tissue $S_{tissue} = \{S_{cortex}, S_{ventricle}\}$ at age t using a Gaussian filter G parametrizable with a weighing parameter δ (cf. Equation 6.7, where $\star$ denotes the convolution operator).

$$C = \delta * (S_{tissue} \star G) \tag{6.7}$$

In this experiment three different penalty terms are evaluated and expressed in Equation 6.8, 6.9 and 6.10:

$$P_1 = \delta * \frac{b}{1 + (a * \|\nabla D\|)} \tag{6.8}$$

$$P_2 = \delta * \frac{b}{1 + (a * \|\nabla P(\mu_{tissue}, \sigma_{tissue})\|)} \tag{6.9}$$

$$P_3 = u + v * exp\left(-\frac{\|\nabla D\|}{w}\right) \tag{6.10}$$

1. **Penalty term 1 (P_1)** is a weighted norm of the gradient of the data term D (cf. Equation 6.8), where δ denotes the same weighting term as used in Equation 6.7 and a, b are constant weighting parameters.

2. **Penalty term 2 (P_2)** denotes an intensity based term and is calculated separately for cortex and ventricle segmentation (cf. Equation 6.9). Tissue type specific gray values are modelled as Gaussian distributions N$\sim(\mu_{tissue}, \sigma_{tissue})$, which parameters μ_{tissue} and σ_{tissue} are estimated using the a-priori atlas segmentation. These parameters are used to calculate the probability of every pixel belonging to cortex or ventricle. Subsequently, the gradient of the resulting probability map P and its norm are computed and weighted by the parameters δ, a, b as shown in Equation 6.8.

3. **Penalty term 3 (P_3)** represents an exponential formulation and is expressed in Equation 6.10. The parameter u is a constant and v a linear weighting parameter. The term w weights the norm of the image's D gradient non-linearly in the exponential term.

6.1.2 Evaluation Setup

For establishing a baseline model of the fetal brain development, a novel longitudinal registration procedure is formulated. According to preliminary experiments, three developmental stage dependent age ranges are defined and corresponding datasets are created. For every age range different option parameters for longitudinal registration are used. It makes it possible to parametrise the vector field regularisation according to the stage of brain development:

- Age range (AR) 1: 20th GW day 6 (146 GD) - 23rd GW day 3 (164 GD).

- Age range 2: 23rd GW day 3 (164 GD) - 26th GW day 2 (184 GD).

- Age range 3: 26th GW day 2 (184 GD) - 30th GW day 2 (212 GD).

For every developmental age range the deformation behaviour of image regression is evaluated using 21 different regularisation kernels $K[\lambda_0, \lambda_1, \lambda_2, \lambda, \mu]$ (cf. Section 6.1.1) and by observing the chosen kernel's effect on cortical volume expansion, changes of the cortical surface area and ventricle volume. The evaluation is performed using leave-one-out-cross-validation, i.e. for every test subject a separate deformation field (Atlas) is computed. Atlas-based cortical and ventricle segmentations are predicted using the corresponding deformation field and a source image at GW 20 for age range 1, GW 23 for age range 2 and GW 26 for age range 3. The estimated segmentations are evaluated against the provided manual segmentation using the Dice Coefficient. Corresponding results using the following chosen kernels are illustrated in red in Figure 6.4:

- AR 1: kernel 1 ($K_1[0.01, 0.01, 9e^{-6}, 1e^{-5}, 1e^{-5}]$)

- AR 2: kernel 4 ($K_4 \left[0.01, 9e^{-6}, 9e^{-6}, 0.01, 1e^{-5}\right]$)

- AR 3: kernel 7 ($K_7 \left[0.01, 0.01, 9e^{-6}, 0.01, 1e^{-5}\right]$)

The first part of the evaluation documents the atlas learning results for each age range. Subsequently, the atlases computed are used to evaluate the tissue labeling procedure as a second part of the evaluation. Estimated atlas templates at the testing time-point are pairwise registered to the test MR volume to obtain a transformation T. The inverse T^{-1} is used to transform the atlas based segmentation to the test-subject's space. As last step the segmentation of the test volume using the transformed atlas is computed. The presented approach is evaluated by computing the overlap between automatic- and manual segmentations of the fetal cortex and ventricles. In the leave-one-out cross validation, the DC [46] between the manual annotations and different automatic segmentations is computed based on (1) the atlas, (2) the transformed atlas, and (3) the Graph Cut (GC) segmentation optimization. Furthermore, the volume of cortex and ventricles, and the area of the cortical surface of the atlas based segmentations is reported. For pairwise registration the following kernel is used for regularisation: K=$\left[5e^{-3}, 5e^{-3}, 3e^{-5}, 1e^{-5}, 9e^{-6}\right]$.

6.1.3 Evaluation Results

Figure 6.3 shows examples of the atlas templates learned and corresponding anatomical details of these at age GW 21 day 4 (GD 151), GW 24 day 3 (GD 171) and GW 29 (GD 203). The brain model at age range 1 is characterised by a smoother cortex surface in comparison to a brain at a higher age range. It also visualises the increase of the cortical folding grade. According to Pugash et al. [173], the ventricles achieve their thickest size in early gestation and regress in the third trimester, which is not visible. The regularisation term for geodesic regression is not able to model location specific volume expansion and shrinkage at the same time. This leads to worse modelling results for ventricles, compared to cortical structure, since a kernel is chosen which models expansion. Additionally, the subject specific variability of age-dependent ventricle size in the dataset and the complex form of ventricles complicate the determination of a suitable kernel and consequently the registration procedure. Observable structures at every age range are Sylvian Fissures (SF), Lateral VENTricle (L-VENT), InterHemispheric Fissure (IHF), Cavum of Septum Pellucidum (CSP), Occipital Lobe (OL) and Frontal Lobe (FL). The SF shows in the coronal and axial slices a smooth bending at age range 1 and develop to a deep fold at the lateral side of the brain at age range 3. Also the IHF shows a deeper folding at age range 3 with Cingulate Sulcus (CiS) as additional forming compared to age range 1. The Germinal MATrix (GMAT) is existent until age range 2 and disappears later in the third trimester of pregnancy. The Central Sulcus (CeS) formation starts at age range 2 and gets more apparent at age range 3 as well as the developing of the PreCentral Gyrus (PreCG) and PostCentral Gyrus (PostCG). The ColLateral Sulcus (CLS) is visible at age range 3 as well as the Calcarine Sulcus (CaS) and PreOccipital Sulcus (POS).
The DC distributions of segmentations of the cortex for age range 1, 2 and 3 are
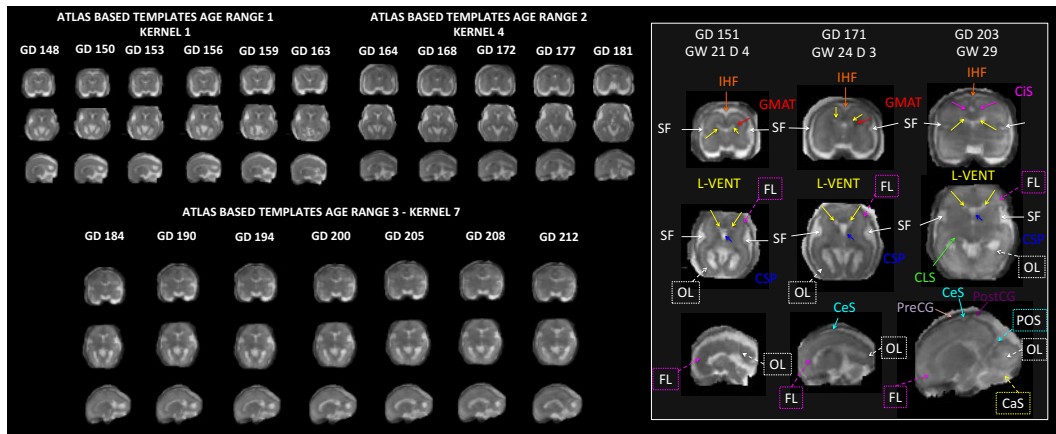
Figure 6.3: Left: Atlas based templates of AR 1, 2 and 3. Coronal (first row), axial (second row) and sagital (third row) slices are illustrated. Denoted structures: Sylvian Fissure (SF), InterHemispheric Fissure (IHF), Germinal MATrix (GMAT), Lateral-VENTricle (L-VENT), Cingulate Sulcus (CiS), ColLateral Sulcus (CLS), Cavum of Septum Pellucidum (CSP), Occipital Lobe (OL), Frontal Lobe (FL), Central Sulcus (CeS), PreCentral Gyrus (PreCG), PostCentral Gyrus (PostCG), ParietoOccipital Sulcus (POS) and Calcarine Sulcus (CaS) [125].

illustrated in Figure 6.4 on the top and for ventricle segmentations on the bottom. The DC distribution of atlas-based and transformed atlas-based segmentations using pairwise registration are illustrated and the three dotted lines visualise the DCs of GC based segmentations computed using penalty terms 1, 2 and 3. For age range 1 the highest DC improvement from 0.727 to 0.771 at GD 158 is achieved by pairwise registration and GC refinement compared to atlas-based segmentations. In contrast to this, no improvement is reached at GD 151, but shows the highest DC of about 0.851. At GDs older than 154 the GC refining using penalty 1 and penalty 2 achieve a higher DC increase of about 0.02 compared to using penalty 3.

At age range 2 no improvement of transformed atlas based segmentations is observable after pairwise registration, which leads to a decrease of the DC. It is observed that the labeling result of the pairwise registration has an influence on the GC labeling since it acts as initialization of this procedure, best visible at GD 184. The GC refinement is able to compensate the results of the pairwise registration between GD 164 and 184 and shows an increase of the DC between atlas and graph-cut based segmentations in average of about 0.02.

At age range 3 an increase of DC at every age range is achievable using GC refinement. The highest improvement between atlas-based segmentations and GC based segmentations is reached at GD 206 with a DC increase from 0.71 to 0.795. The highest DC at age range 3 of about 0.819 is achieved at GD 203 and the lowest of about 0.575 at GD 184. It is observable that pairwise registration is not capable to compensate differences in volume size or absolute displacements. If an estimated segmentation has a bigger volume
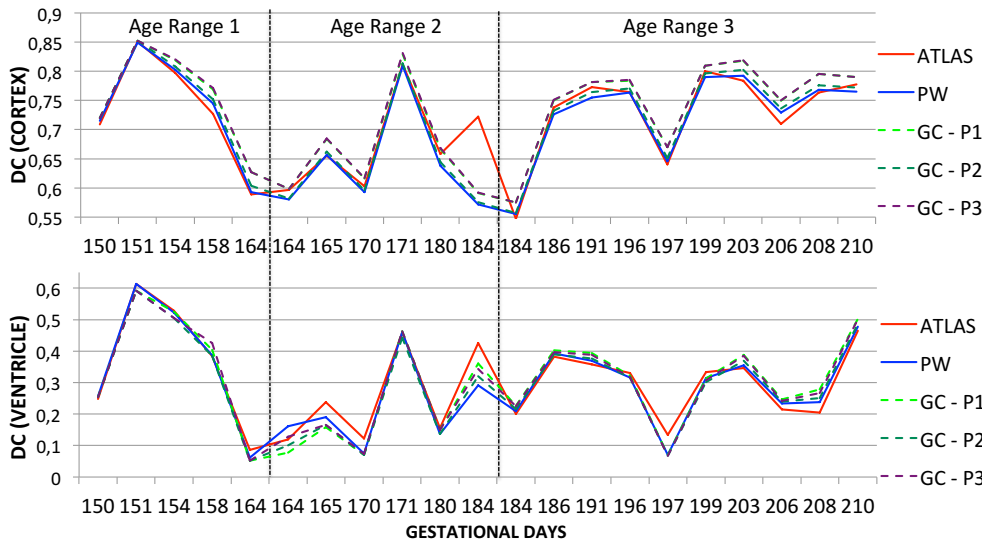
Figure 6.4: DCs of automatically estimated labels of the cortex and ventricle at age range 1, 2 and 3 [125].

than the structure to be segmented or is displaced, then the borders of neighboured tissue prevents the GC approach from cutting through regions of a high gradient, since this would lead to increasing costs in the energy minimisation procedure. Consequently, the GC is not capable to refine the segmentation. In Figure 6.5 an example for a misaligned segmentation and its deformation through the labeling procedure is illustrated. The displacement is observable at the IHF in the first column and the superior part of the anterior horn of the ventricle in the second column. Test data and corresponding
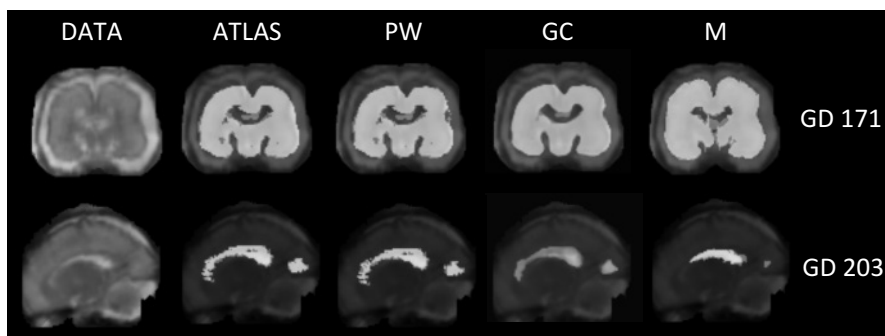
Figure 6.5: Top: Coronal view - segmentations of the cortex at GD 171 (GW 24 day 3), bottom: sagital view - segmentations of the ventricle at GD 203 (GW 29). Segmentations are illustrated estimated by the atlas (ATLAS), after the pairwise registration procedure (PW), estimated by the GC approach (GC) and manual annotations (M) [125].

estimated segmentations, transformed segmentations to subject's space and GC based segmentations of the cortex at GD 171 (top) and of ventricular tissue at GD 203 (bottom) are shown. The GC segmentations are computed using the penalty term 3, since it shows the best improvement between atlas-based and GC based segmentations.

6.2 Spatio Temporal Modelling of DDP of Functional Brain Connectivity for Assessing Reorganisation

The STM presented in this section focuses on modelling DDP of functional connectivity in children to assess functional brain reorganisation patterns in the paediatric cohort after an ischaemic stroke event occurred. In Figure 6.6 the application of the concept proposed is visualised. The spatio temporal baseline model is formed by a longitudinal model of developing functional connectivity. The system dynamics are the age at stroke, stroke region, response to therapy and environmental influences (natural plasticity). The time-dependent dynamics are the functional reorganisation dynamics over the years after the stroke occurred and the developmental functional connectivity dynamics. Following
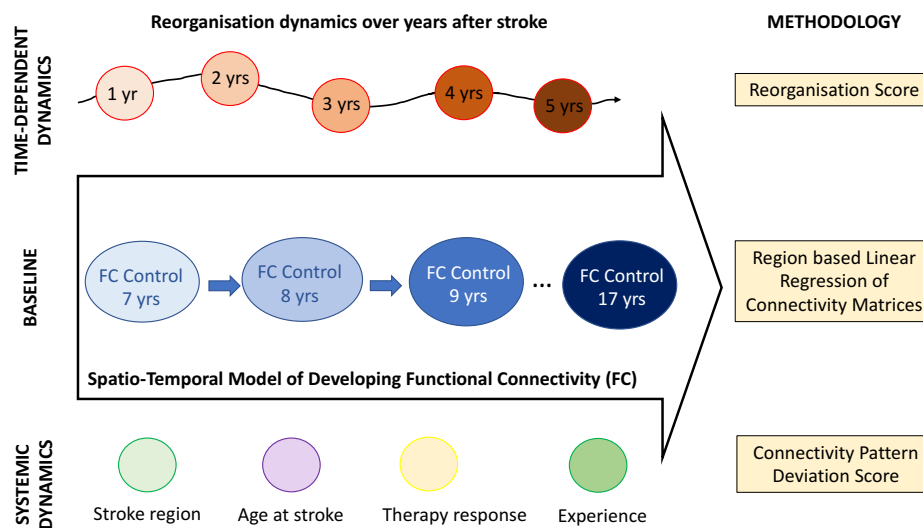
Figure 6.6: Application of the STM concept on DDP of Paediatric Functional Connectivity.

the STM concept, first the baseline development of functional connectivity networks in healthy children is modelled over age. Systemic dynamics of control and stroke subjects are analysed using the baseline model and the *connectivity pattern deviation score* proposed. Reorganisation dynamics are assessed by the baseline model and the proposed *reorganisational score* to track regions, which exhibit similar connectivity characteristics as the baseline area impacted by stroke. It is hypothesized that stroke subjects exhibit higher deviation from a baseline's age specific mean than controls, and that reorganization causes new regions to adopt connectivity characteristics of areas impaired by stroke. Here,

the approach by [154] has been adapted to extract connectivity pattern deviations over development and reorganisation patterns of functional connectivity in children induced by lesions formed after an ischaemic stroke. The modelling process of DDP of functional brain connectivity can be summarized as follows:

- **Input:** rsfMRI acquisitions $X = \{I_1, \ldots, I_P\}$ of P children at age a, where $I \in \mathbb{R}^{L \times K \times S \times t}$, L and K denote the dimension of one slice, S denotes the number of slices in an acquired volume, and t denotes the acquisition time point of the rsfMRI.

- **Representation:** graph-based representation as connectivity matrices $CM \in \mathbb{R}^{N \times N}$, where N is the number of observed nodes in the graph.

- **Baseline Modelling:** region based linear regression of connectivity matrices, which provides age specific baseline connectivity computations $\overline{CM}^{age} \in \mathbb{R}^{N \times N}$.

- **Output:** two novel scores which assist to assess systemic as well as time-dependent dynamics of functional connectivity reorganisation:

  - Connectivity Pattern Deviation (CPD) score
  - ReOrganiSation (ROS) score

- **Evaluation Strategy:**

  - Identification of deviating local connectivity characteristics in control cases in comparison to the age specific baseline.
  - Identification of deviating local connectivity characteristics in stroke cases in comparison to the age specific baseline.
  - Identification and interpretation of target regions of reorganisational processes.

6.2.1   Methodology

Baseline: Longitudinal Modelling of Developing Functional Connectivity
For the proposed baseline formulation a graph based representation of the cortical surface is assumed, which has been previously normalized to a standardized surface. The surface is represented by N nodes $x = \{1, \ldots, N\}$. For every subject a stroke mask is annotated and a connectivity matrix $CM \in \mathbb{R}^{N \times N}$ is computed following the procedure introduced in Section 5.2.1. For more details regarding the preprocessing and dataset used cf. Section 4.2. In Figure 6.7 the schematic concept of baseline modelling is visualised as well as the derivation of an age-matched connectivity matrix. Based on preliminary analysis and the size of the datasets, it has been decided to perform element wise linear regression of correlation coefficient matrices of control subjects for modelling the baseline evolution of connectivity profiles across the cortex by deriving the slope $B \in \mathbb{R}^{N \times N}$. For the

Element-wise Linear Regression of Subjects' Correlation Coefficient Matrices (CM)
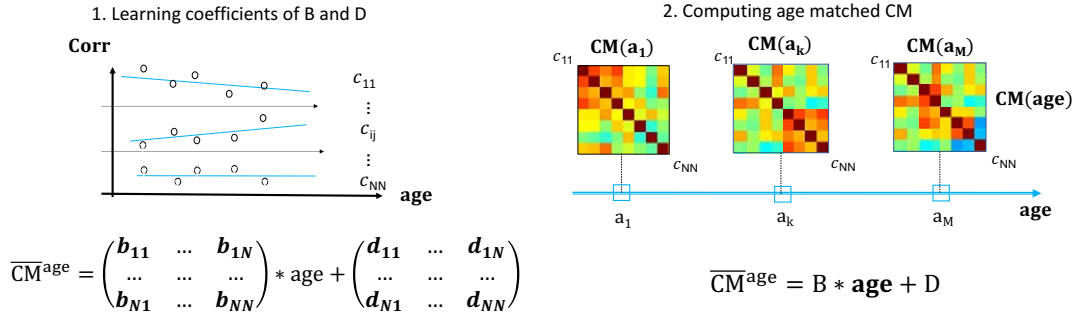
Figure 6.7: Schematic illustration of baseline longitudinal modelling of developing functional connectivity in children using element-wise linear regression.

computation of an age-matched connectivity matrix $\overline{CM}^{age}$ Equation 6.11 is used, under the assumption that $D \in \mathbb{R}^{N \times N}$ is a constant factor.

$$\overline{CM}^{age} = B * age + D \tag{6.11}$$

CPD Score: Addressing Systemic Dynamics of Functional Connectivity
For addressing the systemic dynamics in the observed data the *Connectivity Pattern Deviation (CPD)* score is introduced to identify deviations of local baseline connectivity characteristics of control and stroke subjects. In Figure 6.8 the computation of the CPD score is illustrated. The CPD score $D \in \mathbb{R}^{1 \times N}$ is computed between every single subject's

Connectivity Profile Deviation Score
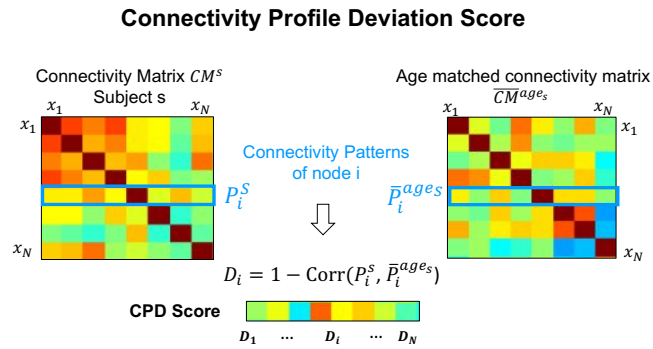
Figure 6.8: Schematic illustration of the computation of the CPD score.

CM^s and the age matched $\overline{CM}^{age_s}$ provided by the baseline model proposed. Therefore the Pearson Correlation Coefficient (PCC) (cf. Equation 6.12) is computed between a connectivity pattern $P_x^s \in \mathbb{R}^{1 \times N}$ of a vertex x and the corresponding age matched

connectivity pattern $\overline{P}_x^{age_s} \in \mathbb{R}^{1 \times N}$ of controls, where $P_x^s = CM_{i=x,j}$, $\overline{P}_x^{age_s} = \overline{CM}_{i=x,j}^{age_s}$, $j = \{1, \ldots, N\}$ (cf. Figure 6.8).

$$D_x^s = 1 - PCC(P_x^s, \overline{P}_x^{age_s}), \text{ where } x = \{1, \ldots, N\} \tag{6.12}$$

This CPD score is computed for every subject s in the dataset (control and stroke cases).

ROS Score: Addressing Time-Dependent Dynamics using Baseline Models
The time-dependent dynamics of functional connectivity reorganisation are assessed using the spatio temporal baseline model proposed. Therefore, a *ReOrganisation Score (ROS)* is presented for identifying possible regions, where functional networks of a stroke region transfer to. For clearer understanding its computation is schematically illustrated in Figure 6.9. In a first step the corresponding stroke case's age matched $\overline{CM}^{age}$ is
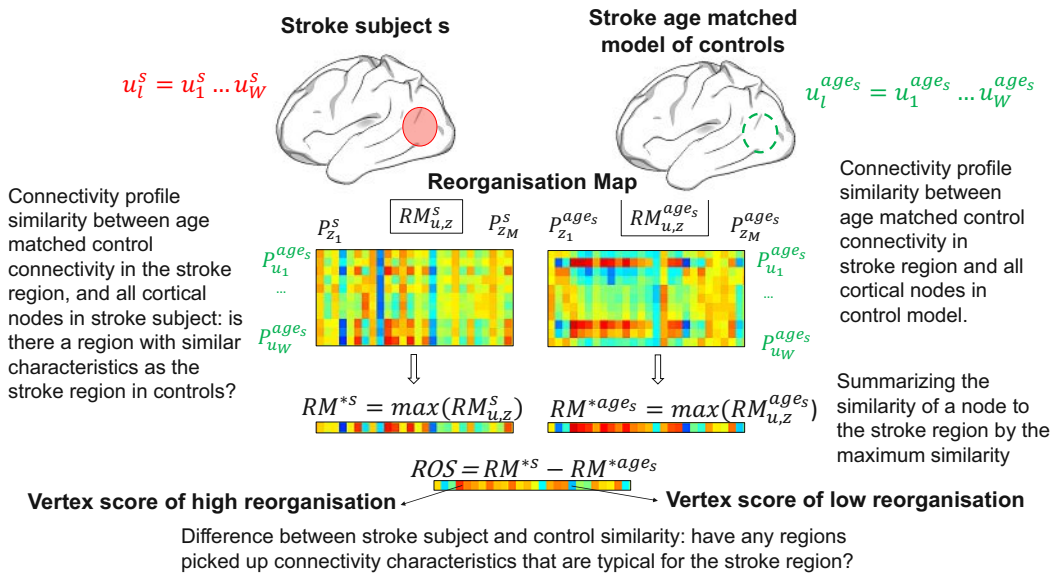
Figure 6.9: Schematic illustration of the computation of the reorganisation score [121].

computed. In a second step for every stroke subject separately the stroke mask is used to determine the set $u = \{1, \cdots W\}, W \leq N$ of nodes corresponding to the stroke regions. In a third step the Reorganisation Maps (RM) $RM_{u,z}^s$ and $RM_{u,z}^{age_s}$ between connectivity patterns is computed using Equation 6.13 and 6.14. By definition $z = x \setminus u$ is a set of nodes not belonging to the stroke region. $\overline{P}_{u_l}^{age_s} = \overline{CM}_{i=u_l,j=z}^{age_s}$, $P_{z_k}^s = CM_{i=z_k,j=z}$, $\overline{P}_{z_k}^{age_s} = \overline{CM}_{i=z_k,j=z}$, $k = 1 \ldots M, M =| x \setminus u |, l = \{1, \ldots, W\}$.

$$RM_{u,z}^s = PCC(\overline{P}_u^{age_s}, P_{z_k}^s), s = \{1, \ldots, S\} \tag{6.13}$$

$$RM_{u,z}^{age_s} = PCC(\overline{P}_u^{age_s}, \overline{P}_{z_k}^{age_s}), s = \{1, \ldots, S\} \tag{6.14}$$

After the calculation of the RM the vertex of set u with the maximum value is extracted. Since RM of the control model show higher values as RM of the stroke, it was decided (for

obtaining comparability for visualisation purposes) to perform histogram equalisation, resulting in two vectors $RM^{*s} \in \mathbb{R}^{1 \times M}$ and $RM^{*age_s} \in \mathbb{R}^{1 \times M}$. Subsequently, the ROS of a subject S is computed as defined in Equation 6.15.

$$ROS = RM^{*s} - RM^{*age_s}, \tag{6.15}$$

6.2.2 Evaluation Results

Deviation of local connectivity characteristics in the control cohort
Figure 6.10 illustrates the CPD score for control subjects of different age (left) and its change over increasing age (right). The intersubject dynamics of controls is minimal in
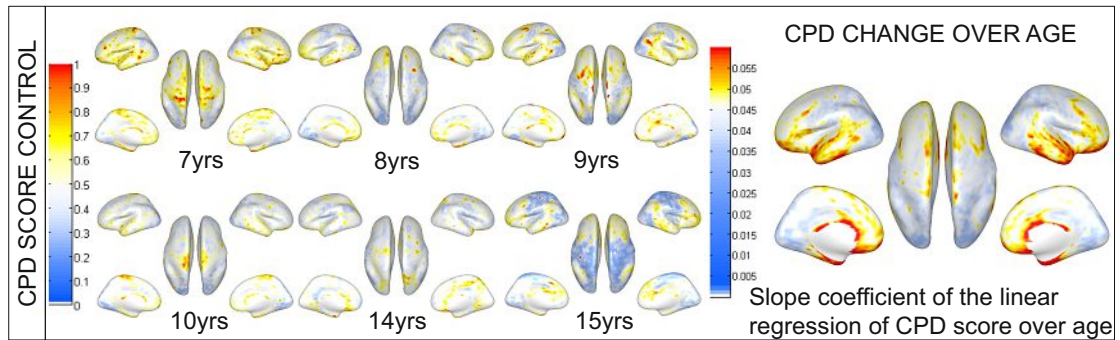
Figure 6.10: Visualisation of the CPD score in control subjects during ageing: 6 control subjects and their deviations to the age matched average, and the visualisation of the change: red regions exhibit increased deviation / deviation change, while blue regions are more stable [121].

the visual, sensory and motor cortices and correlates with increasing age to the deviation estimates in [154] of adult controls. High deviation is observed in the temporal cortex including primary auditory cortex, Wernicke's area, in the prefrontal cortex and parietal lobe. Considering the age a decrease of deviation in the heteromodal regions is observable with increasing age also visible in the corresponding boxplot of CPD scores in Figure 6.11 (left).

Deviation of local connectivity characteristics in the stroke cohort
For the stroke subjects, RH and LH stroke cases are grouped together for clearer visualisation in Figure 6.12. The stroke cohort shows higher variabilities compared to the control cohort, which overlaps with the hypothesis that stroke affects the reorganisation of connectivity networks, resulting in higher CPD. Higher intersubject CPD over 0.8 are observable on the hemisphere of the stroke location and are also visible in the corresponding boxplot of CPD scores in Figure 6.11 (middle, right).

Target regions of reorganisational processes
To evaluate the ability of the ROS to detect reorganisational regions first the brain surface

100
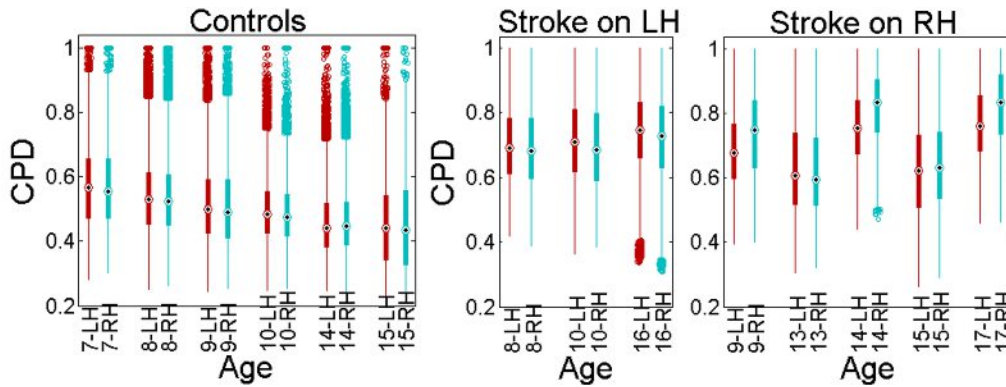
Figure 6.11: Visualisation of CPD score of LH and RH within the stroke and control cohort (CPD scores of all subjects at same age are grouped here). Control cases show symmetric mean CPD between RH and LH and a decrease according to increasing age. The CPD scores of stroke subjects show higher means on the hemisphere of stroke location [121].
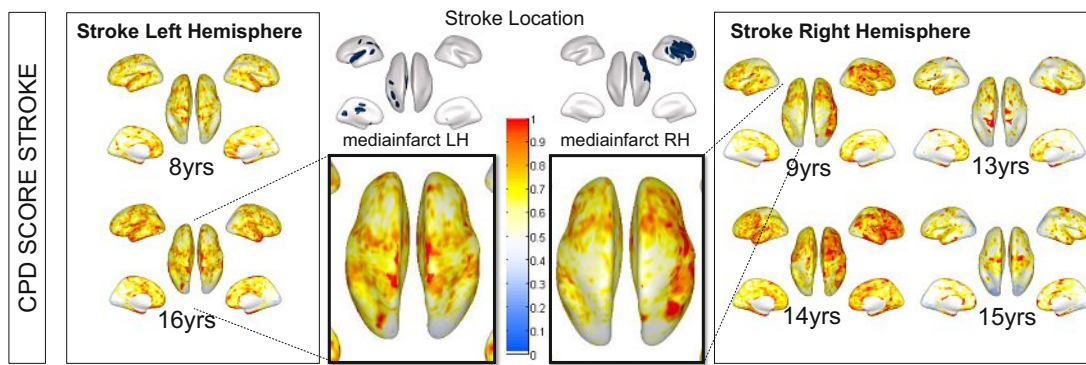
Figure 6.12: Visualisation of CPD score of LH stroke subjects (left) and RH stroke subjects (right) [121].

is divided into 17 cortical networks using the parcellation proposed by Yeo et al. [241], which is computed based on rsfMRI acquisitions of 1000 subjects and additionally provides *fsaverage5* surface labels. For every region (total 36 - LH and RH are observed separately) the ratio of stroke voxels and the region's mean ROS and mean CPD are estimated. In Figure 6.13 the first row illustrates correlation matrices $\in \mathbb{R}^{36 \times 36}$ based on correlations computed between the ratio of stroke voxels and mean CPD for all subjects (first column), for LH stroke subjects (second column) and RH stroke subjects (third column). In Figure 6.13 second row the mean ROS score is used instead of the mean CPD to estimate the correlations. In Figure 6.13 a deviation of correlation values between LH and RH stroke subjects is visible, since correlations can be computed only between stroke voxel ratios (>0) on the ipsilateral side. In the first row of Figure 6.13 positive correlations are observable, which can be interpreted as regions greater affected by a stroke lesion

101
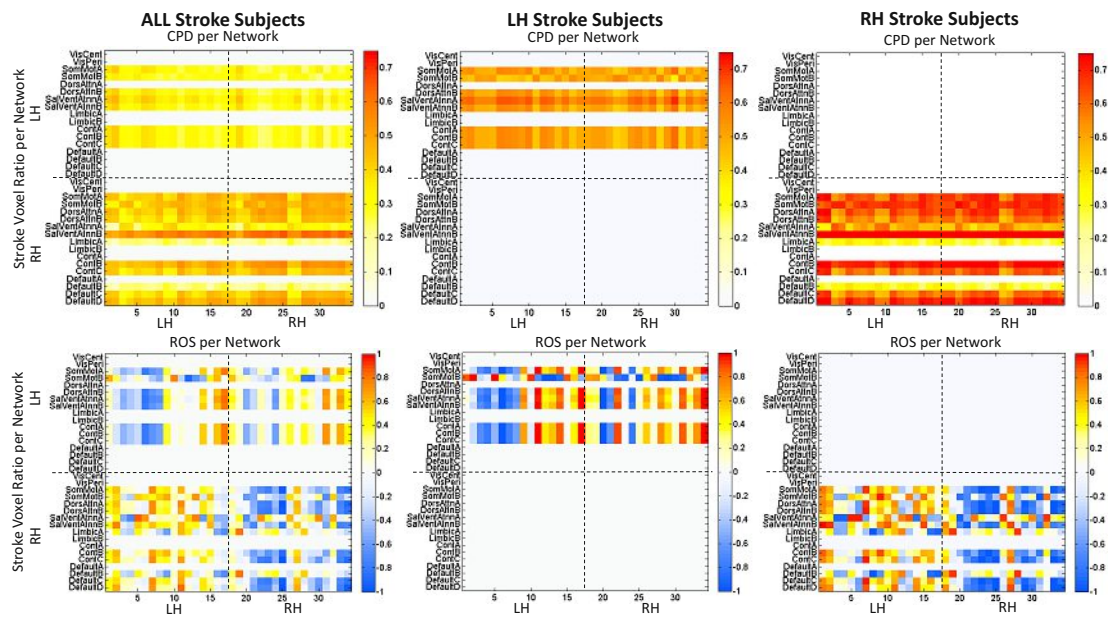
Figure 6.13: Row one visualises the network wise correlations between the stroke voxel ratio and the CPD score using all stroke subjects (first column), LH stroke (second column) and RH stroke subjects (third column). Visualisation of network wise correlations between the stroke voxel ratio and the ROS are shown in row two [121].

show a higher mean CPD and a lower mean CPD if they are less affected. Additionally, stronger blocks of correlation scores are observable in the default mode network regions (except the temporal component Default A) or somato motoric areas. In the second
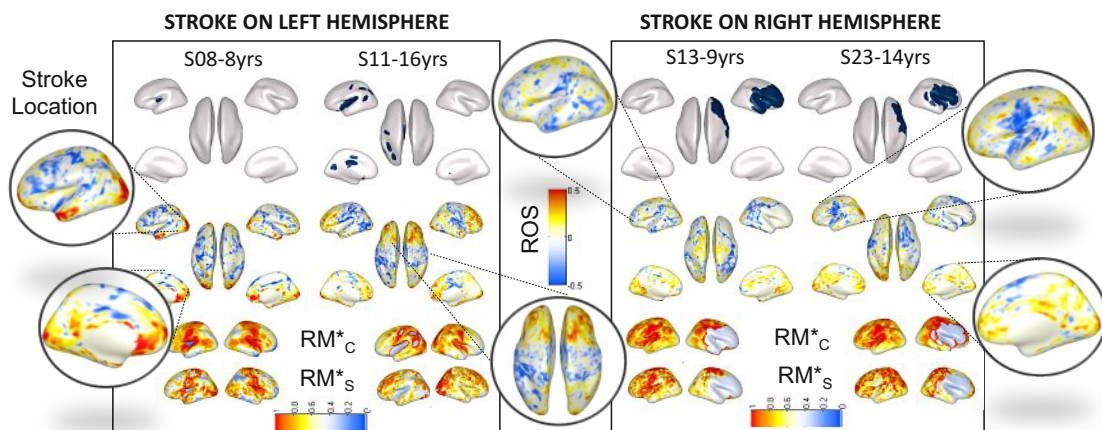
Figure 6.14: Visualisation of regions that pick up connectivity patterns observed in the stroke region in age matched baselines. Red ROS indicates regions that exhibit characteristics typical for the stroke regions, if the subject is a control [121].

row of Figure 6.13 especially for RH stroke subjects (right) a division of RH and LH correlation values according to their sign is visible, since the severity of stroke and the number of subjects is higher in this cohort compared to LH stroke subjects. The voxel ratio positively correlates with the ROS of the controlateral side and negatively with the ROS of the ipsilateral side. This suggests a decrease of the ROS in ipsilateral and an increase of the ROS in controlateral regions with increased stroke voxel ratio in the stroke hemisphere. In Figure 6.14 the target regions for possible reorganisational processes after stroke, computed using the ROS proposed are visualised for LH stroke subjects (left) and RH stroke subjects (right). The first row visualises the stroke location, the second row the ROS and the third and fourth row the histogram equalized reorganisation vectors. Subject S08 shows possible target regions in its strokes' neighbourhood on the ipsilateral side. S11 shows possible symmetric reorganisation targets. S13 and S23 with a severe mediainfarct on the RH show both on the control and ipsilateral side of non-stroke region an increased ROS as well as on the controlateral side in the stroke region.

6.3 Spatio Temporal Modelling of Blood Cell DDP for Treatment Response Assessment

The STM presented in this section focuses on the modelling of DDP of blood cells during leukaemia treatment for cancer cell classification. The application of the proposed concept is visualised in Figure 6.15. The baseline of the STM of DDP in leukaemia is
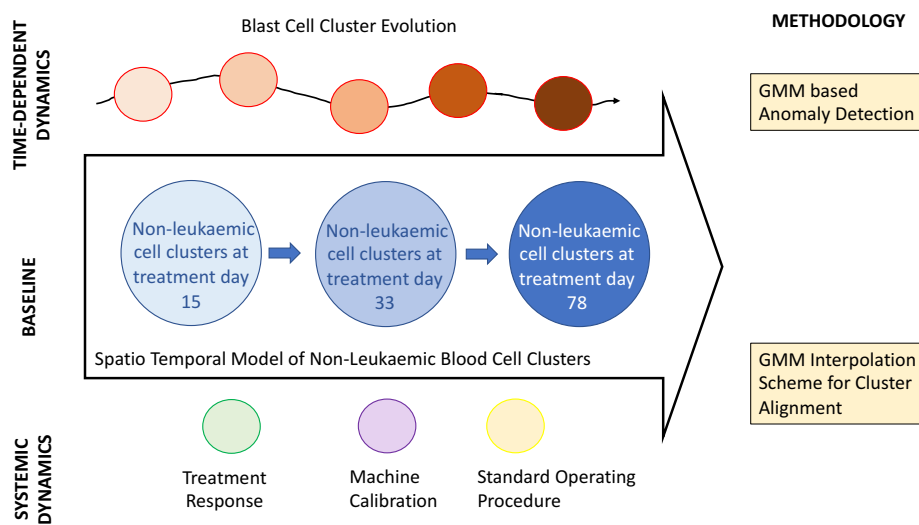
Figure 6.15: Application of the STM concept on DDP of blood cells during leukaemia treatment.

formed by observations of non-leukaemia cells over treatment. The systemic dynamics in this approach are formed by treatment and corresponding response, co-morbidities or machine calibrations. Time-dependent dynamics are the temporal patterns of blast

cell clusters over treatment time points, which in the best case completely disappear in late therapy stages. These dynamics are addressed by robustly aligning the therapy time point matched baseline cell distributions with new input data to identify non-blasts. The blast dynamics are then identified using the anomaly detection approach for GMM representations, proposed in Section 5.1.2. If FCM measured blood cell clusters have to be compared and analysed, distributional shifts and deformations between these are visible according to instrument dependent drifts and calibrations, different acquisition protocols, patient specific variances or treatment responses. In Figure 6.16 two-dimensional plots (feature CD20 and CD10) of FCM measurements of 3 different ALL patients (one patient per row) over three treatment time points (column 1-3) at day 15, 33 and 78 are visualised. The non-blasts are visualised in blue and blasts in red. Even though all patients are
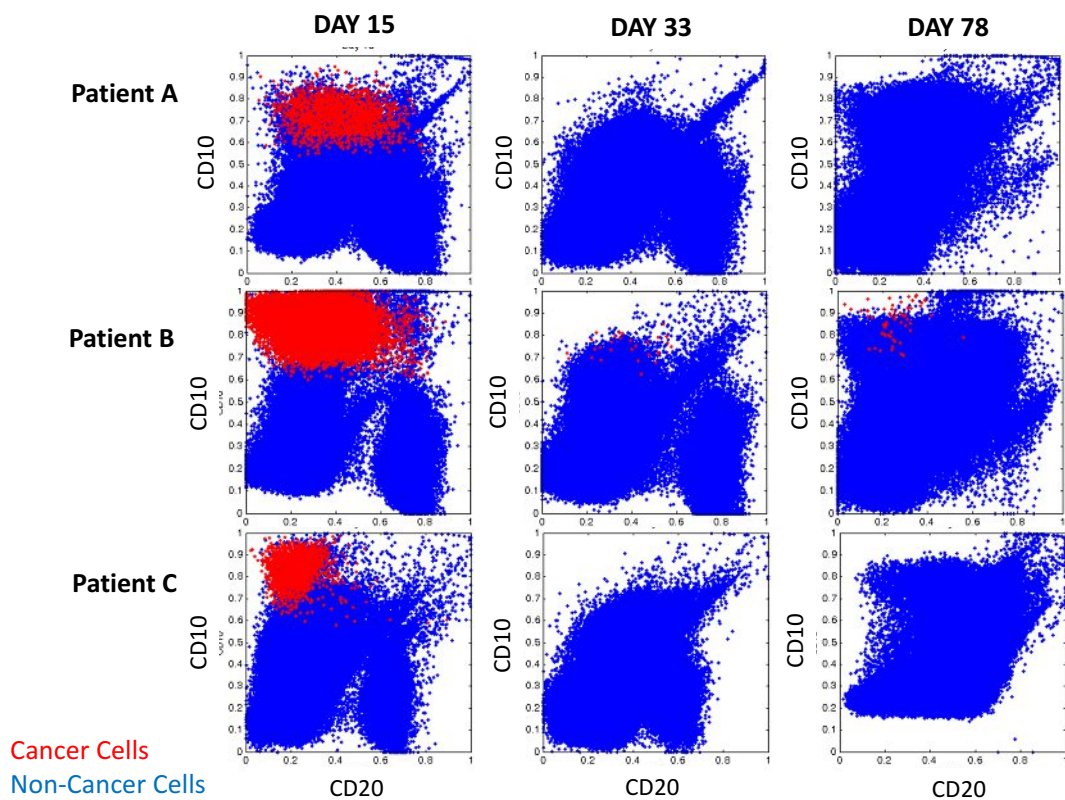
Figure 6.16: Two-dimensional visualisation of FCM measurements (feature CD10 and CD20) of three ALL patients over treatment timepoints day 15, day 33 and day 78. Blasts are marked in red and non-blasts in blue.

measured in the same institution with the same standard operating procedure, the previous discussed dynamics are visible: Non-blast populations show deformed or shifted appearance, although general cluster trends are observable over all three patients at a time point. In comparison to non-blasts, blast populations are more heterogeneous in

their time-specific appearance (cluster size, position, amount of cells) and longitudinal appearance (increasing or decreasing number of blasts, disappearing of populations over time) between patients. There is a need of normalization strategies to be able to describe transitions between baseline populations and to address the blast specific dynamics. Based on preliminary results [129], time specific baselines are defined based on GMM representations of non-blast cells at a specific time-point. An optimal transport technique for FCM data on the manifold of GMMs is proposed to be able to align baseline states at a specific time-point of different patients and over time within a patient. Kim et al. [100] propose an interpolation scheme on the manifold on k-component GMMs using the Kullback Leibler Divergence (KLD) as a metric. The presented GMM interpolation approach is extended by introducing the Wasserstein metric as a distance measure between two GMMs, which was inspired by the approach of Chen et al. [35], who provided an interpolation scheme based on the Wasserstein metric for GMM on the space of Gaussian distributions, so it can be seen as a discrete measure and retains the Gaussian mixture structure. This formulation shows efficiency for high dimensional GMMs with a small number of components, but has not been used for the alignment of cell distributions acquired by FCM. The proposed alignment strategy is developed using the longitudinal *dataset ALL* (cf. Section 4.3.1 for details regarding the dataset used). The modelling process of DDP of blood cells during leukaemia can be summarized as followed:

- **Input:** FCM acquisitions $X = \{X^1, \ldots, X^P\}$, of P children at a treatment timepoint t, where an acquisition $X^p \in \mathbb{R}^{C \times D}$ consists of measurements $x_c \in \mathbb{R}^D$ with D features of C cells per patient p.

- **Representation:** probability density based representation of cell clusters using GMM.

- **Baseline Modelling:** optimal transport interpolation scheme between non-blast cell clusters.

- **Output:** transportation plan from source to target GMM, classification l label for every cell in a new dataset, where $l = \{blast(1), non-blast(0)\}$.

- **Evaluation Strategy:**
  - Evaluation of 3 different parametrisations for data representation
  - Evaluation of 3 different metrics for baseline alignment
  - Evaluation of blast classification and MRD assessment performance

6.3.1 Methodology

A GMM interpolation strategy for spatio temporal alignment of baseline blood cell clusters For the representation of the probability density function $p(x|.)$ of non blast cells x a N component GMM $S(x)$ is used as a weighted sum of N Gaussian distributions $S_i(x) = \mathcal{N}(x|\mu_i, \sigma_i)$ as expressed in Equation 6.16. θ_i is the set of parameters required

to parametrize a Gaussian component i in a GMM (cf. Equation 6.17), where w_i is the Gaussian weighting term, μ_i the mean (cf. Equation 6.18) and Σ_i the covariance (cf. Equation 6.19).

$$S(x) = p(x|\theta) = \sum_{i=1}^{N} w_i S_i(x) \tag{6.16}$$

$$\theta = \{w_i, \mu_i, \Sigma_i\}_{i=1}^{N} \tag{6.17}$$

$$\mu_i = \mathbb{E}_{S_i(x)}[x] \tag{6.18}$$

$$\Sigma_i = \mathbb{E}_{S(x)}[(x - \mu_i)(x - \mu_i)^T] \tag{6.19}$$

GMM based Optimal Transport

The optimal transport problem is the transport of a source distribution $S(\mathrm{x})$ of a mass x on a manifold $\mathcal{M}_{GMM}$ of N component GMMs, in a way that it is transformed into the target distribution $T(x) \in \mathcal{M}_{GMM}$ without loss of mass [35]. Therefore, an optimization function and transport plan γ are defined. Optimizing γ refers to the finding of an optimal interpolation path on $\mathcal{M}_{GMM}$ by minimizing distances D between the Gaussian components $S_i(x), T_j(x)$ in $S(x)$ and $T(x)$ (cf. Equation 6.20). In Figure 6.17 a schematic illustration of the GMM based optimal transport problem for FCM data is visualised. Two physical features (SS INT and FS INT) are used as dimensions for visualisation. Cyan ellipses correspond to Gaussian components of the source GMM and black ellipses to the target GMM. In the optimal case, components of the source GMM overlay with the target GMM components after alignment (left image). Only non-cancer cells are visualised.
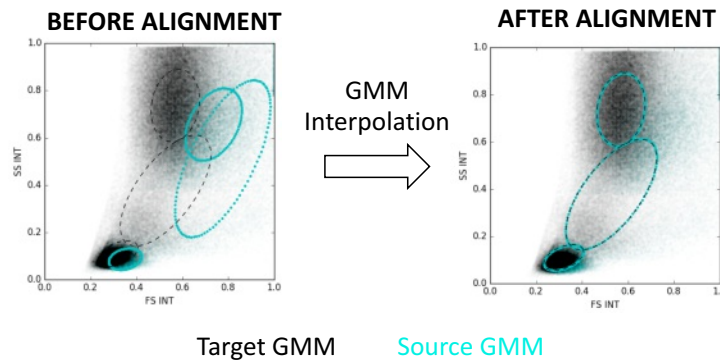
Figure 6.17: Schematic illustration of the GMM based Optimal Transport problem with flowcytometry data. Only 2 measured features (SS INT and FS INT) are visualised. Black ellipses correspond to Gaussian components of the target GMM and cyan to the source GMM. Only non-cancer cells are visualised [126]. [best viewed in color]

$$S^* = argmin_{S(x) \in \mathcal{M}_{GMM}} \sum_{j=1}^{M} D(S(x) || T_j(x)) \tag{6.20}$$

In this experiment the Wasserstein metric (cf. Equation 6.21 [35]) is minimized between the Gaussian components of the source and target GMMs. In the following, $i = 1, \ldots, N$ and $j = 1, \ldots, M$ denote the numbers of Gaussian components in the source and in the target GMM respectively. The interpolation scheme is evaluated by testing Wasserstein Distance (WD)against the KLD (cf. Equation 6.22) and BB (cf. Equation 6.23) distance.

$$W^2 = \|\mu_i - \mu_j\|^2 + tr[\Sigma_i + \Sigma_j - 2\sqrt{(\sqrt{\Sigma_i})\Sigma_j(\sqrt{\Sigma_i})}] \tag{6.21}$$

$$KLD = \frac{1}{2}k \log 2\pi + \log |\Sigma_j| + tr[\Sigma_j^{-1}\Sigma_i] + (\mu_i - \mu_j)^T \Sigma_j^{-1}(\mu_i - \mu_j) \tag{6.22}$$

$$BB = \frac{1}{8}(\mu_j - \mu_i)^T (\frac{\Sigma_i + \Sigma_j}{2})^{-1}(\mu_j - \mu_i) + \frac{1}{2}\ln \frac{|\frac{\Sigma_i + \Sigma_j}{2}|}{|\sqrt{|\Sigma_i||\Sigma_j|}} \tag{6.23}$$

Kim et al. [100] propose EM to estimate the parametrization θ of the transported GMM S^* by minimizing the KLD. Here, this approach is adapted for FCM data by estimating the likelihood of the Wasserstein Distance (WD) (*responsibility*) between every Gaussian component $S_i(x)$ and $T_j(x)$ (cf. Equation 6.24) in the E-step to obtain the transportation matrix $\gamma_{ij} \in \mathbb{R}^{N \times M \times D}$, where D refers to the number of features observed per cell.

$$\gamma_{ij} = \frac{\delta_{i,j}}{\tau_i} \text{ where } \delta_{ij} = w_j \exp -W^2\Big(S_i(x), T_j(x)\Big)$$
$$\text{and } \tau_i = \sum_{j=1}^{M} \delta_{ij} \tag{6.24}$$

In the M-step the parameter set θ is updated using Equations 6.25, 6.26 and 6.27.

$$w_j = \frac{w_j}{\sum_{j=1}^{M} \sum_{i=1}^{N} w_j} \text{where } w_j = \sum_{i=1}^{N} w_i \gamma_{ij} \tag{6.25}$$

$$\mu_j = \sum_{i=1}^{N} \pi_i \mu_i \text{ where } \pi_i = \frac{w_i \gamma_{ij}}{\sum_i w_i \gamma_{ij}} \text{ for fixed j} \tag{6.26}$$

$$\Sigma_j = \sum_{i=1}^{N} \pi_i \Sigma_i + \sum_{i=1}^{N} \pi_i (\mu_i - \mu_j)(\mu_i - \mu_j)^T \tag{6.27}$$

6.3.2 Evaluation Setup

The methodology proposed is evaluated in the following way: As comparable performance measures for non-cancer cell identification after data normalization, the mean sensitivity, accuracy, precision and f-score over all patients in the test fold are computed. 4 fold cross validation is used, where the test fold consisted of 29 patients and the training fold of 87. The measured cells in the training data are subsampled in a random way, by extracting 100,000 non blast cells per patient, resulting in a total of $8.7*10^6$ non blast cells. Subsequently, a GMM representation of the non-blast cells of the training set

(Source) and test set (Target) are learned separately, using the toolbox *mixture* integrated in the python framework *sklearn*[2]. The parameter set of the transformed Source GMM is estimated by using 1,000 iterations of EM and the methodology introduced in Section 6.3.1. Subsequently, the transformed model is used to predict a score for every cell of a test patient's sample to identify non-cancer cells.

6.3.3 Evaluation Results

In Table 6.1 the non-blast classification performance is summarized using three different alignment metrics and 3 different setups of component numbers to represent the source GMM and target GMM. Non-blasts are classified based on WD best with a precision

Table 6.1: Illustration of the non-blast classification performance using GMM interpolation with WD, KLD and BB for different therapy time points, and with different number of components N for the source non blast GMM, and M for the target sample.

Experiment	N	M	Sensitivity	Precision	Accuracy	f-score
KLD	3	4	**0.9780**	0.9488	0.9339	**0.9564**
WD	3	4	0.9732	**0.9505**	**0.9347**	0.9558
BB	3	4	0.6904	0.9441	0.6798	0.7188
KLD	4	5	**0.9821**	0.9489	**0.9366**	**0.9582**
WD	4	5	0.9702	**0.9503**	0.9316	0.9540
BB	4	5	0.8587	**0.9506**	0.8274	0.8703
KLD	4	6	**0.9814**	0.9495	0.9376	**0.9585**
WD	4	6	0.9755	**0.9534**	**0.9402**	**0.9585**
BB	4	6	0.8711	0.9499	0.8419	0.8835

of 0.9534, accuracy of 0.9402 and f-score of 0.9585 in the experiment with a number of components (3,4) and (4,6) compared to the KLD and BB metric. This confirms the observations of Chen et al. [35], that an GMM interpolation scheme based on WD is efficient for high-dimensional GMM with a small number of components. For (4,5) number of components the KLD performs better compared to WD and BB with an accuracy of 0.9366 and f-score of 0.9582. The worst results are achieved by the BB metric with an average difference of -0.2 of the f-score and -0.3 difference in the sensitivity for $N = 3$ and $M = 4$ Gaussian components.

---

[2]Python Toolbox: `https://scikit-learn.org/stable/modules/generated/sklearn.mixture.GaussianMixture.html` [accessed 2021-02-04]

6.4 Spatio Temporal Modelling of DDP in MM for Lesion Evolution Risk Prediction

In this section the application of the STM concept proposed for predicting focal lesion evolution risk in MM is presented. Figure 6.18 visualises the concept of the STM applied. The baseline spatio temporal model is formed by bone regions at different stages of MM progression. Examples for systemic dynamics in this process are imaging artefacts, responses on the therapy or co-morbidity. Time-dependent dynamics are diffuse infiltration patterns and focal lesion evolution patterns taking place in parallel to the disease's progression over time. The aim is to develop a strategy to predict the future
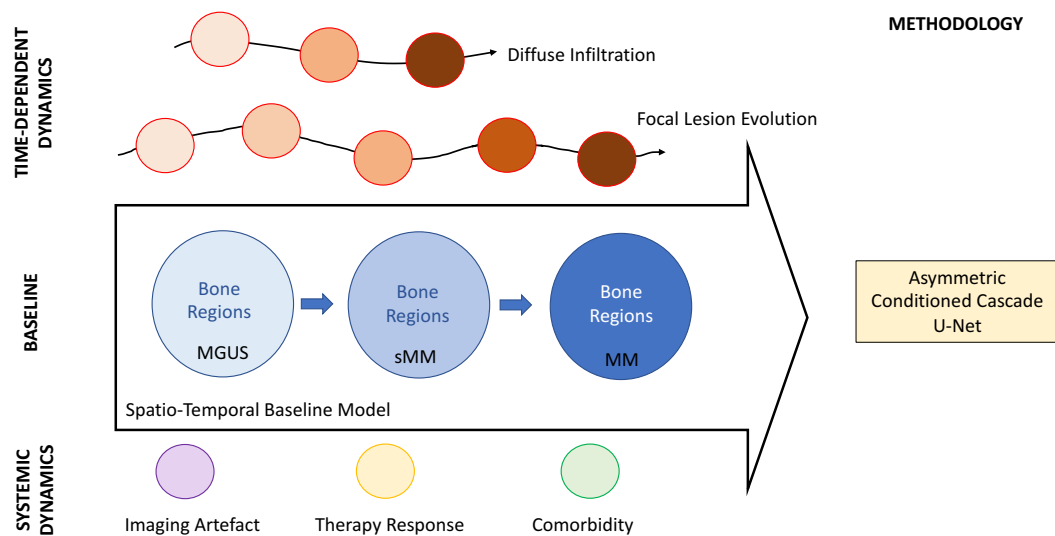
Figure 6.18: Application of the STM concept for prediction of DDP in Multiple Myeloma.

risk of evolving bone lesions in MM during the progression from sMM (a precursor stage of MM) to the symptomatic form of this disease. This is motivated by the fact, that according to recent study results [148], patients with early therapy of MM showed a clear benefit compared to late therapy - reporting delayed disease progression and decreased mortality [246]. Thus, it is particularly important to identify and predict future high-risk bone regions in precursor stages of MM as early as possible, to determine the evolution behaviour towards diffuse or osteolytic bone lesions and to obtain a basis for effective treatment planning and response assessment. The proposed spatio temporal model of whole body focal bone lesion evolution follows the spatio temporal modelling concept introduced in this thesis. For this approach the *dataset BONE* is used (cf. Section 4.4) consisting of longitudinal T1 and T2 weighted whole body MRI acquisitions of 63 MM patients. Within this work, the following research questions are of interest:

1. Is it possible to perform voxel-wise focal lesion evolution risk predictions in wb-MRI? Which technique is suitable? How can we address the disbalance between the size

of lesion regions and the body region.

2. Which property in progressing infiltration patterns can be used to encode a baseline in the spatio temporal model? Is it possible to introduce time-dependent knowledge about the prediction duration and enable the conditioning of future predictions on the duration?

3. Is it possible to model the dynamics of lesion emergence based on a pre-stage? How do bone anomalies and corresponding dynamics affect the prediction result?

The modelling process of DDP in MM can be summarized as follows:

- **Input:** Longitudinal wb-MRI acquisitions I_p of a patient p at acquisition timepoint t, where $I_p \in \mathbb{R}^{M \times N \times S}$

- **Representation:** Image and patch based representation

- **Baseline Modelling:** Bone detection network

- **Output:** time specific lesion evolution risk prediction map D_p, where $D \in \mathbb{R}^{M \times N \times S}$

- **Evaluation Strategy:**

  - Evaluation and feasibility testing of patch-based lesion predictions
  - Evaluation of MM Baseline assessment performance (bone segmentation)
  - Evaluation of MM Dynamics' assessment performance (lesion risk prediction)
    * Evaluation of time-independent lesion prediction performance
    * Evaluation of time-dependent lesion hit performance
  - Evaluation of human reader experiment for false positive prediction analysis

6.4.1   Preliminary Experiments regarding Lesion Dynamics

To the timepoint, when the preliminary experiments were set up, no previous approach reported techniques regarding the prediction of bone lesions in MM. The presented experiments in this section test the predictability of bone lesions based on images acquired at a precursor state, if there is a progression pattern encoded in the longitudinal data and if there is a relation between the intensities of a precursor image and future lesion regions. As a first attempt a lesion predictor based on RF is trained using lesion image patches at a precursor state and annotations of subsequent lesion states of the longitudinal dataset observed. An important prerequisite is the accurate longitudinal alignment of subsequent examination time points of a patient. First it was decided to investigate a lesion predictor based on a random forest classifier, since its setup, parametrisation and evaluation is simpler compared to deep architectures.
The experiments are designed for two different lesion types: (1) *Emerging lesions* (lesion

type LT_E) are defined as lesions that are not annotated in the source image of prediction while (2) *growing lesions* (LT_G) are already visible at the source time point.

Results T1 wb-MRI

For every patient image patches at lesion regions are extracted longitudinally over subsequent states. Three different patch sizes ($10 \times 4 \times 10$, $20 \times 4 \times 20$ and $30 \times 4 \times 30$ voxels with a voxelspacing of 1.302 mm $\times$ 6 mm $\times$ 1.302 mm) are observed for the evaluation of the prediction performance. To obtain a higher number of patches for the predictor training, data augmentation is performed [123]. The obtained results are summarized in Table 6.2 and an visual example is illustrated in Figure 6.19.

Table 6.2: Summary results patch-based lesion prediction performance

Lesion Type	Patch Size	Mean AUC Region 1	Mean AUC Region 2
Emerging	10 x 4 x 10	0.7425	0.769
	20 x 4 x 20	0.7003	0.7144
	30 x 4 x 30	0.6739	0.6874
Growing	10 x 4 x 10	0.7607	0.7221
	20 x 4 x 20	0.7104	0.7491
	30 x 4 x 30	0.6976	0.7096
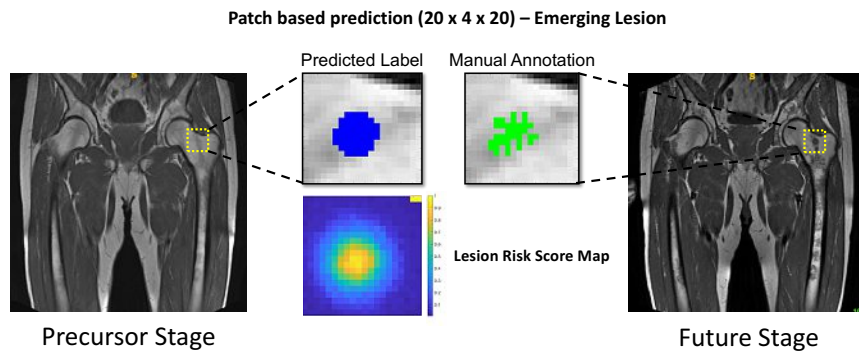
Figure 6.19: Visualisation of preliminary experiment results: a patch based risk prediction of focal lesion emergence is visualised for pelvic/superior legs body region [123].

Results T2 wb-MRI

For every patient image patches at lesion regions are extracted longitudinally over subsequent states. Three different patch sizes ($8 \times 4 \times 8$, $16 \times 4 \times 16$ voxels with a voxelspacing of 1.302 mm $\times$ 6 mm $\times$ 1.302 mm) are observed for the evaluation of the prediction performance in T2-weighted wb-MRI. To obtain a higher number of patches

for the predictor training, data augmentation is performed [122]. The obtained results are summarized in Table 6.3 and an visual example is illustrated in Figure 6.20.

Patch based prediction (16 x 4 x 16) – Growing Lesion
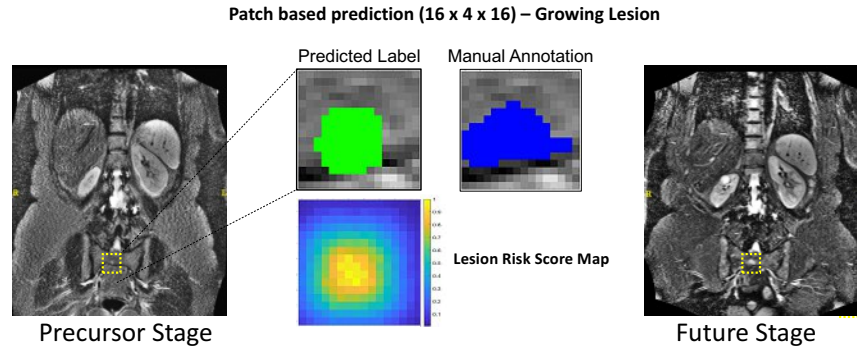
Figure 6.20: Visualisation of preliminary experiment results: a patch based risk prediction result for focal lesion growth is visualised for the thorax/abdomen body region [122].

Table 6.3: Summary results

Lesion Type	Patch Size	Mean AUC
Emerging	8 x 4 x 8	0.904146
	16 x 4 x 16	0.8887
Growing	8 x 4 x 8	0.72949
	16 x 4 x 16	0.89803

Discussion Preliminary Prediction Analysis

The reported preliminary results on image patches using T1 weighted wb-MRI [123] and T2 weighted wb-MRI images [122] lead to the conclusion, that lesions are predictable based on image-patches by the proposed training strategy. The results depend on the chosen patch size and improve with its decrease. In Figure 6.19 and 6.20 patch based risk prediction examples are visualised. On the left side the intensity image at a precursor state is visualised, while on the right the image of a future time point of the same patient is shown. The patch-based lesion risk as well as the corresponding predicted label (obtained by thresholding (0.5)) and corresponding manual annotation of a future lesion is presented. It is observable that the predicted label lies in the lesion region, but since prediction of future evolution on a precursor image is performed, an exact overlap between annotation and predicted label is hardly achievable.

6.4.2   Methodology

In the proposed STM for focal lesion risk prediction, the corresponding task is treated as a mapping from a T1-weighted wb-MRI volume at timepoint t_0 to a lesion risk

map obtained from a future time point t_i, where $t_i > 0$ years. For every observed volume, risk scores are assigned in a voxel-wise way, encoding the region specific risk to evolve towards a focal lesion at a defined timepoint t_i in the future. Preliminary experiments show that a patch-based prediction of focal lesion risk is feasible [123][122], but the method's performance decreases with increasing patch size and the network's training and prediction fails completely on whole body images according to the high disbalance between image size and lesion size. Under consideration of the thesis' concept, a novel network architecture is created. The proposed architecture called **Asymmetric Cascaded Conditioned U-Net**, is visualised in detail in Figure 6.21. In this setup
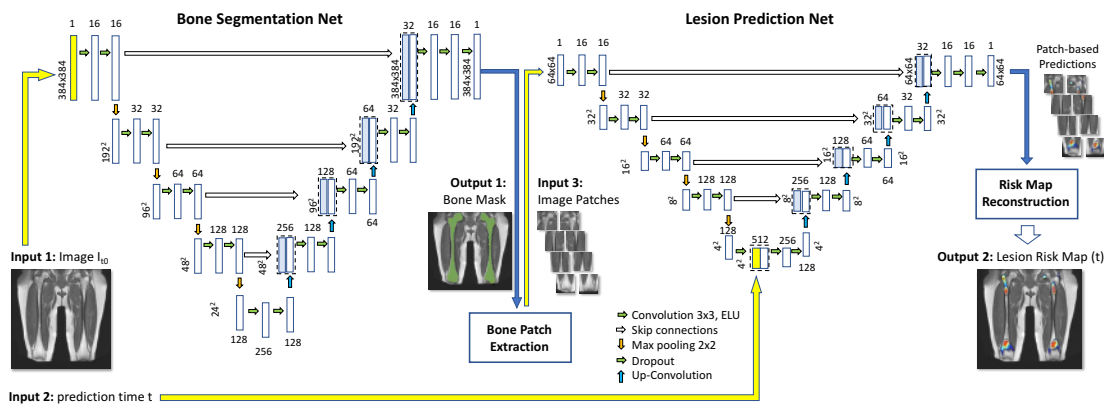
Figure 6.21: Asymmetric Cascade Conditioned U-Net Architecture. The proposed framework consists of a bone segmentation network and a cascaded lesion prediction network, which provides lesion risk maps parametrisable by the prediction time [best viewed in color].

the prediction process is divided into the process of (1) baseline extraction for prediction (finding the bone structure using a *Bone Segmentation Net*) and (2) in predicting the dynamics based on image patches extracted within the baseline (Lesion Risk Prediction within the bone regions using a *Lesion Prediction Net*). This strategy enables the patch-based predictions on the one hand, and forces the network to focus on the prediction on bone regions on the other hand. This strategy reduces computational costs, by decreasing the number of patches observed and the possible regions of false positive prediction, which is a core challenge in this disbalanced setup of focal lesion size and image size. The output of the framework is a voxel-wise wb-MRI risk map, which is obtained by fusing the patch-based predictions. The architecture is referred to be asymmetric, since it consists of two networks, which are configured, trained and parametrized differently and interact in a cascaded way. Additionally, in this approach image based data as well meta data (prediction time) is used in a combined way, to be able to condition the risk estimates on a specific time point in the future.

Data Preprocessing

The training procedure of the asymmetric conditioned cascade network is performed separately for the Bone Segmentation Network and the Lesion Prediction Network. As a prerequisite for the training of both networks images $I_p(t)$ of a patient $p \in \{1, \dots, M\}$ are bias field corrected and subsequently longitudinally aligned over all $t \in \{t_1, \dots, t_{N_p}\}$ acquisition time points. Therefore, the follow-up images for each patient $I_p(t_i)$ are registered to the image $I_p(t_0)$ at the initial examination time points. The aligned image $\overline{I}_p(t_i)$ is obtained following a two step registration procedure (cf. Equation 6.28), where first a rigid alignment R is performed, followed by an affine alignment A. After the longitudinal registration images $\overline{I}_p(t_i)$ of one patient correspond to that at time point t_0 including corresponding bone masks $\overline{B}_p(t_i)$, lesion annotations $\overline{S}_p(t_i)$ where $i > 0$.

$$\overline{I}_p(t_i) = I_p(t_i) \circ A(R(I_p(t_i), I_p(t_0))) \tag{6.28}$$

In the following sections the denotion of registered images will be without an overline.

Network Configurations

The *Bone Segmentation Net* requires as input a 2D intensity image $I \in \mathbb{R}^{384 \times 384}$, i.e. the risk prediction of wb-MRI volumes is performed slice-wise. The output of the Bone Segmentation Net is a bone region prior $B^{pr} \in \mathbb{R}^{384 \times 384}$. For segmenting the bone structures a U-Net architecture [187] is configured with exponential linear units as activation function after the convolutional layers and a sigmoid function as output activation function. The Bone Segmentation Net is trained using a datasets T_1:$\{I_p, B_p^{tr}\}$, which consists of preprocessed images I_p of a patient p and corresponding manual annotated bone masks B_p^{tr} by a trained radiologist. The network's training is performed using an Adam optimizer and by minimizing a binary cross entropy loss function, as introduced in Equation 6.29, where b_j^{tr} denotes the true label and b_j^{pr} the predicted label at image position $j = \{1, \dots, J\}$.

$$\mathcal{L} = -\frac{1}{J} \sum_{j=1}^{J} b_j^{tr} log(b_j^{pr}) + (1 - b_j^{tr}) log(1 - b_j^{pr}) \tag{6.29}$$

The *Lesion Prediction Network* requires as input 2D image patches $Z \in \mathbb{R}^{64 \times 64}$ (spacing $1.302mm \times 1.302mm$) extracted within the bone regions of the input image $I(t_0)$. Bone region priors are used for patch extraction, using the obtained bone masks in a dilated form. An additional input for this network is a scalar value encoding how far into the future (in years) the prediction should be performed. The Lesion Prediction Net is configured as a U-Net similar to the Bone Segmentation Net with exponential linear units after the convolutional layers and sigmoid activation functions for the output. The difference lies in the loss function, which is minimized with an Adam Optimizer during training, and in the bottleneck layer. This layer lies between the contracting path (decoder) and the upsampling path (encoder) of the U-Net. As shown in Figure 6.21 the

output of the Lesion Prediction Net's contracting path is a $4 \times 4 \times 256$ matrix. For feeding the prediction time t as condition to the Lesion Prediction Network, the corresponding scalar value is replicated to form a matrix of the size $4 \times 4 \times 256$ and concatenated with the decoder's output of the same size. The introduction of the condition in this way is inspired by the work of Wang et al. [232]. The replication of the prediction value and concatenation with the advanced feature map from the deepest decoder layer enables the introduction of the condition as map in a balanced way with the same size of the image feature map. This and the skip connections enable the network to propagate context information obtained from higher resolution decoder layers to the encoder conditioned on the prediction time. In the upsampling stream (encoder) the resolution of the network's output is increased, resulting in a refined reconstruction of the patch-based risk score map. For handling the high imbalance between the amount of non-lesion pixels and lesion pixels (1%) in image patches, a weighted loss function is used, by introducing weighting terms (cf. Equation 6.30) penalizing misclassification of a lesion voxel with a higher loss (w_1) compared to mispredictions in non-lesion voxels (w_0). y_x^{tr} denotes the true label and y_x^{pr} the predicted label at image patch position $x = \{1, \ldots, X\}$.

$$\mathcal{L} = -\frac{1}{X} \sum_{x=1}^{X} w_0 y_x^{tr} log(y_x^{pr}) + w_1 (1 - y_x^{tr}) log(1 - y_x^{pr}) \tag{6.30}$$

The Lesion Prediction Net requires a training data set T_2 of triplets ($T_2 : \{Z_p(t_0), Y_p^{tr}(t_i), t_i\}$) as input, consisting of an intensity image patch $Z_p(t_0)$ at the first acquisition time point t_0 of a patient p and a lesion label patch $Y_p^{tr}(t_i)$ of a future acquisition, and the prediction timepoint t_i in years.

The proposed STM provides for a given input image a Lesion Risk (LR) score $\mathcal{R}$ for every voxel j. For its computation at an image position j for a defined future timepoint t, a subset ω_j of overlaying patches at this position is defined and subsequently the average of the corresponding prediction scores y_x^{pr} is computed (cf. Eq.6.31).

$$\mathcal{R}_j(t) = \frac{1}{|\omega_j|} \sum_{x \in \omega_j} y_x^{pr} \tag{6.31}$$

6.4.3   Evaluation Setup

The evaluation of the STM for focal lesion risk prediction can be divided into two parts. Firstly the performance of the baseline assessment is evaluated and secondly the dynamics' assessment performance of the STM is estimated (cf. Section 6.4.4). The evaluation of this STM proposed is performed using a subset of the *dataset BONE* (cf. Section 4.4 for more details):

- For the *Bone Segmentation Net's* evaluation and training, imaging data and corresponding bone segmentations from 34 patients with 15 thorax/abdomen and 19 pelvic/superior leg acquisitions are used, since annotated bone masks are

provided for those regions. In total the data set used consists of 85 acquisitions (40 thorax/abdomen, 45 pelvic/superior leg) with 2 - 4 longitudinal acquisitions per patient.

- For the *Lesion Prediction Net's* training and evaluation, imaging data and meta-data from 28 patients (thorax/abdomen acquisitions of 13 and pelvic/superior leg acquisitions of 15 patients) of this study are used, which evolved focal bone lesions over the disease's progression time. In total 137 acquisitions (60 thorax/abdomen, 77 pelvic/superior leg) are used with 100 annotated lesions (57 thorax/abdomen, 43 pelvic/superior leg). Two different types of lesions are defined: (1) *Emerging lesions* (lesion type LT_E), which are not annotated in the source image of prediction and (2) *Growing lesions* (LT_G), which are already present at the source time point. In total 40 emerging lesions for the thorax part, 25 for the pelvic/superior leg part and 17 growing lesions (thorax/abdomen) and 18 (pelvic/superior leg) are observed within the dataset. For the patch extraction in total 1000 patches per slice, 30k per volume (30 slices) are extracted. To overcome overfitting towards patches without lesions, balancing is performed to train the network with the same amount of negative (not containing a lesion) and positive (lesion containing) patches.

Leave-one-out cross validation is used in all experiments: Therefore, the dataset is divided into a training and a testset. A testset consists of all images, which correspond to one patient, i.e. for each patient a specific bone segmentation and lesion predictor network is trained, without incorporating its data into the training procedure. This resulted in a total number of 6 different networks trained per patient, containing Bone Segmentation Nets for two different bodyparts, and four Lesion Prediction Networks for predicting two types of lesions in two different body regions. The weights w_0 and w_1 for the weighted cross-entropy-loss term in Equation 6.30 are set to 1.0 and 450.0 respectively, after experimental analysis.

A test run is carried out by first computing a bone segmentation map using the Bone Segmentation Net. A binary bone region mask is obtained by thresholding the segmentation map with 0.5 and dilating it with a kernel of pixel size 8. The dilatation step is performed to fill holes in the computed binary mask and to overcome variations in prediction. In a next step patches are extracted, lesion emergence risk is computed for a given future time point and fused to obtain a risk map. This risk map is further used for computing the evaluation measures.

6.4.4   Evaluation Results

Evaluation of Baseline Assessment Performance
In this experiment the performance of extracting the baseline for the STM proposed is assessed. In this application the baseline is formed by bone regions in wb-MRI. Thus, the segmentation accuracy of these regions is evaluated for the pelvic/abdominal and thorax/superior leg region, by computing the DC between the computed bone masks and manual bone annotations. Results report a mean DC of 0.75 for the femoral/pelvic

region and 0.67 for the thoracic/abdominal region. A visualisation of an example of a computed bone mask is provided in Figure 6.22 for two different bodyparts.
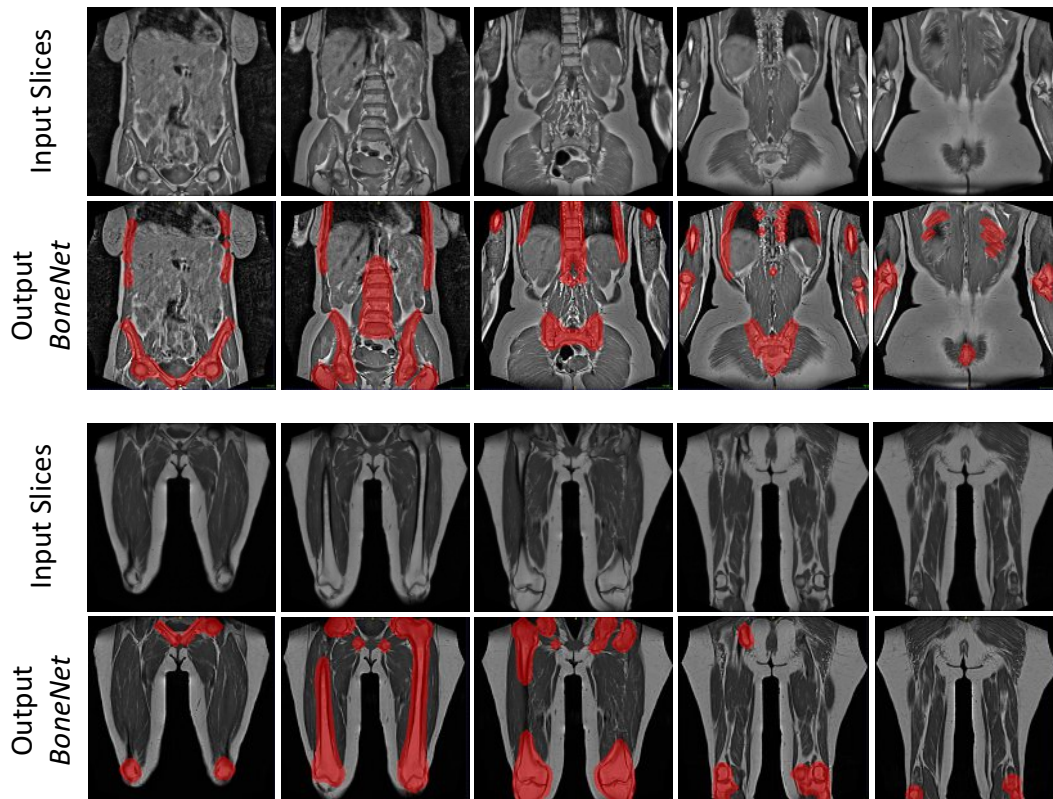
Figure 6.22: Visualisation of the computed baseline bone regions after thresholding and dilatation and corresponding input image slices of the Bone Segmentation Net.

Evaluation of MM Dynamics' Assessment Performance
For evaluating the performance for assessing dynamics in MM for lesion risk prediction, three categories of experiments are designed: (1) the risk prediction performance of focal lesion evolution is analysed, (2) it is evaluated how well the predictions hit the evolving future lesion regions and (3) a specific experiment is created for the analysis of miss-predictions to develop further strategies to improve the results. For the assessment of the general risk, prediction performance of focal lesions to grow or to emerge and risk maps are computed for every acquisition time point of a patients' data.

In the **first experiment** it is investigated, if prediction values within the lesion regions are compared against the values within the bone region, but outside the lesion region. Without considering the prediction time point or lesion evolution time point, for every patient separately, the maximum of voxel-wise prediction values over all time points of a patient are compared inside and outside all lesion regions. For the evaluation of these prediction value differences an independent t-test is performed, which shows significant

$(p < 0.001)$ higher prediction values inside the lesion regions. The results are visualised in Figure 6.23 for the two lesion types evaluated in two different body regions. In a
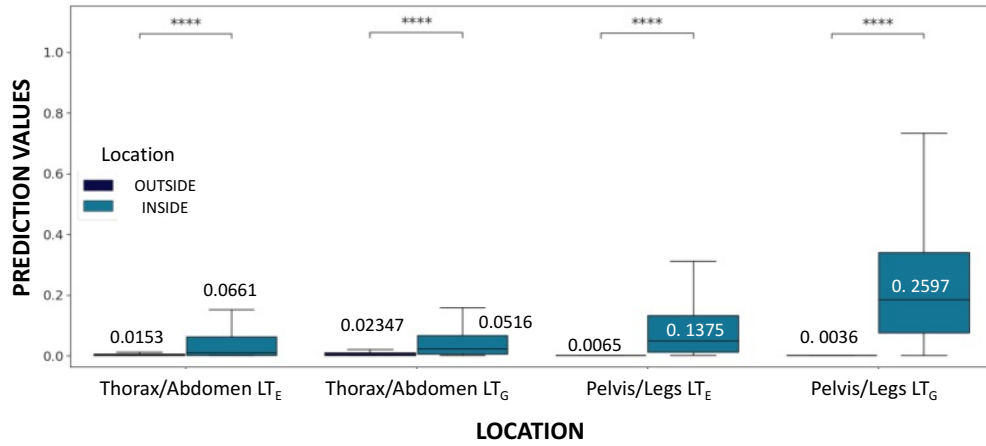
Figure 6.23: Result MM Dynamics Assessment Performance Experiment 1: Boxplot of maximumrisk prediction scores for every patient within the lesion regions and outside these regions within the bone. The visualised numbers denote the mean score of every box plot.

second step for every prediction time point of a patient the AUC is computed using the corresponding computed risk maps and future lesion annotations. Results report a mean AUC between 0.66 for growing lesions in the pelvic/superior-leg region and 0.82 for emerging lesions in the thoracic/abdominal region. The computed ROC-curves for every prediction result are visualised separately in Figure 6.24 for two body regions and lesion types.
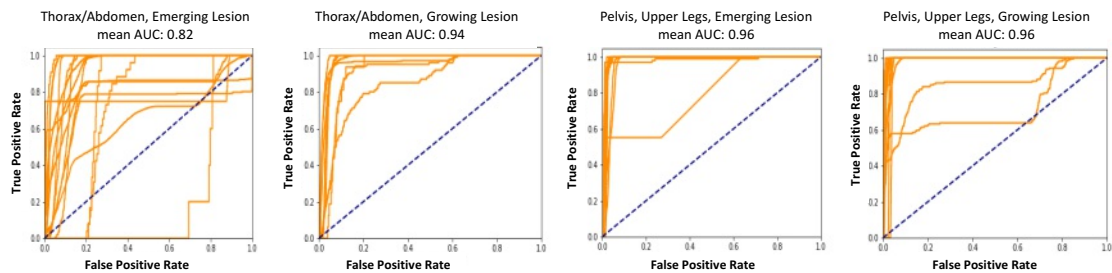
Figure 6.24: ROC curves of prediction scores for every patient are visualised for different body parts and lesion types.

In the **second experiment** the future risk prediction task is evaluated with respect to the performance of hitting future lesion regions with the risk prediction. Since we are evaluating a prediction and not a segmentation task it cannot be expected to obtain a perfect overlay between thresholded risk maps and the manual annotations. Intensity

based information may be missing in the acquisition of the precursor state of the disease and thus the following evaluation scheme is created. Here, the focus lies on estimating the lesion specific sensitivity - further called HitRatio (HR) - which is defined by observing how many voxels are predicted correctly in the lesion region ($HitVoxelNr$) in relation to all voxels in that region $LesionVoxelNr$ (cf. Equation 6.32). A lesion is hit, if the HR is greater than a predefined threshold th_{hit} (cf. Equation 6.33). The threshold is set to 0.01 in this experimental setup and was determined experimentally.

$$HR = \frac{HitVoxelNr}{LesionVoxelNr} \tag{6.32}$$

$$Hit = \begin{cases} 1, & \text{if } HR > th_{hit} \\ 0, & \text{otherwise} \end{cases} \tag{6.33}$$

The results of this experiment are summarized in Table 6.4. The *Ratio* values denote the number of hit lesions in relation to the total number of lesions. *Hit* values list the True Positive (TP) lesion hits, FN the False Negative and FP the False Positive hits. Every experiment was repeated with different thresholds for the lesion risk prediction maps th_{pred} to assess the relation of it to the prediction results. As hypothesized the number of FP predictions increases with decreasing threshold. The emerging as well as growing lesions in the pelvis/legs region are more often hit compared to the thoracic/abdominal region. Emerging lesions have a better hitratio compared to growing lesions. One possible reason is the higher number of emerging lesions in the training set. Additionally, to

Table 6.4: Lesion Hit Evaluation Results

Experiment	Ratio	No. Lesions	Hit	FN	FP	th_{pred}
Thorax/Abdomen - LT_E	0.3659	41	15	26	2300	0.3
Thorax/Abdomen - LT_E	0.2439	41	10	31	1660	0.5
Thorax/Abdomen - LT_E	0.2195	41	9	32	1266	0.7
Thorax/Abdomen - LT_G	0.2353	17	4	13	804	0.3
Thorax/Abdomen - LT_G	0.0588	17	1	16	563	0.5
Thorax/Abdomen - LT_G	0.0000	17	0	17	352	0.7
Pelvis/Legs - LT_E	0.600	25	15	10	603	0.3
Pelvis/Legs - LT_E	0.4400	25	11	14	430	0.5
Pelvis/Legs - LT_E	0.2800	25	7	18	319	0.7
Pelvis/Legs - LT_G	0.5625	16	9	7	421	0.3
Pelvis/Legs - LT_G	0.2500	16	4	12	264	0.5
Pelvis/Legs - LT_G	0.1250	16	2	14	172	0.7

the lesion hit experiment, which is performed for a defined prediction time-point t, it is evaluated, if a false positive hit at this time point converges to a true positive hit at a time point greater or smaller t. This experiment aims at excluding a possible prediction error related to time and tests the potential hit rate in general. Corresponding results of

Table 6.5: Lesion Future Hit Evaluation Results

Experiment	Ratio	No. Lesions	Hit	FN	FP	th_{pred}
Thorax/Abdomen - LT_E	0.3868	106	41	65	2300	0.3
Thorax/Abdomen - LT_E	0.2925	106	31	75	1660	0.5
Thorax/Abdomen - LT_E	0.2170	106	23	83	1266	0.7
Thorax/Abdomen - LT_G	0.2289	83	19	64	804	0.3
Thorax/Abdomen - LT_G	0.0602	83	5	78	563	0.5
Thorax/Abdomen - LT_G	0.000	83	0	83	352	0.7
Pelvis/Legs - LT_E	0.5778	45	26	19	605	0.3
Pelvis/Legs - LT_E	0.400	45	18	27	430	0.5
Pelvis/Legs - LT_E	0.2667	45	12	33	320	0.7
Pelvis/Legs - LT_G	0.5227	44	23	21	419	0.3
Pelvis/Legs - LT_G	0.2273	44	10	34	264	0.5
Pelvis/Legs - LT_G	0.0909	44	4	40	172	0.7

this experiment are summarized in Table 6.5.

In Figure 6.25 a qualitative prediction result for an emerging lesion is visualised. The bone segmentation result is illustrated on the top left, followed by the source image for prediction, the image at time point of prediction with corresponding manual annotation (red) and the source image with the predicted risk map as overlay. Detailed image views are provided, where it is observable, that the prediction of an emerging lesion in the sternum 1.69 years ahead overlays with the manual annotation of the future time-point.

In Figure 6.26 a qualitative prediction result for growing lesions is visualised as well as detailed views on three extracted image patches. Patch A was extracted from a region that was true positively hit by the prediction of focal lesion growth. Patch B and C give detailed views on regions which trigger false positive predictions.

6.4.5 Human Reader Experiment for the Analysis of FP Predictions

In the performed hit analysis experiments a high number of false positive lesion risk predictions are observable. By having a closer look at FP predicted bone regions vs. regions that are manually annotated as focal lesion, similarities between these regions are visible. Patch-based image examples are provided in Figure 6.27 to visualise these observations. Yellow arrows point to regions of focal lesion appearance, classified by medical experts, and yellow circles show regions of false positive risk predictions. According to these results it is hypothesized that bone anomalies trigger false positive prediction. This was the motivation for creating the following experiment to analyse FP risk predictions. The aim is to identify which image regions trigger these results and consequently be able to develop future strategies to overcome these effects. This experiment is performed for every lesion type separately. Therefore, a trained radiologist observes a marked region in an image. In a first run the task is to determine whether a region is of the type normal bone
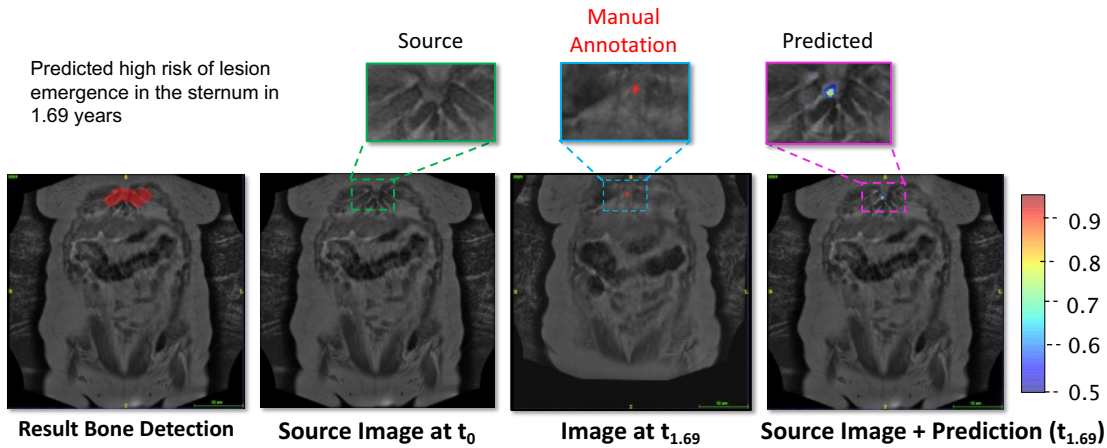
Figure 6.25: Example of a prediction result for an emerging lesion LT_E in the thorax body regions. The prediction source image, the future prediction time point image, the predicted risk map and corresponding image details are visualised [best viewed in color].
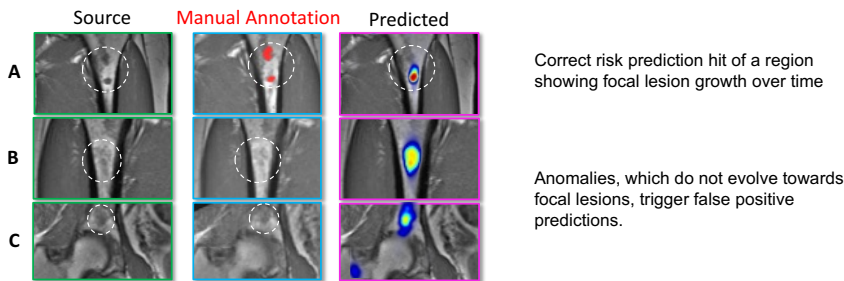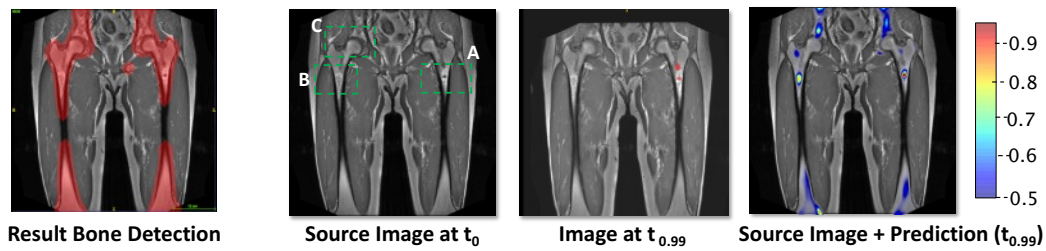
Figure 6.26: Example of prediction results of growing lesions LT_G in the pelvic/sup. legs body region. The prediction source image, the future prediction time point image, the predicted risk map and corresponding image details are visualised [Best viewed in color].

tissue, abnormal bone tissue or no bone tissue. In a second step the abnormal marked samples are sub-categorized into focal lesion, diffuse infiltration or imaging artefact. The information regarding how the region is chosen, is not communicated to the radiologist, to keep the task unbiased towards this detail. Two types of regions are extracted: (1)

121

regions which are false positively predicted to have a risk of focal lesion emergence or growth or (2) regions, which lie within the bone but neither contain focal lesions nor were hit by a FP prediction. For the visualisation of the chosen regions, bounding boxes of different sizes are used. Random sampling is performed to extract 50 examples with FP regions and 50 samples with bone regions from the dataset, for every lesion type each. The radiologist received a document containing the extracted image examples with a random order and a corresponding table, with instruction how to fill out the categories.

The results of this FP analysis experiment are provided in Figure 6.27 on the right side using pie diagrams for visualisation. The ratio of FP regions that are categorized as
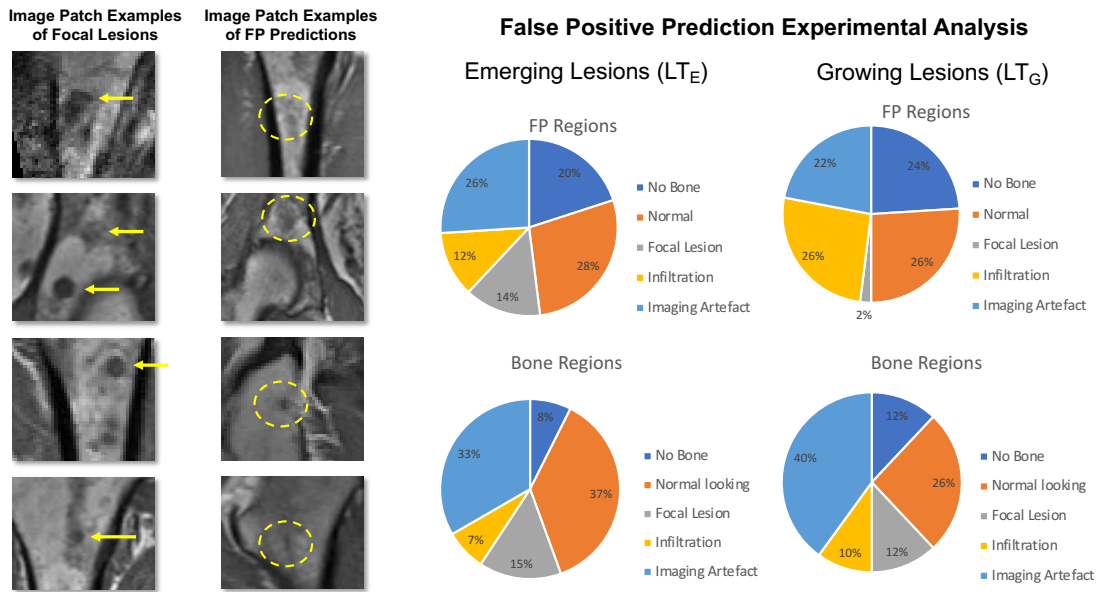
Figure 6.27: Pie diagrams visualising the false positive analysis results. The percentage of present categories in false positive predicted regions (FP Patches) and bone regions that do not contain lesions or false positive predictions (bone patches) are illustrated.

normal bone tissue is similar between LT_E (28%) and LT_G (26%). FP that are triggered by non bone tissue are 20% for LT_E and 24% for LT_G. Since tissue outside the bone region is not included in the training procedure of the *Lesion Prediction Net*, false detected non bone structure by the *Bone Segmentation Net* can lead to false predictions in the subsequent prediction task. Additional sources of an FP trigger are focal lesions that have a smaller diameter than 5 mm. In the training procedure of the *Lesion Prediction Net* only manual lesion annotations $\geq 5mm$ are used, since medical experts followed the guidelines proposed in [180] for this process. It is expected that the focal lesion trigger for LT_E is higher 14% compared to LT_G 2%, since for the training of the LT_G prediction task source images are used, where lesions are already visible. Other triggering factors are diffuse infiltration patterns, which are more a chosen category for FP regions compared

to bone regions. Also around 30% of regions for every setup are categorized as imaging artefact, where most of the regions show hypointense partial volume effects due to the adjacent cortical bone..

6.5   Discussion

In this chapter STMs are presented, which are created following the concept proposed in this thesis, for different dynamic developmental patterns, imaging modalities, populations and applications.

6.5.1   Spatio Temporal Modelling of Fetal Brain DDP

It is demonstrated that a baseline STM of fetal brain DDP is suitable to perform brain tissue segmentation. Geodesic image regression is used to encode the baseline states, by longitudinally modelling the changes of the brain and corresponding baseline variations during the 18th and 30th GW. The advantage is the provision of a time-dependent transformation from a source to a target brain, instead of combining a template building technique and interpolation technique to obtain continuity in time. For the segmentation of a given fetal brain, the alignment with the baseline is performed by registering the atlas-based segmentation to the subject. The fetal specific variations are addressed by segmentation refinement using a graph cut based approach. Within this thesis in the process of creating this STM a novel longitudinal registration scheme is proposed, using separate age ranges for flexible regularisation of the deformation behaviour due to the age range dependent changes. The atlas learned is evaluated using a leave-one-out cross validation approach for every age range and 21 different regularisation kernels are analysed according to their behaviour regarding volume expansion, modelling of cortical surface and Dice similarity to manual annotations. The fetal brain atlas proposed is not capable of modelling the thinning of ventricles from age range 1 to age range 3. Since the proposed method uses one regularisation kernel per age range, geodesic regression is not able to regularise location specific volume expansion and shrinkage at the same time. To overcome this issue, the usage of tissue specific regularisation and consequently the computation of separate ventricle atlases are a possible solution. In contrast to this, the increase of the cortical folding grade and of the volume over time are integrated in the proposed spatio-temporal model. The quality of transformed atlas based segmentations to subject's space using pairwise registration leads to the conclusion that the kernel for pairwise registration has to be defined differently according to the age range and also tissue type, for being able to improve the graph cut initialisation term. Additionally, it is shown that the quality of graph cut labeling is dependent on the initialisation cost term (atlas segmentation) and the penalty term. A false or displaced atlas segmentation hinders as cost term the refinement of the graph cut based labeling. Finally the proposed framework is able to estimate cortex segmentations with a DC up to 0.85 and ventricle segmentations up to 0.60.

6.5.2 Spatio Temporal Modelling of DDP in Childhood Leukaemia

It is demonstrated that the proposed baseline STM of blood cell DDPs is suitable to perform classification of blood cells during leukaemia treatment. An optimal transport scheme for GMM representation of FCM data is proposed to longitudinally encode the changes of baseline (healthy) cell populations over different treatment time points and to obtain a normalized representation of cell clusters of different patients. A novel GMM interpolation strategy is presented by minimizing the WD between GMMs using Expectation Maximization, while preserving that the result lies on the manifold of k-component GMM, to obtain an alignment between baseline timepoints and also the correspondence between Gaussian components. Results suggest that the WD performs best for non-blast identification and data normalization compared to KLD and BB, for a low number of Gaussian mixture components. It is demonstrated that the STM of healthy blood cell clusters can be used to classify baseline cell populations with an f-score of 0.96. This routine is expandable to perform anomaly detection for blast identification of multi-center data and of data from different treatment time points.

6.5.3 Spatio Temporal Modelling of Functional Brain Connectivity DDP

It is demonstrated that the proposed STM of Functional Connectivity DDP is suitable for the assessment of connectivity pattern deviations in developing functional networks. A novel strategy is proposed to estimate possible target regions of reorganisational processes after ischaemic stroke. According to the results it can be concluded that stroke subjects show a higher deviation compared to control subjects, especially more on the hemisphere of stroke location. Control subjects show decreasing deviation over age to age matched controls, with highest changes occurring in the prefrontal cortex and temporal lobe. For the assessment of dynamics with the introduced baseline, a novel score is proposed for the identification of ipsi-lateral and symmetric networks in neighbourhood of the stroke location as possible indicator for reorganisation in developing resting state networks. According to the size of the dataset additional experiments with larger cohorts are required to be able to derive more robust and stable trends in the analysis of these networks. Another challenge is the heterogeneity of the dataset in regard to location and size of stroke regions, age of the subjects and the different duration between stroke event and acquisition time point. However, even with this challenging setup general trends are observable using the STM proposed.

6.5.4 Spatio Temporal Modelling of DDP in MM

It is demonstrated that the proposed STM of DDP in MM is capable of predicting disease progression. A novel approach is presented for the spatio temporal evolution risk prediction of future focal bone lesions. An *asymmetric conditioned cascade network* is developed to mark and assess bone regions of a MM precursor state, if these are at high risk to evolve towards focal lesions. Within this thesis a novel strategy is developed

which divides the prediction task into the process of extracting the bone structure as baseline and into the process of lesion prediction within the region for assessing the underlying dynamics. Here, the STM model concept assists to develop a novel network architecture consisting of two components, while the *Bone Segmentation Net* focuses on the detection of bone in wb-MRI and the cascaded *Lesion Prediction Net* on the patch-based prediction of lesion evolution risk. This strategy assists to overcome the challenges emerging from the high dis-balance between lesion size and image size, and in the increased variability according to possible organ deformation, appearances and tissue contrast. Since focal bone lesions occur only in the bone marrow, the focus is set on extracting the bone tissue first to facilitate the lesion prediction task and to reduce the computational costs, by observing image parts instead of the whole images. This is the first attempt, which is capable of predicting lesions on full volumetric wb-MRI conditioned on the prediction time. The risk prediction of emerging lesions is more challenging compared to the risk prediction of lesion growth, since not every lesion in the future has already dominant imaging markers in a precursor state acquisition. This fact is also mirrored in the evaluation results, where predictions of growing lesions achieve higher evaluation scores compared to emerging lesions. Also the prediction result varies among body parts, where lesions in the extremities and pelvic region are better predicted compared to lesions in the thorax/abdominal region. It is observable, that anomalous bone regions are the main triggers for false positives predictions, which do not progress to lesions.

In this chapter it is demonstrated that the STM concept proposed is applicable in different medical fields and drives the development of new strategies for the comparison, segmentation, classification and prediction of medical data in the image and feature domain. The extraction of baseline-states lead in all applications to a focused investigation of dynamics and disentangled view on these. This lead to improved ability to distinguish between developmental and pathological processes as well as assists in the spatio temporal modelling procedure to find a trade of between modelling the trajectories' variability and patient specific dynamics.

CHAPTER 7

Conclusion

"Remember to look up at the stars and not down at your feet. Try to make sense of what you see and wonder about what makes the universe exist. Be curious. And however difficult life may seem, there is always something you can do and succeed at. It matters that you don't just give up." [Stephen Hawking (1942 - 2018)]

In this thesis a novel concept for the spatio temporal modelling of dynamic developmental patterns is presented, incorporating knowledge from the fields of computer vision, statistics, medical imaging, machine learning and medicine. It was shown how this concept can be used to model different DDPs (fetal brain development, blood cell progression, functional connectivity development, multiple myeloma progression), for different applications (functional connectivity analysis, MRD assessment or morphological modelling) and modalities (flowcytometry, in-utero MRI, rsfMRI and wb-MRI). The growth or age related changes are following a trajectory parallel to the pathological evolution with systemic or time dependent interactions, which makes the specific analysis of age related influences or the relations to pathology induced processes difficult. By breaking down the modelling process in a baseline extraction/trajectory modelling process and a process addressing the dynamics, a disentangled view on data properties is possible in the image but also in the feature domain. This enables the separation of processes, helps to extract a robust and stable observation for reference spaces and assists to address and analyse specific dynamics. The contribution of this thesis spans from novel findings in computer vision but also discovered new approaches and results in the field of medical image analysis.

7.1 Contribution and Novel Findings

The contribution of this thesis in the **Computer Vision** field can be summarized as follows:

127

- A novel diffeomorphic registration scheme for spatio-temporal fetal brain atlas construction is developed as baseline for the proposed automatic segmentation framework. It is shown that geodesic image regression is capable to encode the dynamics of fetal brains over gestation. It was observed that regularization in the longitudinal as well as pairwise registration procedures of fetal brains has to be chosen in dependence of the fetus' age and the tissue type, to be able to address the different interacting developmental dynamics and occurring deformations. Thus, a main focus of future work will lie in the improvement of the labeling procedure, by evaluating age range and tissue dependent regularisation, to improve the quality of graph cut based segmentations. Additionally, a combination of global rigid and local deformable pairwise registration could be analysed for transforming atlas based segmentations to the subject's space as extension. [125] [124].

- A novel semi-supervised representation strategy in combination with a classification framework is developed for high-dimensional data using WGAN based embeddings in combination with a fully connected network. A specific evaluation scenario was created, which use synthetic created small datasets simulating training data of rare disease types. The results show that the proposed framework outperformed both, supervised as well as current state of the art representation/classification frameworks [130].

- A novel alignment strategy is developed for aligning data point clouds robustly by adapting the optimal transport problem for GMM based representations using EM and WD as a metric. The proposed approach preserved that the obtained results by the introduced interpolation scheme lies on the manifold of k-component GMM, to force the alignment between GMMs but also to obtain correspondence between Gaussian components of GMM representations of different datasets. WD metric showed the best results with a small number of components, while KLD showed best results with a higher number of components. This scheme was created to align baseline states of non-leukaemic blood cell clusters represented as GMM. One challenge was the robust alignment of a baseline GMM with a GMM representing a sample containing blast populations. In input samples, where blast components strongly overlaid with non-blast components in the GMM representation, non-blast components of the baseline GMM were put in correspondence with blast components of the input sample. A possible trigger are lower values of the chosen metric in the component wise matching procedure. For future work it is aimed to add additional constraints in the metric computation to avoid this scenario. One option would be to reformulate the GMM one to one component alignment problem as a subgroup component alignment strategy [126].

- A novel deep learning architecture is designed, combining imaging and feature based data, for performing future lesion evolution risk predictions. It is the first attempt to provide a methodology and training strategy to perform time conditioned prediction of future outcome analysis on a voxel-base for wb-MRI. The proposed framework

is capable to learn relations between prediction duration, intensity markers and corresponding regions, to perform region specific predictions, in cases of highly unbalanced data [120] [119]. The limit of this approach lies in the availability of training data and annotations of dynamics, e.g. infiltration patterns or focal lesions smaller five millimetres, which are main triggers of false positive predictions. The main focus of future work lies in incorporating additional annotations in the training procedure as well as combining different modalities to improve the prediction performance by reducing identified false positive triggers.

In the field of **Medical Image Analysis** the following contributions and novel findings can be summarized:

- Within this thesis two novel scores (Connectivity Deviation Score and Reorganisation Score) were developed for the assessment of connectivity pattern deviations in developing functional connectivity networks and for the detection of possible target regions of reorganisational processes after ischaemic stroke. According to the results it was concluded that stroke subjects show a higher deviation from the baseline model compared to control subjects, especially on the hemisphere of stroke location. Control subjects show decreasing deviation over age to age matched controls, with highest changes occurring in the prefrontal cortex and temporal lobe [121].

- It was revealed that the development of the ratio between short-range and long-range functional connectivity in healthy children is substantially different than in children affected by ischaemic stroke [127]. It was observable that a stronger change of short-/long-range connectivity ratio after stroke occured in regions involved in the evolving default mode network as well as initial results indicate asymmetric differences in the ratio between control subjects and stroke patients in regions involved in speech perception. The one-sided-lateralization for language is evident in infancy and increases with age [85][169], and might be linked to these findings [121].

- It was demonstrated that nonleukaemic blood cell features of different leukaemia types are combinable to be used for the training of machine learning approaches, and leading to improved performance of supervised and unsupervised approaches in detecting blasts in AML data. It was discovered that MRD in AML can be estimated on basis of non-blast observations only, which is a huge benefit in the case of rare diseases, where only a limited number of data is available [128].

- It was discovered that MM precursor imaging data encode potential risk markers for symptomatic MM evolution, which can be used for prediction and risk assessment [122][123].

7.2   Reflection and Future Work

The development and evaluation of the spatio-temporal modelling concept proposed in this thesis were driven by the dataset sizes, size of the objects or clusters of interest, representation and appearance of data, available annotations or expert knowledge. The corresponding upcoming challenges and facts can be summarized as follows:

Dataset size: An occurring limitation of spatio temporal modelling approaches, is the requirement of huge time-series or in the best case longitudinal datasets to be able to encode general trends and dependencies over time. Here, the acquisition and study design forms a challenge itself, especially, in studies where patients have to be observed over longer periods, e.g. > 2 years. The traceability of these patients and periodic observation is not always guaranteed, resulting in drop-outs, due to change of the hospital, living situation, death or cure. Another challenging fact, which is also mirrored in longitudinal data of a patient over longer periods, are changing imaging protocols, the effect of treatment change, the shape changes of patients and the positioning of the patient in the scanner and consequently the acquired image snippet. These facts are one limiting factor of dataset sizes, which require accurate alignment and normalization strategies before even starting a spatio temporal modelling process to obtain a robust representation and to reduce the inter- and intra subject variability, which can not be attributed to the developmental dynamics itself. In the recent upcoming trend of using deep learning approaches for diverse applications in the computer vision sector, the availability of data has become essential. While these algorithms show powerful results by being trained on datasets with millions of acquisitions (e.g. ImageNet[1]), these approaches fail in the medical domain, with potential study data set sizes between 20 - 40 cases per study (e.g. with focus on investigating the trajectory of a rare disease). The introduced concept for spatio temporal modelling of dynamic developmental patterns changes the perspective in this procedure from modelling the time-dependent processes with all occurring dynamics at once, to focusing on modelling stable trajectories, extracted from larger cohorts (preferentially controls), and addressing the deviating dynamics of specific cases with the baseline in space, but also over time. Trajectories are encoded in a disentangled way instead of modelling a mean or subject specific trajectory and mixing developmental and disease specific processes over time. A further advantage is the flexibility and extensibility of the developed models, since a well chosen baseline can assist to address a variety of dynamics. For future work a main focus lies on incorporating additional baseline data for the different STMs proposed from additional institutions and repositories and to incorporate additional strategies for assessing specific systemic and time-dependent dynamics.

Object/Cluster of Interest Size: One of the challenges in spatio temporal modelling of DDP is formed by the size of the objects or clusters of interest. Especially, in the medical domain, the size ratio between the region of interest and background/surrounding

---

[1]http://www.image-net.org/[accessed 2021-02-04]

structures can be $< 0.1\%$: e.g. cancer cell populations of 100 cells that have to be detected in late therapy stages in the background of one million cells observed per patient, focal lesion regions' size $< 5mm$ compared to the whole body or bone region size observed in wb-MRI. It was shown that baseline formulations can assist to overcome this challenge by using baselines as region priors, to precisely localise small objects, as priors of distributions, to identify outliers and anomalies, and to be able to compress or limit the observation space, to reduce computational complexity.

Disentanglement & Representation & Normalization A further challenge in spatio temporal modelling is the disentanglement of dynamics from baselines. It was observable, that the disentanglement strongly depends on the measured features and separability of the formed clusters. Especially, in the medical domain features (e.g. anti-body panels) are defined by the standard operating procedure or imaging protocols of a specific study, which are fixed or can only be changed in accordance with clinical requirements. Additionally, even protocols are part of research itself and encode a specific uncertainty. Thus, one focus of this work was to analyse potential representation forms of the data used, to improve the entanglement procedure by computing novel feature and scores, or developing new representation techniques. In all applications and fields observed in this thesis, it is observable that data normalization plays an important role to obtain robust and transferable algorithms. In this thesis techniques for assessing distributional shifts and rigid and non-rigid image deformations were developed. The focus lied on obtaining longitudinal trajectories from data acquired at one institute following a defined protocol. For obtaining generalizability and transferability to clinical routine of the proposed approaches for future work the aim lies to incorporate data from different countries, machines/scanners and diseases and to focus on obtaining machine and country independent data representations.

Preprocessing & Expert Knowledge & Interrater Variability In the spatio temporal modelling procedure an important prerequisite is the establishment of correspondence of structures in space and also over time. The preprocessing and preparation of the data forms a challenge and research field itself. It has to be taken care of how much preprocessing influences the signal/feature appearance itself and to which extent missing or variable expert knowledge influences the spatio temporal model. Unsupervised machine learning techniques give the opportunity to investigate and model the structure of the data without incorporating pre-assumptions. It can assist to extract baselines and reduces the effect of interrater variability in the modelling process. Especially, in the training and evaluation routine of STM, data quality plays an important role. Information which has not been introduced into the training procedure is a potential trigger for false positive predictions, classifications or segmentations.

Prediction Analysis and Evaluation As observed in state of the art approaches predictions are performed regarding the outcome, survival rate or therapy response. In this case statistical tests and outcome analysis provide tools to evaluate the performance

131

of the approaches. In image-based analysis computed label maps are compared to manual annotated label maps, especially in segmentation tasks where the aim is to achieve a perfect overlap. Prediction tasks on image level, especially for precursor stages of a progression pattern, can provide region priors and risk maps, but not exact delineations of future risk regions, since imaging markers may not reflect the complete affected future region at this state. Thus, an alternative evaluation scheme is required to assess image-based prediction performances. The aim of evaluating prediction tasks should lie on estimating the quality of prediction with regard to how well a potential risk region was hit and in time-dependent predictions how accurate the time point of a prediction was hit. In this thesis it was shown that the concept proposed is also applicable to generate a STM for prediction. By the incorporation of baseline states, the prediction's focus could be guided to relevant regions for predictions only, which resulted in reduced computational complexity and disentanglement of training future imaging dependencies (learning the relation of future regions and current imaging markers) and time-specific dependencies (learning imaging markers to detect the baseline of prediction at the observed time point).

List of Figures

136

List of Tables

140

Acronyms

ALL Acute Lymphoblastic Leukaemia. 10, 22, 50, 52, 53, 58, 60, 61, 64, 66, 84, 85, 104, 137

AML Acute Myeloid Leukaemia. 10, 11, 22, 24, 29, 51, 53, 58, 64, 65, 66, 67, 68, 69, 70, 72, 74, 75, 84, 85, 129, 133, 134, 135, 139

AUC Area Under the Curve. 73, 118

BB Bhattacharyya Bound. 37, 38, 42, 107, 108, 124, 139

BOLD Bold Oxygination Level Dependent. 78

CD Cluster of Differentiation. 51, 139

CNN Convolutional Neural Network. 41, 42, 60

CPD Connectivity Pattern Deviation. 98, 99, 100, 101, 102, 136

CSF Cerebro Spinal Fluid. 18

CT Computer Tomography. 1, 12, 41

DC Dice Coefficient. 7, 41, 93, 94, 116, 123

DDP Dynamic Developmental Patterns. xiv, 1, 3, 4, 5, 6, 14, 15, 87, 89, 96, 97, 103, 105, 109, 110, 111, 113, 115, 117, 119, 121, 123, 124, 127, 130

DMN Default Mode Network. 84

DNN Deep Neural Network. 59, 64

EM Expectation Maximization. 32, 61, 65, 107, 108, 128

FCM FlowCytoMetry. 5, 10, 11, 28, 32, 33, 34, 37, 38, 40, 45, 50, 51, 52, 53, 54, 58, 59, 60, 61, 64, 65, 66, 69, 70, 72, 84, 104, 105, 106, 107, 124, 134

fMRI functional Magnetic Resonance Imaging. 1, 8, 27

142

Bibliography

[1] M. Abe. Targeting the interplay between myeloma cells and the bone marrow microenvironment in myeloma. *International Journal of Hematology*, 94(4):334–343, October 2011.

[2] N. Aghaeepour, G. Finak, H. Hoos, T.R. Mosmann, R. Brinkman, R. Gottardo, R.H. Scheuermann, FlowCAP Consortium, DREAM Consortium, et al. Critical assessment of automated flow cytometry data analysis techniques. *Nature methods*, 10(3):228–238, 2013.

[3] K. Akazawa, L. Chang, R. Yamakawa, S. Hayama, S. Buchthal, D. Alicata, T. Andres, D. Castillo, K. Oishi, J. Skranes, T. Ernst, and K. Oishi. Probabilistic maps of the white matter tracts with known associated functions on the neonatal brain atlas: Application to evaluate longitudinal developmental trajectories in term-born and preterm-born infants. *NeuroImage*, 128:167 – 179, 2016.

[4] N.R. Altman and B. Bernal. Clinical applications of functional magnetic resonance imaging. *Pediatric Radiology*, 45(3):382–396, 2015.

[5] A. L. Anderson and M. E. Thomason. Functional plasticity before the cradle: A review of neural functional imaging in the human fetus. *Neuroscience and Biobehavioral Reviews*, 3(9 Pt B):2220–2232, 2013.

[6] V. Anderson, M. Spencer-Smith, and A. Wood. Do children really recover better? Neurobehavioural plasticity after early brain insult. *Brain : a journal of neurology*, 134(Pt 8):2197–221, 2011.

[7] H. Arabi and H. Zaidi. Whole-body bone segmentation from MRI for PET/MRI attenuation correction using shape-based averaging. *Medical Physics*, 43(11):5848–5861, October 2016.

[8] M. Arjovsky, S. Chintala, and B.L. Wasserstein GAN. *arXiv preprint arXiv:1701.07875*, 2017.

[9] J. Ashburner. A fast diffeomorphic image registration algorithm. *NeuroImage*, 38(1):95–113, 2007.

[10] J. Ashburner and K.J. Friston. Diffeomorphic registration using geodesic shooting and Gauss-Newton optimisation. *NeuroImage*, 55(3):954–967, 2011.

[11] J. Ashburner and G.R. Ridgway. Symmetric diffeomorphic modeling of longitudinal structural MRI. *Brain Imaging Methods*, 6:197, 2013.

[12] M. Bach Cuadra, M. Schaer, A. Andre, L. Guibaud, S. Eliez, and J.-Ph. Thiran. Brain tissue segmentation of fetal MR images. In *Workshop on Image Analysis for Developing Brain, in 12th International Conference on Medical Image Computing and Computer Assisted Intervention*, 2009.

[13] G. Balakrishnan, A. Zhao, M. R. Sabuncu, J. Guttag, and A. V. Dalca. Voxelmorph: A learning framework for deformable medical image registration. *IEEE Transactions on Medical Imaging*, 38(8):1788–1800, Aug 2019.

[14] A. Bashashati and R.R. Brinkman. A survey of flow cytometry data analysis methods. *Advances in bioinformatics*, 2009:584603–584603, 2009.

[15] G. Basso, M. Veltroni, M.G. Valsecchi, M.N. Dworzak, R. Ratei, D. Silvestri, A. Benetello, B. Buldini, O. Maglia, G. Masera, et al. Risk of relapse of childhood acute lymphoblastic leukemia is predicted by flow cytometric measurement of residual disease on day 15 bone marrow. *Journal of Clinical Oncology*, 27(31):5168–5174, 2009.

[16] M. Becker and N. Magnenat-Thalmann. Deformable models in medical image segmentation. In N. Magnenat-Thalmann, O. Ratib, and H.F. Choi, editors, *3D Multiscale Physiological Human*, pages 81–106. Springer London, 2014.

[17] L. Bengio, Y.and Yao, G. Alain, and P. Vincent. Generalized Denoising Auto-Encoders as Generative Models, may 2013.

[18] Y. Bengio. Learning deep architectures for AI. *Machine Learning*, 2(1):1–127, 2009.

[19] A. Bhattacharyya. On a measure of divergence between two multinomial populations. *Sankhyā: The Indian Journal of Statistics (1933-1960)*, 7(4):401–406, 1946.

[20] Bing J. and B.C. Vemuri. Robust Point Set Registration Using Gaussian Mixture Models. *IEEE Transactions on Pattern Analysis and Machine Intelligence*, 33(8):1633–1645, August 2011.

[21] C. M. Bishop. *Pattern recognition and machine learning.* Springer, 2006.

[22] D. M. Blei, A. Y. Ng, and M. I. Jordan. Latent Dirichlet Allocation. *Journal of Machine Learning Research*, 3(01):993–1022, January 2003.

[23] F.E. Bloom, M.F. Beal, and D.J. Kupfer. *The Dana Guide to Brain Health a Practical Family Reference from Medical Experts.* Dana; University Presses Marketing [distributor], New York; Bristol, 2006.

[24] D. L. Bolender and S. Kaplan. 3 - basic embryology. In R. A. Polin, S.n H. Abman, D. H. Rowitch, W. E. Benitz, and W. W. Fox, editors, *Fetal and Neonatal Physiology (Fifth Edition)*, pages 23 – 39.e2. Elsevier, 5. edition, 2017.

[25] L. Breiman. Random Forests. *Machine Learning*, 45(1):5–32, 2001.

[26] M. Brett, A. P. Leff, C. Rorden, and J. Ashburner. Spatial normalization of brain images with focal lesions using cost function masking. *NeuroImage*, 14:486–500, 2001.

[27] L. Breysem, H. Bosmans, S. Dymarkowski, D. Van Schoubroeck, I. Witters, J. Deprest, P. Demaerel, D. Vanbeckevoort, C. Vanhole, P. Casaer, and M. Smet. The value of fast MR imaging as an adjunct to ultrasound in prenatal diagnosis. *European Radiology*, 13(7):1538–1548, 2003.

[28] K. Briechle and U.D. Hanebeck. Template matching using fast normalized cross correlation. *Proc. SPIE*, 4387:95–102, 2001.

[29] M. Brüggemann, A. Schrauder, T. Raff, H. Pfeifer, M. Dworzak, O.G. Ottmann, V. Asnafi, A. Baruchel, R. Bassan, Y. Benoit, A. Biondi, H. Cavé, H. Dombret, A.K. Fielding, R. Foà, N. Gökbuget, A.H. Goldstone, N. Goulden, G. Henze, D. Hoelzer, G.E. Janka-Schaub, E.A. Macintyre, R. Pieters, A. Rambaldi, J.-M. Ribera, K. Schmiegelow, O. Spinelli, J. Stary, A. von Stackelberg, M. Kneba, M. Schrappe, and J.J.M. van Dongen. Standardized MRD quantification in European ALL trials: proceedings of the Second International Symposium on MRD assessment in Kiel, Germany, 18-20 September 2008. *Leukemia : official journal of the Leukemia Society of America, Leukemia Research Fund, U.K*, 24(3):521–535, 2010.

[30] S. Budday, P. Steinmann, and E. Kuhl. Physical biology of human brain development. *Frontiers in Cellular Neuroscience*, 9:257, 2015.

[31] M. Cabezas, A. Oliver, X. Lladó, J. Freixenet, and M. Bach Cuadra. A review of atlas-based segmentation for magnetic resonance brain images. *Computer Methods and Programs in Biomedicine*, 104(3):e158–e177, 2011.

[32] B. Casey, N. Tottenham, C. Liston, and S. Durston. Imaging the developing brain: what have we learned about cognitive development? *Trends in Cognitive Sciences*, 9(3):104–110, 2005.

[33] T. Chapman, M. Matesan, E. Weinberger, and D.I. Bulas. Digital atlas of fetal brain MRI. *Pediatric Radiology*, 40(2):153–162, 2009.

[34] M.M. Chen, F.V. Coakley, A. Kaimal, and R.K.Jr Laros. Guidelines for computed tomography and magnetic resonance imaging use during pregnancy and lactation. *Obstetrics & Gynecology August 2008*, pages 333–340, 2008.

[35] Y. Chen, T. T. Georgiou, and A. Tannenbaum. Optimal transport for Gaussian mixture models. *arXiv preprint arXiv:1710.07876*, October 2017.

[36] I. Claude and J.-L. and Sebag, G. Daire. Fetal brain MRI: segmentation and biometric analysis of the posterior fossa. *IEEE transactions on bio-medical engineering*, 51(4):617–626, 2004.

[37] M. Clemence. How to shorten MRI sequences. In D. Prayer, editor, *Fetal MRI*, Medical Radiology, pages 19–32. Springer Berlin Heidelberg, 2011.

[38] L. Clifton, D. A. Clifton, P. J. Watkinson, and L. Tarassenko. Identification of patient deterioration in vital-sign data using one-class support vector machines. In *2011 Federated Conference on Computer Science and Information Systems (FedCSIS)*, pages 125–131, 2011.

[39] D.J.A. Connolly, R. Batty, C. Mooney, D. Jarvis, E. S. Schwartz, and P.D. Griffiths. A Review of Fetal Brain Pathology Acquired In Utero. *Neurographics*, 9(1):79–89, feb 2019.

[40] E.S. Costa, C.E. Pedreira, S. Barrena, Q. Lecrevisse, J. Flores, S. Quijano, J. Almeida, M. del Carmen Garcia-Macias, S. Bottcher, J.J.M. Van Dongen, et al. Automated pattern-guided principal component analysis vs expert-based immunophenotypic classification of b-cell chronic lymphoproliferative disorders: a step forward in the standardization of clinical immunophenotyping. *Leukemia*, 24(11):1927–1933, 2010.

[41] A. J Cowan, C. Allen, A. Barac, H. Basaleem, I. Bensenor, M. P. Curado, K. Foreman, R. Gupta, J. Harvey, H. D. Hosgood, M. Jakovljevic, S. Khader, Y.and Linn, D. Lad, L. Mantovani, V. M. Nong, A. Mokdad, M. Naghavi, M. Postma, G. Roshandel, K. Shackelford, M. Sisay, C.T. Nguyen, T. T. Tran, B. T. Xuan, K. N. Ukwaja, S. E. Vollset, E. Weiderpass, E. N. Libby, and C. Fitzmaurice. Global Burden of Multiple Myeloma: A Systematic Analysis for the Global Burden of Disease Study 2016. *JAMA oncology*, 4(9):1221–1227, September 2018.

[42] U. Creutzig, M. Zimmermann, J.-P. Bourquin, M. N. Dworzak, G. Fleischhack, N. Graf, T. Klingebiel, B. Kremens, T. Lehrnbecher, C. Von Neuhoff, A. Sander, A. Von Stackelberg, J. Star, and D. Reinhardt. Randomized trial comparing liposomal daunorubicin with idarubicin as induction for pediatric acute myeloid leukemia : results from study. *Blood*, 122(1):37–44, 2013.

[43] U. Creutzig, M. Zimmermann, M. N. Dworzak, J. Ritter, G. Schellong, and D. Reinhardt. Development of a curative treatment within the AML-BFM studies. *Klinische Pädiatrie*, 225(SUPPL1):79–86, 2013.

[44] W.R. Crum, T. Hartkens, and D.L.G. Hill. Non-rigid image registration: Theory and practice. *The British Journal of Radiology*, 77 Spec(2):140–153, 2004. PMID: 15677356.

148

[45] P. Dagum and A. Galper. Forecasting sleep apnea with dynamic network models. *Proceedings of the Ninth international conference on Uncertainty in artificial intelligence*, pages 64–71, 1993.

[46] L.R. Dice. Measures of the amount of ecologic association between species. *Ecology*, 26(3):297–302, 1945.

[47] D. A. Dickie, S. D. Shenkin, D. Anblagan, J. Lee, M. Blesa Cabez, D. Rodriguez, J. P. Boardman, A. Waldman, D. E. Job, and J. M. Wardlaw. Whole brain magnetic resonance image atlases: A systematic review of existing atlases and caveats for use in population imaging. *Frontiers in Neuroinformatics*, 11(1):1 – 14, 2017.

[48] J. A. DiGiuseppe, M. D. Tadmor, and D. Pe'er. Detection of minimal residual disease in B lymphoblastic leukemia using viSNE. *Cytometry Part B: Clinical Cytometry*, 88(5):294–304, September 2015.

[49] M. A. Dimopoulos, J. Hillengass, S. Usmani, E. Zamagni, S. Lentzsch, F. E. Davies, N. Raje, O. Sezer, S. Zweegman, J. Shah, A. Badros, K. Shimizu, P. Moreau, C.S. Chim, J. J. Lahuerta, J. Hou, A. Jurczyszyn, H. Goldschmidt, P.r Sonneveld, A. Palumbo, H. Ludwig, M. Cavo, B. Barlogie, K. Anderson, G. D. Roodman, S. V. Rajkumar, B. G.M. Durie, and E. Terpos. Role of Magnetic Resonance Imaging in the Management of Patients With Multiple Myeloma: A Consensus Statement. *Journ. of Clin. Oncology*, 33(6):657–664, February 2015.

[50] G. Doucet, M. Naveau, L. Petit, N. Delcroix, L. Zago, F. Crivello, N. Jobard, G.and Tzourio-Mazoyer, B. Mazoyer, E. Mellet, and M. Joliot. Brain activity at rest: a multiscale hierarchical functional organization. *Journal of Neurophysiology*, 105(6):2753–2763, March 2011.

[51] G. E. Doucet, W. H. Lee, and S. Frangou. Evaluation of the spatial variability in the major resting-state networks across human brain functional atlases. *Human brain mapping*, 40(15):4577–4587, October 2019.

[52] R. O. Duda, P. E. Hart, and D. G. Stork. *Pattern Classification (2nd Edition)*. Wiley-Interscience, New York, NY, USA, 2000.

[53] B. G. M. Durie, R. A. Kyle, A. Belch, W. Bensinger, J. Blade, M. Boccadoro, J. Anthony Child, R. Comenzo, B. Djulbegovic, D. Fantl, G. Gahrton, J. Luc Harousseau, V. Hungria, D. Joshua, H. Ludwig, J. Mehta, A. Rodrique Morales, G. Morgan, A. Nouel, M. Oken, R. Powles, D. Roodman, J. San Miguel, K. Shimizu, S. Singhal, B. Sirohi, P. Sonneveld, G. Tricot, B. Van Ness, and Scientific Advisors of the Intern. Myeloma Foundation. Myeloma management guidelines: a consensus report from the Scientific Advisors of the International Myeloma Foundation. *The Hematology Journal*, 4(6):379–398, 2003.

[54] S. Durrleman, X. Pennec, A. Trouvé, J. Braga, G. Gerig, and N. Ayache. Toward a comprehensive framework for the spatiotemporal statistical analysis of longitudinal shape data. *International Journal of Computer Vision*, 103(1):22–59, May 2013.

[55] M. Dworzak. Minimal residual disease in pediatric acute lymphoblastic leukemia: BFM experience. *Hematología*, 17, October 2013.

[56] M.N. Dworzak, G. Fröschl, D. Printz, G. Mann, U. Pötschger, N. Mühlegger, G. Fritsch, and H. Gadner. Prognostic significance and modalities of flow cytometric minimal residual disease detection in childhood acute lymphoblastic leukemia. *Blood*, 99(6):1952–1958, 2002.

[57] E. Dzierzak and S. Philipsen. Erythropoiesis: development and differentiation. *Cold Spring Harbor perspectives in medicine*, 3(4):a011601, April 2013.

[58] M. Ebner, G. Wang, W. Li, M. Aertsen, P. A. Patel, R. Aughwane, A. Melbourne, T. Doel, A. L. David, J. Deprest, S. Ourselin, and T. Vercauteren. An automated localization, segmentation and reconstruction framework for fetal brain MRI. In A. F. Frangi, J. A. Schnabel, C. Davatzikos, C. Alberola-López, and G. Fichtinger, editors, *Medical Image Computing and Computer Assisted Intervention – MICCAI 2018*, pages 313–320, Cham, 2018. Springer International Publishing.

[59] S.F. Eskildsen, P. Coupé, V. Fonov, J.V. Manjón, K.K. Leung, N. Guizard, S.N. Wassef, L.R. Østergaard, D.L. Collins, and Alzheimer's Disease Neuroimaging Initiative. BEaST: brain extraction based on nonlocal segmentation technique. *NeuroImage*, 59(3):2362–2373, 2012.

[60] K.P. Exarchos, T.P. Exarchos, C. V. Bourantas, M.I. Papafaklis, K.K. Naka, L.K. Michalis, O. Parodi, and D.I. Fotiadis. Prediction of coronary atherosclerosis progression using dynamic Bayesian networks. In *2013 35th Annual International Conference of the IEEE Engineering in Medicine and Biology Society (EMBC)*, pages 3889–3892. IEEE, July 2013.

[61] D.A. Fair, A.L. Cohen, N.U.F. Dosenbach, J.A. Church, F.M. Miezin, D.M. Barch, M.E. Raichle, S.E. Petersen, and B.L. Schlaggar. The maturing architecture of the brain's default network. *Proceedings of the National Academy of Sciences of the United States of America*, 105(10):4028–32, March 2008.

[62] D.A. Fair, A.L. Cohen, J.D. Power, N.U.F. Dosenbach, J.A. Church, F.M. Miezin, B.L. Schlaggar, and S.E. Petersen. Functional brain networks develop from a "local to distributed" organization. *PLoS computational biology*, 5(5):e1000381, May 2009.

[63] G. Ferrazzi, A. N. Price, R. Pedro A. G. Teixeira, L. Cordero-Grande, J. Hutter, A. Gomes, F. Padormo, E. Hughes, T. Schneider, M. Rutherford, M. Kuklisova Murgasova, and J. V. Hajnal. An efficient sequence for fetal brain imaging at 3T with enhanced T1 contrast and motion robustness. *Magnetic resonance in medicine*, 80(1):137–146, 2018.

[64] G. Finak, A. Bashashati, R. Brinkman, and R. Gottardo. Merging mixture components for cell population identification in flow cytometry. *Advances in Bioinformatics*, 2009, 2009.

[65] B. Fischl. FreeSurfer. *Neuroimage*, 62(2), 2012.

[66] B. Fischl, M.I. Sereno, R.B. Tootell, and A.M. Dale. High-resolution intersubject averaging and a coordinate system for the cortical surface. *Human brain mapping*, 8(4):272–84, 1999.

[67] A. Fränzle, J. Hillengass, and R. Bendl. Spinal focal lesion detection in multiple myeloma using multimodal image features. In L. M. Hadjiiski and G. D. Tourassi, editors, *Medical Imaging 2015: Computer-Aided Diagnosis*, volume 9414, page 94143B. International Society for Optics and Photonics, SPIE, March 2015.

[68] G. Gaipa, G. Cazzaniga, M.G. Valsecchi, R. Panzer-Grümayer, B. Buldini, D. Silvestri, L. Karawajew, O. Maglia, R. Ratei, A. Benetello, S. Sala, A. Schumich, A. Schrauder, T. Villa, M. Veltroni, W.-D. Ludwig, V. Conter, M. Schrappe, A. Biondi, M.N. Dworzak, and G. Basso. Time point-dependent concordance of flow cytometry and real-time quantitative polymerase chain reaction for minimal residual disease detection in childhood acute lymphoblastic leukemia. *Haematologica*, 97(10):1582–93, October 2012.

[69] A. Gholipour, A. Akhondi-Asl, J.A. Estroff, and S.K. Warfield. Multi-atlas multi-shape segmentation of fetal brain MRI for volumetric and morphometric analysis of ventriculomegaly. *NeuroImage*, 60(3):1819–1831, 2012.

[70] A. Gholipour, C. K. Rollins, C. Velasco-Annis, A. Ouaalam, A. Akhondi-Asl, O. Afacan, C. M. Ortinau, S. Clancy, C. Limperopoulos, E. Yang, and S. K. Estroff, J. A .and Warfield. A normative spatiotemporal MRI atlas of the fetal brain for automatic segmentation and analysis of early brain growth. *Scientific Reports*, 7(1):476, 2017.

[71] I. Goodfellow, J. Pouget-Abadie, M. Mirza, B. Xu, D. Warde-Farley, S. Ozair, A. Courville, and Y. Bengio. Generative adversarial nets. In *Advances in Neural Information Processing Systems*, pages 2672–2680, 2014.

[72] E. M. Gordon, T. O. Laumann, J. F. Adeyemo, B.and Huckins, W. M. Kelley, and S. E. Petersen. Generation and Evaluation of a Cortical Area Parcellation from Resting-State Correlations. *Cerebral Cortex*, 26(1):288–303, 10 2014.

[73] E.M. Gordon, P.S. Lee, J.M. Maisog, J. Foss-Feig, M.E. Billington, J. Vanmeter, and C.J. Vaidya. Strength of default mode resting-state connectivity relates to white matter integrity in children. *Developmental science*, 14(4):738–51, July 2011.

[74] A.A. Goshtasby. *2-D and 3-D Image Registration: for Medical, Remote Sensing, and Industrial Applications*. Wiley-Interscience A John Wiley & Sons, Inc., Publication, London, 1. edition, 2005.

[75] I. S. Gousias, A. D. Edwards, M. A. Rutherford, S. J. Counsell, J. V. Hajnal, D.Rueckert, and A. Hammers. Magnetic resonance imaging of the newborn brain: Manual segmentation of labelled atlases in term-born and preterm infants. *NeuroImage*, 62(3):1499 – 1509, 2012.

[76] I. S. Gousias, D. Rueckert, R. A. Heckemann, L. E. Dyet, J. P. Boardman, A. D. Edwards, and A. Hammers. Automatic segmentation of brain MRIs of 2-year-olds into 83 regions of interest. *NeuroImage*, 40(2):672 – 684, 2008.

[77] P. Gowland. Safety of fetal MRI scanning. In D. Prayer, editor, *Fetal MRI*, pages 49–54. Springer Berlin Heidelberg, Berlin, Heidelberg, 2010.

[78] M. Greaves. A causal mechanism for childhood acute lymphoblastic leukaemia. *Nature Reviews Cancer*, 18(8):471–484, August 2018.

[79] W.T. Greenough, J.E. Black, and C.S. Wallace. Experience and brain development. *Child Development*, 58(1):539–559, 1987.

[80] M.A. Groen, A.J.O. Whitehouse, N.A. Badcock, and D.V.M. Bishop. Does cerebral lateralization develop? A study using functional transcranial Doppler ultrasound assessing lateralization for language production and visuospatial memory. *Brain and behavior*, 2(3):256–69, May 2012.

[81] I. Gulrajani, F. Ahmed, M. Arjovsky, V. Dumoulin, and A. Courville. Improved training of Wasserstein GANS. *arXiv preprint arXiv:1704.00028*, 2017.

[82] P.A. Habas, K. Kim, J.M. Corbett-Detig, F. Rousseau, O.A. Glenn, A.J. Barkovich, and C. Studholme. A spatiotemporal atlas of MR intensity, tissue probability and shape of the fetal brain with application to segmentation. *NeuroImage*, 53(2):460–470, 2010.

[83] P.A. Habas, K. Kim, F. Rousseau, O.A. Glenn, A.J. Barkovich, and C. Studholme. Atlas-based segmentation of developing tissues in the human brain with quantitative validation in young fetuses. *Human Brain Mapping*, 31(9):1348–1358, 2010.

[84] Y. Hong, Y. Shi, M. Styner, M. Sanchez, and M. Niethammer. Simple geodesic regression for image time-series. In B.M. Dawant, G.E. Christensen, J.M. Fitzpatrick, and D. Rueckert, editors, *Biomedical Image Registration*, number 7359 in Lecture Notes in Computer Science, pages 11–20. Springer Berlin Heidelberg, 2012.

[85] P.R. Huttenlocher. *Neural plasticity : the effects of environment on the development of the cerebral cortex*. Harvard University Press, 2002.

[86] S.J. Hwang, N. Adluru, M.D. Collins, S.N. Ravi, B.B. Bendlin, S.C. Johnson, and V. Singh. Coupled harmonic bases for longitudinal characterization of brain networks. In *Proceedings of the IEEE Conference on Computer Vision and Pattern Recognition*, pages 2517–2525, 2016.

152

[87] H. Inaba, M. Greaves, and C.G. Mullighan. Acute lymphoblastic leukaemia. *Lancet (London, England)*, 381(9881):1943–55, June 2013.

[88] A. J. Izenman. *Modern Multivariate statistical techniques: regression, classification, and manifold learning.* Springer-Publisher New York, 2016.

[89] Hu J., M. Grossberg, and G. Mageras. Survey of recent volumetric medical image segmentation techniques. In C.A. Barros de Mello, editor, *Biomedical Engineering.* InTech, 2009.

[90] M. Jagannathan-Bogdan and L. I. Zon. Hematopoiesis. *Development (Cambridge, England)*, 140(12):2463–7, June 2013.

[91] A. Jakab, E. Schwartz, G. Kasprian, G.M. Gruber, D. Prayer, V. Schöpf, and G. Langs. Fetal functional imaging portrays heterogeneous development of emerging human brain networks. *Front. in Human Neuroscience*, 8:852, 2014.

[92] M. Jenkinson, C.F. Beckmann, T.E.J. Behrens, M.W. Woolrich, and S.M. Smith. FSL. *NeuroImage*, 62(2):782–90, August 2012.

[93] M.V. Johnston. Plasticity in the developing brain: Implications for rehabilitation. *Developmental Disabilities Research Reviews*, 15(2):94–101, 2009.

[94] G. Juliusson, P. Antunovic, A. Derolf, S. Lehmann, L. Möllgård, U. Stockelberg, D.and Tidefelt, A. Wahlin, and M. Höglund. Age and acute myeloid leukemia: real world data on decision to treat and outcomes from the Swedish Acute Leukemia Registry. *Blood*, 113(18):4179–87, April 2009.

[95] K. Kamnitsas, E. Ferrante, S. Parisot, C. Ledig, A. Nori, A. Criminisi, D. Rueckert, and B. Glocker. Deepmedic for brain tumor segmentation. In *MICCAI Brain Lesion Workshop*, October 2016.

[96] M. Karsa, L. Dalla Pozza, N.C. Venn, T. Law, R. Shi, J.E. Giles, A.Y. Bahar, S. Cross, D. Catchpoole, M. Haber, G.M. Marshall, M.D. Norris, and R. Sutton. Improving the identification of high risk precursor B acute lymphoblastic leukemia patients with earlier quantification of minimal residual disease. *PloS one*, 8(10):e76455, January 2013.

[97] K. Kazemi, H. A. Moghaddam, R. Grebe, C. Gondry-Jouet, and F. Wallois. A neonatal atlas template for spatial normalization of whole-brain magnetic resonance images of newborns: Preliminary results. *NeuroImage*, 37(2):463 – 473, 2007.

[98] K. Keraudren, M. Kuklisova-Murgasova, V. Kyriakopoulou, C. Malamateniou, M. A. Rutherford, B. Kainz, J.V. Hajnal, and D. Rueckert. Automated fetal brain segmentation from 2D MRI slices for motion correction. *NeuroImage*, 101:633–643, 2014.

[99]   N. Khalili, N. Lessmann, E. Turk, N. Claessens, R. de Heus, T. Kolk, M.A. Viergever, M.J.N.L. Benders, and I. Išgum. Automatic brain tissue segmentation in fetal MRI using convolutional neural networks. *Magnetic Resonance Imaging*, 64:77 – 89, 2019. Artificial Intelligence in MRI.

[100] H. J. Kim, N. Adluru, M. Banerjee, B. C. Vemuri, and V. Singh. Interpolation on the Manifold of K Component GMMs. In *2015 IEEE International Conference on Computer Vision (ICCV)*, pages 2884–2892. IEEE, December 2015.

[101] A. Klein, J. Warszawski, J. Hillengaß, and K. H. Maier-Hein. Automatic bone segmentation in whole-body CT images. *International Journal of Computer Assisted Radiology and Surgery*, 14(1):21–29, January 2019.

[102] J. K. Kloth, J.s Hillengass, K. Listl, K. Kilk, T. Hielscher, O. Landgren, S. Delorme, H. Goldschmidt, H.-U. Kauczor, and M.-A. Weber. Appearance of monoclonal plasma cell diseases in whole-body magnetic resonance imaging and correlation with parameters of disease activity. *Int. Journ. of Cancer*, 135(10):2380–2386, November 2014.

[103] N. Kohli, S. Ho, S. J. Brown, P. Sawadkar, V. Sharma, M. Snow, and E. García-Gareta. Bone remodelling in vitro: Where are we headed?: -A review on the current understanding of physiological bone remodelling and inflammation and the strategies for testing biomaterials in vitro. *Bone*, 110:38–46, May 2018.

[104] Bryan Kolb and Robbin Gibb. Brain plasticity and behaviour in the developing brain. *Journal of the Canadian Academy of Child and Adolescent Psychiatry = Journal de l'Academie canadienne de psychiatrie de l'enfant et de l'adolescent*, 20(4):265–76, 2011.

[105] S. Kornfeld, J.A. Delgado Rodríguez, R. Everts, A. Kaelin-Lang, R. Wiest, C. Weisstanner, P. Mordasini, M. Steinlin, and S. Grunt. Cortical reorganisation of cerebral networks after childhood stroke: impact on outcome. *BMC neurology*, 15(1):90, January 2015.

[106] A. Kosmala, T. Bley, and B. Petritsch. Imaging of Multiple Myeloma. *RöFo - Fortschritte auf dem Gebiet der Röntgenstrahlen und der bildgebenden Verfahren*, 191(09):805–816, September 2019.

[107] P. K. Kuhl. Brain Mechanisms in Early Language Acquisition. *Neuron*, 67(5):713–727, 2010.

[108] M. Kuklisova-Murgasova, P. Aljabar, L. Srinivasan, S.J. Counsell, V. Doria, A. Serag, I.S. Gousias, J.P. Boardman, M.A. Rutherford, A.D. Edwards, J.V. Hajnal, and D. Rueckert. A dynamic 4D probabilistic atlas of the developing brain. *NeuroImage*, 54(4):2750–2763, 2011.

154

[109] R. A. Kyle and S. V. Rajkumar. Multiple myeloma. *Blood*, 111(6):2962–72, March 2008.

[110] Tarassenko L., Hayton P., Cerneaz N., and Brady M. Novelty detection for the identification of masses in mammograms. In *1995 Fourth International Conference on Artificial Neural Networks*, pages 442–447, 1995.

[111] V. La Corte, M. Sperduti, C. Malherbe, F. Vialatte, S. Lion, T. Gallarda, C. Oppenheim, and P. Piolino. Cognitive Decline and Reorganization of Functional Connectivity in Healthy Aging: The Pivotal Role of the Salience Network in the Prediction of Age and Cognitive Performances. *Front. in Aging Neuroscience*, 8:204, 2016.

[112] L. Lambert, P. Ourednicek, Z. Meckova, G. Gavelli, J. Straub, and I. Spicka. Whole-body low-dose computed tomography in multiple myeloma staging: Superior diagnostic performance in the detection of bone lesions, vertebral compression fractures, rib fractures and extraskeletal findings compared to radiography with similar radiation. *Oncology letters*, 13(4):2490–2494, April 2017.

[113] G. Langs, B. H. Menze, D. Lashkari, and P. Golland. Detecting stable distributed patterns of brain activation using gini contrast. *Neuroimage*, 56(2):497–507, 2011 May 15 2011.

[114] G. Langs, A. Sweet, D. Lashkari, Y. Tie, L. Rigolo, A. J. Golby, and P. Golland. Decoupling function and anatomy in atlases of functional connectivity patterns: language mapping in tumor patients. *NeuroImage*, 103:462–475, December 2014.

[115] M. Leach, M. Drummond, and A. Doig. *Practical Flow Cytometry in Haematology Diagnosis*. John Wiley & Sons, Oxford, April 2013.

[116] K. Van Leemput. Encoding probabilistic brain atlases using bayesian inference. *IEEE Transactions on Medical Imaging*, 28(6):822–837, 2009.

[117] B. Lei, M. Yang, P. Yang, F. Zhou, W. Hou, W. Zou, X. Li, T. Wang, X. Xiao, and S. Wang. Deep and joint learning of longitudinal data for alzheimer's disease prediction. *Pattern Recognition*, 102:107247, 2020.

[118] G. Li, L. Wang, F. Shi, A.E. Lyall, W. Lin, J.H. Gilmore, and D. Shen. Mapping Longitudinal Development of Local Cortical Gyrification in Infants from Birth to 2 Years of Age. *The Journal of Neuroscience*, 34(12):4228–4238, 2014.

[119] R. Licandro, J. Hofmanninger, M. Perkonigg, S. Röhrich, M.-A. Weber, M. Wennmann, L. Kintzele, M. Piraud, B. Menze, and G. Langs. Spatio temporal prediction of future focal bone lesions in multiple myeloma. Submitted September 2020.

[120] R. Licandro, J. Hofmanninger, M. Perkonigg, S. Röhrich, M.-A. Weber, M. Wennmann, L. Kintzele, M. Piraud, B. Menze, and G. Langs. Asymmetric cascade networks for focal bone lesion prediction in multiple myeloma. In *International Conference on Medical Imaging with Deep Learning (MIDL)*, London, GB, 2019.

[121] R. Licandro, J. Hofmanninger, M.-A. Weber, B. Menze, and G. Langs. Assessing Reorganisation of Functional Connectivity in the Infant Brain. In J. Cardoso, T. Arbel, A. Melbourne, H. Bogunovic, P. Moeskops, X. Chen, E. Schwartz, Mona K. Garvin, E. Robinson, E. Trucco, M. Ebner, Y. Xu, A. Makropoulos, A. Desjardin, and T. Vercauteren, editors, *Fetal, Infant and Ophthalmic Medical Image Analysis*, pages 14–24. Springer, Cham, 2017.

[122] R. Licandro, J. Hofmanninger, M.-A. Weber, B. Menze, and G. Langs. Early predictors of bone infiltration in multiple myeloma patients from T2 weighted MRI images. In M. Welk, M. Urschler, and P. M. Roth, editors, *Proceedings of the 42nd Austrian Association for Pattern Recognition (OAGM/AAPR) workshop 2018*, pages 9–12. Verlag der TU Graz, 2018.

[123] R. Licandro, J. Hofmanninger, M.-A. Weber, B. Menze, and G. Langs. Predicting future bone infiltration patterns in multiple myeloma. In B. G. Wenjia, G. Sanroma, B. C. M. Wu, Z. Yiqiang, and C. Pierrick, editors, *Patch-Based Techniques in Medical Imaging*, pages 76–84. Springer, Cham, 2018.

[124] R. Licandro, G. Langs, G. Kasprian, R. Sablatnig, D. Prayer, and E. Schwartz. Longitudinal atlas learning for fetal brain tissue labeling using geodesic regression. In *WiCV Workshop at the IEEE Conference on Computer Vision and Pattern Recogntition (CVPR)*, Las Vegas, U.S., 2016.

[125] R. Licandro, G. Langs, G. Kasprian, R. Sablatnig, D. Prayer, and E. Schwartz. A longitudinal diffeomorphic atlas-based tissue labeling framework for fetal brains using geodesic regression. In V. Štruc L. Čehovin, R. Mandeljc, editor, *21st Computer Vision Winter Workshop 2016*, volume 21, Rimske Toplice, Slovenia, 2016. Slovenian Pattern Recognition Society, Ljubljana 2016.

[126] R. Licandro, K. Miloserdov, R. Reiter, and M. Kampel. GMM interpolation for blood cell cluster alignment in childhood leukaemia. In A. Pichler, P.M. Roth, R. Sablatnig, G. Stúbel, and M. Vincze, editors, *Proceedings of the ARW I& OAGM workshop 2019*, pages 179–182. Verlag der TU Graz, 2019.

[127] R. Licandro, K.-H. Nenning, E. Schwartz, K. Kollndorfer, L. Bartha-Doering, and G. Langs. Changing functional connectivity in the child's developing brain affected by ischaemic stroke. *MICCAI Workshop on Perinatal, Preterm and Paediatric Image Analysis (PIPPI)*, October 2016.

[128] R. Licandro, M. Reiter, M. Diem, M. Dworzak, A. Schumich, and M. Kampel. Application of machine learning for automatic mrd assessment in paediatric acute myeloid leukaemia. In *Proceedings of the 7th International Conference on Pattern Recognition Applications and Methods - Volume 1: ICPRAM,*, pages 401–408. INSTICC, SciTePress, 2018.

[129] R. Licandro, P. Rota, M. Reiter, and M. Kampel. Flow Cytometry based automatic MRD assessment in Acute Lymphoblastic Leukaemia: Longitudinal evaluation of time-specific cell population models. In *2016 14th International Workshop on Content-Based Multimedia Indexing (CBMI)*, pages 1–6. IEEE, June 2016.

[130] R. Licandro, T. Schlegl, M. Reiter, M. Diem, M. Dworzak, A. Schumich, G. Langs, and M. Kampel. Wgan latent space embeddings for blast identification in childhood acute myeloid leukaemia. In *2018 24th International Conference on Pattern Recognition (ICPR)*, pages 3868–3873, August 2018.

[131] F. Liese and I. Vajda. On Divergences and Informations in Statistics and Information Theory. *IEEE Transactions on Information Theory*, 52(10):4394–4412, 2006.

[132] W. Lin, T. Tong, Q. Gao, D. Guo, X. Du, Y. Yang, G. Guo, M. Xiao, M. Du, X. Qu, and The Alzheimer's Disease Neuroimaging Initiative . Convolutional neural networks-based mri image analysis for the alzheimer's disease prediction from mild cognitive impairment. *Frontiers in Neuroscience*, 12:777, 2018.

[133] H. Lippert and T. Deller. *Lehrbuch Anatomie*. Urban & Fischer, Munich, 6. edition, 2003.

[134] Y.-Y. Liu, S. Li, F. Li, L. Song, and J.M. Rehg. Efficient Learning of Continuous-Time Hidden Markov Models for Disease Progression. In *Neural Information Processing Systems Conference*, pages 1–9, Montréal, 2015.

[135] K. Lo, R.R. Brinkman, and R. Gottardo. Automated gating of flow cytometry data via robust model-based clustering. *Cytometry Part A*, 73(4):321–332, 2008.

[136] P. Lorenzen, M. Prastawa, B. Davis, G. Gerig, E. Bullitt, and S. Joshi. Multi-modal image set registration and atlas formation. *Medical Image Analysis*, 10(3):440 – 451, 2006. Special Issue on The Second International Workshop on Biomedical Image Registration (WBIR'03).

[137] M. Lorenzi, G. Ziegler, D.C. Alexander, and S. Ourselin. Efficient gaussian process-based modelling and prediction of image time series. In *International Conference on Information Processing in Medical Imaging*, pages 626–637. Springer International Publishing, 2015.

[138] B. Löwenberg, J. D. Griffin, and M. S. Tallman. Acute myeloid leukemia and acute promyelocytic leukemia. *Hematology / the Education Program of the American Society of Hematology. American Society of Hematology. Education Program*, pages 82–101, January 2003.

[139] E. Lugli, M. Roederer, and A. Cossarizza. Data analysis in flow cytometry: the future just started. *Cytometry. Part A : the journal of the International Society for Analytical Cytology*, 77(7):705–13, July 2010.

[140] B. Luo, R. C. Wilson, and E. R. Hancock. Spectral embedding of graphs. *Pattern Recognition*, 36(10):2213–2230, October 2003.

[141] J.K. Lynch and C.J. Han. Pediatric Stroke - What Do We Know and What Do We Need to Know? *Sem. in Neurology*, 25(4):410–423, 2005.

[142] D. Machado, R.S. Costa, M. Rocha, E.C. Ferreira, B. Tidor, and I. Rocha. Modeling formalisms in Systems Biology. *AMB Express*, 1(1):45, January 2011.

[143] N. Magnenat-Thalmann, H.F. Choi, and D. Thalmann. Towards effective diagnosis and prediction via 3D patient model: A complete research plan. In N. Magnenat-Thalmann, O. Ratib, and H.F. Choi, editors, *3D Multiscale Physiological Human*, pages 3–22. Springer London, 2014.

[144] P.C. Mahalanobis. Reprint of: Mahalanobis, P.C. (1936) "On the Generalised Distance in Statistics.". *Sankhya A*, 80(1):1–7, 2018.

[145] J.B.A. Maintz and M.A. Viergever. A survey of medical image registration. *Medical Image Analysis*, 2(1):1–36, 1998.

[146] A. Makropoulos, P. Aljabar, R. Wright, B. Hüning, N. Merchant, T. Arichi, N. Tusor, J. V. Hajnal, A. D. Edwards, S. J. Counsell, and D. Rueckert. Regional growth and atlasing of the developing human brain. *NeuroImage*, 125:456 – 478, 2016.

[147] D. S. Margulies, S. S. Ghosh, A. Goulas, M. Falkiewicz, J. M. Huntenburg, G. Langs, G. Bezgin, S. B. Eickhoff, F. X. Castellanos, M. Petrides, E. Jefferies, and J. Smallwood. Situating the default-mode network along a principal gradient of macroscale cortical organization. *Proceedings of the National Academy of Sciences of the United States of America*, 113(44):12574–12579, November 2016.

[148] M.-V. Mateos, M.-T. Hernández, P. Giraldo, J. de la Rubia, F. de Arriba, L. L. Corral, L. Rosiñol, B. Paiva, L. Palomera, J. Bargay, A. Oriol, F. Prosper, J. López, J.-M. Arguiñano, N. Quintana, J.-L. García, J. Bladé, J.-J. Lahuerta, and J.-F. S. Miguel. Lenalidomide plus dexamethasone versus observation in patients with high-risk smouldering multiple myeloma (QuiRedex): long-term follow-up of a randomised, controlled, phase 3 trial. *The Lancet. Oncology*, 17(8):1127–1136, 2016.

[149] J. Mazziotta, A. Toga, A. Evans, P. fox, J. Lancaster, K. Zilles, R. Woods, T.Paus, G. Simpson, B. Pike, C. Holmes, L. Collins, P. Thompson, D. MacDonald, M. Iacoboni, T. Schormann, K. Amunts, N. Palomero-Gallagher, S. Geyer, L. Parsons, K. Narr, N. kabani, G. Le Goualher, D. Boomsma, T. Cannon, R. Kawashima, and B. Mazoyer. A probabilistic atlas and reference system for the human brain: International consortium for brain mapping (icbm). *Philosophical Transaction of the Royal Society B*, 356(1412), 2001.

158

[150] M.Breccia, M. Stefania De Propris, C. Minotti, C. Stefanizzi, S. Raponi, G. Colafigli, R. Latagliata, A. Guarini, and R. Foà. Aberrant phenotypic expression of cd15 and cd56 identifies poor prognostic acute promyelocytic leukemia patients. *Leukemia Research*, 38(2):194 – 197, 2014.

[151] M. Merz, T. Hielscher, B. Wagner, S. Sauer, S. Shah, M. S. Raab, A. Jauch, K. Neben, D. Hose, G. Egerer, M.-A. Weber, S. Delorme, H. Goldschmidt, and J. Hillengass. Predictive value of longitudinal whole-body magnetic resonance imaging in patients with smoldering multiple myeloma. *Leukemia*, 28(9):1902–1908, September 2014.

[152] M. Modat, D. M. Cash, P. Daga, G. P. Winston, J. S. Duncan, and S. Ourselin. Global image registration using a symmetric block-matching approach. *Journal of medical imaging (Bellingham, Wash.)*, 1(2):024003, 2014.

[153] M. Mongelli and J. Gardosi. Birth weight, prematurity and accuracy of gestational age. *International Journal of Gynecology & Obstetrics*, 56(3):251–256, 1997.

[154] S. Mueller, D. Wang, M.D. Fox, B.T.T. Yeo, J. Sepulcre, M.R. Sabuncu, R. Shafee, J. Lu, and H. Liu. Individual Variability in Functional Connectivity Architecture of the Human Brain. *Neuron*, 77(3):586–595, 2013.

[155] I. Naim, S. Datta, J. Rebhahn, J.S. Cavenaugh, T.R. Mosmann, and G. Sharma. Swift - scalable clustering for automated identification of rare cell populations in large, high-dimensional flow cytometry datasets, part 1: Algorithm design. *Cytometry Part A*, 85(5):408–421, 2014.

[156] V. Nair and G.E. Hinton. Rectified linear units improve restricted boltzmann machines. In *Proceedings of the 27th international conference on machine learning (ICML-10)*, pages 807–814, 2010.

[157] M. Niethammer, Y. Huang, and F.X. Vialard. Geodesic regression for image time-series. *Medical image computing and computer-assisted intervention: MICCAI International Conference on Medical Image Computing and Computer-Assisted Intervention*, 14(Pt 2):655–662, 2011.

[158] K. Oishi, L. Chang, and H. Huang. Baby brain atlases. *NeuroImage*, 185:865 – 880, 2019.

[159] R. O'Rahilly and F. Müller. Neurulation in the normal human embryo. In CIBA Foundation Symposium, editor, *Neural Tube Defects*, pages 70–82. John Wiley & Sons, Institut für Anatomie und Spezielle Embryologie, Universität Freiburg, Freiburg, Switzerland, 1994.

[160] S. H. Orkin and L. I. Zon. Hematopoiesis: An Evolving Paradigm for Stem Cell Biology. *Cell*, 132(4):631–644, February 2008.

[161] D. Y. Orlova, S. Meehan, D. Parks, W. A. Moore, C. Meehan, Q. Zhao, E. E. B. Ghosn, L. A. Herzenberg, and G. Walther. QFMatch: multidimensional flow and mass cytometry samples alignment. *Scientific Reports*, 8(1):3291, December 2018.

[162] D. Y. Orlova, N. Zimmerman, S. Meehan, C. Meehan, J. Waters, E. E. B. Ghosn, A. Filatenkov, G. A. Kolyagin, Y. Gernez, S. Tsuda, W. Moore, R. B. Moss, L. A. Herzenberg, and G. Walther. Earth mover's distance (EMD): A true metric for comparing biomarker expression levels in cell populations. *PLOS ONE*, 11(3):1–14, March 2016.

[163] E. J. Pauwels and G. Frederix. Image segmentation by nonparametric clustering based on the kolmogorov-smirnov distance. In David Vernon, editor, *Computer Vision — ECCV 2000*, pages 85–99, Berlin, Heidelberg, 2000. Springer Berlin Heidelberg.

[164] N. Pawlowski and B. Jaques, M.and Glocker. Efficient variational Bayesian neural network ensembles for outlier detection, March 2017.

[165] F. Pedregosa, G. Varoquaux, A. Gramfort, V. Michel, B. Thirion, O. Grisel, M. Blondel, P. Prettenhofer, R. Weiss, V. Dubourg, J. Vanderplas, A. Passos, D. Cournapeau, M. Brucher, M. Perrot, and E. Duchesnay. Scikit-learn: Machine learning in Python. *Journal of Machine Learning Research*, 12:2825–2830, 2011.

[166] M. Perkonigg, J. Hofmanninger, B. Menze, M.-A. Weber, and G. Langs. Detecting bone lesions in multiple myeloma patients using transfer learning. In A. Melbourne and R. Licandro et al., editors, *Data Driven Treatment Response Assessment and Preterm, Perinatal, and Paediatric Image Analysis*, pages 22–30, Cham, 2018. Springer International Publishing.

[167] M. A.F. Pimentel, D. A. Clifton, L. Clifton, and L.Tarassenko. A review of novelty detection. *Signal Processing*, 99:215 – 249, 2014.

[168] R. A. Poldrack, J. A. Mumford, and T. E. Nichols. *Handbook of Functional MRI Data Analysis*. Cambridge University Press, 2011.

[169] J. D. Power, D.A. Fair, B.L. Schlaggar, and S.E Petersen. The development of human functional brain networks. *Neuron*, 67(5):735–48, September 2010.

[170] J. D. Power, B. L. Schlaggar, and S. E. Petersen. Recent progress and outstanding issues in motion correction in resting state fMRI. *Neuroimage*, 105:536–551, 2015.

[171] D. M. W. Powers. Evaluation: From precision, recall and f-measure to roc., informedness, markedness & correlation. *Journal of Machine Learning Technologies*, 2(1):37–63, 2011.

[172] M. Prastawa, J.H. Gilmore, W. Lin, and G. Gerig. Automatic segmentation of MR images of the developing newborn brain. *Medical Image Analysis*, 9(5):457–466, 2005.

160

[173] D. Pugash, U. Nemec, P.C. Brugger, and D. Prayer. Fetal MRI of Normal Brain Development. In D. Prayer, editor, *Fetal MRI*, Medical Radiology, pages 147–175. Springer Berlin Heidelberg, 2011.

[174] C.-H. Pui, L.L. Robison, and A.T. Look. Acute lymphoblastic leukaemia. *The Lancet*, 371(9617):1030–1043, 2008.

[175] S. E. Puumala, J. A. Ross, R. Aplenc, and L. G. Spector. Epidemiology of childhood acute myeloid leukemia. *Pediatric blood & cancer*, 60(5):728–33, May 2013.

[176] S. Pyne, X. Hu, K. Wang, E. Rossin, T.-I. Lin, L.M. Maier, C. Baecher-Allan, G.J. McLachlan, P. Tamayo, D.A. Hafler, et al. Automated high-dimensional flow cytometric data analysis. *Proceedings of the National Academy of Sciences*, 106(21):8519–8524, 2009.

[177] J. A. Quinn and C. K. I. Williams. Known unknowns: Novelty detection in condition monitoring. In J. Martí, J. M. Benedí, A. M. Mendonça, and J. Serrat, editors, *Pattern Recognition and Image Analysis*, pages 1–6, Berlin, Heidelberg, 2007. Springer Berlin Heidelberg.

[178] A. Radford, L. Metz, and S. Chintala. Unsupervised representation learning with deep convolutional generative adversarial networks. *arXiv preprint arXiv:1511.06434*, 2015.

[179] G. Rajkowska and P.S. Goldman-Rakic. Cytoarchitectonic Definition of Prefrontal Areas in the Normal Human Cortex: I. Remapping of Areas 9 and 46 using Quantitative Criteria. *Cerebral Cortex*, 5(4):307–322, 1995.

[180] S. V. Rajkumar, M. A. Dimopoulos, A. Palumbo, J. Blade, G. Merlini, M.-V. Mateos, S. Kumar, J. Hillengass, Ef. Kastritis, P. Richardson, O. Landgren, B. Paiva, A. Dispenzieri, B. Weiss, X. LeLeu, S. Zweegman, S. Lonial, L. Rosinol, E. Zamagni, S. Jagannath, O. Sezer, S. Y Kristinsson, J. Caers, S. Z. Usmani, J. J. Lahuerta, H. E. Johnsen, M. Beksac, M. Cavo, H. Goldschmidt, E. Terpos, R. A Kyle, K. C. Anderson, B. G. M. Durie, and J. F. S. Miguel. International Myeloma Working Group updated criteria for the diagnosis of multiple myeloma. *The Lancet Oncology*, 15(12):e538–e548, November 2014.

[181] C. Ramsenthaler, P. Kane, W. Gao, R. J. Siegert, P. M. Edmonds, S. A. Schey, and I. J. Higginson. Prevalence of symptoms in patients with multiple myeloma: a systematic review and meta-analysis. *European Journal of Haematology*, 97(5):416–429, November 2016.

[182] C.E. Rasmussen and C.K.I. Williams. *Gaussian processes for machine learning.* MIT Press, 2006.

[183] M. Reiter, P. Rota, F. Kleber, M. Diem, S. Groeneveld-Krentz, and M. Dworzak. Clustering of cell populations in flow cytometry data using a combination of Gaussian mixtures. *Pattern Recognition*, 60:1029–1040, December 2016.

[184] M. Ringnér. What is principal component analysis? *Nature Biotechnology*, 26:303, March 2008.

[185] L. Risser, F.-X. Vialard, A. Serag, P. Ajabar, and D. Rueckert. Construction of diffeomorphic spatio-temporal atlases using Kärcher means and LDDMM: Application to early cortical development. In *Workshop on Image Analysis of Human Brain Development (IAHBD), in MICCAI International Conference on Medical Image Computing and Computer Assisted Intervention*, 2011.

[186] T. Rohlfing, N. M. Zahr, E. V. Sullivan, and A. Pfefferbaum. The sri24 multichannel atlas of normal adult human brain structure. *Human Brain Mapping*, 31(5):798–819, 2010.

[187] O. Ronneberger, P. Fischer, and T. Brox. U-net: Convolutional networks for biomedical image segmentation. In N. Navab, J. Hornegger, W. M. Wells, and A. F. Frangi, editors, *Medical Image Computing and Computer-Assisted Intervention – MICCAI 2015*, pages 234–241, Cham, 2015. Springer International Publishing.

[188] P. Rota, S. Groeneveld-Krentz, and M. Reiter. On automated flow cytometric analysis for mrd estimation of acute lymphoblastic leukaemia: A comparison among different approaches. In *IEEE International Conference on Bioinformatics and Biomedicine (BIBM)*, November 2015.

[189] P. Rota, S. Groeneveld-Krentz, M. Reiter, F. Kleber, and M. Kampel. The role of machine learning in medical data analysis. a case study: Flow cytometry. In *VISAPP*, February 2016.

[190] P. Rota, M. Reiter, S. Groeneveld-Krentz, and M. Kampel. The role of machine learning in medical data analysis. a case study: Flow cytometry. In *Proceedings of the Internaction Conference on Computer Vision Theory and Applications*, 2016.

[191] F. Rousseau, E. Oubel, J. Pontabry, M. Schweitzer, C. Studholme, M. Koob, and J. Dietemann. BTK: An Open-Source Toolkit for Fetal Brain MR Image Processing. *Computer methods and programs in biomedicine*, 109(1):65–73, 2013.

[192] D. Ruan, J.A. Fessler, M. Roberson, J. Balter, and M. Kessler. Nonrigid registration using regularization that accomodates local tissue rigidity. *Proc. SPIE*, 6144:614412–1–614412–9, 2006.

[193] M. Rubinov and O. Sporns. Complex network measures of brain connectivity: uses and interpretations. *NeuroImage*, 52(3):1059–69, 2010.

[194] J. E. Rubnitz and H. Inaba. Childhood acute myeloid leukaemia. *British Journal of Haematology*, 159(3):259–276, 2012.

[195] S.N. Saleem. Fetal MRI: An approach to practice: A review. *Journal of advanced research*, 5(5):507–23, September 2014.

162

[196] J. Santamaría, O. Cordón, and S. Damas. A comparative study of state-of-the-art evolutionary image registration methods for 3D modeling. *Computer Vision and Image Understanding*, 115(9):1340–1354, 2011.

[197] T. Saul, R. E. Lewiss, and M.D.R. Rivera. Accuracy of emergency physician performed bedside ultrasound in determining gestational age in first trimester pregnancy. *Critical Ultrasound Journal*, 4(1):1–5, December 2012.

[198] J. Scheithe, R. Licandro, P. Rota, M. Reiter, M. Diem, and M. Kampel. Monitoring acute lymphoblastic leukemia therapy with stacked denoising autoencoders. In J. D. Peter, S. L. Fernandes, C. Eduardo Thomaz, and S. Viriri, editors, *Computer Aided Intervention and Diagnostics in Clinical and Medical Images*, pages 189–197, Cham, 2019. Springer International Publishing.

[199] T. Schlegl, P. Seeböck, S. M. Waldstein, U. Schmidt-Erfurth, and G. Langs. Unsupervised anomaly detection with generative adversarial networks to guide marker discovery. *CoRR*, abs/1703.05921, 2017.

[200] T. Schlegl, S.M. Waldstein, W.-D. Vogl, U. Schmidt-Erfurth, and G. Langs. Predicting Semantic Descriptions from Medical Images with Convolutional Neural Networks. In S. Ourselin, D. C. Alexander, C.-F. Westin, and M.J. Cardoso, editors, *Ipmi*, volume 9123, pages 437–448. Springer International Publishing, 2015.

[201] V. Schöpf, G. Kasprian, P.C. Brugger, and D. Prayer. Watching the fetal brain at 'rest'. *International Journal of Developmental Neuroscience*, 30(1):11–17, February 2012.

[202] P. Schulam and S. Saria. A Framework for Individualizing Predictions of Disease Trajectories by Exploiting Multi-Resolution Structure. In C. Cortes Garnett, N.D. Lawrence, D.D. Lee, M. Sugiyama, R. Garnett, and R., editors, *Advances in Neural Information Processing Systems 28*, pages 748—-756. Curran Associates, Inc., 2015.

[203] E. Schwartz, K.-H. Nenning, G. Kasprian, A.-L. Schuller, L. Bartha-Doering, and G. Langs. Multivariate manifold modelling of functional connectivity in developing language networks. In M. Niethammer, M. Styner, S. Aylward, H. Zhu, I. Oguz, P.-T. Yap, and Dinggang Shen, editors, *Information Processing in Medical Imaging*, pages 311–322, Cham, 2017. Springer International Publishing.

[204] J.A. Scott, P.A. Habas, K. Kim, V. Rajagopalan, K.S. Hamzelou, J.M. Corbett-Detig, A.J. Barkovich, O.A. Glenn, and C. Studholme. Growth trajectories of the human fetal brain tissues estimated from 3D reconstructed in utero MRI. *International Journal of Developmental Neuroscience*, 29(5):529–536, 2011.

[205] N. M. Sepahvand, T. Hassner, D. L. Arnold, and T. Arbel. Cnn prediction of future disease activity for multiple sclerosis patients from baseline mri and lesion labels. In A. Crimi, S. Bakas, H. Kuijf, F. Keyvan, M. Reyes, and T. van Walsum, editors,

Brainlesion: Glioma, Multiple Sclerosis, Stroke and Traumatic Brain Injuries, pages 57–69, Cham, 2019. Springer International Publishing.

[206] J. Sepulcre, H. Liu, T. Talukdar, I. Martincorena, B.T. T. Yeo, and R.L. Buckner. The organization of local and distant functional connectivity in the human brain. *PLoS Computational Biology*, 6(6):1–15, 2010.

[207] A. Serag, P. Aljabar, G. Ball, S.J. Counsell, J.P. Boardman, M.A. Rutherford, A.D. Edwards, J.V. Hajnal, and D. Rueckert. Construction of a consistent high-definition spatio-temporal atlas of the developing brain using adaptive kernel regression. *NeuroImage*, 59(3):2255–2265, 2012.

[208] A. Serag, V. Kyriakopoulou, M.A. Rutherford, A.D. Edwards, J.V. Hajnal, P. Aljabar, S.J. Counsell, J.P. Boardman, and D. Rueckert. A multi-channel 4D probabilistic atlas of the developing brain: Application to fetuse and neonates. *Annals of the BMVA*, 2012(3):1–14, 2012.

[209] F. Shi, A. P. Salzwedel, W. Lin, J. H. Gilmore, and W. Gao. Functional Brain Parcellations of the Infant Brain and the Associated Developmental Trends. *Cerebral Cortex*, 28(4):1358–1368, March 2017.

[210] F. Shi, P.-T. Yap, G. Wu, H. Jia, J. H. Gilmore, W. Lin, and D. Shen. Infant brain atlases from neonates to 1- and 2-year-olds. *PloS one*, 6(4):e18746–e18746, April 2011.

[211] W. R. Shirer, S. Ryali, E. Rykhlevskaia, V. Menon, and M. D. Greicius. Decoding Subject-Driven Cognitive States with Whole-Brain Connectivity Patterns. *Cerebral Cortex*, 22(1):158–165, May 2011.

[212] F.W. Smith, A.H. Adam, and W.D.P. Phillips. NMR imaging in pregnancy. *The Lancet*, 321(8314-8315):61–62, 1983.

[213] S. M. Smith, P. T. Fox, K. L. Miller, D. C. Glahn, P. M. Fox, C. E. Mackay, N. Filippini, K. E. Watkins, R. Toro, A. R. Laird, and C. F. Beckmann. Correspondence of the brain's functional architecture during activation and rest. *Proceedings of the National Academy of Sciences*, 106(31):13040 LP – 13045, August 2009.

[214] J. C. González Sánchez, M. Magnusson, M. Sandborg, Å. Carlsson Tedgren, and A. Malusek. Segmentation of bones in medical dual-energy computed tomography volumes using the 3D U-Net. *Physica Medica*, 69:241 – 247, 2020.

[215] A. Sotiras, C. Davatzikos, and N. Paragios. Deformable medical image registration: A survey. *IEEE Transactions on Medical Imaging*, 32(7):1153–1190, 2013.

[216] O. Sporns. *Networks of the brain*. MIT Press, 2011.

164

[217] O. Sporns, D. R. Chialvo, M. Kaiser, and C. C. Hilgetag. Organization, development and function of complex brain networks. *Trends in Cognitive Sciences*, 8(9):418 – 425, 2004.

[218] D. Stegner, J. M. M. VanEeuwijk, O. Angay, M. G. Gorelashvili, D. Semeniak, J. Pinnecker, P. Schmithausen, I. Meyer, M. Friedrich, S. Dütting, C. Brede, A. Beilhack, H. Schulze, B. Nieswandt, and K. G. Heinze. Thrombopoiesis is spatially regulated by the bone marrow vasculature. *Nature Communications*, 8(1):127, December 2017.

[219] K. Supekar, M. Musen, and V. Menon. Development of large-scale functional brain networks in children. *PLoS biology*, 7(7):e1000157, July 2009.

[220] J. Talairach and P. Tournoux. *Co-planar Stereotaxic Atlas of the Human Brain: 3-Dimensional Proportional System - an Approach to Cerebral Imaging.* Thieme Medical Publishers, New York, 1. edition, 1988.

[221] E. Terpos, D. Christoulas, M. Gavriatopoulou, and M.A. Dimopoulos. Mechanisms of bone destruction in multiple myeloma. *European Journal of Cancer Care*, 26(6):e12761, November 2017.

[222] M.E. Thomason. Children in Non-Clinical Functional Magnetic Resonance Imaging (fMRI) Studies Give the Scan Experience a "Thumbs Up". *Am J Bioeth.*, 9(1):25–27, 2009.

[223] M.E. Thomason, E.L. Dennis, A.A. Joshi, S.H. Joshi, I.D. Dinov, C. Chang, M.L. Henry, R.F. Johnson, P.M. Thompson, A.W. Toga, G.H. Glover, J.D. Van Horn, and I.H. Gotlib. Resting-state fMRI can reliably map neural networks in children. *NeuroImage*, 55(1):165–75, March 2011.

[224] J. Toedling, P. Rhein, R. Ratei, L. Karawajew, and R. Spang. Automated in-silico detection of cell populations in flow cytometry readouts and its application to leukemia disease monitoring. *BMC bioinformatics*, 7(1):282, 2006.

[225] M. Toews, W. M. Wells, and L. Zöllei. A feature-based developmental model of the infant brain in structural mri. In N. Ayache, H. Delingette, P. Golland, and K. Mori, editors, *Medical Image Computing and Computer-Assisted Intervention – MICCAI 2012*, pages 204–211, Berlin, Heidelberg, 2012. Springer Berlin Heidelberg.

[226] P. Tosi. Diagnosis and treatment of bone disease in multiple myeloma: spotlight on spinal involvement. *Scientifica*, 2013:104546, December 2013.

[227] D.S. Tsze and J.H. Valente. Pediatric stroke: a review. *Emergency medicine international*, 2011:734506, 2011.

[228] L. van der Maaten. Barnes-Hut-SNE. *arXiv*, January 2013.

[229] V. van Unen, T. Höllt, N. Pezzotti, M. J. T. Li, N.and Reinders, E. Eisemann, F. Koning, A. Vilanova, and B. P. F. Lelieveldt. Visual analysis of mass cytometry data by hierarchical stochastic neighbour embedding reveals rare cell types. *Nature Communications*, 8(1):1740, December 2017.

[230] P. Vincent, H. Larochelle, I. Lajoie, Y. Bengio, and P.-A. Manzagol. Stacked denoising autoencoders: Learning useful representations in a deep network with a local denoising criterion. *The Journal of Machine Learning Research*, 11:3371–3408, 2010.

[231] D. Wang, R.L. Buckner, and H. Liu. Functional Specialization in the Human Brain Estimated By Intrinsic Hemispheric Interaction. *Journal of Neuroscience*, 34(37):12341–12352, 2014.

[232] F. Wang, Y. Song, J. Zhang, J. Han, and D. Huang. Temporal unet: Sample level human action recognition using wifi, 2019.

[233] M. Wang and P. Li. A Review of Deformation Models in Medical Image Registration. *Journal of Medical and Biological Engineering*, 39(1):1–17, 2019.

[234] Y. Wang, S.M. Resnick, and C. Davatzikos. Spatio-temporal analysis of brain MRI images using hidden Markov models. *International Conference on Medical Image Computing and Computer-Assisted Intervention (MICCAI)*, 13(Pt 2):160–8, 2010.

[235] N.I. Weisenfeld and S.K. Warfield. Automatic segmentation of newborn brain MRI. *NeuroImage*, 47(2):564–572, 2009.

[236] M. Wennmann, L. Kintzelé, M. Piraud, B. H. Menze, T. Hielscher, J. Hofmanninger, B. Wagner, H.-U. Kauczor, M. Merz, J. Hillengass, G. Langs, and M.-A. Weber. Volumetry based biomarker speed of growth: Quantifying the change of total tumor volume in whole-body magnetic resonance imaging over time improves risk stratification of smoldering multiple myeloma patients. *Oncotarget*, 9(38):25254–25264, 2018.

[237] M. Wilke, S.K. Holland, J.S Myseros, V.J. Schmithorst, and W.S. Ball. Functional magnetic resonance imaging in pediatrics. *Neuropediatrics*, 34(5):225–33, 2003.

[238] R. Wright, V. Kyriakopoulou, C. Ledig, M.A. Rutherford, J.V. Hajnal, D. Rueckert, and P. Aljabar. Automatic quantification of normal cortical folding patterns from fetal brain MRI. *NeuroImage*, 91:21–32, May 2014.

[239] L. Xu, G. Tetteh, J. Lipkova, Y. Zhao, H. Li, P. Christ, M. Piraud, A. Buck, K. Shi, and B. H. Menze. Automated Whole-Body Bone Lesion Detection for Multiple Myeloma on 68 Ga-Pentixafor PET/CT Imaging Using Deep Learning Methods. *Contrast Media & Molecular Imaging*, 2018:1–11, January 2018.

166

[240] H. Xue, L. Srinivasan, S. Jiang, M. Rutherford, A.D. Edwards, D. Rueckert, and J.V. Hajnal. Automatic segmentation and reconstruction of the cortex from neonatal MRI. *NeuroImage*, 38(3):461–477, 2007.

[241] B.T.T. Yeo, F.M. Krienen, J. Sepulcre, M.R. Sabuncu, D. Lashkari, M. Hollinshead, J.L. Roffman, J.W. Smoller, L. Zöllei, J.R. Polimeni, B. Fischl, H. Liu, and R.L. Buckner. The organization of the human cerebral cortex estimated by intrinsic functional connectivity. *Journal of neurophysiology*, 106(3):1125–65, September 2011.

[242] J. Yuan, E. Bae, X.-C. Tai, and Y. Boykov. A continuous max-flow approach to potts model. In K. Daniilidis, P. Maragos, and N. Paragios, editors, *Computer Vision – ECCV 2010*, number 6316 in Lecture Notes in Computer Science, pages 379–392. Springer Berlin Heidelberg, 2010.

[243] H. Zare, P. Shooshtari, A. Gupta, R. R. Brinkman, T.S. Hawley, R.G. Hawley, S.P. Perfetto, P.K. Chattopadhyay, M. Roederer, A. Bashashati, R. Brinkman, D. Klinke, K. Brundage, E. Lugli, M. Roederer, A. Cossarizza, M. Boedigheimer, J. Ferbas, U. Simon, H. Mucha, R. Bruggemann, Q. Zeng, J. Pratt, J. Pak, D. Ravnic, H. Huss, S. Mentzer, R. Scheuermann, Y. Qian, C. Wei, I Sanz, U. Naumann, G. Luta, M Wand, D. Jeffries, I Zaidi, B de Jong, M. Holland, D. Miles, U. Naumann, M. Wand, N. Shulman, M. Bellew, G Snelling, D. Carter, Y. Huang, H. Li, S. Self, M. McElrath, S. De Rosa, F Preffer, D. Dombkowski, C. Pedreira, E Costa, S Barrena, Q Lecrevisse, J. Almeida, J. van Dongen, A Orfao, M.P. Conrad, L. Fu, M Yang, R Braylan, N Benson, L Boddy, M Wilkins, C. Morris, W.G. Finn, K.M. Carter, R Raich, L.M Stoolman, A.O. Hero, S. Pyne, X. Hu, K. Wang, E. Rossin, TI Lin, L.M. Maier, C. Baecher-Allan, G.J. Mclachlan, P. Tamayo, D.A. Hafler, PL De Jager, JP Mesirov, K. Lo, F Hahne, R Brinkman, R Gottardo, G Finak, A. Bashashati, R.R. Brinkman, R. Gottardo, C. Chan, F. Feng, J. Ottinger, D. Foster, M. West, T.B. Kepler, U. von Luxburg, A.Y. Ng, M.I. Jordan, Y. Weiss, A. Azran, Z. Ghahramani, W. Pentney, M Meila, F.R. Bach, M.I. Jordan, U. von Luxburg, M. Belkin, O. Bousquet, L.N. Trefethen, D. Bau, J.K. Cullum, R.A. Willoughby, C. Fowlkes, S. Belongie, F. Chung, J. Malik, K.M. Carter, R. Raich, WG Finn, A.O. Hero, RC Mann, D. Yan, L Huang, M. Jordan, R.I. Kondor, J. Lafferty, T. Biyikoglu, J. Leydold, P.F. Stadler, T. Xiang, S. Gong, N. Biggs, F.R.K. Chung, J. Shi, J. Malik, S.V. Dongen, A.D. Donnenberg, V.S. Donnenberg, M.R. Gil Alterovitz, Roseann Benson, B. Dykstra, D. Kent, M. Bowie, L McCaffrey, M Hamilton, K Lyons, S Lee, R. Brinkman, C. Eaves, G. Baerlocher, I. Vulto, J.G. De, P. Lansdorp, R. Brinkman, M. Gasparetto, S. Lee, A. Ribickas, J. Perkins, W. Janssen, R. Smiley, C. Smith, C. Yeh, B. Hsi, S. Lee, W. Faulk, N. Aghaeepour, A.H. Khodabakhshi, and R.R. Brinkman. Data reduction for spectral clustering to analyze high throughput flow cytometry data. *BMC Bioinformatics*, 11(1):403, 2010.

[244] H. Zare, P. Shooshtari, A. Gupta, and R.R. Brinkman. Data reduction for spectral clustering to analyze high throughput flow cytometry data. *BMC bioinformatics*, 11(1):403, 2010.

[245] J. Zhan, I.D. Dinov, J. Li, Z. Zhang, S. Hobel, Y. Shi, X. Lin, A. Zamanyan, L. Feng, G. Teng, F. Fang, Y. Tang, F. Zang, A.W. Toga, and S. Liu. Spatial–temporal atlas of human fetal brain development during the early second trimester. *NeuroImage*, 82:115–126, 2013.

[246] A.-L. Zhao, K.-N. Shen, J.-N. Wang, L.-Q. Huo, J. Li, and X.-X. Cao. Early or deferred treatment of smoldering multiple myeloma: a meta-analysis on randomized controlled studies. *Cancer management and research*, 11:5599–5611, June 2019.

[247] K. Zilles, N. Palomero-Gallagher, and K. Amunts. Development of cortical folding during evolution and ontogeny. *Trends in Neurosciences*, 36(5):275–284, 2013.

[248] B. Zitová and J. Flusser. Image registration methods: A survey. *Image and Vision Computing*, 21(11):977–1000, 2003.

TU Wien, Institute of Visual Computing and Human-Centered Technology, Computer Vision Lab, Favoritenstraße 9-11/193-1, 1040 Vienna, Austria, https://www.cvl.tuwien.ac.at, +43/1/58801-193179, licandro@cvl.tuwien.ac.at

Medical University of Vienna, Department of Biomedical Imaging and Image-guided Therapy, Computational Imaging Research Lab, Währinger Gürtel 18-20, 1090 Vienna, Austria, https://www.cir.meduniwien.ac.at, +43/1/40400-73724, roxane.licandro@meduniwien.ac.at

ORCID ID: https://orcid.org/0000-0001-9066-4473

Date Prepared: January 31st, 2021

Name: Roxane Licandro

Nationality: Austria, Italy

Place of Birth: Vienna, Austria

Education

09/1999 – 06/2004	General qualification of university entrance	Biomedical Engineering - Electronics	Technologisches Gewerbe Museum (TGM) - Secondary College for Electronics
10/2004 – 09/2006	Non graduated	Human Medicine	Medical University of Vienna
10/2006 – 09/2009	Bachelor of Science (BSc)	Medical Informatics	Technische Universität (TU) Wien
10/2009 – 01/2016	Master of Science (MSc)	Medical Informatics	Technische Universität (TU) Wien
03/2016 – 02/2021	Philosophical Doctorate (PhD)	Medical Computer Vision (Advisor: Martin Kampel and Georg Langs)	Technische Universität (TU) Wien

Faculty Academic Appointments

03/2011 – 07/2011	Teaching Assistant	Institute of Computer Aided Automation	Technische Universität (TU) Wien
10/2011 – 02/2012	Research Assistant	Institute of Computer Graphics and Algorithms, Pattern Recognition Image Processing (PRIP) Lab	Technische Universität (TU) Wien
03/2012 – 07/2015	Teaching Assistant	Institute of Computer Graphics and Algorithms, Computer Graphics (CG)	Technische Universität (TU) Wien
03/2015 – 07/2015	Teaching Assistant	Institute of Computer Aided Automation, Computer Vision Lab (CVL)	Technische Universität (TU) Wien
01/2016 – present	Research Associate	Department of Biomedical Imaging and Image-guided Therapy, Computational Imaging Research (CIR)	Medical University of Vienna
01/2016 – 09/2020	Project Assistant	Institute of Visual Computing and Human-Centered Technology, Computer Vision Lab (CVL)	Technische Universität (TU) Wien
03/2016 – 09/2020	Lecturer	Institute of Visual Computing and Human-Centered Technology, Computer Vision Lab (CVL)	Technische Universität (TU) Wien

10/2020 – present	University Assistant	Institute of Visual Computing and Human-Centered Technology, Computer Vision Lab (CVL)	Technische Universität (TU) Wien

Other Professional Positions

02/2003 – 12/2010	Assistant of Creative Director	Kunsthistorisches Museum (KHM) Wien, photographer's studio	Image processing, database administration, budget calculations, parttime
03/2011 – 12/2011	Software Developer	AGFA Healthcare RIS/PACs	Ultrasound measurement software implementation, parttime
03/2017	Research Fellow	Charité Berlin, Experimental and Clinical Research Center (ECRC)	Development of an automatic MRD assessment approach for flowcytometry data, fulltime
04/2017 – 05/2017	Research Fellow	University Children's Hospital Zurich, Center of MR-Research	Training on paediatric and fetal MR imaging, Computational prae-/post-surgical brain analysis in spina bifida, fulltime
06/2017 – 07/2017	Research Fellow	University College London (UCL), Centre for Medical Image Computing, TIG	Functional connectivity analysis of preterm/term children, Development of motion correction techniques for fetal functional MRI, fulltime

Major Administrative Leadership Positions

Local

2019	Organizing Committee Member	BrainHack Vienna 2019, Medical University of Vienna, Vienna (Austria).
2020	Scientific Committee Member	Medical Imaging Cluster Festival 2020, Medical University of Vienna, Vienna (Austria).

International

2017	Organizing Committee Member	Women in Computer Vision (WiCV) Workshop, held in conjunction with the International Conference on Computer Vision and Pattern Recognition (CVPR) in Honolulu (Hawaii, United States).
2018	Organizing Committee Member	Data Driven Treatment Response Assessment (DATRA) Satellite Event, held in conjunction with the International Conference on Medical Image Computing and Computer Assisted Intervention (MICCAI) in Granada (Spain).
2018 – present	Organizing Committee Member	PerInatal, Preterm and Paediatric Imaging (PIPPI) Satellite Event held in conjunction with MICCAI in Granada (Spain) and Shenzhen (China).

Professional Societies

2016 – present	MICCAI Society	
	11/2016 – 10/2017	Member, MICCAI Student Board Professional Events Officer
	11/2017 – 10/2019	Member, MICCAI Student Board President

	11/2019 – present	Advisory Member, MICCAI Student Board
2017 – present	Marie Curie Alumni Association	Member of the Austrian Chapter
2019 – present	European Society of Radiology	Member

Editorial Activities

- Journal Reviewer:
  Medical Image Analysis, Magnetic Resonance Imaging, Machine Vision and Applications, Journal on Computing and Cultural Heritage, NeuroImage: Clinical, NeuroImage, European Radiology

- Reviewer/Program Committee:

  MICCAI (since 2018), ACCV-AMV2018, ECCV-WiCV 2018, CVPR-WiCV (since 2017), CVWW 2017, MICCAI-FIFFI 2017, MICCAI-RAMBO 2017, CIARP (since 2017), ICCV-WiCV 2018, ICMLA since 2017, ACM MM2020, ICPR 2020, NeurIPS-PreReg2020, IPMI 2021, MICCAI 2021

- Other Editorial Roles

2018	Co-Editor with A. Melbourne, M. DiFranco, P. Rota, M. Gau, M. Kampel, R. Aughwane, P. Moeskops, E. Schwartz, E. Robinson, A. Makropolous	"Data Driven Treatment Response Assessment and Preterm, Perinatal, and Paediatric Image Analysis", Proceedings of the First International Workshop, DATRA 2018 and Third International Workshop, PIPPI 2018, Held in Conjunction with MICCAI 2018, LNCS volume 11076, Springer Cham, Print ISBN 978-3-030-00806-2, DOI: https://doi.org/10.1007/978-3-030-00807-9, September 2018
2019	Co-Editor with Q. Wang, A. Gomez, J. Hutter, K. McLeod, V. Zimmer, O. Zettinig, E. Robinson, D. Christiaens, E. Abaci Turk, A. Melbourne	"Smart Ultrasound Imaging and Perinatal, Preterm and Paediatric Image Analysis", Proceedings of the First International Workshop, SUSI 2019, and 4th International Workshop, PIPPI 2019, Held in Conjunction with MICCAI 2019, LNCS volume 11798, Springer Cham, ISBN: 978-3-030-32874-0, https://doi.org/10.1007/978-3-030-32875-7, October 2019.
2020	Co-Editor with Y. Hu, A. Noble, J. Hutter, S. Aylward, A. Melbourne, E. Abaci Turk, J. Torrents Barrena	"Medical Ultrasound, and Preterm, Perinatal and Paediatric Image Analysis", LNCS volume 12437, Springer International Publishing, ISBN: 978-3-030-60333-5, DOI: https://doi.org/10.1007/978-3-030-60334-2, October 2020

Honors and Prizes

2016	3rd Austrian Biomarker Symposium on Early Diagnostics Best Poster Award 2016	Austrian Institute of Technology	3rd place for outstanding poster presentation
2016	Travel Grant "Doktorandinnen ans Rednerpult"	Faculty of Informatics – TU Wien	
2017	Travel Grant "Doktorandinnen ans Rednerpult"	Faculty of Informatics – TU Wien	
2018	International Conference on Clinical and Medical Image Analysis, Best Paper Award	Karunya Institute of Technology and Sciences, Coimbatore, India	
2018	Micro Travel Grant	Marie Curie Alumni Association	
2019	Team Nomination, Best Lecture Award 2019	TU Wien	

Report of Funded and Unfunded Projects

2012 – 2014	FETALMORPHO Austrian National Bank, 14812 Early-stage Researcher (ESR), PI: Georg Langs Quantitative morphometry of fetal brain development for disease modeling and diagnosis
2016 – 2018	Reorganisation of semantic language brain networks after paediatric stroke Austrian Science Fund (FWF) – KLI544-B27 Early-stage Researcher (ESR), PI: Lisa Bartha-Doering Development of methodologies to assess reorganizational patterns of developing functional connectivity after ischaemic stroke and the influence on semantic language networks.
2016 – 2018	FlowCLUSTER (https://cvl.tuwien.ac.at/project/flowcluster/) ZIT-Life Sciences –1207843 Early-stage Researcher (ESR), PI: Martin Kampel Development of a fully automated, quality assured treatment response assessment in patients with childhood acute myeloid leukaemia based on flowcytometry.
2018 – 2020	DACHMM (https://www.cir.meduniwien.ac.at/projects/dachmm/) Deutsche ForschungsGesellschaft (DFG) and Austrian Science Fund (FWF) – I2714-B31 Early-stage Researcher (ESR), PI: Georg Langs, Bjoern Menze, Marc-André Weber Whole body image analysis for diagnosing patients with monoclonal plasma cell disorders

Training Grants and Mentored Trainee Grants

| 2010 | Academic excellence scholarship
Faculty of Informatics, TU Wien
Graduation of the Master Study Medical Informatics at TU Wien |
| 2017 | Marie-Skłodowska-Curie Fellowship
European Commission, FP7-PEOPLE-2013-IAPP
Early-stage researcher (ESR), PI: Martin Kampel
AutoFLOW: Automation of flow cytometric analysis for quality-assured follow-up assessment to guide curative therapy for acute lymphoblastic leukaemia in children |

Unfunded Current Projects

| 2017 –
present | Fetal4D (https://www.cir.meduniwien.ac.at/projects/fetal4d/)
PI
Development of high-resolution reconstruction and motion correction techniques and corresponding longitudinal functional connectivity analysis strategies for in-utero functional magnetic resonance imaging |
| 2019 –
present | 4D-Paediatric-Functional-BrainAtlas
PI
Development of a spatio temporal model of developing functional connectivity in children |

Report of Local Teaching and Training

Teaching of Students in Courses:

03/2011– 07/2011	Lecture, Object Oriented Modelling, bachelor students	TU Wien
10/2011– 02/2012	Exercise, Introduction to Image Processing, bachelor students	TU Wien, Pattern Recognition and Image Processing Lab
03/2012 – 07/2015	Lecture and Exercise, Introduction to Visual Computing, bachelor students	TU Wien, Computer Graphics Group
03/2015- 07/2015	Exercise, 3D Vision, master students	TU Wien, Computer Vision Lab

03/2016 – present	Excursion, Applications of Computer Vision, master students	TU Wien, Computer Vision Lab
01/2017, 01/2018, 06/2020	Lecture, Deep Learning for Visual Computing, guest lecture, master students	TU Wien, Computer Vision Lab
10/2020 - present	Lecture and Exercise, Computer Vision, master students	TU Wien, Computer Vision Lab
10/2020 - present	Seminar in Computer Vision and Pattern Recognition, master students	TU Wien, Computer Vision Lab
10/2020 - present	Project Medical Computer Vision, master students	TU Wien, Computer Vision Lab
10/2020 - present	Seminar Scientific Research and Writing, bachelor students	TU Wien, Computer Vision Lab

Research Supervisory and Training Responsibilities:

01/2016 – present	Co-Supervision master's thesis	TU Wien, Computer Vision Lab
10/2020 – present	Supervision bachelor's thesis	TU Wien, Computer Vision Lab

Local Invited Presentations

2016	Automatic MRD Assessment in Flow Cytometry of Different Leukaemia Types in Children: An Overview"
	Workshop on the ICT Contribution to the Development of Clinical Applications, TU Wien
2021	Machine Learning Approaches to Detangle Development and Disease from Large Cohorts – a primer; Congress: Ultrasound meets Magnetic Resonance Imaging, Medical University of Vienna, Vienna

Report of Regional, National and International Invited Teaching and Presentations

Regional

2019	Whole-body MRI based Lesion Prediction in Multiple Myeloma (selected oral abstract), European Congress of Radiology (ECR), Vienna

International

2014	Longitudinal Diffeomorphic Fetal Brain Atlas Learning for Tissue Labeling using Geodesic Regression and Graph Cuts / invited presentation
	Institut Universitai de Technologie (IUT), Le Puy-En Velay, Auvergne France
2017	Spatio Temporal Modelling of Developmental Processes / invited presentation
	University Children's Hospital Zurich (UZH), Zurich, Switzerland
2017	Spatio Temporal Assessment of Developing Patterns from Fetal MR Imaging to Flow-cytometry / invited presentation
	Health Tech Lunch, University of Applied Sciences Western Switzerland, Sierre (HES-SO), Switzerland
2017	Spatio Temporal Assessment of Developing Patterns from Fetal MR Imaging to Flow-cytometry / invited presentation
	ETH Zürich, Computer Vision Lab, Zurich, Switzerland
2017	Spatio Temporal Assessment of Developing Patterns: from Fetal MR Imaging to Flow-cytometry / invited presentation
	University College London, Centre of Medical Image Computing, Translational Imaging Group, London, United Kingdom

2019	Mapping Dynamic Developmental Patterns: Precision Medicine Models from Spatio Temporal Data / invited presentation
	King's College London (KCL), London, United Kingdom
2019	Learning Dynamic Models from Spatio Temporal Data / invited presentation
	Zuse Institute Berlin, Berlin, Germany
2020	Machine Learning in Medical Imaging / invited presentation
	Summer School on Image Processing (SSIP2020), Szeged, Hungary

Report of Education of Patients and Service to the Community

| 2020 | Interview on national TV regarding deep learning applications in medicine, Channel ORF1 (Austria), scientific TV show Newton |

Report of Scholarship

ORCID ID: https://orcid.org/0000-0001-9066-4473

Peer-Reviewed Scholarship in print or other media:

Research Investigations

Licandro R., Langs G., Kasprian G., Sablatnig R., Prayer D., Schwartz E., "A Longitudinal Diffeomorphic Atlas-Based Tissue Labeling Framework for Fetal Brains using Geodesic Regression ", Computer Vision Winter Workshop, Rimske Toplice, February 2016, ISBN: 978-961-90901-7-6.

Licandro R., Rota P., Reiter M., Kampel M., „Flow Cytometry Based Automatic MRD Assessment in Acute Lymphoblastic Leukaemia: Longitudinal Evaluation of Time-Specific Cell Population Models", 14th International Workshop on Content-based Multimedia Indexing, Bucharest, June 2016. pp. 1-6, http://doi.org/10.1109/CBMI.2016.7500274.

Licandro R., Nenning K.-H., Schwartz E., Kollndorfer K., Bartha-Doering L., Langs G., "Changing Functional Connectivity in the Child's Developing Brain Affected by Ischaemic Stroke", 1st International Workshop PerInatal, Preterm and Paediatric Image Analysis Workshop (MICCAI - PIPPI), Athens, October 2016. http://pippi.cs.ucl.ac.uk/pippi2016/proceedings.html.

Licandro R., Nenning K.-H, Schwartz E., Kollndorfer K., Bartha-Doering L., Liu H., Langs G., "Assessing Reorganisation of Functional Connectivity in the Infant Brain". In: Cardoso M. et al. (eds) Fetal, Infant and Ophthalmic Medical Image Analysis. FIFI 2017, OMIA 2017. Lecture Notes in Computer Science, vol 10554. Springer, Cham. ISBN: 978-3-319-67560-2, https://doi.org/10.1007/978-3-319-67561-9_2

Licandro R., Reiter M., Diem M., Dworzak M., Schumich A., Kampel M., "Application of Machine Learning for Automatic MRD Assessment in Paediatric Acute Myeloid Leukaemia". 7th International Conference on Pattern Recognition Applications and Methods (ICPRAM), Volume 1: pages 401-408, ISBN 978-989-758-276-9, Funchal Madeira (Portugal), January 2018, https://doi.org/10.5220/0006595804010408

Licandro R., Hofmanninger J., Weber M.-A., Menze B., Langs G., "Early Predictors of Bone Infiltration in Multiple Myeloma Patients from T2 weighted MRI images", Proceedings of the 42nd Austrian Association for Pattern Recognition (OAGM/AAPR) workshop, pages 9-12, Hall in Tyrol (Austria), May 2018, https://doi.org/10.3217/978-3-85125-603-1

Licandro R. and Schlegl T., Reiter M., Diem M., Dworzak M., Schumich A., Langs G., Kampel M., "WGAN Latent Space Embeddings for Blast Identification in Childhood Acute Myeloid Leukaemia", 24th International Conference on Pattern Recognition (ICPR) 2018, Beijing, August 2018. https://doi.org/10.1109/ICPR.2018.8546177

Licandro R., Hofmanninger J., Weber M.-A., Menze B., Langs G., "Predicting Future Bone Infiltration Patterns in Multiple Myeloma", 4th International Workshop on Patch-based Techniques in Medical Imaging (MICCAI Patch-MI 2018), Granada (Spain), September 2018. https://doi.org/10.1007/978-3-030-00500-9

Scheithe J., Licandro R., Rota P., Reiter M., Diem M., Kampel M. "Monitoring Acute Lymphoblastic Leukemia Therapy with Stacked Denoising Autoencoders". In: Peter J., Fernandes S., Eduardo Thomaz C., Viriri S. (eds) Computer Aided Intervention and Diagnostics in Clinical and Medical Images. Lecture Notes in Computational Vision and Biomechanics, vol 31. Springer, Cham, https://doi.org/10.1007/978-3-030-04061-1_19

Licandro R., Miloserdov K., Reiter M., Kampel M., „GMM Interpolation for Blood Cell Cluster Alignment in Childhood Leukaemia", Proceeding of the ARW and OAGM workshop 2019, Steyr (Austria), May 2019. https://doi.org/10.3217/978-3-85125-663-5-39

Sobotka D., **Licandro R.**, Ebner M., Schwartz E., Vercauteren T., Ourselin S., Kasprian G., Prayer D., Langs G., „Reproducibility of Functional Connectivity Estimates in Motion Corrected Fetal fMRI", Smart Ultrasound Imaging and Perinatal, Preterm and Paediatric Image Analysis, LNCS volume 11798, Springer, Cham, ISBN: 978-3-030-32874-0, October 2019. https://doi.org/10.1007/978-3-030-32875-7

Non-peer reviewed scholarship in print or other media:

Proceedings of meetings or other non-peer reviewed scholarship

Langs G., Attenberger U., **Licandro R.**, Hofmanninger J., Perkonigg M., Zusag M., Röhrich S., Sobotka D., Prosch H., "Maschinelles Lernen in der Radiologie: eine Begriffsbestimmung vom Einzelzeitpunkt bis zur Trajektorie" [Machine Learning in Radiology – Terminology from Individual Timepoint to Trajectory], Radiologe, https://doi.org/10.1007/s00117-019-00624-x, January 2020.

Thesis:

Licandro R., 2009, "Asset Management for Luxury Hotels with RFID", Bachelor's thesis, TU Wien, in cooperation with Siemens, Advisor: A. Min Tjoa.
Licandro R., 2016, "Longitudinal Diffeomorphic Fetal Brain Atlas Learning for Tissues Labeling using Geodesic Regression and Graph Cuts", Master's thesis, TU Wien, Vienna (Austria), Advisors: Robert Sablatnig, Georg Langs.
Licandro R., 2021, "Spatio Temporal Modelling of Dynamic Developmental Patterns", PhD thesis, TU Wien, Vienna (Austria), Advisors: Martin Kampel, Georg Langs.

Abstracts, Poster Presentations and Exhibits Presented at Professional Meetings:

Licandro R., Schwartz E., Langs G., Sablatnig R., "Longitudinal Diffeomorphic Fetal Brain Atlas Learning for Tissue Labeling using Geodesic Regression and Graph Cuts", poster, Medical Imaging Summer School (MISS), Favignana, July 2014.
Licandro R., Rota P., Reiter M., Kampel M., "AutoFLOW: A Novel Heuristic Method to Automatically Detect Leukaemic Cells in Flow Cytometric Data", poster presentation, 3rd Austrian Biomarker Symposium on Early Diagnostics, Vienna, March 2016. – Best Poster Award
Licandro R., Langs G., Kampel M., "Spatio Temporal modelling of Dynamic Developmental Patterns", poster, International Computer Vision Summer School (ICVSS), Sicily, July 2016.
Licandro R., Langs G., Kasprian G., Sablatnig R., Prayer D., Schwartz E., "Longitudinal Atlas Learning for Fetal Brain Tissue Labeling using Geodesic Regression", poster, Woman in Computer Vision (WiCV) Workshop at the IEEE Conference on Computer Vision and Pattern Recognition (CVPR), Las Vegas, June 2016.
Licandro R., Rota P., Reiter M., Kleber F., Diem M., Kampel M., "Automatic Detection of Leukaemic Cells in Flow Cytometric Data for Minimal Residual Disease Assessment", poster, EuroScience Open forum (ESOF) – Marie Skłodowska-Curie Actions Satellite Event 'Research and Society', Manchester, July 2016.
Licandro R., Nenning K.-H., Kollndorfer K., Bartha-Doering L., Langs G., "Longitudinal influence assessment of paediatric stroke events on resting state networks", poster, 5th Biennial Conference on Resting State Brain Connectivity, Vienna, September 2016.
Licandro R., Langs G., Kampel M., "Spatio Temporal Modelling of Dynamic Developmental Patterns", poster, Medical Image Computing Summer School (MedICSS), London (United Kingdom), July 2017.
Licandro R., Hofmanninger J., Menze B., Weber M.-A., Langs G., "Whole body image analysis for diagnosing patients with monoclonal plasma cell disorders", European Project Space on Intelligent Systems and Machine Learning (EPS-IST), 7th International Conference on Pattern Recognition Applications and Methods, Funchal - Madeira (Portugal), January 2018.
Frauenstein L., Nenning K.-H., Schwartz E., **Licandro R.**, Bühler K., Langs G., „Dimensionality reduction for analysis of functional connectivity in the developing human brain", Forum of Neuroscience (11th FENS 2018), Berlin (Germany), July 2018.
Licandro R. and Schlegl T., Reiter M., Diem M., Dworzak M., Schumich A., Langs G., Kampel M., "Blast Identification in Childhood Acute Myeloid Leukaemia using WGAN Latent Space Embeddings, Medical Imaging Summer School (MISS 2018), Favignana, July 2018.

Licandro R., Hofmanninger J., M.-A. Weber, B. Menze, G. Langs, "Whole-body MRI based Lesion Prediction in Multiple Myeloma", European Congress of Radiology (ECR) 2019, Vienna, February 2019.

Licandro R., Hofmanninger J., Perkonigg M., Röhrich S., Weber M.-A., Wennmann M., Kintzele L., Piraud M., Menze B., Langs G., "Asymmetric Cascade Networks for Focal Bone Lesion Prediction in Multiple Myeloma", International Conference on Medical Imaging with Deep Learning (MIDL), London, July 2019. https://arxiv.org/abs/1907.13539

Licandro R., Hofmanninger J., Perkonigg M., Röhrich S., Weber M.-A., Wennmann M., Kintzele L., Piraud M., Menze B., Langs G., "Evolution Risk Prediction of Bone Lesions in Multiple Myeloma", European Congress of Radiology (ECR), March 2020.

Taymourtash A., Schwartz E., Nenning K.-H., **Licandro R**., Diogo M., Golland P., Grant E., Kasprian G., Prayer D., and Langs G., "Functional thalamocortical connectivity development revealed by in-utero resting state fMRI", In Proceedings of In Utero-MRI Workshop, Oxford, United Kingdom, January 2020.

Taymourtash A., Schwartz E., Nenning K.-H., **Licandro R.,** Sobotka D., Diogo M., Prayer D., Kasprian G., Langs G., "Evaluation of confound regression strategies for denoising in-utero resting-state functional MRI", OHBM 2020, June 2020.